4D reconstruction of the Aar Massif: An evolutionary history from a passive margin to the Central Swiss Alpine valleys

Inaugural dissertation

of the Faculty of Science,

University of Bern

presented by

Ferdinando Musso Piantelli

from Genova, Italy

Supervisor of the doctoral thesis:

Prof. Dr. Marco Herwegh

Prof. Dr. Alfons Berger

Institute of Geological Science

4D reconstruction of the Aar Massif: An evolutionary history from a passive margin to the Central Swiss Alpine valleys

Inaugural dissertation

of the Faculty of Science,

University of Bern

presented by

Ferdinando Musso Piantelli

from Genova, Italy

Supervisor of the doctoral thesis:

Prof. Dr. Marco Herwegh

Prof. Dr. Alfons Berger

Institute of Geological Science

Accepted by the Faculty of Science.

Bern,   The Dean

Prof. Dr. M. Herwegh

ABSTRACT

In this thesis, a methodology for the construction of an explicit large-scale 3D geological model of Alpine regions has been developed. The selected study area is the Aar Massif, the easternmost of the External Crystalline Massifs of the European Alps. This methodology allowed us to integrate a complete dataset into a large-scale 3D geological model of the main lithostratigraphic and tectonic boundaries of the massif. The development of a coherent structural interpretation of the area, coupled with the knowledge gained from the 3D structural modelling, has provided fundamental insights into its present-day 3D geometry. In addition, the application/integration of the 3D model with a wide range of complementary methods allowed us to design three scientific studies to unravel the evolution of the massif under different points of view. In fact, cross-section restoration, remote sensing techniques, drone mapping, 3D paleo-temperature distribution, and field-based rock hardness analyses were used to study the evolution of: (i) the crystalline units of the entire Aar Massif; (ii) the sedimentary cover of the massif; and (iii) the valley morphologies as a consequence of tectonic preconditioning. Three main outcomes summarise the obtained results: (1) The Aar Massif results from inversion of the former passive European margin, characterized by complex rifting structures that formed local half graben basins and a topographic high. Exhumation of the basement units occurred in a distinct in-sequence deformation style, where inherited along-strike variations in the thickness and density of the basement units induced a non-cylindrical exhumation resulting in the present dome-shape of the massif. (2) The variations in the thickness of sedimentary units, defined by the initial basement geometry of the passive margin, controlled the architecture of the developing nappes before the exhumation of the Aar Massif. The case of the Doldenhorn Nappe showed that large half grabens with thick sedimentary units developed a large amplitude nappe with a single detachment horizon. In contrast, the thinner sedimentary units developed a small amplitude nappe dissected by in-sequence set of detachment horizons. (3) The efficiency of erosional processes active in Alpine valleys is closely related to the inherited collisional tectonic architecture of the orogen. Indeed, variations in fault frequency and orientation, induced by the collisional dynamics, largely control the bedrock erosion processes, revealing an integral link between deep-seated collisional dynamics and long-term landscape erosion patterns.

This work highlights the importance of incorporating 3D considerations when investigating complex geological systems, such as a fold-and-thrust belt or an orogen. It is essential to broaden single cross-sectional interpretations into the third dimension and incorporate their immense along-strike 3D variability. This is the key to gaining a deep understanding of the evolution and dynamics of such systems.

AKNOWLEDGMENTS

Table of contents

Chapter I

The 3D Geological Model of the Aar Massif

Chapter II

4D geodynamic evolution of the Aar Massif: a deep dive into the upper crust of the European Alps

Chapter III

4D reconstruction of the Doldenhorn nappe-basement system in the Aar Massif: insights into late-stage continent-continent collision in the Swiss Alps

Chapter IV

The control of collisional tectonics over valley morphology: the case of the largest glacier in the European Alps

Appendixes

INTRODUCTION

With the recent improvements of modelling software and computational power, 3D geological modelling has become one of the leading techniques of exploring the complexity of the subsurface.

The production of geological models and their applications will increase significantly in the future as they provide additional information about the still largely unexplored subsurface. In fact, this new knowledge is expected to be crucial for the development of our future society, where the underground will be widely used. Extended underground 3D geological modelling will allow a better understanding of the subsurface geology, including structural systems (e.g., faults, shear zones, folds, tectonic nappes) and lithological disposition. This will lead to: more efficient planning for the construction of infrastructure, improved understanding of subsurface water circulation systems for geothermal energy, but also for drinking water, as well as advanced overview and volume estimation for geo-resources exploration.

For these reasons, the Swiss Geological Survey (swisstopo) has plans for the near future to cover the entire country with 3D geological models. However, the great variability of Switzerland's landscape and geological setting poses major challenges to such a program. Indeed, from the 'classic' fold-and-thrust belt of the Jura in the north, through the Molasse Basin (Plateau Molasses and imbricate units of the Subalpine Molasse) in the center, to the complexly overthrusted and folded inner core of the Central Alps in the south, the diversity and complexity of the geological subsurface is considerable. Furthermore, the landscape defines the type and quality of data available for 3D interpolation and modelling. On the one hand, the dense network of seismic lines and boreholes, available in the Jura and the Molasse regions, makes it possible to study the subsurface in great detail (e.g., Jura 3D, GeoMol projects). On the other hand, the lack of such dense data coverage in the less accessible Alpine regions is partly compensated by the reduced vegetation and the high relief. This allows the valuable exposure of geological contacts and structures, providing the great possibility to unravel the 3D geometry of geological bodies, the extrapolation of which yields important insight into the Alpine subsurface. Therefore, the style and type of interpolation methods in such 3D modelling projects must vary and be adapted to the geological context and the data available in the region under consideration.

In this framework, swisstopo founded this project "pilot study 3D-model of the Aar Massif" to develop a methodology and workflow for the generation of large-scale explicit 3D geological models of the Alpine regions. The selected study site is the Aar Massif, the easternmost of the External Crystalline massifs of the European Alps. The Aar Massif was chosen because of the detailed cartographic work and the more than 100 years of research carried out in the area (see Chapter 1). Such a large compilation of scientific

work and mapping provided an excellent initial dataset for understanding the geological architecture at the regional scale, which is fundamental for the construction of a 3D geological model.

Our construction of a large-scale 3D geological model of the Aar Massif, has allowed to integrate various structural, thermochronological and geochemical studies scattered across the Massif into one coherent structural interpretation for the first time (e.g., Burkhard, 1988; Krebs, 1925; Collet and Paréjas, 1928; Hänni and Pfiffner, 2001; Herwegh and Pfiffner, 2005; Pfiffner et al., 2011; Berger et al., 2016, 2017, 2020; Wehrens et al., 2016, 2017; Berger et al., 2017; Schneeberger, 2017; Herwegh et al., 2017, 2020; Mair et al., 2018; Nibourel et al., 2018, 2021a,b; Baumberger et al., 2022; Goncalves et al., 2012; Krayenbuhl and Steck, 2009). This effort, coupled with the knowledge gained from 3D structural modelling, have provided not only fundamental insights into the 3D shape of today's Aar Massif but also allowed to unravel the evolution of the entire Massif, from the paleogeographic precursor structures, over the onset of the late-stage Alpine collision (30 Ma) till today's active landscape shaping processes. Three scientific studies have been developed through the application/integration of the 3D model with a wide variety of complementary methods. In fact, cross-section restoration, remote sensing techniques, drone mapping, knowledge on the 3D paleo-temperature distribution and field-based rock hardness analysis allowed us to investigate the following scientific questions:

1. How do the geometry of the pre-collision passive margin, the rheology and density of the crust, and the inhibition/reactivation of inherited crustal structures influence the late-stage thick-skinned evolution of an orogen?

2. What is the effect of inherited structures and along strike variations in the thickness of sedimentary units on the evolution of a fold-and-thrust belt?

3. To what extent is the efficiency of the erosive processes active in a mountain chain influenced by tectonic preconditioning due to deep-seated collision dynamics?

Building on the above research questions, the studies have progressively focused on: (i) the evolution of the crystalline units of the entire Aar Massif; (ii) the evolution of the sedimentary cover of the massif; and (iii) evolution of the valley morphology of the largest European glacier in the Alps, located in the centre of the Aar Massif.

Consequently, this thesis is structured into four chapters, which are enclosed between the introduction and a conclusion section. The chapters are presented and briefly outlined below. The contribution of each author is given at the end of each chapter. Supplementary material for Chapters 2, 3 and 4 are included as Appendices at the end of the thesis.

Chapter I: *The 3D Geological Model of the Aar Massif*

This chapter constitutes a technical report describing the workflow developed in this PhD project to process geological information for the construction of a large-scale 3D geological model of the subsurface of mountainous regions.

Chapter II: *4D geodynamic evolution of the Aar Massif: a deep dive into the upper crust of the European Alps*

In this chapter, explicit three-dimensional geological modelling of the Aar massif, cross-section restoration coupled with metamorphic peak temperature data, allowed us to construct a 4D geodynamic evolution of the basement units of the massif during the late stage of Alpine orogeny (22-0 Ma). Here we unravel how inherited along-strike variations in the thickness and density of the basement units induced a non-cylindrical exhumation of the massif, resulting in the present dome shape of the massif.

Chapter III: *4D reconstruction of the Doldenhorn nappe-basement system in the Aar massif: Insights into late-stage continent-continent collision in the Swiss Alps*

In this chapter, a three-dimensional model of the western Aar massif and sedimentary cover, in combination with balanced cross-section restoration were used to reconstruct the evolution of the Doldenhorn nappe during the late stage Alpine orogeny (30 to 0 Ma). Such a nappe-basement system provided an excellent example to document the influence of inherited structures of parts of a former proximal passive continental margin and its along-strike variations in the thickness of the sedimentary units on the evolution of a fold-and-thrust belt. This manuscript was published in September 2022 in Tectonophysics.

Chapter IV: *The control of collisional tectonics over valley morphology: the case of the largest glacier in the European Alps*

In this chapter, remote sensing and field-based rock hardness analyses allowed us to demonstrate how variations in fault frequency and orientation across the Central Aar Massif control the local erodibility of the valley of the Aletsch Glacier, the largest glacier of the European Alps. The results of this chapter highlight how tectonic preconditioning exerts a first-order control on the efficiency of erosion in the mountain chain, revealing an intriguing link between deep-seated collisional dynamics and surface-based mountain shaping. This manuscript was published in May 2023 in Terra Nova.

Chapter I
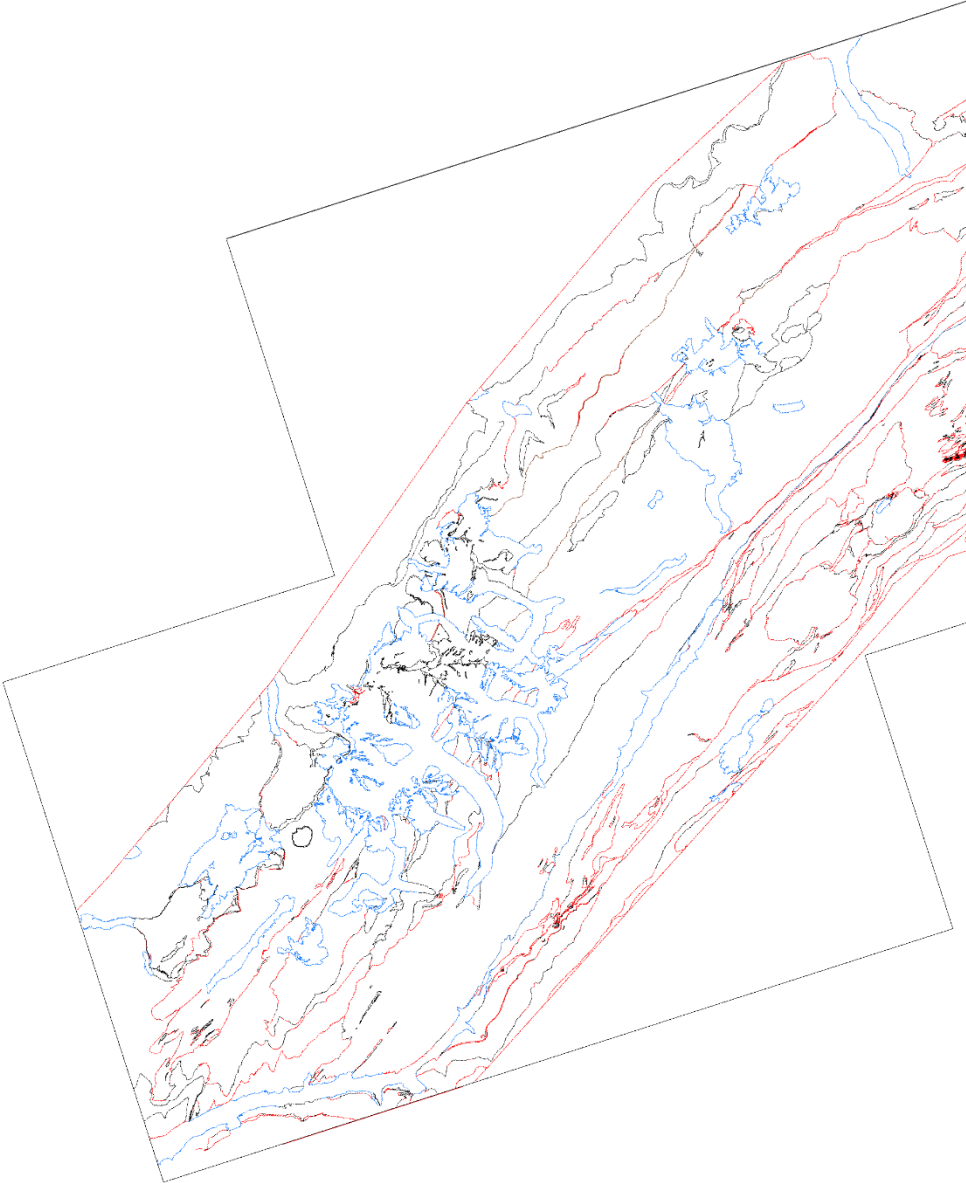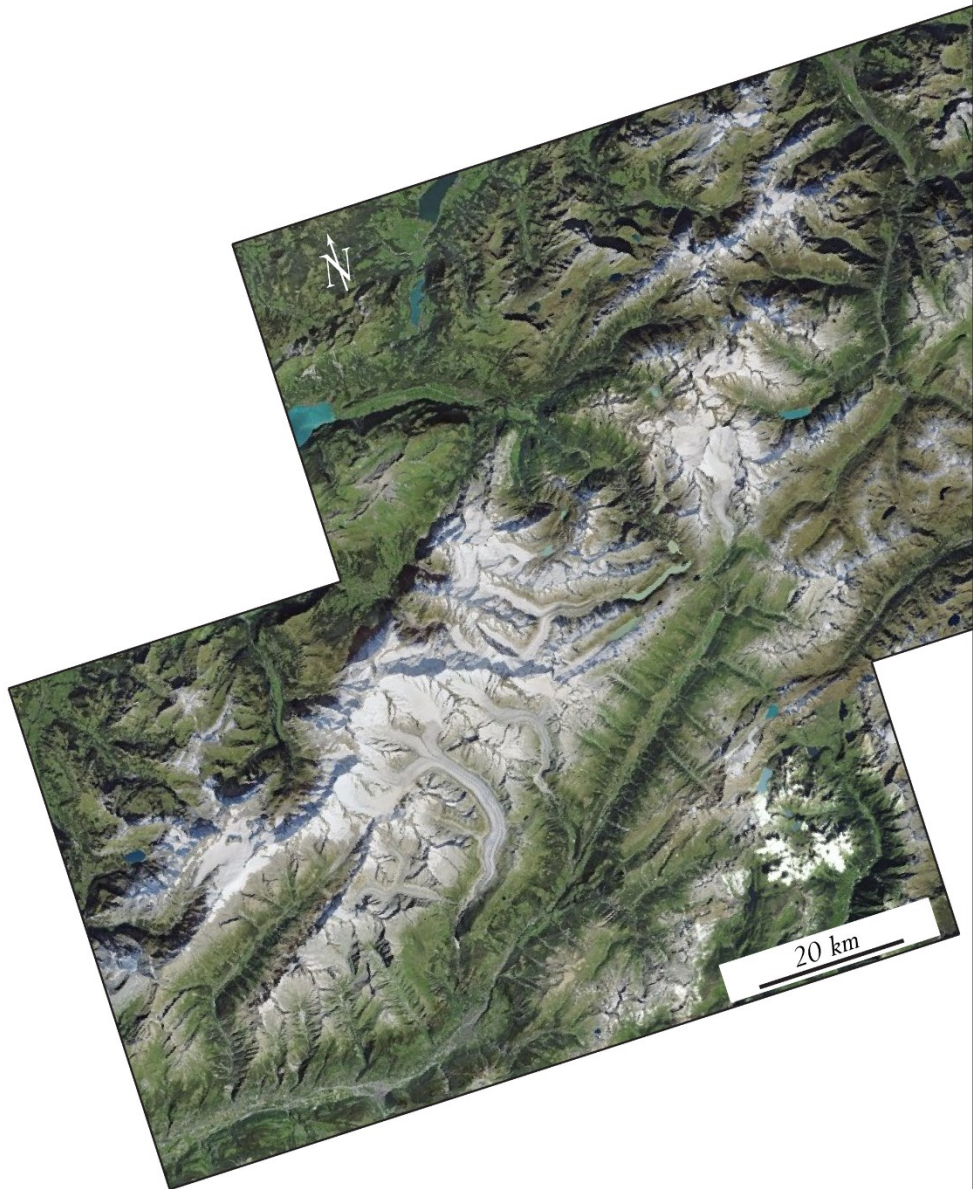
Orthophoto and main geological boundaries of the western and central Aar Massif
SWISSIMAGE (swisstopo)

The 3D Geological Model of the Aar Massif

Ferdinando Musso Piantelli[1,2*], Michael Wiederkehr[2], Eva Kurmann[2], Alfons Berger[1], Roland Baumberger[2], Andreas Möri[2] and Marco Herwegh[1]

[1] *Institute of Geological Sciences University of Bern, Baltzerstrasse 1+3, 3012 Bern, Switzerland*

[2] *Swiss Geological Survey, Federal Office of Topography swisstopo, Seftigenstrasse 264, 3084 Bern, Switzerland*

Keywords	Abstract
Explicit 3D geological modelling Aar Massif Alpine regions	*Due to the lack of underground information, 3D geological modelling in mountainous environments is a challenging task. However, the high relief, sparse vegetation and the large number of scientific studies rendered the Aar Massif (Central Alps, Switzerland) an excellent area for advanced surface-based explicit 3D modelling. A 1:25'000 scale geological map was produced by verifying and harmonising a 2D geological dataset compiled for the study (published maps, strike and dip data, tunnel and seismic data). The software package Move™ was then used to generate a network of regularly spaced (500 m) NNW-SSE trending geological cross sections throughout the area. By applying 3D interpolation and meshing techniques between the cross sections and the surface outcrop lines (i.e., spline curve method), lithological and structural boundaries were then interpolated to generate 3D surfaces of each horizon of the model. Following this approach, a large-scale 3D geological model of the main lithostratigraphic and tectonic boundaries of the Aar Massif has been constructed. The 3D model incorporates field observations, outcrop-scale structural analyses, tunnel and literature data, maps and large-scale seismic profiles. This chapter provides a technical report that describes the workflow and methods used to construct the 3D model of the entire Aar Massif.*

1.1. INTRODUCTION

3D modelling of complex and irregular geological bodies is an expanding discipline that combines two-dimensional cartographic and structural data managed by GIS technology. The main objective of this PhD project was to construct a large-scale 3D geological model of the main stratigraphic and tectonic boundaries of the Aar Massif, located in the Central Alps of Switzerland. The area has an average elevation of ca. 2200 m a.s.l. and extends over 2000 km^2, of which 320 km^2 are covered by glaciers (Fig. 1.1). Due to the lack of borehole and subsurface information, 3D geological modelling in such mountainous environments is a challenging task. However, the high relief, sparse vegetation and subsurface data provided by the Lötschberg and Gotthard railway tunnels (see traces in Fig. 1.1) and seismic sections (Pfiffner
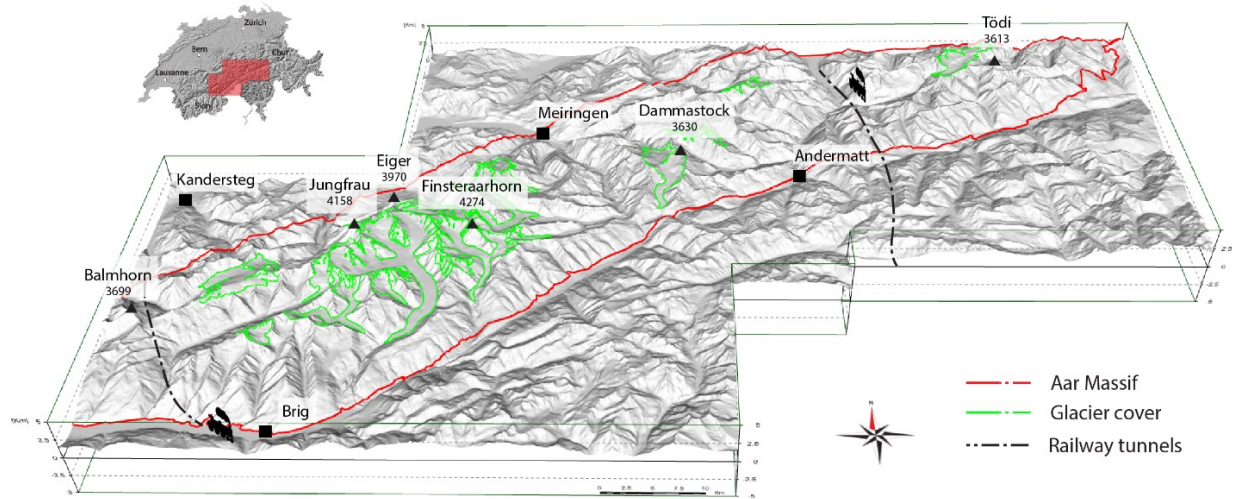
Figure 1.1. 3D overview of the study area. The digital elevation model highlights the great topographic relief of the area. The overview shows the geographical locations, the localities covered by major glaciers, and the traces of the Lötschberg (west) and Gotthard (east) railway tunnels.

et al., 1997) make the study area suitable for advanced surface-based 3D explicit modelling. The Aar Massif was selected for this study because of the more than 100 years of research conducted in the area and the recently published special geological map 1:100'000 of the Aar Massif, Tavetsch and Gotthard Nappes (Berger et al., 2017). Such a large compilation of scientific work and geological mapping provided an excellent starting point for understanding the geological architecture at the regional scale, which is fundamental for the construction of a model. This chapter constitutes a technical report describing the workflow developed in this PhD project to process geological information for the construction of a large-scale 3D geological model of the subsurface of mountainous regions.

1.1.1 Workflow and modelling subdomains

Due to the large dimensions of the massif, the model could not be designed and constructed all at the same time. In addition, the 3D dome-shape of the massif and the curvature of the northern rim posed a challenge to the geological modelling process. For this reason, two strategic decisions were made at the beginning of the project. The Aar Massif was divided into three modelling sub-areas, which were modelled separately and finally assembled together (Fig. 1.2a). It was then decided to start modelling the massif from the western side (Area 1), then move to the eastern side (Area 2) and finally model the central region of the massif (Area 3). Indeed, important constraints for the construction of the modelled surfaces were provided by the basement/sediment contact, which is
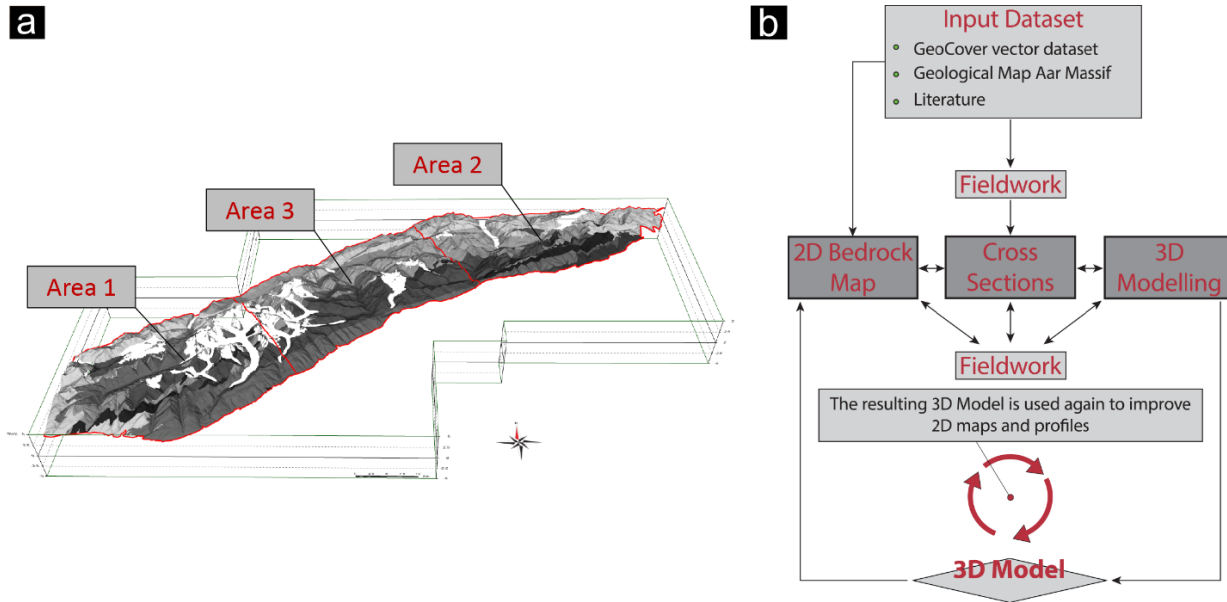
Figure 1.2. (a) 3D view of the Aar Massif and relative subdivision into modelling areas. (b) Workflow diagram illustrating the steps taken to generate the 3D geological model of the Aar Massif.

extensively outcropping on the western and eastern sides of the massif but is almost entirely eroded in the central part. The related uncertainties present in the central area were then constrained by the two models on the sides of the massif. Figure 1.2b shows the workflow used to construct the model, which consists of three main stages: (i) development of a validated and homogenised bedrock map of the main lithostratigraphic and tectonic boundaries of the study area; (ii) construction of geological sections; and (iii) 3D interpolation of the constructed geological sections and generation of the 3D geological model. In addition, these steps required fieldwork to achieve uniform and consistent data coverage and to verify information in key areas. Following this approach, the 3D model incorporates field observations, outcrop-scale structural analyses, tunnel and literature data and large-scale

seismic profiles. The following paraphs of the chapter are structured according to these three stages.

1.2 GEOLOGICAL DATA COMPILATION, MAPPING, AND FIELDWORK

This section describes the 2D work that was carried out prior to the actual 3D modelling. A stratigraphy for the project was defined and a 2D geological dataset was compiled from all the geological data available in the area. This dataset was then revised and harmonized in a 1:25'000 scale bedrock map of the major lithostratigraphic and tectonic boundaries of the cover and basement units of the Aar Massif.

1.2.1 The Aar Massif 3D project legend

The Geological Special Map 1:100'000 of the Aar Massif, Tavetsch and Gotthard Nappes

Aar Massif 3D project legend
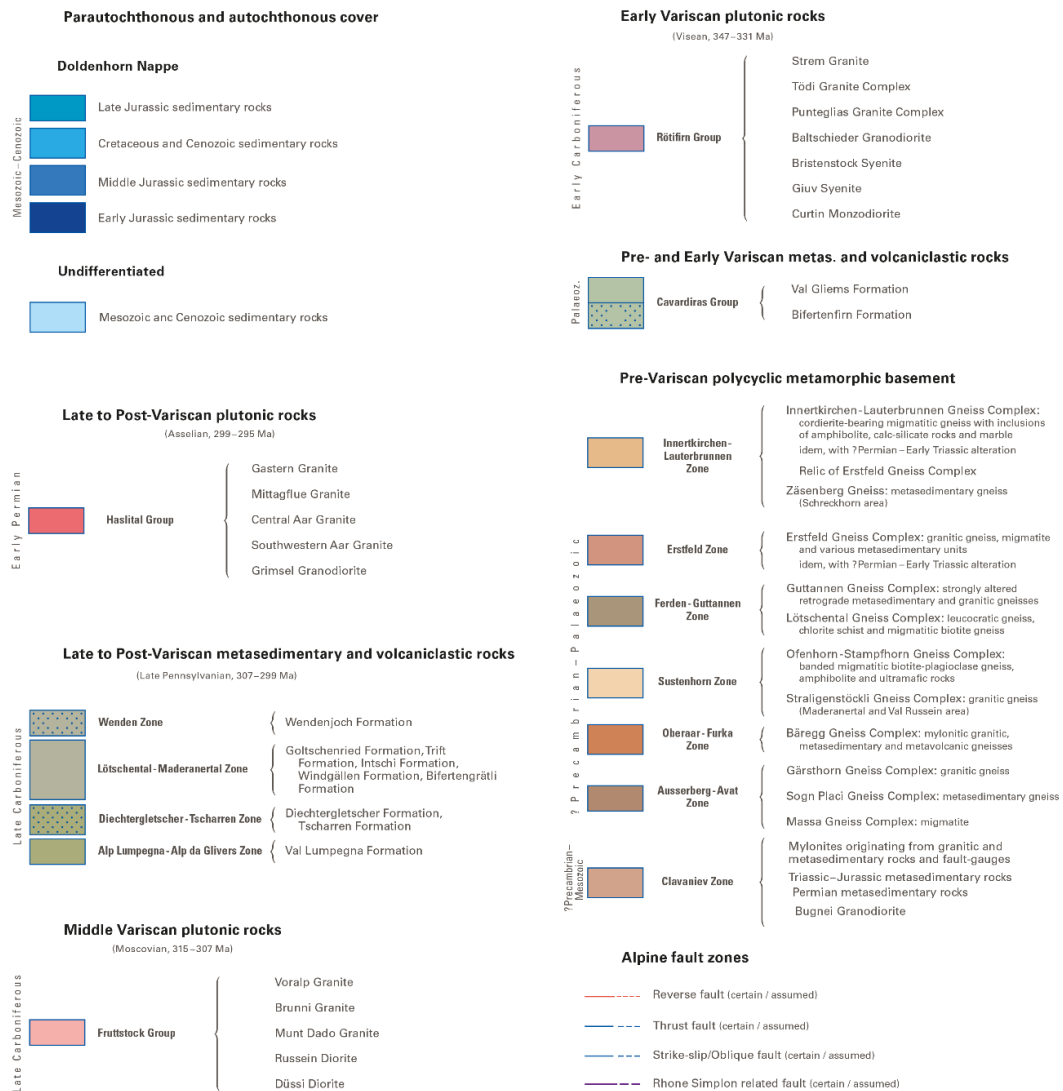
Figure 1.3. Legend of the Aar Massif 3D project, the different lithological units have been subdivided into five main groups: (i) Pre-Variscan polycyclic metamorphic basement; (ii) Plutonic rocks; (iii) Permo-Carboniferous metasedimentary and volcaniclastic rocks; (iv) Para- and autochthonous sedimentary cover; (v) Alpine fault zones.

published by the Swiss Geological Survey (Berger et al., 2017) was used to assess the geological architecture at the regional scale andto define the map legend and consequently the modelling units. Based on the work of Abrecht (1994) and Berger et al. (2017), the modelling units were divided into five main groups as follows (Fig. 1.3).

1.2.1.1 *Pre-Variscan polycyclic metamorphic basement*

This group consists mainly of gneisses and minor parts of schists, migmatites and

amphibolites which form the pre-Variscan polycyclic metamorphic basement of the massif. Volumetrically, these gneissic complexes are the most dominant rock type in the area. The term polycyclic refers to the complex tectono-metamorphic history recorded in these rocks. The basement has been divided into seven zones based on the lithological, mineralogical and textural character of the rocks: (1) Innertkirchen-Lauterbrunnen Zone, (2) Erstfeld Zone, (3) Ferden-Guttannen Zone, (4) Sustenhorn Zone, (5) Oberaar-Furka Zone, (6) Ausserberg-Avat Zone, and (7) Clavaniev Zone.

1.2.1.2 *Plutonic rocks*

Plutonic rocks intruded the basement units in early, middle and late to post-Variscan times. On the basis of the age of the intrusions events these plutonic rocks were divided into three groups (1) Haslital Group (late to post-Variscan intrusions), (2) Fruttstock Group (middle Variscan intrusions), and (3) Rötfirn Group (early Variscan intrusions).

1.2.1.3 *Permo-Carboniferous metasedimentary and volcaniclastic rocks*

These sequences of clastic, volcaniclastic and volcanic rocks were deposited in troughs that opened during syn- to post-collisional Variscan tectonics. These deposits are small in size and appear as thin discontinuous bands, steeply dipping and oriented parallel to the strike of the massif. However, they proved to be crucial for the Jurassic and Paleogene–Neogene Alpine evolution of the massif (see Chapter 2

and 3). For this reason, they have been included in the modelled units, even though they are at the limit of the resolution of the 3D model. These deposits are subdivided on the basis of depositional time and rock associations: (1) Wenden Zone, (2) Lötschental-Maderanertal Zone, (3) Diechtergletscher-Tscharren Zone, (4) Alp Lumpegna-Alp da Glivers Zone, and (5) Cavardiras Group.

1.2.1.4 *Para and autochthonous sedimentary cover*

With the exception of the units belonging to the Doldenhorn Nappe (Western Aar Massif), most of the sedimentary cover of the Aar Massif was kept undifferentiated. The target horizon for this project was the sedimentary basement/cover contact, often outlined by the Triassic Röti Dolomite. This lithostratigraphic unit was included as a horizon in the model. For the case study of the Doldenhorn Nappe, described in Chapter 3 (Musso Piantelli et al., 2022), the sedimentary units of the nappe were subdivided into: (1) Early Jurassic, (2) Middle Jurassic, (3) Late Jurassic, and (4) Cretaceous and Cenozoic sedimentary rocks.

1.2.1.5 Alpine *fault zones*

During the Alpine collision, the Aar Massif underwent a long history of exhumation with the generation of faults and shear zones. Given the ductile and brittle nature of the structures, we generally refer to them as faults, following the nomenclature of Sibson (1977). Based on the kinematics of the structures described in previous studies (Herwegh et al., 2017, 2020;
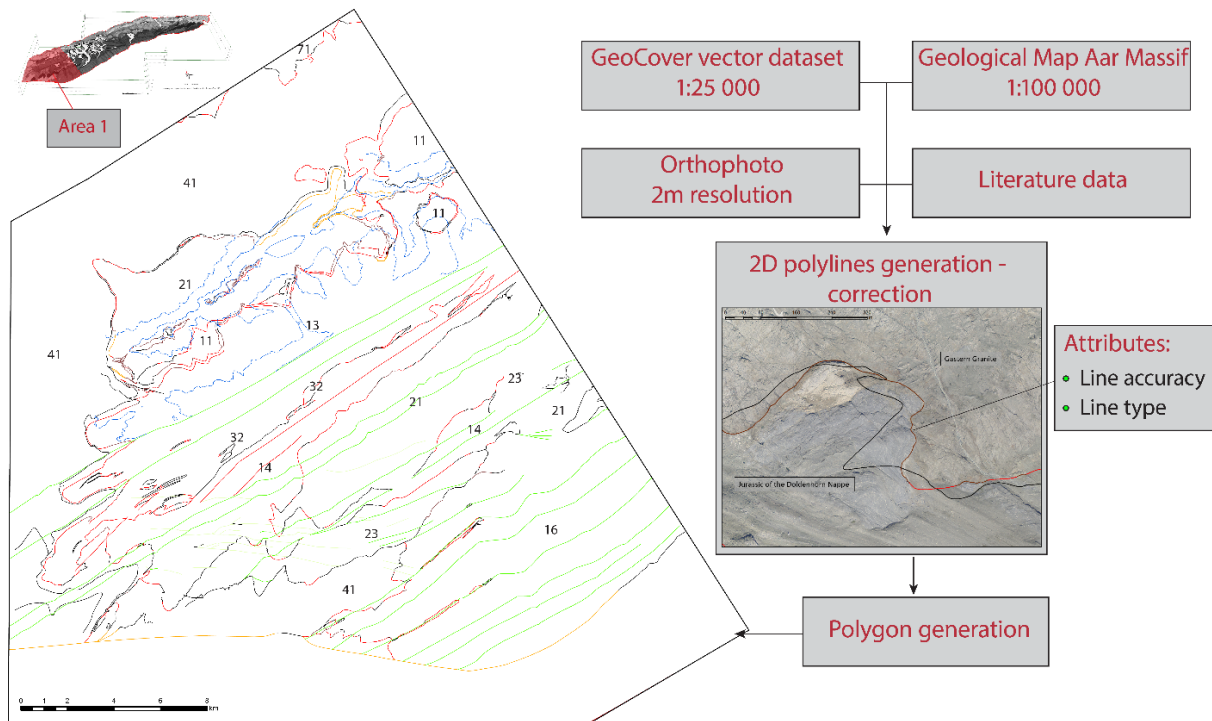
Figure 1.4. Workflow diagram summarizing the validation and homogenisation process of the compiled 2D dataset. The orthophoto image shows an example of updating an incorrectly marked line of the GeoCover vector dataset. The lines were corrected, interpreted below Quaternary cover and renamed according to the Line accuracy and Line type attributes. The result of the process is the generation of multiple polylines that are then converted to polygons after label positioning for the geological map redaction.

Nibourel et al., 2021; Wehrens et al., 2016, 2017) and in the work carried out for this project, the faults have been subdivided into: (1) reverse faults, (2) thrust faults, (3) strike slip/oblique faults, and (4) faults related to the Rhone-Simplon fault system.

1.2.2 2D dataset compilation

The 2D dataset was compiled from a wide range of data published by swisstopo (untill 2022) or in scientific publications. This dataset consists of the following items:

- *Maps:* The initial dataset was compiled from the following pre-existing maps: Krebs (1925), Collet and Paréjas (1928), Mair et al. (2018), and the GeoCover vector datasets (swisstopo) containing the following mapsheets: LK no. 1191, 1192, 1193, 1210, 1211, 1212, 1213, 1229, 1230, 1231, 1232, 1233, 1248, 1249, 1250, 1251, 1252, 1267, 1268, 1269, 1270, 1287, 1288, and 1289. In addition, the Geological Special Map 1:100'000 of the Aar Massif, Tavetsch, and Gotthard Nappes of the Swiss Geological Survey (Berger et al., 2017) was used to understand the geological architecture at the regional scale and to define the legend of the map.

- *Geological profiles:* Profiles of the Geological Atlas of Switzerland, published profiles of: Pfiffner et al. 2011; Nibourel et al. 2021; Hänni and Pfiffner, 2001; Herwegh and Pfiffner, 2005; Krayenbuhl and Steck, 2009 and Mair et al., 2018.

- *Seismic data:* Seismic profile published in Diehl et al., 2021; Pfiffner et al., 1997, NEAT 9001 and lines W1, C1 and E1.

- *Orthophoto:* SwissImage with a raster resolution of 0.25 x 0.25 m; provided by swisstopo

- *Digital Elevation Model (DEM):* Swiss ALTI3D with a downsampled raster resolution of 2 x 2 m, version 2013 provided by swisstopo

- *Hillshade maps:* Derived from the DEM and generated in ArcGIS (ESRI's ArcGIS, v.10.8).

- *Structural work:* The structural work compiled from the PhD theses of Baumberger, 2015; Wehrens, 2015; and Nibourel 2019.

1.2.3 Data validation, interpretation below Quaternary cover and fieldwork

Due to discrepancies between the individual map sheets, or scientific publications, the entire dataset underwent a validation and homogenisation process to produce a geologically consistent map. The process was carried out in in ArcGIS (ESRI's ArcGIS, v.10.8) and is summarised in the diagram in Figure 1.4. Lithological and structural boundaries were verified and updated remotely using with high-resolution orthophotos (SwissImage with a

raster resolution of 0.25 x 0.25 m; provided by swisstopo), a high-resolution digital elevation model (DEM) (swiss ALTI3D with a downsampled raster resolution of 2 x 2 m, version 2013, provided by swisstopo). In the case of Quaternary cover (e.g., moraine deposits, glaciers), the underlying trends of stratigraphic and tectonic boundaries were interpreted.

As shown in Figure 1.4, during the verification and updating process of the lithological boundaries and structures, polylines were generated in ArcGIS with two attributes. The first was *Line Accuracy* in values from 1 to 4, where: *1.* corresponded to line overtaken by the GeoCover vector dataset. *2.* Line modified with high level of accuracy. *3.* Line interpreted with high degree of confidence, i.e. below a thin ice/Quaternary cover for a length < 500m. *4.* Line interpreted with low degree of confidence, i.e. below thick ice/Quaternary cover for a length > 500m. The second one was *Line type*, indicating the nature of the line e.g., lithological boundary, fault zone.

To extend the structural dataset, a fault zone map (1:25'000) was generated on remotely sensed images following the workflow of Baumberger et al. (2022), see also Musso Piantelli et al. (2023). On the basis of the kinematics of the structures described in previous studies and field information the structural sets were subdivided as indicated in Section 2.1.5. Data were verified in the field at key locations by mapping and collecting structural field data (see Musso Piantelli et al.,
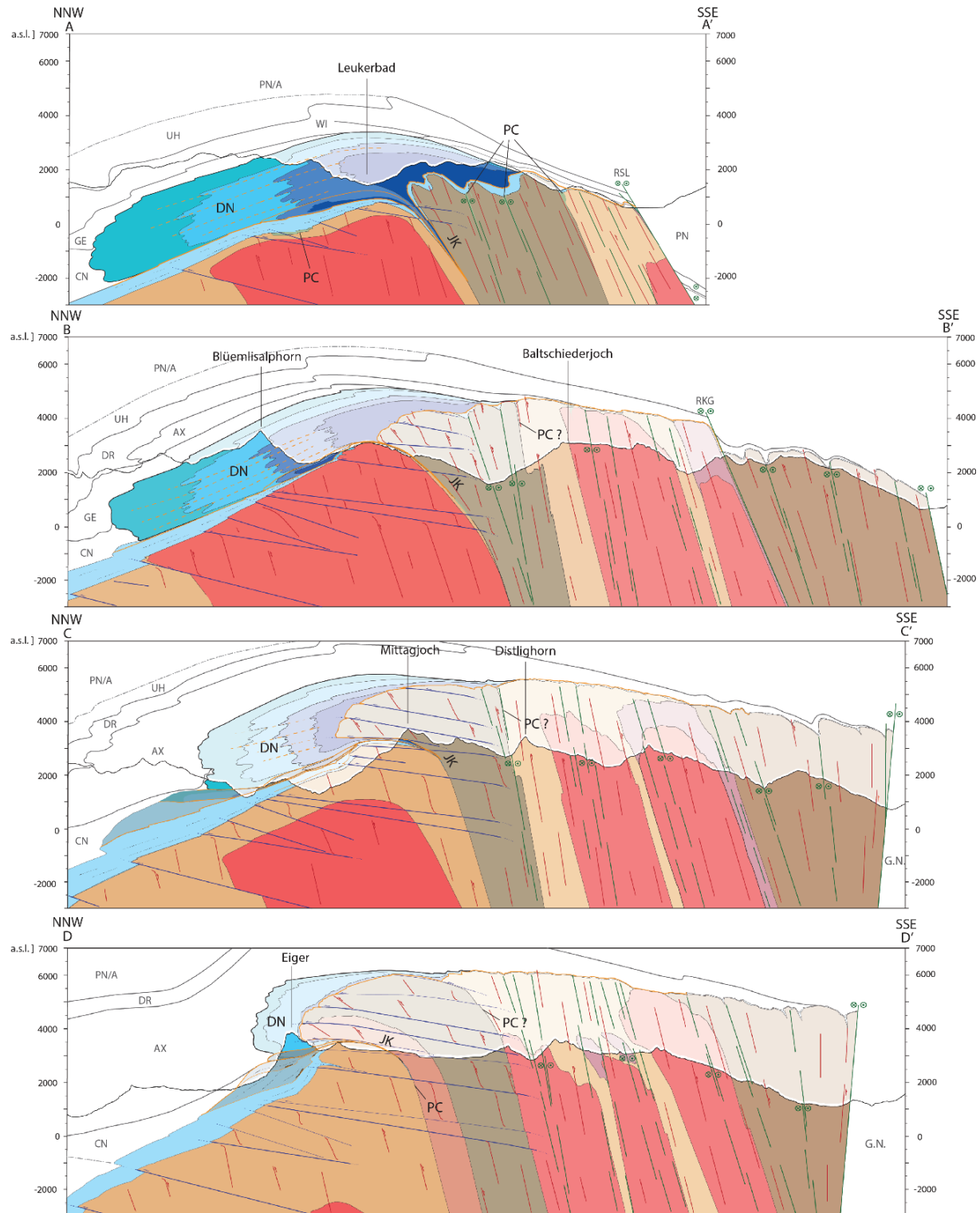
Figure 1.5. Reference geological cross-sections through the Area 1 of the massif (see Fig. 1.7 for cross-section traces). In the profiles are indicated: the structural deformation phases, the overlying Helvetic nappes (GE, Gellihorn; WI: Wildhorn; AX: Axen; DR: Drusberg; UH: Ultrahelvetic), including the Cenozoic sediments (CN), and the Penninic and Austroalpine sediments (PN/A). In section A-A' and B-B' the outline of the overlying upper Helvetic nappes was modified after Herwegh and Pfiffner (2005) and Hänni and Pfiffner (2001), respectively.
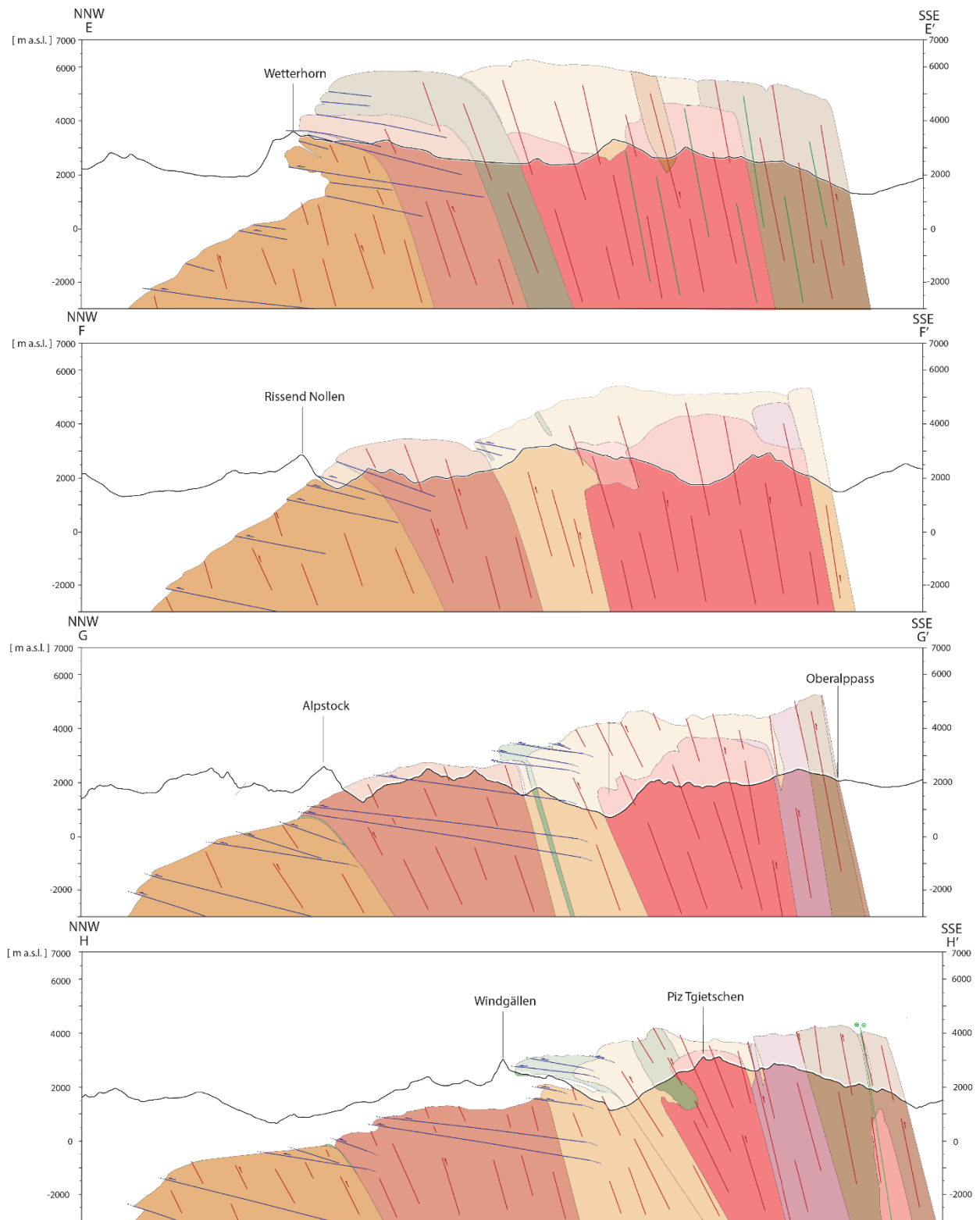
Figure 1.6. Reference geological cross-sections through the Areas 2 and 3 of the massif (see Fig. 1.7 for cross-sections traces). Profile HH'was modified after Nibourel et al., 2021.
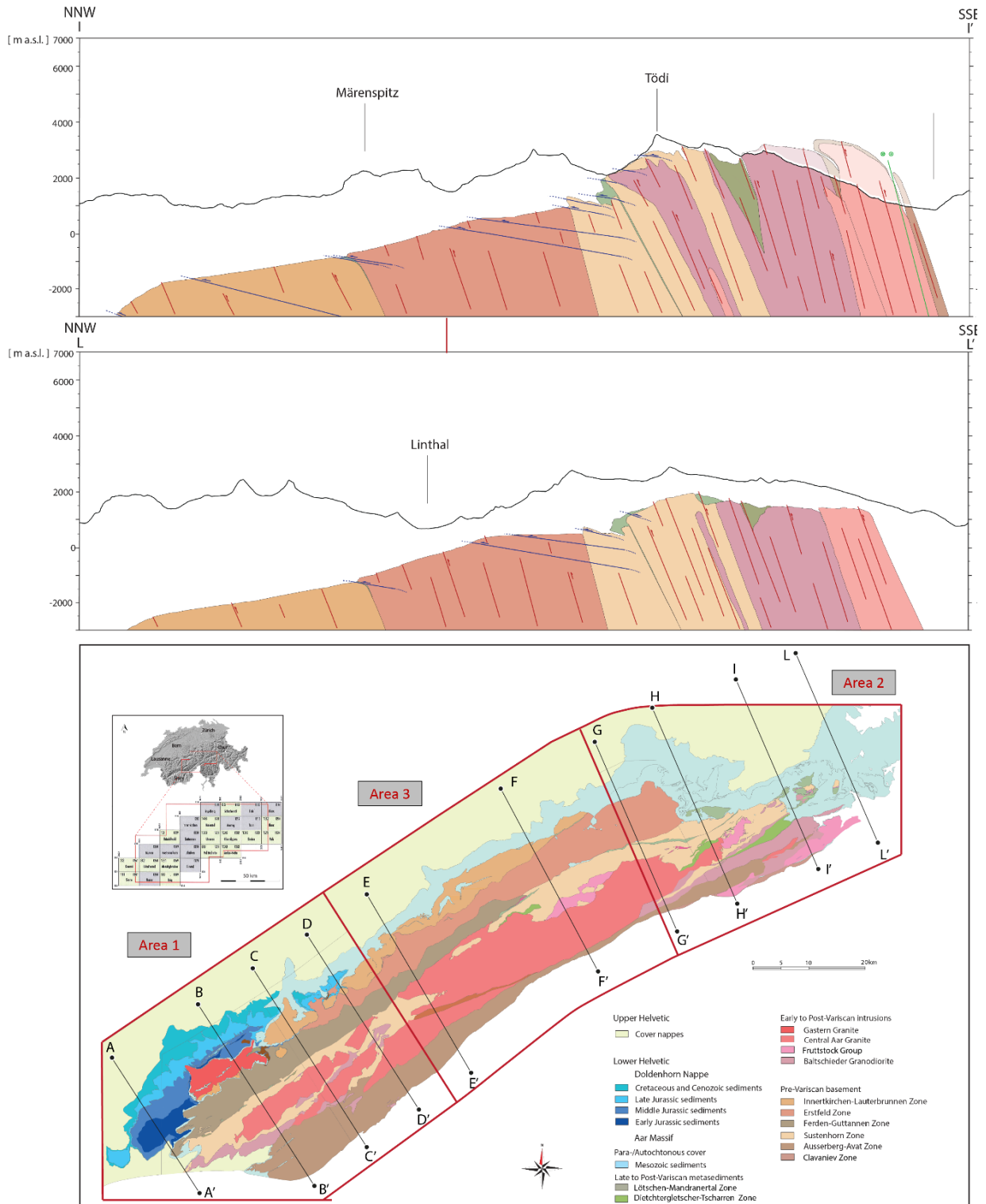
Figure 1.7. Reference geological cross-sections through the Area 2 of the massif and map showing the cross-sections traces.

2022 and 2023). The kinematics of the structures were characterised by the compilation of over 2500 field measurements (fault planes dip direction/dip angle, and stretching lineations; of which over 1000 collected in this study), and by the generation of rose-plots automatically derived from the striking of the remotely-detected structures (see Chapter 2). Based on this collected information, the structure datasets were subdivided as described in section 2.1.5.

1.2.4 The Aar Massif 3D Project Map

The result of the compilation and validation process was the generation of the bedrock project map of the massif. The map includes all the lithological units and structural elements, which were then used as the initial dataset for the construction of the 3D geological model. The map was printed at the scale of 1:100'000 as attachment for this contribution Attachment 1.

1.3 REFERENCE GEOLOGICAL CROSS-SECTIONS

The construction of geological cross sections is a crucial step in linking the second and third dimensions. To develop a structurally consistent interpretation of the massif's
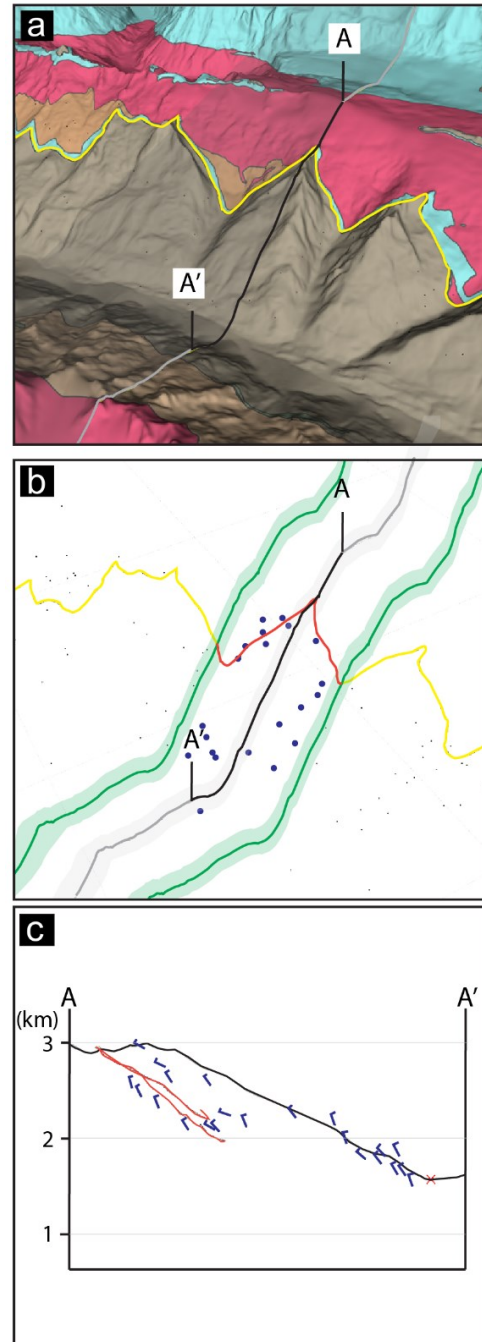
Figure 1.8. Sequence of images showing an example of projection technique used to construct the geological contact of a profile. (a) All the available data are projected onto the DEM and imported in Move™. (b) All the data lying within 2 km on either side of the cross-section are selected. (c) The data are normally projected onto the cross-section. Red line: sediment/basement contact; blue symbols: dip/strike indications; x point: intersection with fault plane. As can be seen on the section, the over 1 km exposure of the outcrop line and the strike and dip information provide important constraints for estimating the trend of the geological contact at depth.

underground, ten reference geological cross-sections have been constructed along the strike of the massif, perpendicular to the strike of the large-scale structures and boundaries (A – A'; to L - L' in the area; see Figs. 1.5,1.6,1.7; traces in Fig. 1.7). Four cross sections were located in Area 1, four in Area 2 and two in Area 3. Fewer profiles were required in Area 3, as a large number of scientific studies have already focused on the central regions of the massif. For the construction of the geological cross-sections, surface and contacts line intersections were collected in the software Move™ (Petex, v.2019.1; Fig. 1.8a). Dip-data information, as well as lithological and tectonic boundaries as well as literature data in the vicinity (2000 m) of the cross sections, were orthogonally projected onto the latter to better constrain the geometric and structural relationships of the different units (e.g., Fig. 1.8b,c). The resulting profiles were used as guideline for the generation of the constructional cross section during the 3D modelling phase.

1.4   3D GEOLOGICAL MODELLING

The bedrock map, lithological and tectonic boundaries, and strike/dip data were vertically projected onto a high-resolution digital elevation model (DEM) (swissALTI3D with a raster resolution of 2 x 2 m, version 2013 provided by swisstopo, Fig. 1.9a) and then loaded into the software Move™ (Petex, v.2019.1). Throughout the area, and based on the structural concepts developed with the reference geological profiles, a multiple set of over 330 constructional geological cross

sections was generated with a regular spacing of 500 m (Fig. 1.9b). With an alternation of projection techniques, and mesh generation along each constructional cross-section, the geological boundaries and structures were developed with lines in an along length sampling interval of 25 m (Fig. 1.9b). Then, by selecting all the digitized lines for each modelling horizon and by applying 3D interpolation (meshing technique: spline curve method), a mesh (triangulated surface) was developed for each of the modelling horizons (Fig. 1.9c).

The 3D geological model of the study area thus consists of a series of meshes representing the major lithological unit and tectonic boundaries. The meshes have a grid size of 25 m and were designed to fulfil the principle of a watertight or sealed model. Therefore, each stratigraphic horizon is defined continuously over the area of interest and has clean intersections with either lateral boundaries, faults, unconformities, or erosion surfaces (e.g., Caumon et al., 2004).

1.4.1 Uncertainties estimation

The 3D geological model has a maximum resolution at the surface of 1:25'000, which is determined by the scale of the 2D input dataset (see Section 2.3). Moving away from the surface and the tunnel data the resolution varies within the model. However, within 400 and 4200 m a.s.l., representing the highest and lowest topographic points of the area, the model has the maximum resolution. A test performed with the modelled surfaces of the

a 2D data loading and projection onto 3D digital elevation model
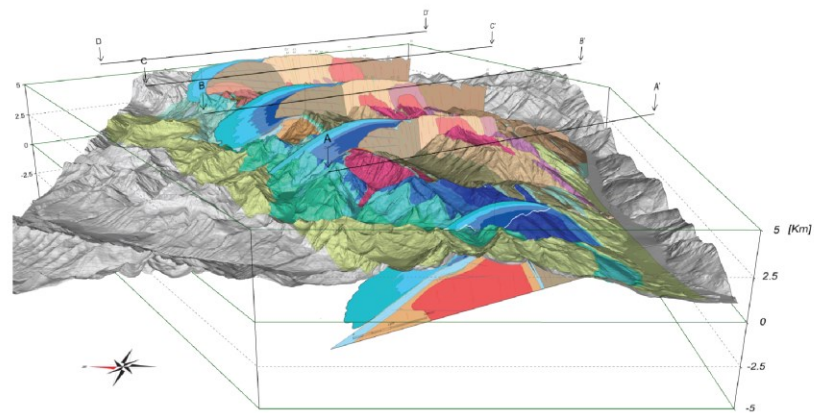
b Multiple cronstructional cross-section generation and digitalization

Digitalized horizons along cronstructional cross-sections

c 3D interpolation
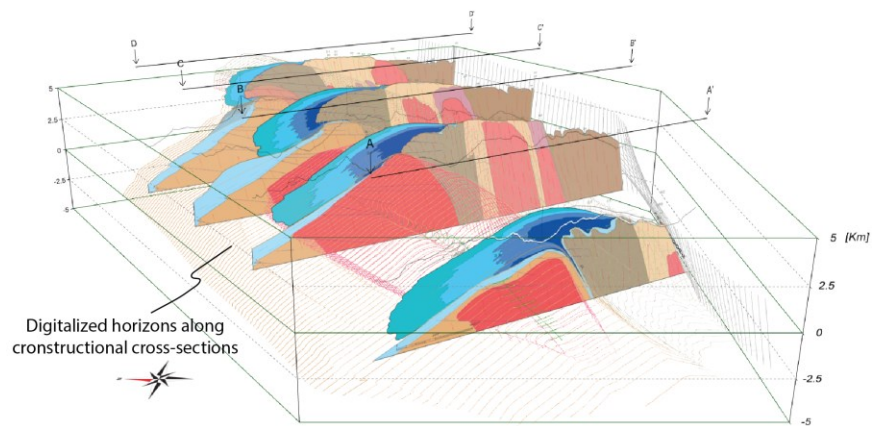
Surface of the interpolated horizon
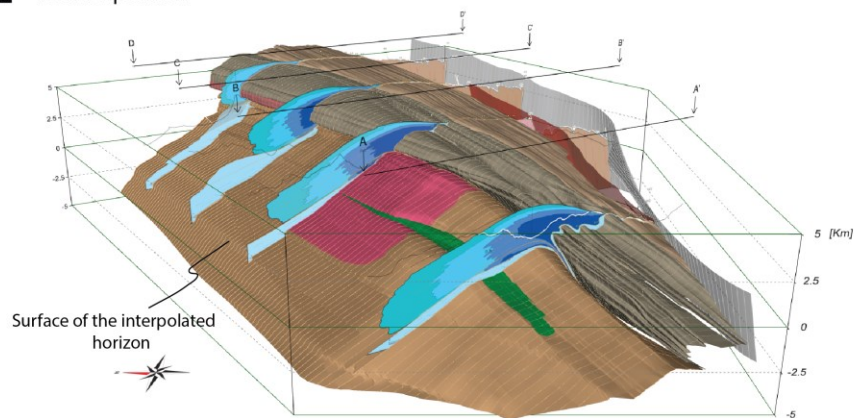
Figure 1.9. Series of 3D block diagrams that show the modelling sequence followed for constructing the 3D geological model of the massif. The example is taken by the model generated for Area 1 in the western Aar Massif. (A) Projection of 2D dataset onto the 3D digital elevation model and loading of the geological cross-sections. (B) Generation of regularly 500 m spaced constructional cross-sections and line digitalization of the modelled horizons along the sections. (C) 3D interpolation: by applying 3D projection and meshing techniques, surface and cross-sections boundaries are interpolated generating surfaces for each horizon of the model.

29
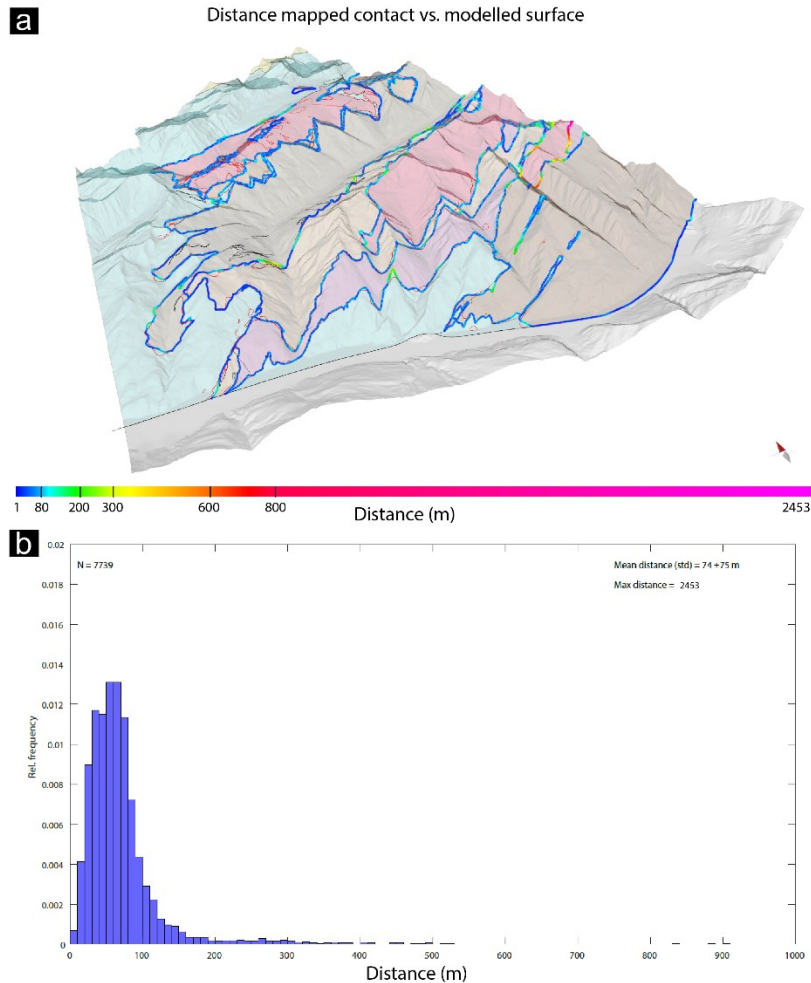
Figure 1.10. (A) 3D view of the deviation of the Modelled surfaces from the input lithostratigraphic boundaries. Most of the surfaces are less than 100 m far from the original input lines (blue colours). Only one outlier in the East indicates a >2000 m deviation, but this was due to a wrong exportation of the surface. (B) The density plot illustrates the distances of modelled surfaces from the input boundaries.

Area 1 (Fig. 1.10) indicated that most of the modelled surfaces lie within a distance of 200 m from the input lithostratigraphic contacts (average 74 ±75 m), indicating an uncertainty of ±200 m uncertainty for the modelled surfaces. The interpretation in air of the basement/sediment contact was constrained by the 3D shape of the contact on the western, eastern sides and the northern front of the massif. At depth, the profiles have been drawn with a resolution of 1:25'000, however uncertainties deriving from (i) interpretation, (ii) lack of data, (iii) quality of the data were not estimated.

Uncertainties estimation in 3D geological models is an expanding discipline. Research is making progresses in the last years regarding developing methodologies of carrying out

Permo-Carboniferous rocks

Wenden- Lötschental-Maderanertal Zone	
Diech.T.- Alp L.- Cavardiras Group	

Plutonic rocks

Haslital Group	
Fruttstock Group	
Rötfirn Group	

Pre-Variscan basement (northern units)

Innertkirchen-Lauterbrunnen Zone	
Erstfeld Zone	
Ferden-Guttannen Zone	
Basement slices	
Sustenhorn Zone	
Oberaar-Furka Zone	

Ausserberg-Avat Zone	
Clavaniev Zone	

Molasse top-basement
Aar massif basal thrust

Figure 1.11. 3D overview of the geological model of the Aar Massif. From the proposed perspective, the east-northeast-trending structural dome shape of the massif in the central Swiss Alps is visible. The northern front of the massif is cut by multiple NW-vergent thrusts and dips steeply towards the NW to the basal thrust, which separates the massif from the basement units of the foreland. To the west and east, the massif gradually loses elevation to 4000 m a.s.l. in the west and -2000 m a.s.l. in the east. Top of the crystalline units of the Molasse, reconstructed from Pfiffner et al. (2011).

uncertainty quantification in models (Bond et al., 2011; Wellmann and Regenauer-Lieb, 2012; Wellmann et al., 2014; Schneeberger et al., 2017; Wellmann and Caumon, 2018; Pakyuz-Charrier et al., 2018; Baumberger et al., 2022). However, most of the contributions focus on simplified geological settings (e.g., Wellmann et al., 2010) and very few studies concern Alpine domains (e.g., Brisson et al., 2023). Methodologies for assessing uncertainties in 3D

models of complex geological settings are not yet fully developed. For this reason, no further uncertainty quantification was carried out within the 3D model of the Aar Massif.

1.4.2 Results

The main outcome of this project was the construction of a structurally consistent 'watertight' 3D geological model of the main lithological and tectonic boundaries of the Aar

Molasse top-basement
Aar massif basal thrust

Pre-Variscan basement (northern units)

Innertkirchen-Lauterbrunnen Zone
Erstfeld Zone
Ferden-Guttannen Zone
Basement slices
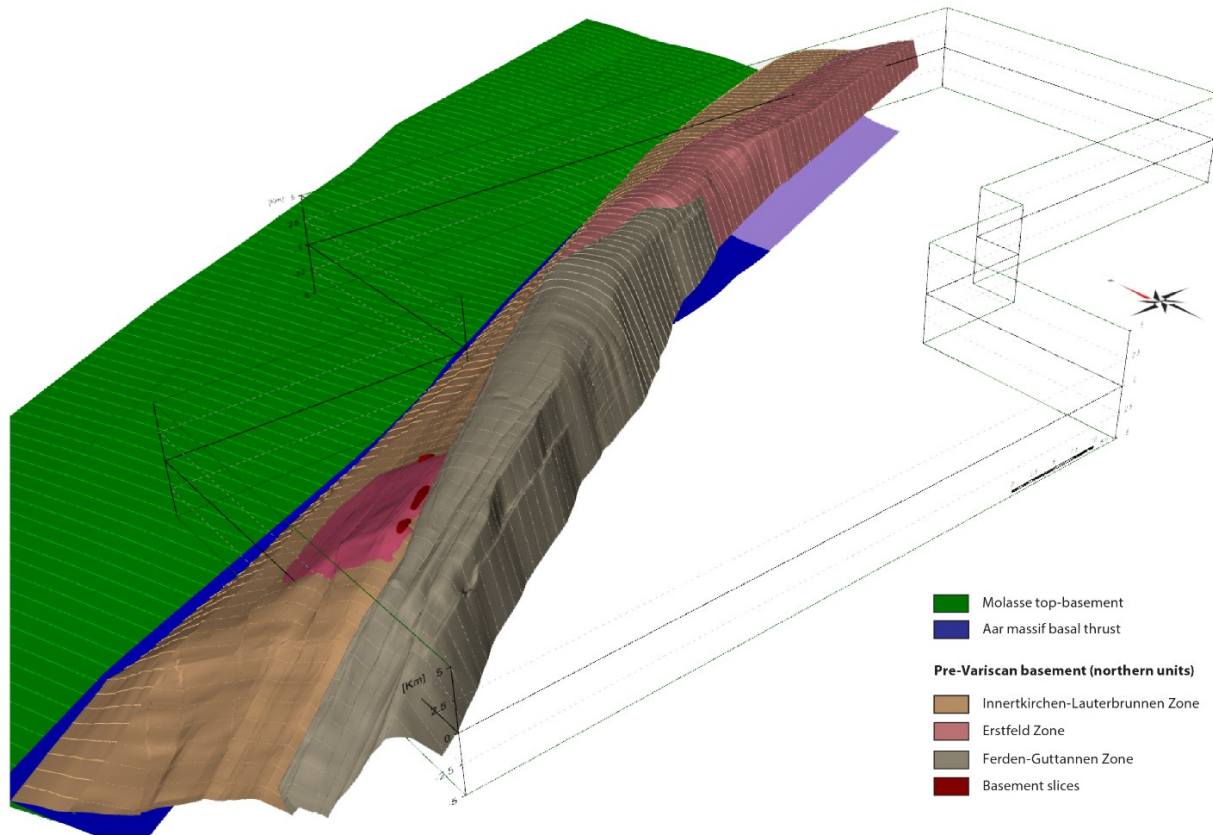
Figure 1.12. 3D view of the northern units of the Pre-Variscan polycyclic metamorphic basement of the Aar Massif. These units are largely affected by horizontal thrusting and consequent extrusion of bedrock slabs into the autochthonous and parautochthonous sedimentary units.

Massif. The model was built with more than 330 constructional cross sections for 118 mesh surfaces. The model covers 5300 km^2 of surface area. The surfaces were constructed from an elevation of 6000 m a.s.l. to a depth of -3000 m a.s.l., with the exception of the northern rim of the massif. This was constructed to a depth of -8000 m a.s.l. to include in the model the crucial frontal thrust of the massif and the connection with the crystalline basement units of the Molasse. The surface of the top of the crystalline units in the Molasse was interpolated from the contour map published

by Pfiffner et al. 2011. The modelled surfaces are grouped according to the project legend defined in Section 2.1. The following figure panels Fig. 1.11 to Fig. 1.15 show an overview of the modelled surfaces. The export of the modelled surfaces is available as GOCAD ASCII export upon request.

1.6 APPLICATION OF THE MODEL AND OUTLOOK

Due to the geological complexity of Alpine regions, explicit techniques are currently the most efficient for 3D structural geological
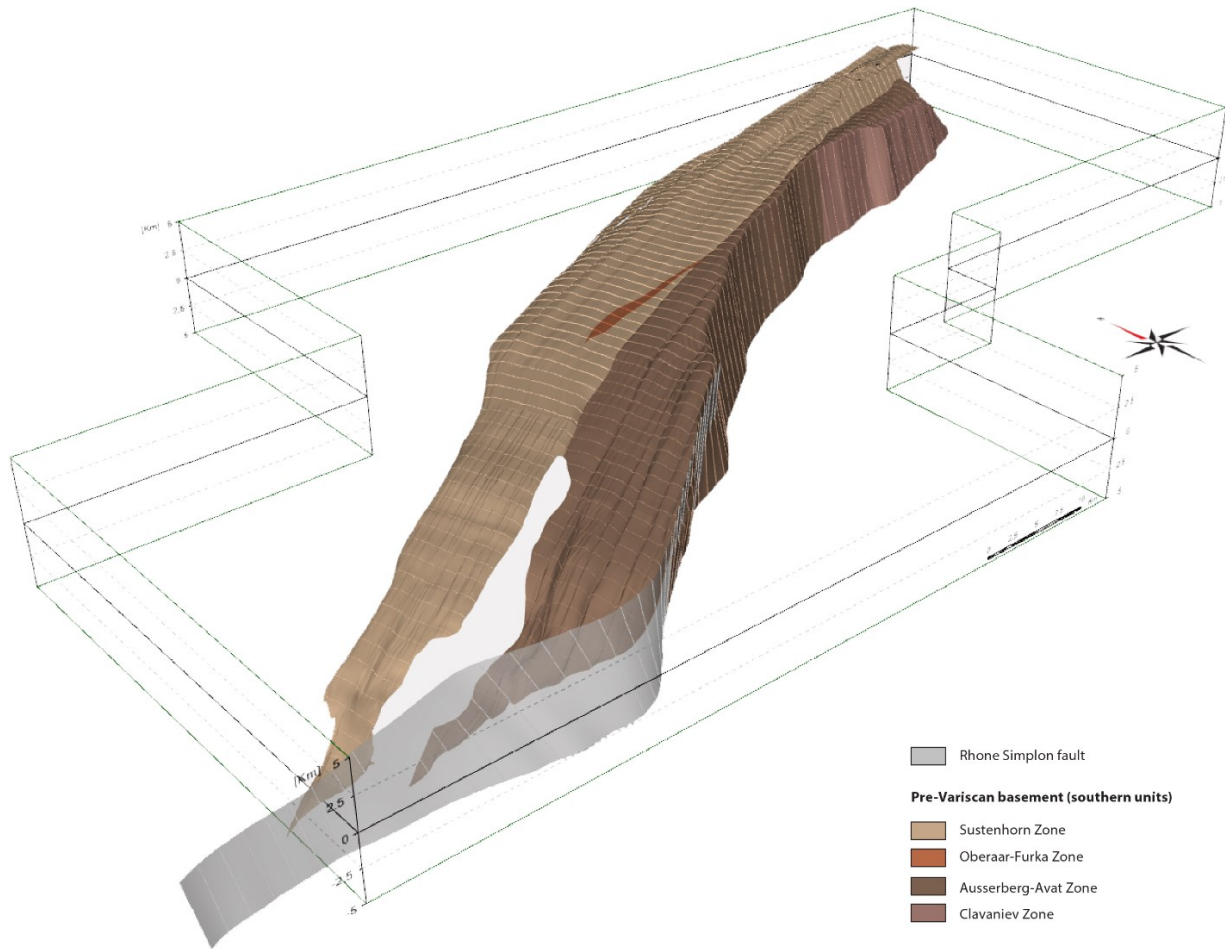
Figure 1.13. 3D view of the northern units of the Pre-Variscan polycyclic metamorphic basement. These units reach their highest point at an elevation of ~6000 m a.s.l. in the centre of the massif.

modelling. The making of the large-scale 3D model of the Aar Massif was relevant to test the efficiency and the limits of explicit modelling in the Alpine environment. As discussed in Section 1.4.1, the 3D geological model of the Aar Massif has a minimal uncertainty estimate. A challenge for the future is to incorporate and visualise uncertainty information within the 3D geological model of Alpine domains. An additional challenge would be to include implicit 3D modelling methods to improve the efficiency of the modelling process and meshing techniques. The Swiss Geological Survey (swisstopo) plans to cover the entire Switzerland with these models in the near future, as they provide additional information about the still largely unexplored subsurface. In fact, this new knowledge is expected to be crucial for the development of our future society, where the underground will be widely utilised. Extended underground 3D geological modelling will allow an improved
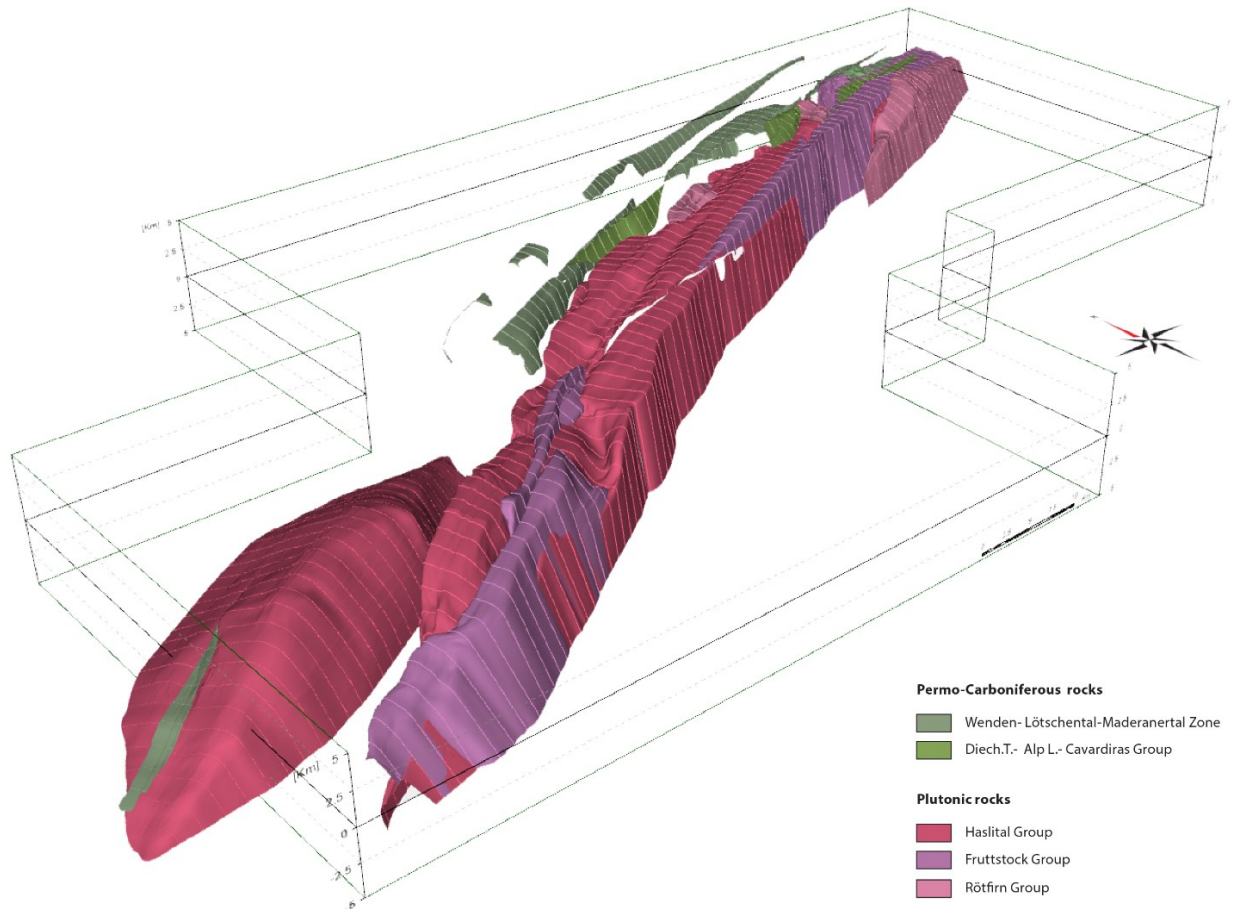
Figure 1.14. 3D view of the intrusive plutonic rocks and of the Permo-Carboniferous troughs of the Aar Massif. The shape of the intrusive bodies was reconstructed thanks to the great exposure of the intrusion contacts. This has allowed resolving the shape of the intrusions in great detail within 400 and 4200 m a.s.l. of elevation. The larger volumes of intrusions are mainly located in the central units of the massif. The Permo-Carboniferous troughs are arranged in the form of small-scale wedges, pinched within the basement units.

understanding of the underground geology, including structural systems and lithological disposition. What was experienced while modelling the Aar Massif is that a large-scale interpretation of the structural systems provides fundamental insights for understanding the processes that are active today, but also the evolution of our landscape. The knowledge gained from the advanced 3D modelling employed, has enabled us to develop the three scientific studies presented in the next three chapters of the thesis.

ACKNOWLEDGMENTS
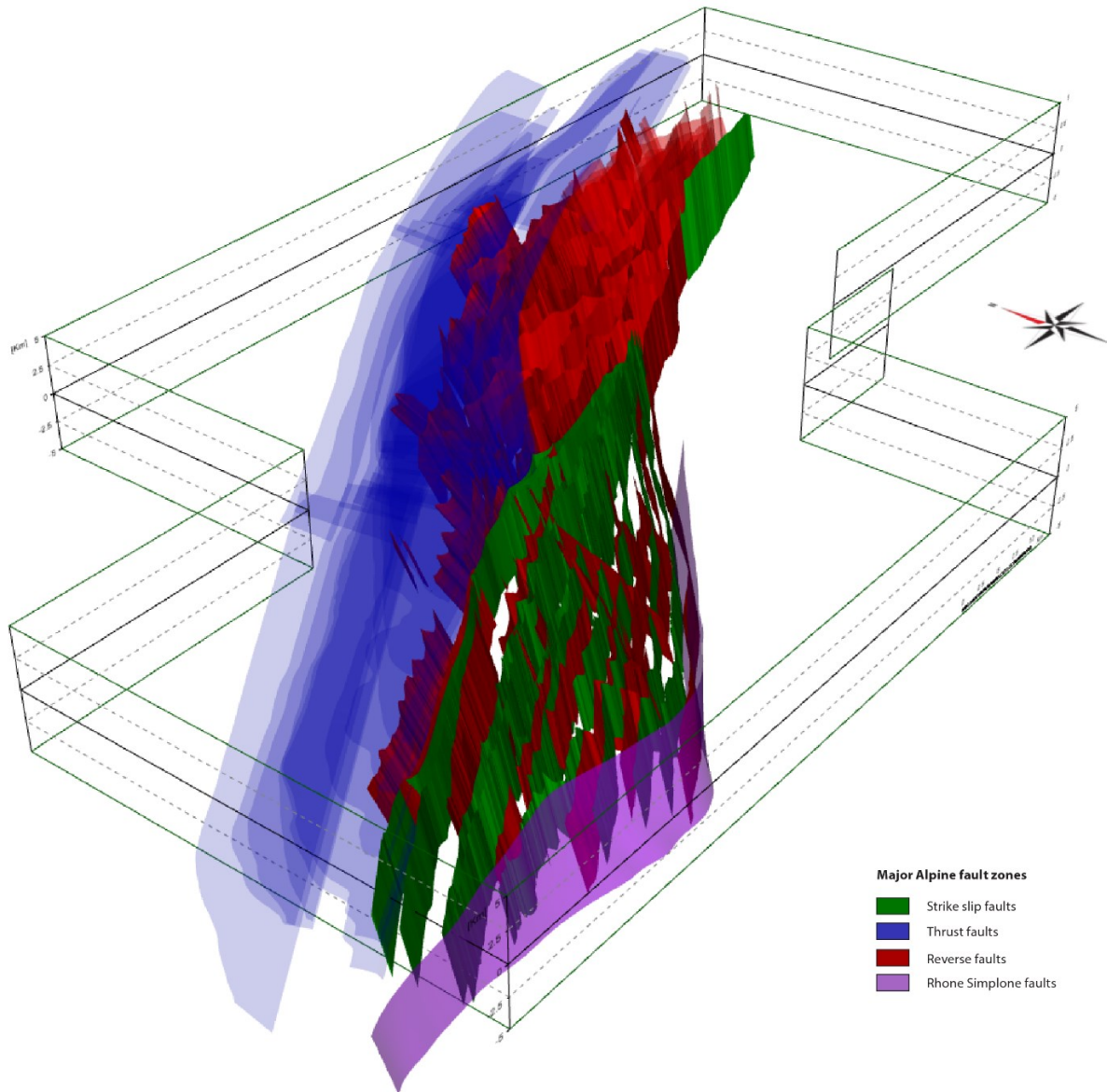
Figure 1.15. 3D view of the modelled major large-scale Alpine fault zones. The fault zones are subdivided in: (1) reverse faults (red planes), (2) thrust faults (blue planes), (3) strike-slip/oblique faults (green planes), and (4) Rhone-Simplon related faults (purple plane). The reverse faults are distributed throughout the massif with a SW-NE striking trend, and a curved trend that rotates form a SSW-NNE strike in the west, to an almost E-W strike in the east. The thrust faults are present in the northern regions, cut, and offset the northern front of the massif. The strike-slip-oblique faults are mainly present in the southwestern regions of the massif, as well as the Rhone-Simplon fault zone.

AUTHOR CONTRIBUTIONS

LITERATURE

Abrecht, J., 1994. Geologic units of the Aar Massif and their pre-Alpine rock associations: a critical review. The pre-Alpine crustal evolution of the Aar, Gotthard and Tavetsch Massifs. Schweiz. Mineral. Petrogr. Mitt. 74, 5–27.

Baumberger, R., 2015. Quantification of Lineaments: Link between Internal 3D Structure and Surface Evolution of the Hasli Valley (Aar Massif, Central Alps, Switzerland). PhD Thesis. Bern University, pp. 132.

Baumberger, R., Herwegh, M., Kissling, E., 2022. Remote sensing and field data based structural 3D modelling (Haslital, Switzerland) in combination with uncertainty estimation and verification by underground data. 3D Digital Geological Models: From Terrestrial Outcrops to Planetary Surfaces, 159-197.

Berger, A., Mercolli, I., Herwegh, M., and Gnos E.: Geological Ma of the Aar Massif, Tavetsch and Gotthard Nappes 1 : 100 000, Federal Office of Topography Swisstopo, Wabern, 2017

Bond, C.E., Philo, C., Shipton, Z.K., 2011. When there isn't a Right Answer: interpretation and reasoning, key skills for twenty-first century geoscience. Int. J. Sci. Educ. 33, 629–652. https://doi.org/10.1080/09500691003660364.

Brisson, S., Wellmann, F., Chudalla, N., von Harten, J., & von Hagke, C. (2023). Estimating uncertainties in 3-D models of complex fold-and-thrust belts: A case study of the Eastern Alps triangle zone. Applied Computing and Geosciences, 18, 100115.

Caumon, G., Lepage, F., Sword, C. H., Mallet, J. L., 2004. Building and editing a sealed geological model. Mathematical Geology, 36(4), 405-424.

Diehl, T., Kissling, E., Herwegh, M., & Schmid, S. M., 2021. Improving Absolute Hypocenter Accuracy With 3D Pg and Sg Body-Wave Inversion Procedures and Application to Earthquakes in the Central Alps Region. Journal of Geophysical Research: Solid Earth, 126(12), e2021JB022155.

Hänni, R., Pfiffner, O. A., 2001. Evolution and internal structure of the Helvetic nappes in the Bernese Oberland. Eclogae Geologicae Helvetiae, 94(2), 161- 171.

Herwegh, M., Pfiffner, O.-A., 2005. Tectono-metamorphic evolution of a nappe stack: A case study of the Swiss Alps. Tectonophysics 404 (1-2), 55–76.

Herwegh, M., Berger, A., Baumberger, R., Wehrens, P., Kissling, E., 2017. Large-scale crustal-block-extrusion during late Alpine collision. Sci. Rep. 7 (1), 1–10.

Herwegh, M., Berger, A., Glotzbach, C., Wangenheim, C., Mock, S., Wehrens, P., Baumberger, R., Egli, D., Kissling, E., 2020. Late stages of continent-continent collision: timing, kinematic evolution, and exhumation of the Northern rim (Aar Massif) of the Alps. Earth Sci. Rev. 200, 102959 https://doi.org/10.1016/j.earscirev.2019.102959.

Collet, L. and Paréjas, E.: Carte géologique de la chaîne de la Jungfrau, 1:25 000, Francke, Bern, 1928.

Krayenbuhl, T. and Steck, A.: Structure and kinematics of the Jungfrau syncline, Faflertal (Valais, Alps), and its regional significance, Swiss Journal of Geosciences, 102, 441–456, https://doi.org/10.1007/s00015- 009-1333-1, 2009.

Krebs, J.: Geologische Beschreibung der BlümlisalpGruppe, Beiträge zur Geol. Karte der Schweiz, N.F. 54, Francke, Bern, 1925.

Mair, D., Lechmann, A., Herwegh, M., Nibourel, L., Schlunegger, F., 2018. Linking Alpine deformation in the Aar Massif basement and its cover units–the case of the Jungfrau–Eiger Mountains (Central Alps, Switzerland). Solid Earth 9, 1099–1122.

Musso Piantelli, F., Mair, D., Berger, A., Schlunegger, F., Wiederkehr, M., Kurmann, E., Moeri, A., Baumberger, R., and Herwegh, M. (2022). 4D reconstruction of the Doldenhorn nappe-basement system in the Aar massif: Insights into late-stage continent-continent collision in the Swiss Alps. Tectonophysics, 843, 229586.

Musso Piantelli, F., Truttmann, S., & Herwegh, M. (2023). The control of collisional tectonics over

valley morphology: the case of the largest glacier in the European Alps. Terra Nova.

Nibourel, L., Berger, A., Egli, D., Heuberger, S., & Herwegh, M. (2021). Structural and thermal evolution of the eastern Aar Massif: insights from structural field work and Raman thermometry. Swiss journal of geosciences, 114(1), 9.

Nibourel, L., 2019. The structural and thermo-kinematic evolution of the eastern Aar Massif, Switzerland. Institut für Geologie, University of Bern, pp. 1–175 PhD thesis.

Pakyuz-Charrier, E., Lindsay, M., Ogarko, V., Giraud, J., Jessell, M., 2018. Monte Carlo simulation for uncertainty estimation on structural data in implicit 3-D geological modeling, a guide for disturbance distribution selection and parameterization. Solid Earth 9, 385–402. https://doi.org/10.5194/se-9-385-2018.

Pfiffner, O. A., Lehner, P., Heitzmann, P., Mueller, S., & Steck, A. (1997). Deep structure of the Swiss Alps: results of NRP 20. Birkhäuser.

Pfiffner, O. A., Ramsay, J. G., & Schmid, S. M. (2011). Structural map of the Helvetic Zone of the Swiss Alps. Geological special map, 1(100,000).

Rohr, K., 1926. Stratigraphische und tektonische Untersuchung der Zwischenbildungen am Nordrand des Aarmassivs (zwischen Wendenjoch und Wetterhorn). Beiträge zur Geologie der Schweiz NF57.

Schneeberger, R., de La Varga, M., Egli, D., Berger, A., Kober, F., Wellmann, F., Herwegh, M., 2017. Methods and uncertainty estimations of 3-D structural modelling in crystalline rocks: a case study. Solid Earth 8, 987-1002.

Sibson, R. H., 1977. Fault rocks and fault mechanisms. Journal of the Geological Society, 133(3), 191–213.

Wehrens, P.C., 2015. Structural Evolution in the Aar Massif (Haslital Transect): Implications for Mid-Crustal Deformation. Institut für Geologie, University of Bern, pp. 1–139 PhD thesis.

Wehrens, P., Berger, A., Peters, M., Spillmann, T., Herwegh, M., 2016. Deformation at the frictional-viscous transition: evidence for cycles of fluid-assisted embrittlement and ductile deformation in the granitoid crust. Tectonophysics 693, 66–84.

Wehrens, P., Baumberger, R., Berger, A., Herwegh, M., 2017. How is strain localized in a meta-granitoid, mid-crustal basement section? Spatial distribution of deformation in the central Aar massif (Switzerland). J. Struct. Geol. 94, 47–67.

Wellmann, J.F., Horowitz, F.G., Schill, E., Regenauer-Lieb, K., 2010. Towards incorporating uncertainty of structural data in 3D geological inversion. Tectonophysics 490, 141–151. https://doi.org/10.1016/j.tecto.2010.04.022.

Wellmann, J.F., Regenauer-Lieb, K., 2012. Uncertainties have a meaning: information entropy as a quality measure for 3-D geological models. Tectonophysics 526, 207–216. https://doi.org/10.1016/j.tecto.2011.05.001.

Wellmann, J.F., Lindsay, M., Poh, J., Jessell, M., 2014. Validating 3-D structural models with geological knowledge for improved uncertainty evaluations. Energy Proc. 59, 374–381. https://doi.org/10.1016/j.egypro.2014.10.391.

Wellmann, F., Caumon, G., 2018. 3D structural geological models: concepts, methods, and uncertainties. In: Advances in Geophysics, vol. 59. Elsevier, pp. 1–121. https://doi.org/10.1016/bs.agph.2018.09.001.

Chapter II

Aar Massif
- Para/Autochtonous cover
- Basement units
- —·— Alpine thrust faults
- —·— Alpine reverse faults

N

S

550 m
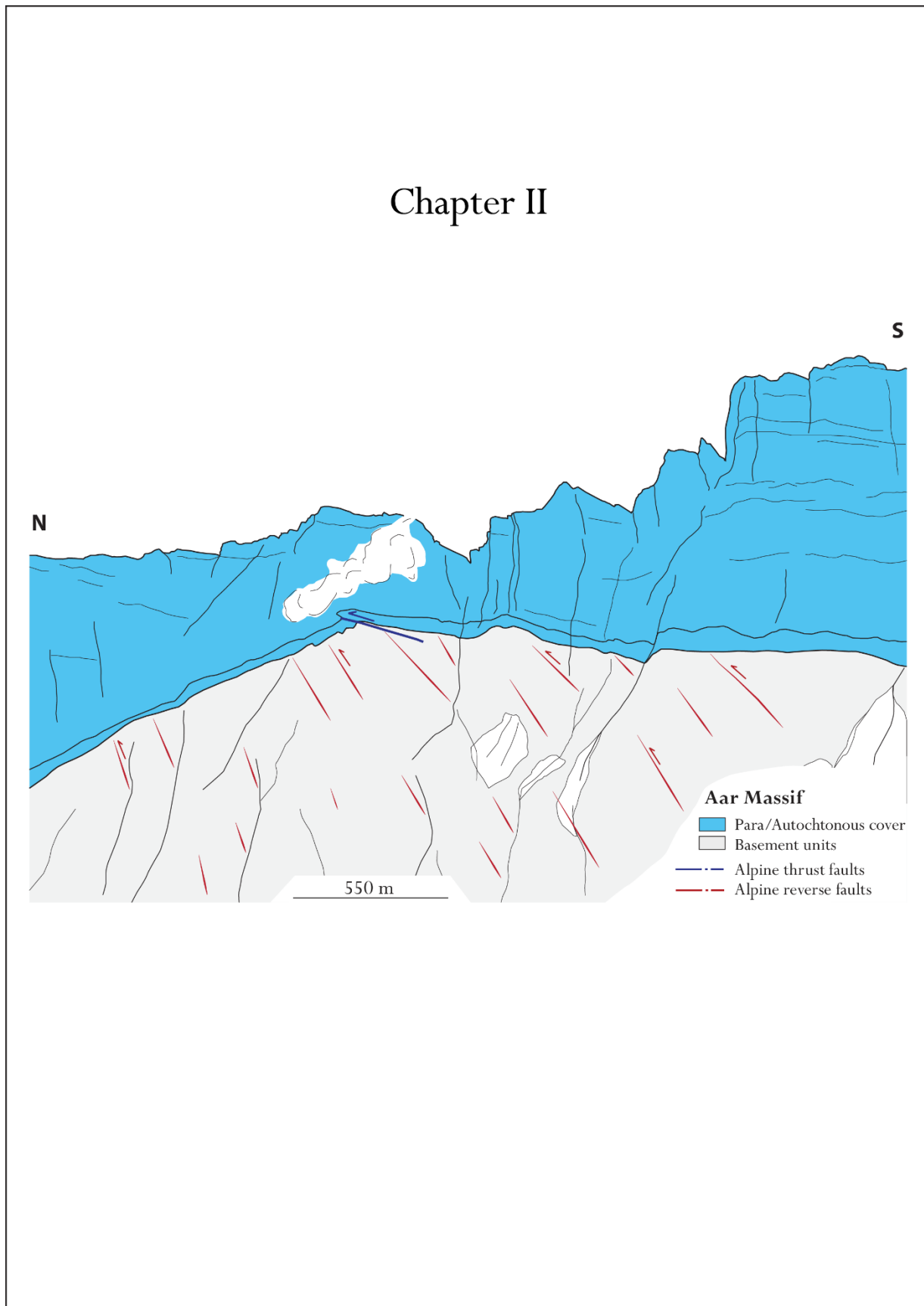
Panoramic view and geological interpretation of the Aar Massif basement-cover contact at Clariden (Linthal)

Viepoint: X: 2715340 / Y: 1186685

4D geodynamic evolution of the Aar Massif: a deep dive into the upper crust of the European Alps

Ferdinando Musso Piantelli[1,2*], Lukas Nibourel[3], Alfons Berger[1], and Marco Herwegh[1]

[1] *Institute of Geological Sciences University of Bern, Baltzerstrasse 1+3, 3012 Bern, Switzerland*

[2] *Swiss Geological Survey, Federal Office of Topography swisstopo, Seftigenstrasse 264, 3084 Bern, Switzerland*

[3] *ETH Zürich, Dep. of Earth Sciences, Sonneggstrasse 5, 8092 Zürich, Switzerland*

Abstract

The inversion of crystalline units of former passive continental margins is a typical feature during late-stage collision. In this work, we selected the Aar Massif, the easternmost of the External Crystalline Massifs of the European Alps, to investigate how the 3D geometry of the passive margin, inherited structures, and crustal density variations influenced the late stage continent-continent collision. Explicit three-dimensional geological modelling, cross-section restoration coupled with metamorphic peak temperature data, allowed us to construct a 4D geodynamic evolution of the Aar Massif during the late-stage Alpine orogeny. Our results show that: (i) The Aar Massif results from the inversion of the former passive European margin, consisting of spatially complex rifting structures. These outlined variable distribution of local half graben basins and a topographic high from the Permian to the Mesozoic. (ii) The reconstruction shows that at the onset of Alpine deformation (22 Ma), peak metamorphism was reached by burial at depths between -8 and -18 km with a horizontal geothermal gradient of 26°C/km. (iii) Exhumation of the basement units occurred in a distinct in-sequence deformation style. Inherited along-strike variations in the thickness and density of the basement units induced a non-cylindrical exhumation of the massif by activation of dense networks of reverse, thrust and strike-slip faults. Complex interactions between these fault systems resulted in the present shape of the massif. The in-sequence non-cylindrical exhumation of the basement units was controlled by an interplay between deep crustal dynamics and structural inheritance in the middle to the upper crust of the former European passive continental margin.

2.1 INTRODUCTION

In advanced stages of continent-continent collision, the development of orogens is dominated by the involvement of basement in thick-skinned tectonics (e.g., Lacombe and Bellahsen, 2016; Pfiffner 2006). This process generally involves the formation of thrusts and reverse faults that allow the exhumation of large-scale antiformal complexes with crystalline cores (e.g., Muñoz, 1992; Boutoux et al.,1014, 2016; Rosenberg et al., 2015; Lacombe and Bellahsen, 2016 and reference therein; Granado and Ruh, 2019). In many orogens around the

world, this late stage is associated with the inversion of former passive continental margins (e.g., Taiwan: Beyssac et al., 2007; Zagros: Vergés et al., 2011; Western Alps: Tricart, 1949; Bellanger et al., 2014; Spitz et al., 2020). The evolution of the belts and forelands depends, among other factors, on the geometry of the pre-collision passive margin, the rheology and density of the crust, and the inhibition or reactivation of inherited crustal structures (e.g., Rosenberg and Kissling, 2013; Lafosse et al., 2016; Herwegh et al., 2017; Nibourel et al., 2021a,b; Musso Piantelli et al., 2022).

Along the Western and Central European Alps, the External Crystalline Massifs (from southwest to northeast, the Argentera, Pelvoux, Belledonne, Aiguilles Rouges, Mont Blanc, and Aar Massifs; Schmid et al., 2004, Fig. 2.1) are examples of such antiformal complexes resulting from the inversion of the European passive continental margin. These massifs form a laterally discontinuous belt of basement domes, which are separated by structural saddles (e.g., Egli & Mancktelow, 2013; Granado and Ruh, 2019). A large number of field, numerical and petrochronological studies have been conducted to understand the geodynamic process for the deformation and emplacement of such basement domes (e.g., Frey et al., 1980; Frey, 1987; Burkhard, 1988; Pfiffner, 2006; Boutoux et al., 2014; Bauville and Schmallholz, 2015 and 2017; Lacombe and Bellahsen, 2016; Granado and Ruh, 2019; Girault et al., 2020, 2022). However, previous approaches have often been limited to two-dimensional sections. Therefore,

the three-dimensional and non-cylindrical architecture and evolution of these complexes remain unexplored.

In this work, we selected the Aar Massif (Central Swiss Alps; Fig. 2.1), the easternmost of these domes, to examine how passive margin geometry, inherited structures and crustal density variations influenced the late stages of continent-continent collision. To include the three-dimensional architecture of the massif, we constructed a large-scale explicit 3D geological model of the main lithological, and structural boundaries of the area, which was then retrodeformed. Such 4D reconstructions are a powerful tool for understanding the evolution of complex geological features, such as mountain belts. In fact, such reconstructions allow multiple regional observations to be combined into a single reconstruction at the scale of the orogen. By combining cross-section restoration, published metamorphic peak temperature data (Nibourel et al., 2021b, and references therein), and a series of structural, geomorphological, thermochronological, and geochemical studies conducted in recent years (Burkhard, 1988; Hänni and Pfiffner, 2001; Herwegh and Pfiffner, 2005; Pfiffner et al., 2011; Berger et al., 2017, 2020; Wehrens et al., 2016, 2017; Schneeberger, 2017; Herwegh et al., 2017, 2020; Mair et al., 2018; Nibourel et al., 2018, 2021a,b; Baumberger et al., 2022; Musso Piantelli et al., 2022, 2023;), we built a 4D crustal geodynamic reconstruction of the Aar Massif during the late stage of Alpine evolution (25-0 Ma). In particular,
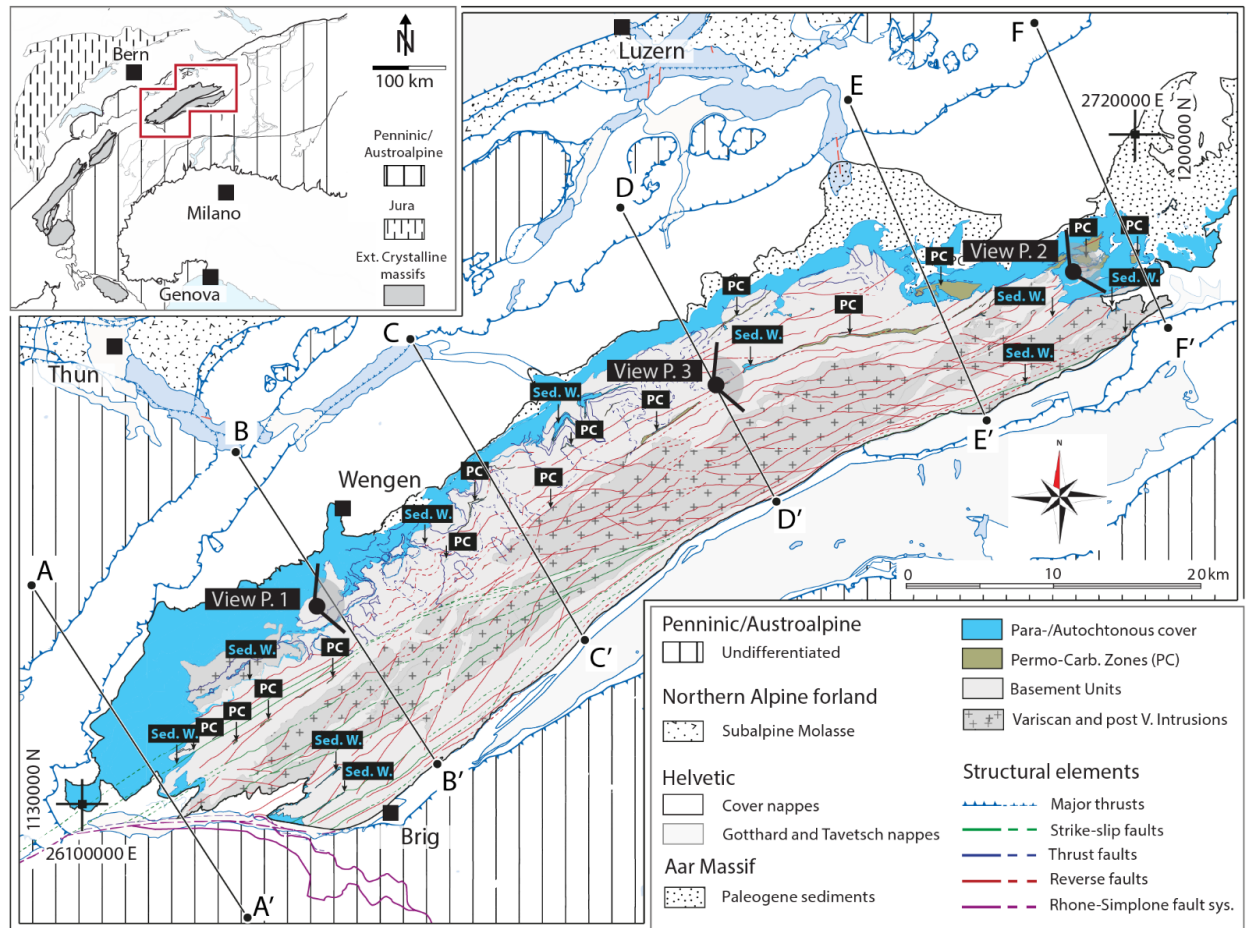
Figure 2.1 - Geological map of the study area, (insert simplified after Schmid et al., 2010). The map shows the large-scale trends of the main structural elements, the profile traces of Fig. 2.2, the viewpoints of Fig. 2.3, the locations of the thin sediment wedges (Sed. W.), and the locations of the Permo-Carboniferous troughs (PC).

the reconstruction showed that a part of the structural relief of the massif is a legacy of the 3D architecture of the former passive continental margin. The subsequent in-sequence non-cylindrical exhumation of the basement units was controlled by a crucial interplay between deep crustal dynamics (e.g., Herwegh et al., 2017) and crustal inheritances.

2.2 GEOLOGICAL SETTING AND AGE CONSTRAINTS

The Aar Massif is an east-northeast-trending structural dome outcropping for more than 2000 km^2 at an average elevation of ~2200m a.s.l. in the central Swiss Alps (Fig. 2.1). The Aar Massif is the largest and easternmost of the External Crystalline Massifs. It exposes the basement of the thickened lower European plate as a result of the convergence with the Adriatic plate and the associated post-35 Ma continent-continent collision (e.g., Froitzheim et al., 1996; Pfiffner, 2015; Schmid et al., 1996, 2004).

The basement units consist predominantly of pre-Variscan polycyclic metamorphic gneisses, migmatites and amphibolites (Abrecht, 1994;

45

Berger et al., 2017b; Herwegh et al., 2020). These gneissic units were intruded by Variscan to post-Variscan plutons, mostly in the central regions of the massif, where they outcrop over ~760 km^2 (Figs. 2.1 and 2.2). The evolution of these plutons was associated with the formation of Permo-Carboniferous half-graben structures in the upper crust, which were filled by volcanic-, volcanoclastic and pure sedimentary sequences. The overlying succession of limestones, marls, shales, and sandstones, that compose the Para/Autochthonous sedimentary units, were deposited during the Mesozoic.

The geometry of the margin and the sedimentation pattern were constrained by extensional Mesozoic faults, resulting in large thickness variations that can still be observed along the strike of the massif (Fig. 2.2; Burkhard, 1988; Pfiffner, 2015; Musso Piantelli et al., 2022). Along the strike of the massif, also Permo-Carboniferous to Cenozoic sediments are locally preserved in narrow WSW-ENE-trending steep wedges (Figs. 2.1 and 2.3c; e.g., Rohr, 1926; Nibourel et al., 2021a). The occurrence of these wedges is aligned along specific intensely deformed zones, traceable along the strike of the massif (see Berger et al., 2017a).

The Aar Massif has undergone a long exhumation history (22 Ma – present). Temperatures at the northern rim of the massif never exceeded ~250 °C (e.g., Bambauer et al., 2009, Herwegh et al., 2017, Rosenberg et al. 2021), whereas at the southern boundary peak

Alpine conditions were in the range of 450 °C and 600 MPa (Goncalves et al., 2012).

During the exhumation of the basement units, a dense network of Alpine fault zones was formed. The maximum formation depth of the exhumed fault zones ranged within 18–20 km, resulting in upper greenschist facies metamorphic conditions (e.g., Goncalves et al., 2012). At these depths, the basement units were deformed by ductile deformation, with the occurrence of mylonites and ultramylonites (Wehrens et al., 2016; 2017). Subsequently, with progressive exhumation, the basement units reached shallower crustal levels and brittle deformation localised within the ductile precursors, forming brittle fractures, cataclasites, fault gauges and breccias. Because of both, ductile and brittle nature of the structures, we refer to them in this contribution as fault zones, following the nomenclature of Sibson (1977).

The kinematics and the age of these fault zones have been investigated over the past decades (see Herwegh et al., 2017, 2020; Nibourel et al., 2021a, and reference therein). At 22 Ma, the exhumation of the basement units was initiated with the formation of an early set of steep to sub-vertical NW-SE striking faults with mostly S-block up kinematics (e.g., Handegg phase; Herwegh et al., 2017; Nibourel et al., 2021; Steck, 1968; Wehrens et al., 2017; Bergemann et al. 2017). These reverse faults were dated at ca. 21–17 Ma, based on isotopic ages on syn-kinematic micas (Challandes et al., 2008; Rolland et al., 2009). Already from the early stages of inversion,
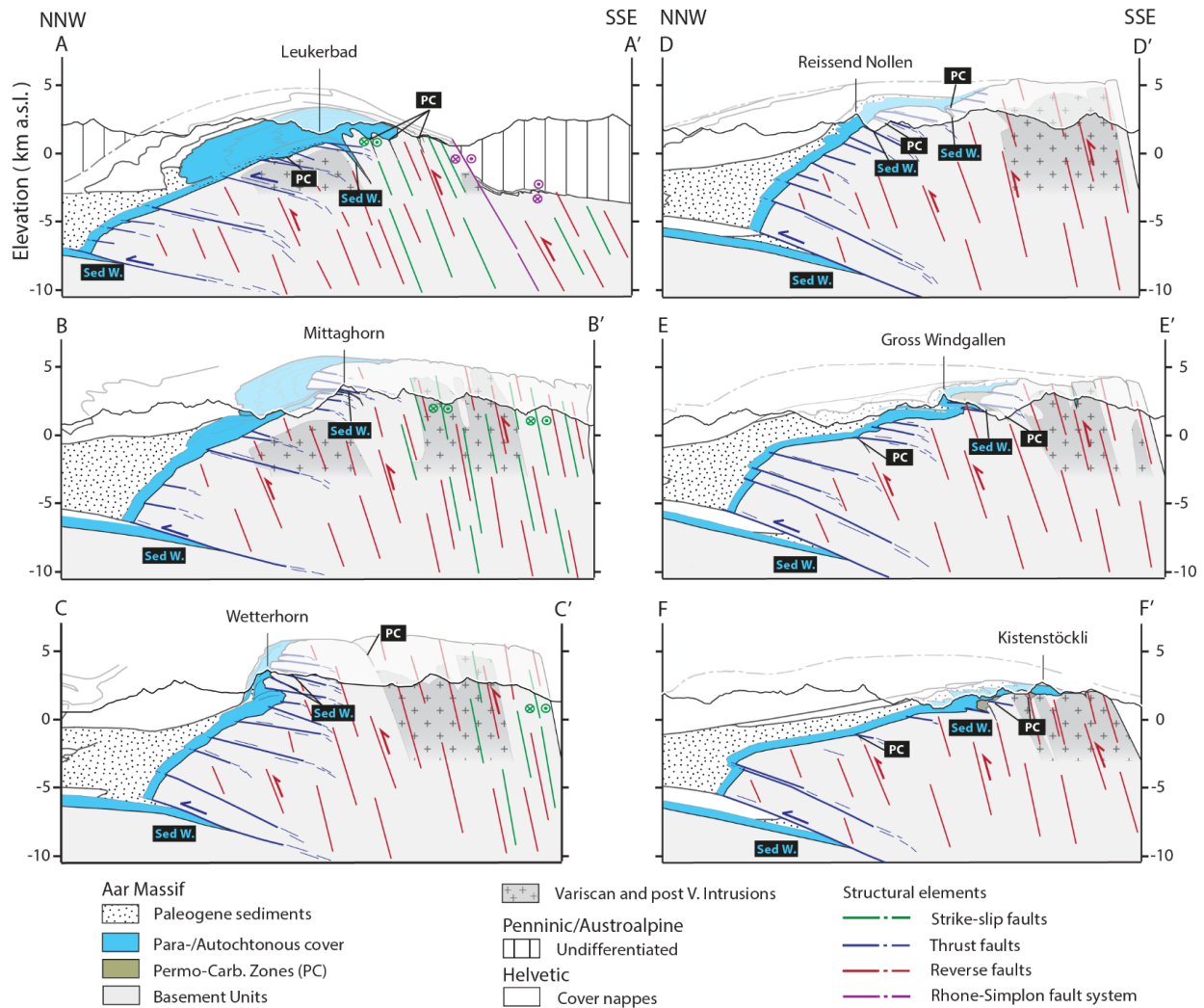
Figure 2.2 – Cross-sections of the study area (see Fig. 2.1 for cross-sections traces). The profiles show: the structural elements, the overlying Helvetic, Penninic, and Austroalpine nappes. In sections AA', BB' and CC' the outline of the overlying upper Helvetic nappes has been modified after Herwegh and Pfiffner (2005) and Hänni and Pfiffner (2001). The sections highlight the dome-shape of the massif, which reaches an elevation of ~6 km a.s.l. in the central regions (CC') and loses elevation on the sides (AA' and FF'). Furthermore, along the strike of the massif, it is possible to observe significant changes in the thickness of the Para/Autochthonous sedimentary cover and in the volumes of the intrusive rocks.

NNW-directed thrust faults overprinted the steep reverse faults (e.g., Windgällen phase; Nibourel et al., 2021a, and references therein). This dichotomy of exhumation of the basement units with reverse faulting and thrusting lasted until 12-10 Ma, and led to the formation of the

structural relief of the massif as well as the passive up-doming of the overlaying nappe stack (Fig. 2.2; i.e., Handegg and Pfaffenchopf faults; Mock, 2014; Herwegh et al., 2020; Nibourel et al., 2021a,b; Wehrens et al., 2017). A major kinematic switch occurred at 14-10 Ma whereby:

47
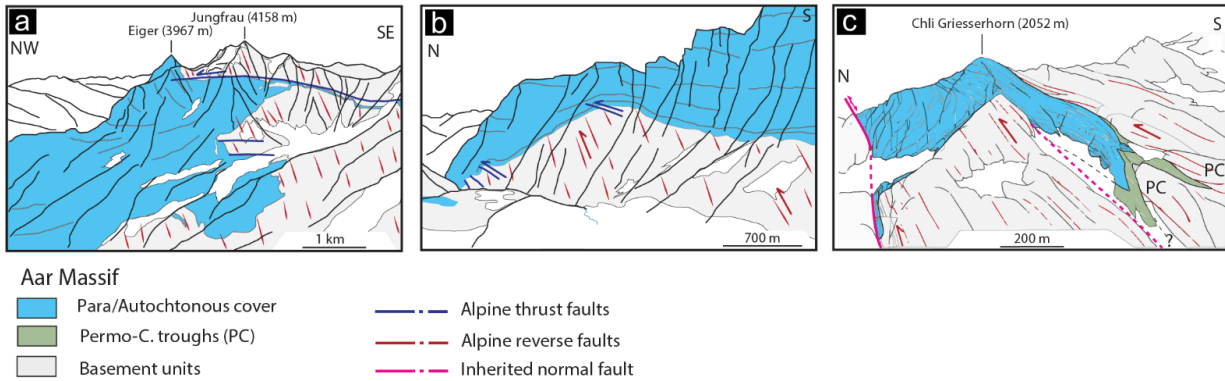
Figure 2.3 – Profile-like views of three type localities of the Aar Massif, viewpoints are indicated in Fig. 2.1. (A) Profile-like view of the Eiger-Mönch-Jungfrau complex. A large-scale thrust dissects the basement units, and pushes a rigid basement slab into the sedimentary cover. The main thrust plane is bent and dips to the NW on the northern front. Coordinates of the viewpoints are given in Appendix A. (B) Profile-like view of the sedimentary cover-basement contact. The basement units are dissected by several reverse faults and small-scale thrust faults. At the northern front, the contact dips steeply to the NW. (C) Profile-like view of the Färnigen zone (modified after Nibourel et al., 2021a). The zone comprises two synformal sediment wedges, bounded by two early Jurassic normal faults, and associated Permo-Carboniferous sediments. The former half-graben geometry is still recognizable.

(a) large-scale NNW-vergent thrust structures developed at the northern front of the massif, causing an 'en bloc' exhumation of the massif (Herwegh et al., 2020; Nibourel et al., 2021a,b). A distinct jump of ZFT ages across such uppermost (today exposed) thrust planes indicates active thrusting after ca. 13 Ma (Berger et al., 2027; Herwegh et al., 2020). In the adjacent Subalpine Molasse, compressional deformation initiated in the Oligocene (Kempf et al., 1999; Schlunegger et al., 1997) and lasted until ca. 6–4 Ma (Mock et al., 2020; von Hagke et al., 2012, 2014). (b) In the southwestern units of the massif, strike-slip to oblique faults reactivated the precursor reverse fault planes (Fig. 2.1; Oberaar phase, Wehrens et al., 2017; Herwegh et al., 2020). The age of such transition was indicated by isotopic ages on syn- to post-kinematic minerals from cross-cutting strike-slip faults and associated Alpine clefts (Bergemann et al., 2017; Berger, Wehrens, et al., 2017; Challandes et al., 2008; Janots et al., 2012; Ricchi et al., 2019; Rolland et al., 2009) (c) Transtensional movements along the Rhone-Simplon fault system affected the southern margin of the massif and adjacent units(Fig. 2.2; e.g., Grosjean et al., 2004; Campani et al., 2014).

2.3 METHODS

In order to reconstruct the geodynamic evolution of the Aar Massif during the different stages of the continent-continent collision, it was necessary to first construct a complete large-scale explicit 3D geological model of the study area. A 2D dataset was compiled and validated within a geographic information system software (ESRI's ArcGIS, v.10.8). The 3D tectonic architecture of the Aar Massif was then explicitly

modelled using the Move™ software (Petex, v.2019.1). Six geological cross-sections across the study area were retro-deformed with line balancing. Finally, the 4D-geodynamic reconstruction of the Aar Massif was built using the MoveT M software, applying interpolation and meshing techniques between the retro-deformed cross-sections at five specific time intervals.

2.3.1 Geological data compilation, establishment of a stratigraphic model and fieldwork

A detailed structural map of the exposed basement units of the Aar Massif was generated on remotely sensed images with the aim of extending the structural dataset, following the workflow of Baumberger et al. (2022) (Fig. 2.3). The detection of the structures was performed at a scale of 1:25 000 using high-resolution orthophotos (SwissImage with a raster resolution of 0.25 x 0.25 m; provided by swisstopo), a high-resolution digital elevation model (DEM) (swiss ALTI3D with a down-sampled raster resolution of 2 x 2 m, version 2013 provided by swisstopo), and hillshade maps. All data were verified at key locations in the field by mapping and collecting structural field data (see Musso Piantelli et al., 2022 and 2023). The kinematics of the structures were characterised by the compilation of over 2500 field measurements (fault planes dip direction/dip angle, and stretching lineation; of which over 1000 were collected in this study), and by the generation of rose-plots. The latter was based on the remotely drawn lineament

maps, and calculated with a line-bearing python algorithm. The mapping was extended in a next step to include the major stratigraphic and tectonic boundaries of the cover and basement units, including the Permo-Carboniferous troughs, as well as structural information from previous maps (see Chapter 1). For the sake of simplicity, the stratigraphic suite of the Autochthonous and Parautochthonous units was synthesized into one unit (Fig. 2.1).

2.3.2 3D Geological modelling

All available 2D data (mapped boundaries and structures, strike and dip data, tunnels and seismic sections) were imported into the software Move™ and projected over a DEM (raster resolution 35x35 m). A dense regularly spaced (500 m) network of NNW-SSE striking constructional cross-sections was then generated (see Chapter 1). By applying 3D interpolation and meshing techniques (i.e. the spline curve method), lithological and structural boundaries were interpolated between the DEM surface and cross-sections to generate surfaces for each horizon of the model. Following this approach, the explicit 3D model of the study area incorporates field observations, structural analysis at the outcrop scale, tunnel and literature data, and large-scale seismic profiles (see Chapter 1).

2.3.3 Cross-section restoration and 4D reconstruction

To reconstruct the tectonic evolution of the Aar Massif during the Alpine collision (22 – 0 Ma), six NNW-SSE cross-sections (see traces AA',

BB', CC', DD', EE', and FF' in Fig. 2.1) were retro-deformed by line-balancing (i.e. for the basement-cover contact; see Appendix A). Furthermore, all the peak temperature data compiled by Nibourel et al. (2021a), lying within 3 km at the sides of each section and in close contact with the sedimentary cover-basement contact, were selected and normally projected onto the sections. The peak temperature data were restored along with the cross-sections to obtain a paleo-gradient of the basement units at 22 Ma (see Appendix A). The cross section restoration involved five fundamental assumptions: (i) constant length of top basement and constant area of the crustal basement. (ii) Pre-collisional geometry of the proximal part of the European passive continental margin bent by ~10° below the tectonically active boundary of the overriding plate (see Nibourel et al. 2018, and 2021). (iii) No significant Alpine deformation in the basement units of the Aar Massif prior to the thermal peak. (iv) Constant mean topographic elevation throughout the restored sections, as stated by Campani et al. (2012) and Schlunegger and Kissling (2015). (v) The location of Permo-Carboniferous and sedimentary wedges (Figs. 2.1, 2.3, and 2.4) served as markers for the locations of syn-rift faults. The throws of the normal faults were reconstructed using the vertical extent of the multiple sedimentary wedges and Permo-Carboniferous troughs as a minimum estimate (e.g., Musso Piantelli et al., 2022).

The retro-deformation was performed considering the following five time stages: 0 (present), 10, 15, 18, and 22 Ma. During the 0 to 10 Ma time-interval, a strike-slip to oblique movement was also active in the southwestern units of the massif (Wehrens et al. 2016, 2017). The strike-slip displacement was partitioned into a large number of shear zones and it is difficult to quantify in the field. However, at the contact between the sedimentary cover and the basement in the western Aar Massif, the displacement is limited to a few meters at maximum, indicating small displacement only (Fig. 2.1; note that the major Rhone-Simplon related strike-slip displacements occurred in the Rhone valley; see 3D model of Campani et al. 2014). For this reason, the strike-slip phase was neglected as a first order of approximation and therefore not included into the overall estimation of shortening and exhumation of the basement units.

Each cross-section resulting from the retrodeformation at the above mentioned time stages was then digitised in Move™. Subsequently, 3D interpolation and meshing techniques (spline curve method) were applied within the reconstructed sections to produce a 3D model of each stage of retrodeformation.

2.4   RESULTS

The present day dome-shaped architecture of the Aar Massif is unravelled with a new structural map of the exposed basement units and a DEM of the top of the basement units derived from the 3D model constructed for this study (Figs. 2.4 and 2.5). The results of the restoration of the CC' section (see trace in Fig.

2.1) are presented in a stepwise evolution, highlighting the in-sequence exhumation of the basement units of the massif from 25 Ma to the present day (Fig. 2.6). Finally, the progression of exhumation and shortening rates is outlined by combining the horizontal shortening and maximum vertical uplift collected along all six restored sections (Fig. 2.7).

2.4.1 Structural map of the Aar Massif

The more than 120 km long axis of the Aar Massif shows a bend in the central regions, along a line that can be drawn between Innertkirchen and Furkapass (Fig. 2.4). The shear zone map presented in Figure 2.4 shows a pervasive distribution of structures arranged in networks of brittle-ductile fault zones. Most of the structures described are limited in width (dm to few m), but are very persistent laterally and often traceable for several kilometers, under circumstances even over tens of kilometers. The 3D network of the structures encloses un- to weakly-deformed basement blocks (see also Steck, 1968; Choukroune and Gapais, 1983; Wehrens et al., 2016, 2017; Herwegh et al., 2017, 2020; Nibourel et al.2021a). According to the orientations and kinematics characterised in the field, our new data subdivide the Aar Massif into five structurally different regions (named A1-A5; Fig. 2.4). Regions A1, A2, and A3 belong to the southern domain of the Aar Massif, whereas regions A4 and A5 to the northern one (Fig. 2.4).

The southern domains (A1-A3) are characterised by an increasing fault frequency as it approaches the southern boundary of the massif (Musso

Piantelli et al., 2023). The fault zones are organised in steep reverse fault systems (red in Fig. 2.4), locally reactivated as strike-slip to oblique faults mainly in domain A1 (green in Fig. 2.4). It is interesting to note that the fault zone networks A1 and A3 domains show in map view (Fig. 2.4) as first-order approximation a mirror-like symmetry with respect of the massif's bending axis, which is confirmed by the stereo and rose plots (Fig. 2.4). While domain A1 displays 146/60 as average dip direction/dip angle of the steep reverse faults (Figure 2.4), 153/57 average dip direction/dip angle in domain A3 reflect their mirror pairs. Domain A2 represents a transition zone, where fault zone orientations display a 149/67 average dip direction/dip angle.

In this way, the fault of domain A1 is connected with domain A3 in a bow-shaped geometry. Irrespective of the faults' strike and the domain in which they occur, the reverse faults are steeply SE-dipping, with down-dip stretching lineations and kinematic indicators of an up-movement of the S-block (stereoplots in Fig. 2.4). Strike-slip reactivation localised mainly along the preexisting SW-NE striking reverse fault planes. In region A1, where most of the reactivation occurred, stretching lineation indicate dextral strike-slip movement. In regions A2 and A3, however, reactivation is restricted to the southern boundary of the massif (Fig. 2.4) with stretching lineations indicating dextral oblique movements. In contrast to the southern domains (A1-A3), fault zones in the northern domain show
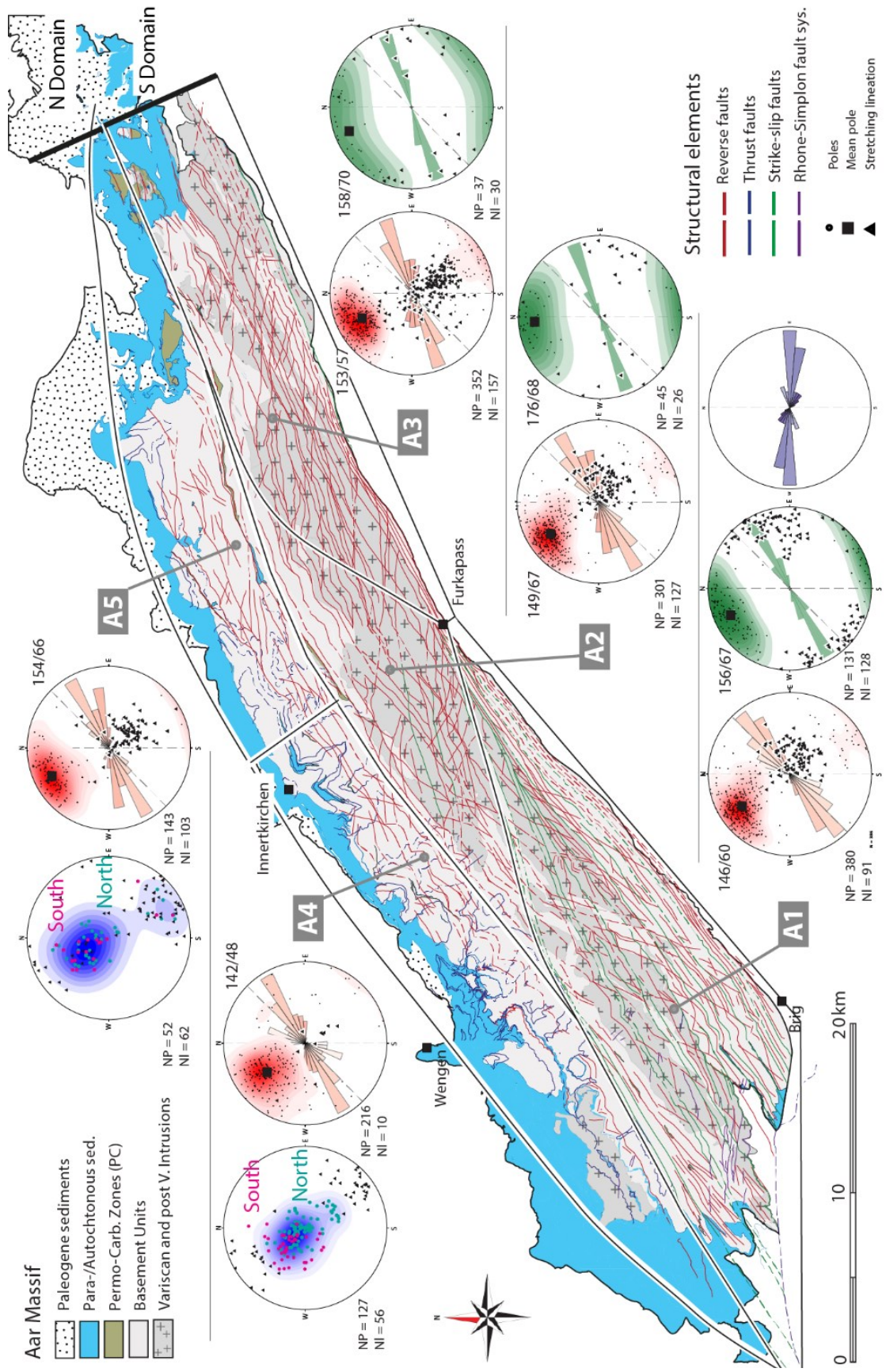
Figure 2.4 – Structural map of the Aar Massif, showing the main fault zones detected with remote sensing techniques at the scale of 1:25'000. The fault zones are subdivided into: reverse faults, thrust faults, strike-slip faults and Rhone-Simplon fault system. The massif is subdivided into five structurally consistent domains A1 to A5. On the sides of the map, the stereoplots show the poles, mean poles and lineation of the reverse faults, thrusts and strike-slip faults for each domain. In A4 and 5, note that in the stereoplots of the thrust faults, as highlighted by the colour code of the poles, the fault planes progressively increase their dip angle from north to south.

consistent strike and dip directions across both domains (A4, A5; Fig. 2.4). In these two domains, NW-vergent thrusts and reverse faults dominate. These two sets of fault zones record a long-lasting evolution and exhibit complex cross-cutting relationships. As shown by the overall pole distribution (Fig. 2.4), exposed thrust planes in the southern areas of the domains A4-A5 dip moderately SW, then progressively become horizontal in the central areas and even dip to the NW towards the northern rim of the massif (e.g., the thrust plane at Jungfrau, Fig. 2.3a). The reverse faults, in both regions A4 and A5, strike SW-NE and dip towards the SE at gentler angles than in the southern parts. The reverse faults are generally truncated by the thrust planes, but as described by Nibourel et al 2021a, towards the northern limit of the massif, younger generations of reverse faults also cut the thrust planes indicating a diachronous and repetitive formation of the two fault zone types.

2.4.2 Overall 3D shape of the massif

In this work, a 3D geological model of the top of the basement units of the Aar Massif was built with explicit modelling techniques (Chapter 1). This is a key result, fundamental for the rest of the study. The reconstructed top of the basement shows the dome-shape of the Aar

Massif (Fig. 2.5a). If erosion is neglected, the centre of the massif reached a height of > 6 km. However, 3820 km^3 of basement have been eroded down to a maximum height of 4.2 km (summit of Mt. Finsteraarhorn). The northern front of the top basement is dissected by multiple NW-vergent thrusts and dips steeply to the NW to the basal thrust, which separates the massif from the basement units of the foreland. To the west and east of the massif, the top basement loses gradually elevation to -4 km in the west and -2 km in the east (Fig. 2.5a). The pattern of the peak temperature isograds published by Nibourel et al. (2021a) closely resembles the trend of the structures and reflects the three-dimensional dome-shape of the Aar Massif, both in massif-perpendicular and along-strike directions (Fig. 2.5b).

2.4.3 Basal thrust of the Aar Massif and Permo-Carboniferous-sedimentary wedges

As visible in Fig. 2.2, the basal thrust is a prominent feature of the Aar Massif. The offset of the basement units increases along the strike of the massif from west to east. Indeed, in profile AA' the trust offsets the basement for ca. 3 km, whereas in profile FF' for ca. 9 km. Within the more than 2000 km^2 of exposed basement units, Permo-Carboniferous, Triassic, Early and Middle
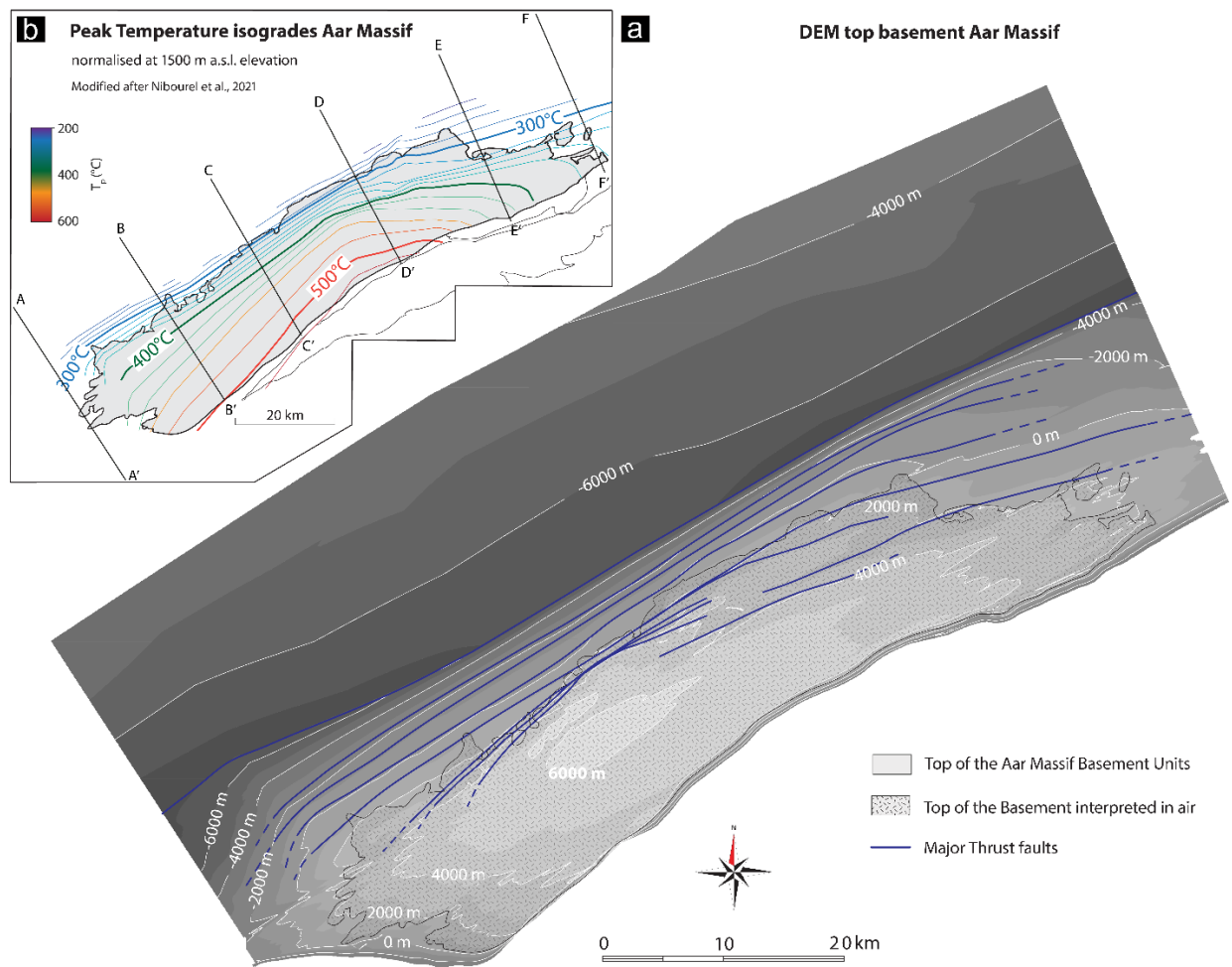
Figure 2.5 – (A) Modelled elevation of top basement units of the Aar Massif. The massif exhibits a pronounced dome-shape with the central regions exhumed to an elevation of 6 km a.s.l. and the sides at elevations of -6 and -4 km. Multiple large-scale thrusts (blue lines) dissect the northern front of the massif. The northern front, as also shown in Figs. 2.2 and 2.3, dips steeply towards the NW to the basal thrust, which separates the massif from the basement units of the foreland. (B) Paleo-isotemperature map (published by Nibourel et al., 2021b) showing the peak Alpine metamorphic conditions reached in the massif. The general pattern of isograds closely follows the trend of the structures and reflects the three-dimensional dome-shape of the Aar Massif, in both its perpendicular and along-strike directions.

Jurassic sediments are aligned along major structures and locally pinched between the basement in several synformal sedimentary wedges (Figs. 2.1 and 2.3c). The 3D dome shape of the massif and consequent erosion of the basement units, coupled with the variation in lateral extent of these wedges, has resulted in different degrees of preservation and exposure of the latter (Figs. 2.1 and 2.3c).

2.4.4 Dynamics of Alpine deformation

Six NNW-SSE striking geological cross-sections (A–A' to F-F'; traces in Fig. 2.1) were retro-deformed to unravel how the Aar Massif

reached its present-day geometry during the Alpine deformation in space and time. As a representative example, this section shows the result of the retro-deformation of section C-C', from the onset of Alpine deformation to the present-day configuration (Fig. 2.6; coordinates and the other retro-deformed sections are stored in Appendix A).

2.4.4.1 C–C' section restoration

The exhumation of the Aar Massif was divided into the five aforementioned evolutionary stages:

Time stage 22 Ma (Fig. 2.6a). The former passive continental margin of the European plate was bent by ~10° and buried at a maximum depth of -15 km in the footwall of the overriding nappes (Ebert et al., 2008; and Nibourel et al., 2018, 2021a). The basement units have been dissected by several normal faults, often associated with former Permo-Carboniferous half grabens (e.g., Burkhard, 1988; Spillmann et al., 2011; Musso Piantelli et al., 2022). By interpolation of the peak temperature data (compiled by Nibourel et al., 2021) the thermal structure at the onset of Alpine deformation was reconstructed. This indicated an average geothermal gradient of 26°C/km with nearly horizontal isotherms (see Appendix A).

Time interval 22 to 18 Ma (Fig. 2.6b). In the southern Aar Massif, the uplift of the basement units started at 22 Ma, triggered by basement internal steep reverse faults (red lines). Most of the south-dipping Jurassic normal faults were not reactivated by the collisional deformation (Nibourel et al. 2021a; Musso Piantelli et al., 2022). Instead, new reverse faults developed in the hanging wall of the latter, leading to the uplift of the southern basement blocks. At the same time, early thrusts were active at the front of the uplifting massif.

Time interval 18 to 15 Ma (Fig. 2.6c). With ongoing convergence, exhumation of the basement units progressed towards the central regions of the massif. As already described in the previous stage, Sub-vertical reverse faulting and shallow-dipping thrusting were simultaneously active. This resulted in the formation of thin synformal wedges of Mesozoic and Permo-Carboniferous sediments formed, with steeply dipping and locally even overturned strata (e.g., Fig. 2.3c).

Time interval 15 to 10 Ma (Fig. 2.6d). Basement exhumation moved into the northern units with a large reverse fault component (red lines). This internal basement differential shearing and reverse faulting cumulated with the previous stages, and caused the formation of the steep northern front of the massif and the passive up-doming of the entire overlying Helvetic/Penninic nappe stack.

Time interval 10 Ma to present-day (Fig. 2.6e). In contrast to the previous time interval, only horizontal to moderately SE-dipping thrust faults (blue lines) were active, dissecting the basement and forcing a NW-directed thrusting and shortening. The deformation was mostly localised at depth and led to an 'en bloc' exhumation of the massif (Herwegh et al. 2020; Nibourel et al.
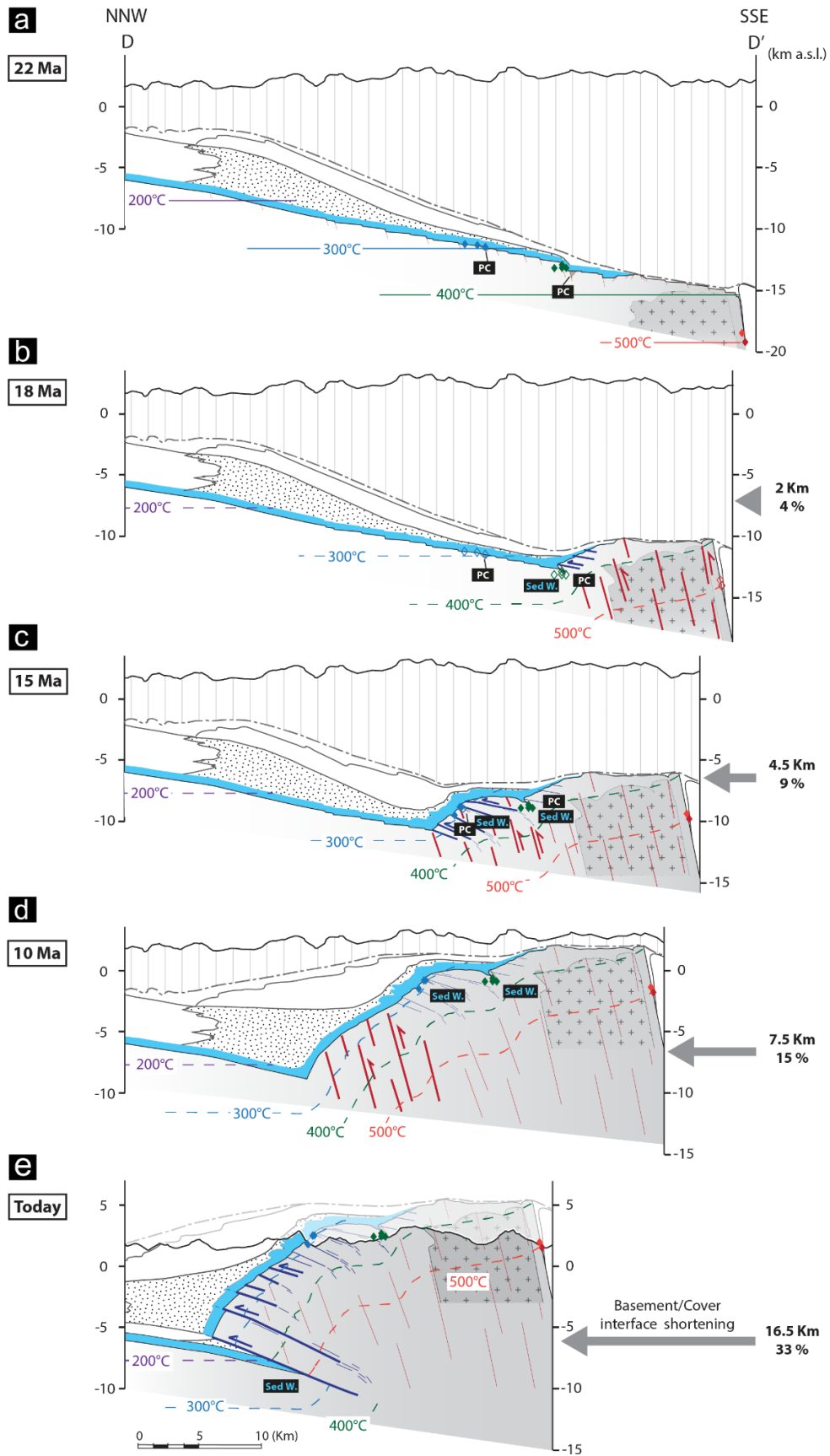
Figure 2.6 – Cross-section restoration of the D–D' section from 22 Ma to the present. For each deformation stage, the corresponding active deformation phase is highlighted by a larger line weight and color. (A) The Aar Massif is part of the European passive continental margin at 22 Ma. The massif is buried below the Helvetic Penninics and Austroalpine nappe stack and, to the north, Paleogene sediments. (B) At 18 Ma, internal steep reverse faults (red lines) and thrust faults (blue lines) exhumed the southern block of the massif. (C) At 15 Ma, the exhumation of the basement units progressed to the central block of the massif with simultaneously active subvertical reverse faults and shallow dipping thrusts. (D) At 10 Ma, the exhumation migrated to the northern block of the massif with a strong reverse fault component. This phase formed the steep northern front of the massif and the vertical uplift of the basement units, cumulated with the previous stages, and passively up-domed the entire overlying nappe stack. (E) In contrast to the previous time intervals, only flat-to-moderately SE dipping thrust faults (blue lines) dissected the basement units, promoting a NW-directed thrusting/shortening. The deformation was mostly localised at depth and resulted in an 'en bloc' exhumation (Herwegh et al. 2020; Nibourel et al. 2018, 2021b) of the basement units with ~9 km of horizontal shortening. Legend and section trace provided in Fig. 2.1.

2018, 2021b) with 9 km of horizontal shortening and 3.5 km of vertical uplift of the basement-cover interface. The deformation sequence culminated in a total of 16.5 km of horizontal shortening and up to 19.5 km of uplift of the basement-cover interface (see next section 2.4.5).

2.4.5 Horizontal Shortening and Vertical Uplift

The plots in Figure 2.7 show the total horizontal shortening and vertical uplift recorded by the basement-cover interface in the six retro-deformed sections at relative time intervals. Horizontal shortening and vertical exhumation in the Aar Massif were initiated at 22 Ma with the onset of subvertical reverse faulting and horizontal thrusting. The deformation recorded in the Aar Massif ranged from 15 to 19 km of total horizontal shortening and from 16.5 to 20.5 km of uplift of the basement cover interface (Fig. 2.7a and b). These trends, therefore, indicate average shortening and exhumation rates of 0.7 mm/yr and 0.9 mm/yr, respectively. However, a more detailed analysis of the sequential evolution of the shortening and exhumation rates shows that they have varied over time and along-strike of the massif.

Horizontal shortening rates between 22 Ma and 12-10 Ma are relatively low, ranging from 0.46 to 0.98 mm/yr, and show a stronger shortening component in the central area of the massif than at the sides of the massif. From 12-10 Ma to the present, the rates increase to 0.67 - 1 mm/yr and show the opposite trend, with greater shortening at the massif sides than the central region (Fig. 2.7a).

Exhumation rates between 22 Ma and 12-10 Ma are relatively high, ranging from 1.1 to 1.5 mm/yr, and show a high exhumation component in the central Aar Massif decreasing toward the eastern and western side of the massif. From 12-10 Ma to present, exhumation rates decrease drastically and progressively from east to west along-strike, with a decreasing trend from 0.4 in
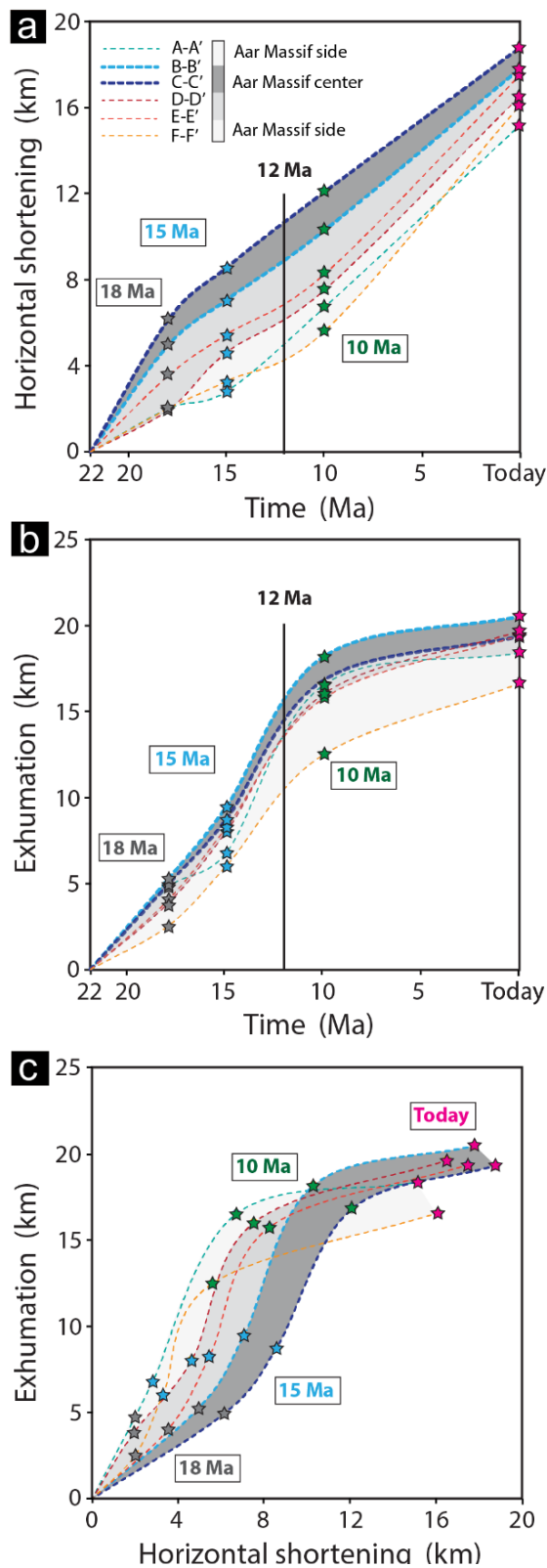
the east down to 0.18 mm/yr in the west. (Fig. 2.7b). The cumulative trajectory of each section, shown in Figure 2.7c, highlights how the central units of the massif have experienced greater exhumation and horizontal shortening than the sides of the massif.

2.5   DISCUSSION

The results obtained by restoring the six cross-sections in the study area provide significant insights into the 3D tectonic evolution of the Aar Massifs during the late-stage Alpine evolution and into the broader perspective of a 4D inversion of passive continental margins. Indeed, by generating a 3D model of each stage of retro-deformation, it was possible to reconstruct the inversion of 6350 km^2 of the former European passive continental margin. In this light, our study allows for the first time to build a complete 3D crustal reconstruction of the exhumation of one of the External Crystalline Massif of the Alps. In this section, the 4D

Figure 2.7 - Plots of the horizontal shortening (A) and exhumation (B) recorded by the basement-cover interface (dashed lines) along the six cross-sections during the restoration time intervals. (A) Horizontal shortening recorded by the Aar Massif was greater in the central units than on the sides of the massif. (B) Strong exhumation component of the basement units between 22 and 12 Ma. The exhumation then decreased to lower values since 12 Ma. (C) The plot of the combination of horizontal shortening and exhumation highlights how the central units of the massif have generally experienced a larger exhumation and shortening than the sides of the massif.

geodynamic evolution of the Aar Massif is discussed, particularly focussing on the deformation processes and structural inheritances.

2.5.1 The Aar Massif, a large portion of the European passive margin

The Aar Massif (Fig. 2.8) was located on the proximal domain of the European passive continental margin. As visible in present-day examples of the mid-Norwegian, Iberian, or Angola-Gabon proximal domains along the Atlantic rift system, such regions of extensional tectonics are characterised by weakly developed rift-related lithospheric and crustal thinning (e.g., Mohn et al., 2011; Peron-Pinvidic et al., 2013). The generation of accommodation space is, therefore, restricted to graben and half-graben basins (e.g., Wilson et al., 2001; Tugend et al., 2015). This tectonic scenario fits well with our reconstructed 3D architecture of the investigated Aar Massif portion of the European passive continental margin. Local asymmetric half-graben basins, such as Doldenhorn, Susten-Windgällen, and Tödi, were located on the western and eastern sides of a topographic high named Alemannic Land (see Fig. 2.8a; Trümpy, 1952; Musso Piantelli et al., 2022). The basins were bounded by northeast-southwest trending, southeast-dipping rotational normal faults. As indicated by the vertical extent of the sedimentary wedges distributed within today's Aar Massif, the throw of such normal faults was larger at the sides of the massif (up to about 2 km) and decreased towards the Alemannic Land in the centre (a few hundred metres; Fig. 2.8a).

This asymmetric tectonic rifting scenario resulted in a differential formation of accommodation space, which had a direct impact on the volumetric disposition and stratigraphic thickness of the Para- and Autochthonous sedimentary units of the massif. Up to 2 km thick sedimentary sequences were deposited in the basins, at the sides of the massif, whereas only a few hundred metres thick sedimentary sequences were deposited onto the topographic Alemannic high (Fig. 2.8b; see also Kempf and Pfiffner, 2004; Cardello and Mancktelow, 2014; Musso Piantelli et al., 2022). This palaeogeographic reconstruction explains the along-strike nowadays-observable thickness variation of the Aar Massif's para- and autochthonous sedimentary units (Fig. 2.2). Furthermore, it indicates that a portion of the Alpine dome-shape of the Aar Massif is in parts inherited from the passive margin geometry. In fact, already before the onset of Alpine collision, a height difference of the basement-cover contact of about 2 km existed already at that time between the evolving massif's sides (basins) and the central regions (high; Fig. 2.8b).

Besides this large-scale 3D margin architecture, our palegeographic reconstruction reveals a direct link between Mesozoic margin topography/basin asymmetries to the pre-existing crustal structures of the basement units imposed by the multiple Permo-Carboniferous troughs (e.g., Santantonio and Carminati, 2011; Lafosse et al., 2016; Balàzs et al., 2017). In fact, the large number of wedges with Mesozoic sediments associated with the occurrence of the
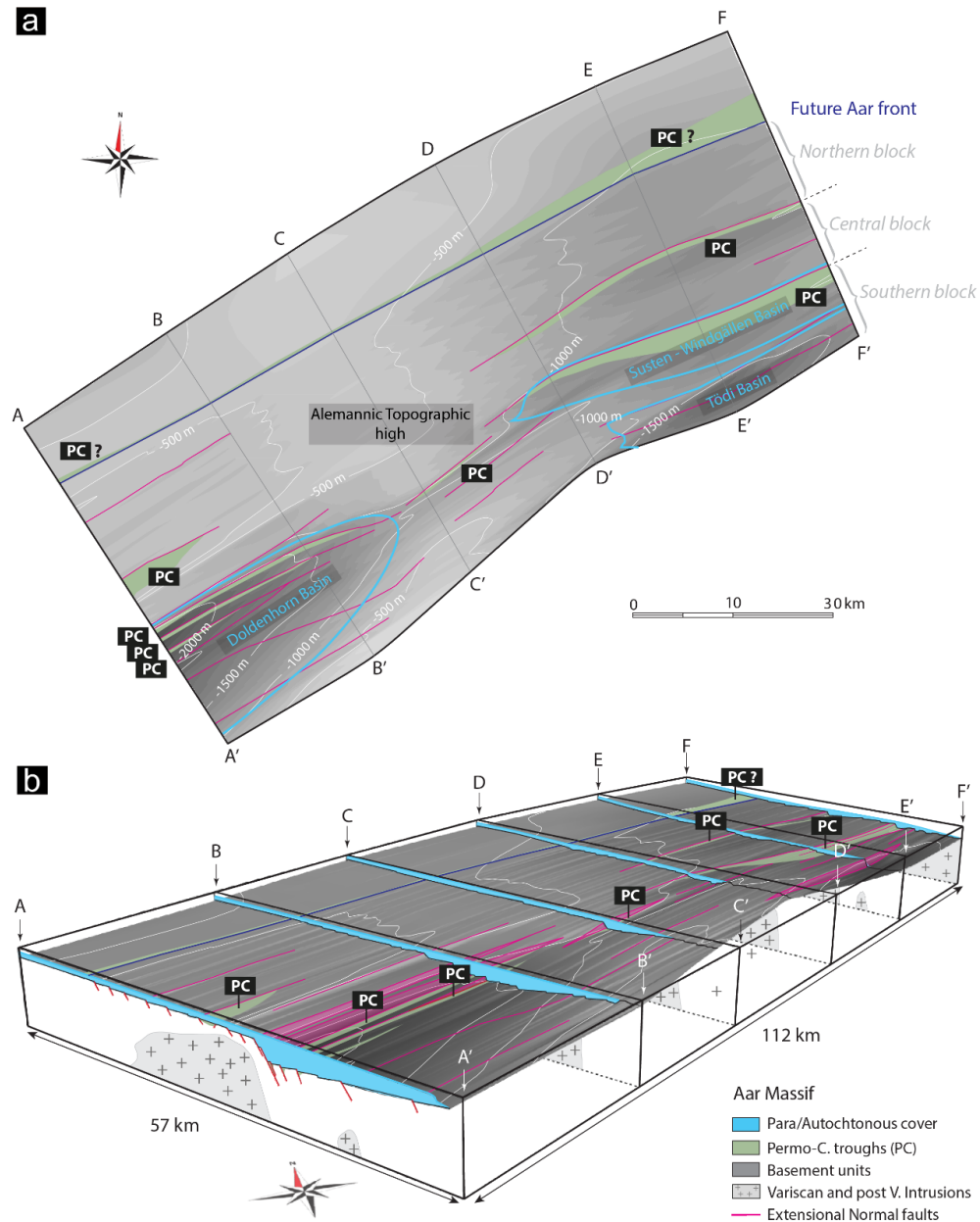
Figure 2.8 – (A) Map view of the top basement units of the reconstructed passive margin. The elevation contour highlights the ~2 km elevation difference between the Alemannic high and the basins on both sides of the massif. The map view also illustrates the subdivision of the massif blocks and the strong control of Permo-Caroniferous troughs and the associated fault system on the Jurassic rift structures and related basins and basement high. (B) 3D block reconstruction of the Aar Massif continental passive margin and sediment basins. A series of Jurassic normal faults opened three asymmetric half-grabens on the western and eastern sides of the margin. The central regions of the massif were characterized by a topographic high called the Alemannic Land (Trümpy, 1952). This asymmetric tectonic rifting scenario had a direct impact on the volumetric disposition of the Para-/Autochthonous sediments, with thicker units in the basins and a thinner cover in the central region of the massif. The reconstruction also shows the presence of intrusive rocks, larger volumes of which are located in the central regions of the massif.

pre-existing Permo-Carboniferous troughs (e.g., Fig. 2.3c) indicates a strong correlation between Mesozoic normal faulting and inherited crustal transtentional structures. This suggests that the geometry of the European proximal continental margin was largely controlled by the localisation of normal faults within pre-existing Late Carboniferous-Permian crustal structures (see also, e.g., Badertscher and Burkhard, 1998; Masini et al., 2013; Ballèvre et al., 2018, Musso Piantelli et al., 2022). In the case of the Aar Massif, the alignment of the numerous Permo-Carboniferous troughs divided the margin into three major large-scale crustal blocks (Fig. 2.8a). On the western and eastern sides of the massif, the block boundaries were marked by large Mesozoic normal fault offsets. In contrast, in the central regions of the massif, the fault offset was limited and therefore the block boundaries were less pronounced.

Our new findings on the local geometry of the Mesozoic Aar Massif's paleogeography may also have implications for the plate tectonics scale of the proximal European Passive margin and its associated rift kinematics: (1) Belledonne, Aiguilles Rouges/Mont Blanc and Aar Massifs are all of lentoid shape with their axes parallel to the former plate margin (Fig. 2.1). (2) These three massifs form a laterally discontinuous belt of basement domes which are separated by structural saddles arranged in an en echelon manner. (3) As demonstrated in this study, at least the Aar Massif laterally transfers into basins, which gradually decrease both depth and basin width towards the basement high (Fig.

2.8). All these geometric facts (1-3) could be best explained by an initial stage of oblique rifting, with a relative sinistral shear component between Europe and Adria, where pull-apart-like basins (today forming the structural saddles) alternate with basement highs in between (today forming the outcropping massifs). Such tectonic framework is well known from oblique rift systems developed during rock analog modelling experiments (e.g., McClay and White, 1995; Mart and Dauteuil, 2000; Corti et al., 2007).

2.5.2 Peak temperature and P-T boundaries

The general pattern of the peak temperature isograds recorded in the study area (Nibourel et al., 2021b) closely resembles the three-dimensional dome shape of the massif and the trend of the exhumation-related structures (compare Figs. 2.4 and 2.5). Such observations strengthen the interpretation that most of the deformation and the associated development of the present structural relief occurred after the peak temperature conditions, which is also generally consistent with the data and models of Burkhard (1988), Rahn and Grasemann (1999), Glotzbach et al., (2010), Nibourel et al., 2018, Challandes et al. 2008, Rolland et al. 2009, Berger et al. 2017, and Herwegh et al. 2020.

Retrodeformation along the six cross-sections of the peak temperature data allowed reconstruction of the paleo-gradient of peak temperature conditions, at 22 Ma, before the onset of Alpine deformation (Fig. 2.9a). Interpolation of the retrodeformed peak

temperature data indicates a horizontal gradient in the European margin of 26°C/km (see Appendix A). Peak metamorphism in the study area was reached by burial in the footwall to the basal Helvetic thrust, the main active tectonic boundary at the time, above which the Alpine nappe stack of Helvetic, Penninic and Austroalpine nappes was situated (Fig. 2.6a; Pfiffner, 2015). Temperature perturbations across the active thrust could have caused a gentle climb of the isotherms towards the interior of the orogen (e.g., Girault et al., 2020). However, this effect is considered negligible, as numerical models (e.g., Shi & Wang, 1987) demonstrated that temperature perturbations across shallow-dipping active thrusts with slip rates of no more than 5 mm/yr, such as the basal Helvetic thrust, rapidly re-equilibrate (Nibourel et al., 2021b; Pfiffner, 2015).

The peak-temperature at the reconstructed sedimentary-basement contact of the margin increased from ~240°C in the north to ~380–460°C in the south. Along strike of the southern regions, temperatures increased from 380°C in the center to up to 460°C on the sides of the massif, at a depth ranging between 18-20 km, reflecting the inherited topography of the passive margin (see 400°C isograd in Fig. 2.9a). Such reconstruction is in good agreement with the data models of Nibourel et al. 2021b Berger et al. 2020, Herwegh et al. 2017, 2020; and the pressure estimate of 6.5 kbar from Goncalves et al., 2012. The P-T boundary conditions at the onset of Alpine deformation ranged therefore from lower greenschists in the north (2.4 kbar;

~240°C) to upper greenschists facies in the south Aar Massif (6.5 kbar; ~380-460°C; see also Wehrens et al., 2016; 2017; Nibourel et al., 2021b).

2.5.3 3D Inversion of the Aar Massif

Our results indicate a distinct in-sequence exhumation of the basement units, showing how deformation localised in the southern block of the massif, migrating then gradually towards today's northern front of the massif. As a new outcome of our 3D modelling approach, the non-cylindrical exhumation of the massif owes to differential strain partitioning along different sets of reverse faults and NW-directed thrust faults. In the following, we present our 4D crustal-scale geodynamic reconstruction of the Aar Massif evolution, which can be subdivided into five stages (Fig. 2.9). In the map view of Figure 2.9, the active faults, the presence of Permo-Carbonifeous troughs, and the associated development of the structural relief at are highlighted at respective intervals. The 3D view shows the in-sequence activation of the crustal blocks and the development and onset of the dome shape of the massif from 22 Ma to the present.

1. 22–18 Ma: (Fig. 2.9a,b). As described in Section 5.2, at 22 Ma the European plate was bent by 10° and buried beneath a thick wedge of nappes at depths of -8 to -18 km (Fig. 2.9a). During this early stage deformation, steeply south-dipping to sub-vertical reverse faults were localised in the southern block of the massif. This deformation phase has been

interpreted as induced by buoyancy forces acting on mid- to upper-crustal rocks that were decoupled from the underlying European lower crust and lithospheric mantle (Herwegh et al., 2017, 2020; Kissling and Schlunegger, 2018). The reverse faults were localised as a dense network of anastomosing brittle-ductile fault zones that did not, or only in part, reactivate inherited normal faults. The fault zones arranged in the curved SSW-NNE to E-W and in the SW-NE striking trend (Fig. 2.9b). Permo-Carboniferous to Mesozoic and bounding faults of the Doldenhorn and Susten-Windgällen basins (Fig. 2.8a) defined the northern rim of the southern block. At these locations in addition to the reverse faults, thrust faults localized. It was during this stage that the thrusts nowadays observable at Jungfrau, Windgällen, and Wetterhorn developed (Fig. 2.3; Butler et al., 2006; Mair et al., 2018; Nibourel et al., 2021a). In the Aar Massif's central region, a combination of enhanced horizontal shortening and vertical exhumation rates (Fig. 2.7c) induced a basement rise by differential uplift to - 10 km (basement-cover contact) further pronouncing the Mesozoic inheritance of the basement high (Fig. 2.9b).

2. 18–15 Ma: (Fig. 2.9b,c). Owing to progressive shortening and buoyancy-driven differential vertical uplift by reverse faulting gradually extended towards the north within the Aar Massif's central block. During this stage, and incorporating again local thrusting, synformal sedimentary wedges of Mesozoic and Permo-Carboniferous sediments formed between basement units. In addition, thrust structures generated in the previous stage were overprinted by the vertical uplift of the central block. The thrust planes were indeed bent and, as observed by Nibourel et al. (2021a), cut by newly formed reverse faults (Fig. 2.3a).

3. 15–10 Ma: (Fig. 2.9c, d). The exhumation of the basement units progressed into the northern crustal block. The reverse faulting induced vertical rock uplift decreased toward the northern end of the block. As a consequence of this accumulated vertical uplift between 22-10 Ma., substantial updoming of the Aar Massif resulted, affecting also the overlaying nappe stack with their basal thrusts (e.g. see bent Glarus, Doldenhorn basal thrusts, for example, in Pfiffner et al. 2011). In this reconstruction, the 3D dome shape of the massif at 10 Ma shows the central regions that have reached the surface and started to be exposed to erosional processes. On the contrary, to the west and east, the massif gradually lost elevation to -4 km.

4. 10 Ma to present: (Fig. 2.9d,e). The last stage of deformation focused on the northern block with formation of large-scale NW-directed thrust structures forcing a passive "en bloc" uplift of the Aar Massive (Herwegh et al. 2017, 2020; Nibourel et al., 2021a). Exhumation rates decreased to lower values, with a decreasing trend from east to west

a **22 Ma**

Map view

Northern block
Central block
Southern block

200°C
300°C
400°C
-8 km
-10 km
-12 km
-14 km
-16 km

3D view

200°C
300°C
400°C
500°C

10 km

b **18 Ma**

Northern block
Central block
Southern block

-8 km
-10 km
-12 km
-10 km
-12 km

10 km

c **15 Ma**

Northern block
Central block
Southern block

-8 km
-10 km
-10 km
-8 km
-6 km
-10 km

10 km

d **10 Ma**

Northern block
Central block
Southern block

-6 km
-8 km
-4 km
-2 km
0 km
2 km

10 km

e **Today**

Northern block
Central block
Southern block

-4 km
-3 km
-2 km
0 km
2 km
4 km
6 km

30 km

10 km

Aar Massif

- Para/Autochtonous cover
- Permo-C. troughs (PC)
- Basement units

Structural elements

- Strike slip faults
- Thrust faults
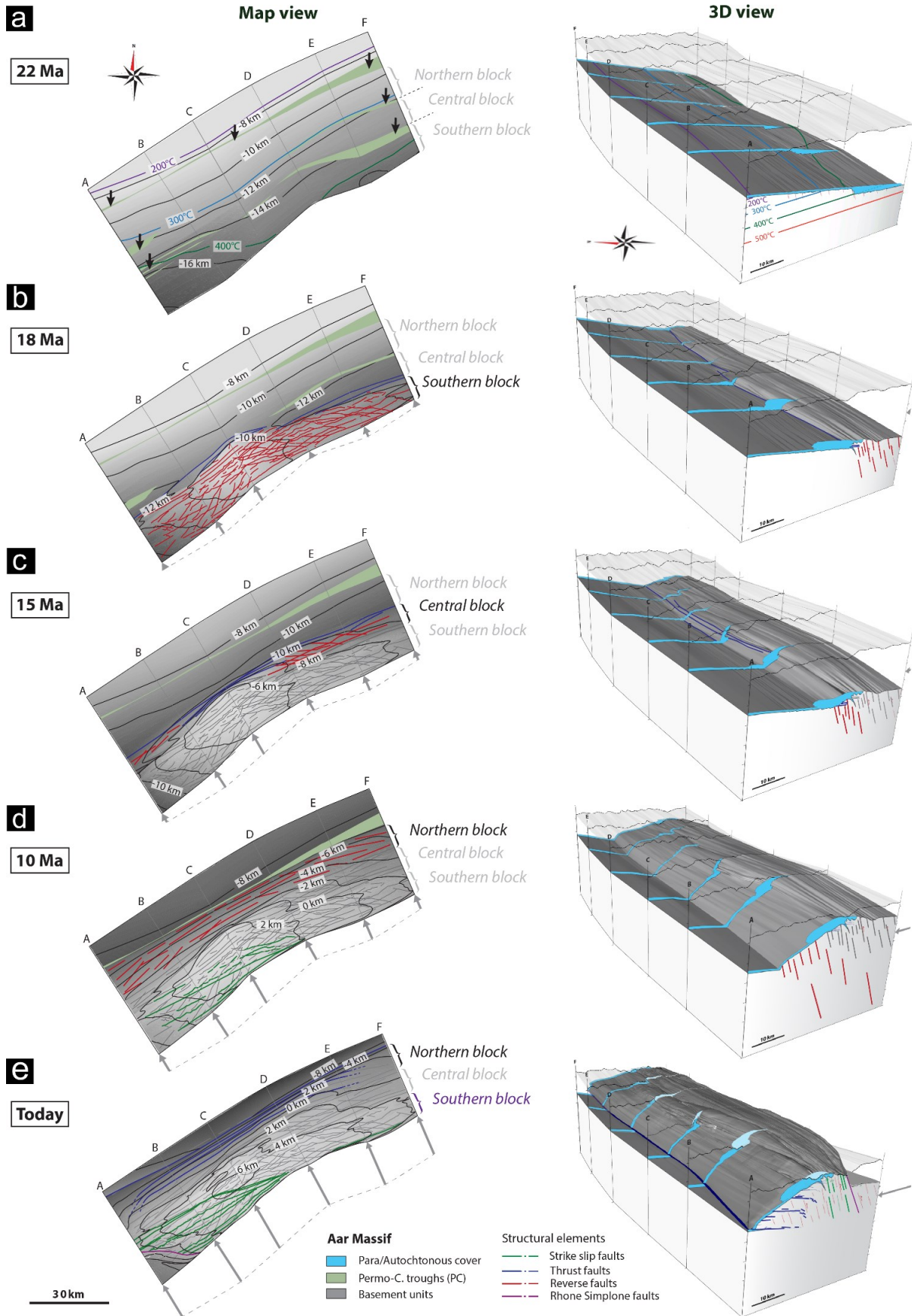- Reverse faults
- Rhone Simplone faults

64

Figure 2.9 - 4D geodynamic evolution of the Aar Massif during the late-stage Alpine orogeny. The left column shows the evolution in map view, while the right column shows the evolution in 3D view. (A) At 22 Ma, the Aar Massif margin is buried at a depth ranging between -8 and -18 km with a horizontal gradient of 26°C/km. (B) At 18 Ma, the southern block of the massif is exhumed with diffuse reverse faults. Thrust faulting localised at the front of the block. Greater shortening and exhumation in the central units accentuates the already inherited height difference between the sides and the centre of the massif. (C) Exhumation migrates in the central block of the massif. Diffuse reverse faulting of the block bends and cut the thrust structures developed in the southern block in the previous stage. New thrust fault structures were localized at the front of the central block. (D) Strong vertical exhumation of the northern block of the massif until 10 Ma with reverse fault structures. During this stage, the steep northern front of the massif was formed and the basement units in the central Aar Massif reached the surface and started to be eroded. (E) Between 10 Ma and the present day, large-scale thrust structures dissected and displaced the northern block of the massif, causing an 'en bloc' exhumation of the basement units (Nibourel et al., 2021b). Contemporarily, reverse faults in the south-western units of the massif were reactivated as strike slip/oblique structures (green lines). In addition, the Rhone-Simplon fault (purple) was also active and was responsible for the displacement of the southern margin of the massif.

along the strike of the massif, from 0.4 to 0.18 mm/yr, respectively (Fig. 2.7b). On the other hand, the shortening rates increased due to the horizontal thrust component, which was larger in the east, 9 km (F-F') compared to 7 km in the central Aar Massif (C-C'). This resulted in higher rates of shortening at the sides of the massif (0.85 to 1 mm/yr) and lower rates in the central regions of the massif (0.67 to 0.75 mm/yr). At the same time, compressional deformation along the northern front of the massif progressed towards the North Alpine Foreland, where new north-northwest-vergent crustal ramps/thrusts were activated, correlating with imbricate thrusting in the Subalpine Molasse (Mock et al., 2020; von Hagke et al., 2012).

Furthermore, during this stage, the south-west basement units have been subjected to strike-slip to oblique reactivation of the reverse fault structures and by the possibly related motion of the Rhone-Simplon System (Grosjean et al., 2004; Campani et al., 2014; Wehrens et al., 2016, 2017).

2.5.4 Interplay between crustal inheritance and deep crustal tectonics

From a geodynamic point of view, the External Crystalline Massifs of the European Alps provide an opportunity to study the kinematics, timing, and driving forces of exhumation processes during the inversion of passive margins in continent-continent collision (Bellahsen and Lacombe, 2016; Herwegh et al. 2020). Our unravelled exhumation dynamics of the Aar Massif demonstrate how the present-day dome geometry results from an interplay between deep crustal tectonics, crustal inheritances and their link with erosion.

On the one hand, deep-seated decoupling between the middle and the lower European

crust (Herwegh et al., 2017, 2020) triggered the formation of reverse faults with a strong rock uplift component. These reverse faults formed pervasively within the basement, did not reactivate inherited crustal structures, and formed the structural relief of the massif.

On the other hand, as also suggested by Nibourel et al. 2021b, inherited variations in the thickness and density of the basement units induced variations in the magnitude of the buoyancy forces. Indeed thicker less stretched and dense crust in the central regions of the massif, due to presence of large intrusive bodies, recorded a strong exhumation component, compared to the side regions dominated by dense gneisses, migmatites, and amphiblotes. Furthermore, inherited shallow crustal Permo-Carboniferous troughs controlled the location of Mesozoic normal faulting and hence the development of the topography and basin asymmetries of the European margin (Fig. 2.8). Subsequently, during the inversion and exhumation of the crustal blocks of the margin, local thrust structures were localized along the same Permo-Carboniferous troughs in the forming Aar Massif.

As also shown in numerical models (Lafosse et al., 2016), within this interplay, temperature and tectonic burial favour or inhibit the reactivation of inherited crustal structures. Indeed, at high temperatures (>300°C), as in the case of the buoyancy-induced reverse fault zones, pervasive localisation of structures occurs without reactivation of inherited structures. At low temperatures (<300°C), reactivation or localization of newly formed structures takes place. This has been observed in the massif during the extension of the European margin and during the localisation of horizontal thrusts during the inversion of the massif.

2.6   CONCLUSION

The 4D geodynamic reconstruction discussed in this contribution allowed us to quantitatively describe the structural evolution of the Aar Massif during the late stage of the Alpine collision and to link it to the Permo-Carboniferous to Mesozoic paleogeographic preconditioning. The 3D dome shape of the Aar Massif is the result of several preconditioning factors and deep-seated tectonic dynamics that have shaped this complex in space and time. These are in particular:

i)   The Aar Massif is the result of the inversion of former 6350 km^2 of passive European continental margin. Reconstruction of the proximal margin has revealed an asymmetric architecture with local half-graben basins, on the western and eastern sides of the massif and a topographic high in the central regions of the massif. This geometry was largely controlled by normal faulting within inherited Late Carboniferous-Permian crustal structures. This asymmetric tectonic rifting scenario resulted in a differential accommodation space, which explains the nowadays-observable thickness variation along the strike of the Aar Massif's Para- and Autochthonous sedimentary units (Figs. 2.1 and 2.2).

ii)   Interpolation of the compiled retrodeformed peak temperature data indicates

a horizontal geothermal gradient at the European margin of 26°C/km. Peak metamorphism in the study area was reached by burial at depths between -8 and -18 km in the footwall of the basal Helvetic thrust, below the overlying Penninic and Austroalpine nappes. The P-T boundary conditions at the onset of Alpine deformation therefore ranged from lower greenschist in the north (2.4 kbar; ~240°C; Herwegh et al., 2017,2020; Nibourel et al., 2021) to upper greenschist facies in the southern Aar Massif (6.5 kbar, Goncalves et al., (2012); ~380-460°C).

iii) Uplift of the basement units was localised in the southern block of the massif and then gradually migrated to the northern front of the massif, in a distinct in-sequence deformation style. Inherited along strike variations in the thickness and density of the crust, due to the extensional architecture of the margin and presence of large intrusive bodies, induced variations in the magnitude of the buoyancy forces. This resulted in a non-cylindrical exhumation of the massif, with larger shortening and exhumation rates in the central regions of the massif, compared to the sides.

The reconstruction highlights the importance of incorporating 3D considerations when investigating the evolution of an orogen. The case of the Aar Massif has shown how inversion of passive margins in continent-continent collision is controlled by inherited basement geometries and P-T conditions during the inversion. Our paleogeographic and 4D geodynamic reconstruction could motivate future studies including the Belledonne and Aiguilles Rouges/Mont Blanc Massifs to enlarge the scale of the reconstruction and gain a deeper understanding of the thickening processes of the lower plate during advanced stages of collision of the European Alps.

AUTHOR CONTRIBUTIONS

MH, AB, acquired the founding for this project. FMP, MH, and AB designed the study; All the authors over the past years carried out the fieldwork in the area. FMP made the retrodeformation and 3D modelling with additional scientific input from MH, AB, and LN. LN provided the paleo peak temperature dataset. FMP prepared the manuscript and figures with contribution from all co-authors. All authors read and approved the manuscript.

REFERENCES

Abrecht, J., 1994. Geologic units of the Aar massif and their pre-Alpine rock associations: a critical review: the pre-Alpine crustal evolution of the Aar-, Gotthard-and Tavetsch massifs. Schweizerische mineralogische und petrographische Mitteilungen, 74(1), 5-27.

Badertscher, N., Burkhard, M., 1998. Inversion alpine du graben Permo-Carbonifère de Salvan-Dorénaz et sa relation avec le chevauchement de la nappe

de Morcles sus-jacente. Eclogae Geologicae Helvetiae, 91, 359–373.

Balázs, A., Burov, E., Matenco, L., Vogt, K., Francois, T., Cloetingh, S., 2017. Symmetry during the syn- and post-rift evolution of extensional back-arc basins: The role of inherited orogenic structures. Earth and Planetary Science Letters, 462, 86-98.

Ballevre, M., Manzotti, P., Dal Piaz, G. V., 2018. Pre-Alpine (Variscan) inheritance: a key for the location of the future Valaisan Basin (Western Alps). Tectonics, 37(3), 786-817.

Bambauer, H.U., Herwegh, M., Kroll, H., 2009. Quartz as indicator mineral in the swiss alps: the Quartz recrystallization isograd in the rock series of the northern Aar Massif. Swiss J. Geosci. 102, 345–351.

Baumberger, R., Herwegh, M., Kissling, E., 2022. Remote sensing and field data based structural 3D modelling (Haslital, Switzerland) in combination with uncertainty estimation and verification by underground data. 3D Digital Geological Models: From Terrestrial Outcrops to Planetary Surfaces, 159-197.

Bauville, A., Schmalholz, S. M., 2015. Transition from thin-to thick-skinned tectonics and consequences for nappe formation: Numerical simulations and applications to the Helvetic nappe system, Switzerland. Tectonophysics 665, 101–117.

Bauville, A., Schmalholz, S. M., 2017. Tectonic inheritance and kinematic strain localization as trigger for the formation of the Helvetic nappes, Switzerland. Swiss Journal of Geosciences 110 (2), 523–534.

Bellahsen, N., Mouthereau, F., Boutoux, A., Bellanger, M., Lacombe, O., Jolivet, L., Rolland, Y., 2014. Collision kinematics in the western external Alps. Tectonics, 33(6), 1055-1088.

Bellanger, M., Bellahsen, N., Jolivet, L., Baudin, T., Augier, R., Boutoux, A., 2014. Basement shear zones development and shortening kinematics in the Ecrins Massif, Western Alps. Tectonics 33, 84-111.

Bergemann, C., Gnos, E., Berger, A., Whitehouse, M., Mullis, J., Wehrens, P., Pettke, T., Janots, E., 2017. Th-Pb ion probe dating of zoned hydrothermal monazite and its implications for repeated shear zone activity: An example from the Central Alps, Switzerland. Tectonics 36, 671–689.

Berger, A., Wehrens, P., Lanari, P., Zwingmann, H., Herwegh, M., 2017. Microstructures, mineral chemistry and geochronology of white micas along a retrograde evolution: An example from the Aar massif (Central Alps, Switzerland). Tectonophysics, 721, 179-195.

Berger, A., Mercolli, I., Herwegh, M., and Gnos E. 2017b. Geological Ma of the Aar Massif, Tavetsch and Gotthard Nappes 1 : 100 000, Federal Office of Topography Swisstopo, Wabern.

Berger, A., Engi, M., Erne-Schmid, S., Glotzbach, C., Spiegel, C., de Goede, R., Herwegh, M., 2020. The relation between peak metamorphic temperatures and subsequent cooling during continent–continent collision (western Central Alps, Switzerland). Swiss journal of geosciences, 113(1), 1-18.

Beyssac, O., Simoes, M., Avouac, J. P., Farley, K. A., Chen, Y. G., Chan, Y. C., and Goffé, B., 2007. Late Cenozoic metamorphic evolution and exhumation of Taiwan. Tectonics, 26(6).

Boutoux, A., Bellahsen, N., Lacombe, O., Verlaguet, A., Mouthereau, F., 2014. Inversion of pre-orogenic extensional basins in the external Western Alps: structure, microstructures and restoration. Journa of Structural Geology 60, 13–29.

Boutoux, A., Bellahsen, N., Nanni, U., Pik, R., Verlaguet, A., Rolland, Y., Lacombe, O., 2016. Thermal and structural evolution of the external Western Alps: Insights from (U–Th–Sm)/He thermochronology and RSCM thermometry in the Aiguilles Rouges/Mont Blanc massifs. Tectonophysics 683, 109-123.

Burkhard, M., 1988. L'Helvétique de la bordure occidentale du massif de l'Aar (évolution tectonique et métamorphique). Eclogae Geologicae Helvetiae 81, 63–114.

Butler, R. W., Tavarnelli, E., Grasso, M., 2006. Structural inheritance in mountain belts: an Alpine–Apennine perspective. Journal of structural geology, 28(11), 1893-1908.

Campani, M., Mulch, A., Kempf, O., Schlunegger, F., Mancktelow, N., 2012. Miocene paleotopography of the Central Alps. Earth and Planetary Science Letters, 337, 174-185.

Campani, M., Mancktelow, N., Courrioux, G., 2014. The 3D interplay between folding and faulting in a syn-orogenic extensional system: the Simplon Fault Zone in the Central Alps (Switzerland and

Italy). Swiss Journal of Geosciences, 107(2), 251-271.

Cardello G. L., Mancktelow N., 2014. Cretaceous syn-sedimentary faulting in the Wildhorn Nappe. Swiss Journal of Geoscience 107(2-3), 223–250. https://doi.org/10.1007/s00015-014-0166-8

Challandes, N., Marquer, D., Villa, I., 2008. P-T-t modelling, fluid circulation, and 39Ar- 40Ar and Rb-Sr mica ages in the Aar Massif shear zones (Swiss Alps). Swiss J. Geosci. 101, 269–288.

Choukroune, P., Gapais, D., 1983. Strain patterin in the Aar granite (Central Alps): orthogneiss developed by bulk inhomogeneous flattening. Journal of Structural Geology 5, 411-418.

Corti, G., van Wijk, J., Cloetingh, S., and Morley, C. K. (2007). Tectonic inheritance and continental rift architecture: Numerical and analogue models of the East African Rift system. Tectonics, 26(6).

Curzi, M., Aldega, L., Bernasconi, S. M., Berra, F., Billi, A., Boschi, C., Franchini, S., Van der Lelij, R., Viola, G., Carminati, E., 2020. Architecture and evolution of an extensionally-inverted thrust (Mt. Tancia Thrust, Central Apennines): Geological, structural, geochemical, and K–Ar geochronological constraints. Journal of Structural Geology, 136, 104059.

Ebert, A., Herwegh, M., Berger, A., Pfiffner, A., 2008. Grain coarsening maps for polymineralic carbonate mylonites: a calibration based on data from different Helvetic nappes (Switzerland). Tectonophysics 457, 128–142.

Egli, D., Mancktelow, N., 2013. The structural history of the Mont Blanc Massif with regard to models for its recent exhumation. Swiss J. Geosci. 106, 469–489.

Froitzheim, N., Schmid, S. M., & Frey, M. (1996). Mesozoic paleogeography and the timing of eclogite-facies metamorphism in the Alps: A working hypothesis. Eclogae Geologicae Helvetiae, 89(1), 81. https://doi.org/10.5169/seals-167895

Frey, M., Teichmueller, M., Teichmueller, R., Mullis, J., Kuenzi, B., Breitschmid, A., Gruner, U., Schwizer, B., 1980. Very low grade metamorphism in external parts of the Central Alps: illite crystallinity, coal rank and fluid inclusion data. Eclogae geol. Helv. 73 (1), 173–203.

Frey, M., 1987. The reaction-isograd kaolinite+quartz=pyrophyllite+H2O, Helvetic Alps,

Switzerland. Schweiz. Mineral. Petrogr. Mitt. 67, 1–11.

Girault, J.B., Bellahsen, N., Boutoux, A., Rosenberg, C., Nanni, U., Verlaguet, A., Beyssac, O., 2020. 3D thermal structure of the Helvetic nappes of the European Alps: implications for collisional processes. Tectonics. doi: 10.1029/2018TC005334.

Girault, J. B., Bellahsen, N., Bernet, M., Pik, R., Loget, N., Lasseur, E., Rosenberg, C. L.,Balvay, M., Sonnet, M., 2022. Exhumation of the Western Alpine collisional wedge: New thermochronological data. Tectonophysics, 822, 229155.

Glotzbach, C., Reinecker, J., Danisik, M., Rahn, M., Spiegel, C., 2010. Thermal history of the central Gotthard and Aar massifs, European Alps: Evidence for steady state, longterm exhumation. J. Geophys. Res. - Earth Surface 115. https://doi.org/10.1029/2009jf001304.

Goncalves, P., Oliot, E., Marquer, D., Connolly, J.A.D., 2012. Role of chemical processes on shear zone formation: An example from the Grimsel metagranodiorite (Aar Massif, Central Alps). J. Metamorph. Geol. 30, 703–722.

Granado, P., Ruh, J. B., 2019. Numerical modelling of inversion tectonics in fold-and-thrust belts. Tectonophysics 763, 14–29.

Grosjean, G., Sue, C., Burkhard, M., 2004. Late Neogene extension in the vicinity of the Simplon fault zone (central Alps, Switzerland). Eclogae Geologicae Helvetiae 97(1), 33-46.

Hänni, R., Pfiffner, O. A., 2001. Evolution and internal structure of the Helvetic nappes in the Bernese Oberland. Eclogae Geologicae Helvetiae, 94(2), 161-171.

Herwegh, M., Pfiffner, O.-A., 2005. Tectono-metamorphic evolution of a nappe stack: A case study of the Swiss Alps. Tectonophysics 404 (1-2), 55–76.

Herwegh, M., Berger, A., Baumberger, R., Wehrens, P., Kissling, E., 2017. Large-scale crustal-block-extrusion during late Alpine collision. Scientific reports, 7(1), 1-10.

Herwegh, M., Berger, A., Glotzbach, C., Wangenheim, C., Mock, S., Wehrens, P., Baumberger, R., Egli, D., Kissling, E., 2020. Late stages of continent-continent collision: Timing, kinematic evolution,

and exhumation of the Northern rim (Aar Massif) of the Alps. Earth-science reviews, 200, 102959.

Janots, E., Berger, A., Gnos, E., Whitehouse, M., Lewin, E., & Pettke, T. (2012). Constraints on fluid evolution during metamorphism from U–Th–Pb systematics in Alpine hydrothermal monazite. Chemical Geology, 326, 61–71 https://doi.org/10.1016/j.chemgeo.2012.07.014

Kempf, O., Matter, A., Burbank, D. W., & Mange, M. (1999). Depositional and structural evolution of a foreland basin margin in a magnetostratigraphic framework: The eastern Swiss Molasse Basin. International Journal of Earth Sciences, 88(2), 253–275. https://doi.org/10.1007/s005310050263

Kempf, O., Pfiffner, O. A., 2004. Early Tertiary evolution of the North Alpine Foreland Basin of the Swiss Alps and adjoining areas. Basin Research, 16(4), 549-567.

Kissling, E., Schlunegger, F., 2018. Rollback orogeny model for the evolution of the Swiss Alps. Tectonics 37, 1097-1115.

Lacombe, O., Bellahsen, N., 2016. Thick-skinned tectonics and basement-involved fold–thrust belts: insights from selected Cenozoic orogens. Geological Magazine 153, 763–810.

Lafosse, M., Boutoux, A., Bellahsen, N., Le Pourhiet, L., 2016. Role of tectonic burial and temperature on the inversion of inherited extensional basins during collision. Geological Magazine 153, 811-826.

Mair, D., Lechmann, A., Herwegh, M., Nibourel, L., Schlunegger, F., 2018. Linking Alpine deformation in the Aar Massif basement and its cover units–the case of the Jungfrau–Eiger mountains (Central Alps, Switzerland). Solid Earth 9, 1099–1122.

Mart, Y., and Dauteuil, O. 2000. Analogue experiments of propagation of oblique rifts. Tectonophysics, 316(1-2), 121-132.

Masini, E., Manatschal, G., Mohn, G., 2013. The Alpine Tethys rifted margins: Reconciling old and new ideas to understand the stratigraphic architecture of magma-poor rifted margins. Sedimentology, 60(1), 174-196.

McClay, K. R., and White, M. J. 1995. Analogue modelling of orthogonal and oblique rifting. Marine and Petroleum Geology, 12(2), 137-151.

Mock, S., 2014. Deformation of the Sediment-Crystalline Contact in the Northern Aar Massif (Innertkirchen, Bernese Oberland) MSc Thesis. University of Bern, pp. 1–92.

Mock, S., von Hagke, C., Schlunegger, F., Dunkl, I., Herwegh, M., 2020. Long-wavelength late-Miocene thrusting in the north Alpine foreland: implications for late orogenic processes. Solid Earth 11, 1823-1847.

Mohn, G., Manatschal, G., Masini, E., Müntener, O., 2011. Rift-related inheritance in orogens: a case study from the Austroalpine nappes in Central Alps (SE-Switzerland and N-Italy). International Journal of Earth Sciences, 100(5), 937-961.

Musso Piantelli, F., Mair, D., Berger, A., Schlunegger, F., Wiederkehr, M., Kurmann, E., Moeri, A., Baumberger, R., and Herwegh, M. (2022). 4D reconstruction of the Doldenhorn nappe-basement system in the Aar massif: Insights into late-stage continent-continent collision in the Swiss Alps. Tectonophysics, 843, 229586.

Musso Piantelli, F., Truttmann, S., & Herwegh, M. 2023. The control of collisional tectonics over valley morphology: the case of the largest glacier in the European Alps. Terra Nova.

Muñoz, J. A., 1992. Evolution of a continental collision belt: ECORS-Pyrenees crustal balanced cross-section. In Thrust tectonics (pp.235–246). Springer. https://doi.org/10.1007/978-94-011-3066-010.1007/978-94-011-3066-0_21

Nibourel, L., Berger, A., Egli, D., Luensdorf, N. K., Herwegh, M., 2018. Large vertical displacements of a crystalline massif recorded by Raman thermometry. Geology 46 (10), 879–882.

Nibourel, L., Berger, A., Egli, D., Heuberger, S., Herwegh, M., 2021a. Structural and thermal evolution of the eastern Aar Massif: insights from structural field work and Raman thermometry. Swiss journal of geosciences, 114(1), 1-43.

Nibourel, L., Rahn, M., Dunkl, I., Berger, A., Hermann, F., Diehl, T., Heuberger, S., Herwegh, M., 2021b. Orogen-parallel migration of exhumation in the eastern Aar Massif revealed by low-T thermochronometry. J. Geophys. Res. Solid Earth 126 e2020JB020799.

Peron-Pinvidic, G., Manatschal, G., Osmundsen, P. T., 2013. Structural comparison of archetypal Atlantic rifted margins: A review of observations and

concepts. Marine and petroleum geology, 43, 21-47.

Pfiffner, O.A., 2006. Thick-skinned and thin-skinned styles of continental contraction. Special Papers-Geological Society of Aamerica 414, 153.

Pfiffner, O.A., Burkhard, M., Hänni, R., Kammer, A., Kligfield, R., Mancktelow, N., Menkveld, J., Ramsay, J., Schmid, S., Zurbriggen, R., 2011. Structural map of the Helvetic zone of the Swiss Alps, including Vorarlberg (Austria) and Haute Savoie (France).

Pfiffner, O.A., 2015. Geologie der Alpen. volume 8416. UTB

Rahn, M., & Grasemann, B. (1999). Fission track and numerical thermal modeling of differential exhumation of the Glarus thrust plane (Switzerland). Earth and Planetary Science Letters, 169(3–4), 245–259. https://doi.org/10.1016/S0012821X(99)00078-3

Ricchi, E., Bergemann, C., Gnos, E., Berger, A., Rubatto, D., & Whitehouse, M. (2019). Constraining deformation phases in the Aar Massif and the Gotthard Nappe (Switzerland) using Th-Pb crystallization ages of fissure monazite-(Ce). Lithos, 342, 223–238. https://doi.org/10.1016/j.lithos.2019.04.014

Rohr, K., 1926. Stratigraphische und tektonische Untersuchung der Zwischenbildungen am Nordrand des Aarmassivs (zwischenWendenjoch undWetterhorn), Beiträge zur Geol. Karte der Schweiz, N.F. 57, Francke, Bern.

Rolland, Y., Cox, S.F., Corsini, M., 2009. Constraining deformation stages in brittle–ductile shear zones from combined field mapping and 40Ar/39Ar dating: The structural evolution of the Grimsel Pass area (Aar massif, Swiss Alps). J. Struct. Geol. 31, 1377–1394.

Rosenberg, C.L., and Kissling, E., 2013. Three-dimensional insight into Central-Alpine collision: Lower-plate or upper-plate indentation? Geology 41, 1219–1222.

Rosenberg, C. L., Berger, A., Bellahsen, N., & Bousquet, R., 2015. Relating orogen width to shortening, erosion, and exhumation during Alpine collision. Tectonics, 34(6), 1306-1328.

Rosenberg, C. L., Bellahsen, N., Rabaute, A., and Girault, J. B., 2021. Distribution, style, amount of collisional shortening, and their link to Barrovian

metamorphism in the European Alps. Earth-Science Reviews, 222, 103774.

Santantonio, M., Carminati, E., 2011. Jurassic rifting evolution of the Apennines and Southern Alps (Italy): Parallels and differences. Bulletin, 123(3-4), 468-484.

Schlunegger, F., Kissling, E., 2015. Slab rollback orogeny in the Alps and evolution of the Swiss Molasse basin. Nature communications, 6(1), 1-10.

Schmid, S.M., Pfiffner, O.A., Froitzheim, N., Schönborn, G., Kissling, E., 1996. Geophysical-geological transect and tectonic evolution of the Swiss-Italian Alps. Tectonics 15, 1036–1064.

Schmid, S.M., Fügenschuh, B., Kissling, E., Schuster, R., 2004. Tectonic map and overall architecture of the Alpine orogen. Eclogae Geologicae Helvetiae 97, 93–117.

Schlunegger, F., Matter, A., Burbank, D. W., & Klaper, E. M. (1997). Magnetostratigraphic constraints on relationships between evolution of the central Swiss Molasse basin and Alpine orogenic events. Geological Society of America Bulletin, 109(2), 225–241. https://doi.org/ 10.1130/0016-7606(1997)109<0225:mcorbe>2.3.co;2

Schneeberger, R., de La Varga, M., Egli, D., Berger, A., Kober, F., Wellmann, F., Herwegh, M., 2017. Methods and uncertainty estimations of 3-D structural modelling in crystalline rocks: A case study. Solid Earth 8, 987–1002.

Shi, Y., and Wang, C.-Y., 1987. Two-dimensional modeling of the p-t-t paths of regional metamorphism in simple overthrust terrains. Geology, 15(11), 1048–1051. https://doi.org/10.1130/0091-7613(1987)15<1048:tmotpp>2.0.co;2

Sibson, R. H., 1977. Fault rocks and fault mechanisms. Journal of the Geological Society, 133(3), 191–213.

Spitz, R., Bauville, A., Epard, J. L., Kaus, B. J., Popov, A. A., Schmalholz, S. M., 2020. Control of 3-D tectonic inheritance on fold-and-thrust belts: insights from 3-D numerical models and application to the Helvetic nappe system. Solid Earth, 11(3), 999-1026.

Steck, A., 1968. Die alpidischen Strukturen in den zentralen Aaregraniten des westlichen Aarmassivs. Eclogae Geologicae Helvetiae 61, 19-48.

Tricart, P., 1984. From passive margin to continental collision: A tectonic scenario for the Western Alps. Am. J. Sci. 284, 97–120.

Trümpy, R., 1952. Der Nordrand der Liasischen Tethys in den Schweizer Alpen. Geologische Rundschau, 40(2), 239-242.Tugend, J., Manatschal, G., Kusznir, N. J., Masini, E., 2015. Characterizing and identifying structural domains at rifted continental margins: application to the Bay of Biscay margins and its Western Pyrenean fossil remnants. Geological Society, London, Special Publications, 413(1), 171-203.

Tugend, J., Manatschal, G., Kusznir, N.J., Masini, E., 2015. Characterizing and identifying structural domains at rifted continental margins: application to the Bay of Biscay margins and its Western Pyrenean fossil remnants. Geol. Soc. Lond., Spec. Publ. 413 (1), 171–203.

Vergés, J., Saura, E., Casciello, E., Fernandez, M., Villaseñor, A., Jimenez-Munt, I., and García-Castellanos, D., 2011. Crustal-scale cross-sections across the NW Zagros belt: implications for the Arabian margin reconstruction. Geological Magazine, 148(5-6), 739-761.

von Hagke, C., Cederbom, C., Oncken, O., Stöckli, D., Rahn, M., Schlunegger, F., 2012. Linking the northern Alps with their foreland: The latest exhumation history resolved by low-temperature thermochronology. Tectonics 31, TC5010.

von Hagke, C., Oncken, O., Evseev, S., 2014. Critical taper analysis reveals lithological control of variations in detachment strength: An analysis of the Alpine basal detachment (Swiss Alps). Geochemistry, Geophysics, Geosystems 15, 176-191.

Wehrens, P., Berger, A., Peters, M., Spillmann, T., Herwegh, M., 2016. Deformation at the frictional-viscous transition: Evidence for cycles of fluid-assisted embrittlement and ductile deformation in the granitoid crust. Tectonophysics, 693, 66-84.

Wehrens, P., Baumberger, R., Berger, A., Herwegh, M., 2017. How is strain localized in a meta-granitoid, mid-crustal basement section? Spatial distribution of deformation in the central Aar massif (Switzerland). Journal of structural geology, 94, 47-67.

Wilson, R.C.L., Manatschal, G., Wise, S., 2001. Rifting along non-volcanic passive margins: stratigraphic and seismic evidence from the Mesozoic successions of the Alps and western Iberia. In: Wilson, R.C.L., Whitmarsh, R.B., Taylor, B., Froitzheim, N. (Eds.), Non-volcanic Rifting of Continental Margins: a Comparison of Evidence from Land and Sea. Geological Society, London, pp. 429-452.

Chapter III

S
N

Walchergrat

Eiger 3967 *m.a.s.l.*

DN

PC

JK

1 Km
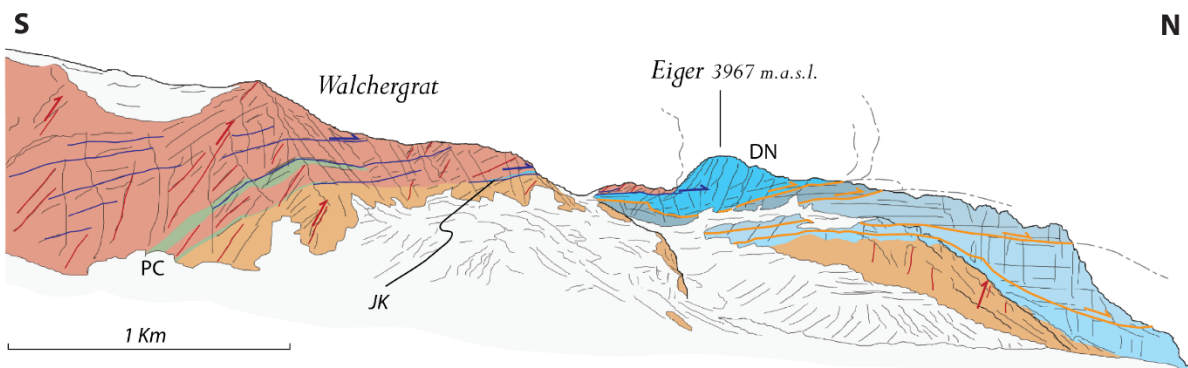
Panoramic view and geological interpretation SE face of the Eiger and Walchergrat.
Viewpoint: Long.: 7°43'20" / Lat.: 46°25'18"

4D reconstruction of the Doldenhorn nappe-basement system in the Aar Massif: insights into late-stage continent-continent collision in the Swiss Alps

Ferdinando Musso Piantelli[1&2], David Mair[1], Alfons Berger[1], Fritz Schlunegger[1], Michael Wiederkehr[2], Eva Kurmann[2], Roland Baumberger[2], Andreas Möri[2] and Marco Herwegh[1]

[1] *Institute of Geological Sciences University of Bern, Baltzerstrasse 1+3, 3012 Bern, Switzerland*

[2] *Swiss Geological Survey, Federal Office of Topography swisstopo, Seftigenstrasse 264, 3084 Bern, Switzerland*

Abstract

The inversion of passive margins and their transportation into fold-and-thrust belts is a critical stage of mountain-building processes. In this study, we selected the Doldenhorn Nappe and Aar/Gastern Massifs (Central Swiss Alps) system as an ideal laboratory to document the impact of inherited structures, their along-strike variations, and basement tectonics on the evolution of a fold-and-thrust belt. Three-dimensional geological modelling and cross-section restoration allowed us to reconstruct the 4D evolution of the investigated area during the late-stage Alpine orogeny (30 to 0 Ma). Our results demonstrate that: (i) the Doldenhorn Nappe is the product of the inversion of an asymmetric half-graben basin; (ii) variations in incipient basin sediment thicknesses correlate directly with the along-strike variation of the deformation of the Doldenhorn Nappe; and (iii) the multiphase thick-skinned deformation that overprinted the Doldenhorn Nappe from 22 Ma until today changed the shape of the Doldenhorn Nappe and Aar/Gastern Massifs. This reconstruction shows how thin-skinned nappe formation mechanisms and the nappe geometries are controlled by the initial basement geometry and by the rheological strength contrasts between basement and cover sediments. Basement-involved uplift and shortening controls then the late-stage collisional 3D overprint and mechanics of the fold-and-thrust belts.

3.1 INTRODUCTION

Fold-and-thrust belts are an essential component in the mid- to upper crustal deformation of most orogenic systems. Recognition of the controlling factors on their evolution is fundamental for understanding the long- and short-term dynamics of mountain building processes (e.g., Cooper, 2007; Lacombe and Bellahsen, 2016; Bigi et al., 2018; Ghani et al., 2018). Using analogue, field and numerical studies researchers have attempted for several decades to disclose the process of mechanical

deformation controlling the evolution of fold-and-thrust belts (e.g., Chamberlin, 1919; Rodgers, 1949; Bally et al., 1966; Macedo and Marshak, 1999; Pfiffner, 2006; Bauville and Schmallholz, 2015 and 2017; Lacombe and Bellahsen, 2016; Granado and Ruh, 2019). Quite often, however, related approaches have been restricted to two-dimensional sections neglecting the three-dimensional and often non-cylindrical architecture of fold-and-thrust belts. With the evolving capabilities in 3D modelling software and the increase in computational power, recent studies included observations regarding the along-strike 3D variability of these systems (e.g., Macedo and Marshak, 1999; McClay et al., 2004; Sala et al., 2014; Santolaria et al., 2015; von Tscharner et al., 2016; Ghani et al., 2018; Balestra et al., 2019). Such 3D considerations are of high relevance for an improved understanding of the evolution of fold-and-thrust belts and mountain chains in general. However, the 3D structural complexity of these systems that frequently record the result of a large range of tectonic processes renders the parameters that control the evolution of fold-and-thrust belts elusive to detect, and therefore they are still poorly understood. Hence, a single cross-sectional view of a fold-and-thrust belt does not allow resolving their entire complexity (e.g Watts et al., 1995; Allmendinger et al., 1997; Mouthereau et al., 2002; Hamilton, 1988; Nemcok et al., 2013). The use of three-dimensional modelling and restoration techniques is thus a crucial and necessary step for characterizing the structural disposition of a fold-and-thrust belt, including reconstructing the fault network and detecting inconsistencies in structural interpretations (e.g., Turrini et al., 2014; Balestra et al., 2019).

It is documented that in several fold-and-thrust belts around the world (e.g., Taiwan, Himalaya) the pre-collisional geometries have controlled the kinematics of the subsequent collisional processes (Mouthereau et al., 2002; Butler et al., 2006; Zanchi et al., 2006; Bellahsen et al., 2014; Ghani et al., 2018; Curzi et al., 2020). For example, the 3-D architecture of the involved former passive continental margins, consisting of a combination of discontinuous fault systems and geometrical asymmetries, form local basins and topographic highs that can lead to extreme along-strike variations (Lacombe et al., 2003; Turrini et al., 2016; Lymer et al., 2019). These variations primarily affect the shape and topography of the basins' basement and in consequence also the resulting sedimentary thicknesses, whereby basins may taper gradually or terminate with abrupt steps on their margins (Taylor et al., 1995; Mouthereau et al., 2002; Spitz et al., 2020; Vitale and Ciarcia, 2021; Tavani et al., 2021). Such structures can control the architecture of the developing fold-and-thrust belt when these systems are inverted and incorporated into an orogenic wedge during collision, (e.g., Gillcrist et al., 1987; Letouzey et al., 1990; Doglioni, 1992; Macedo and Marshak, 1999; Mohn et al., 2011; Boutoux et al., 2014; Mohn et al., 2014). This results in considerable differences across belts as well as along strike variability within individual belts (Lacombe and Mouthereau, 2002; Fitz-Diaz et al., 2011, Ghani et al., 2018).
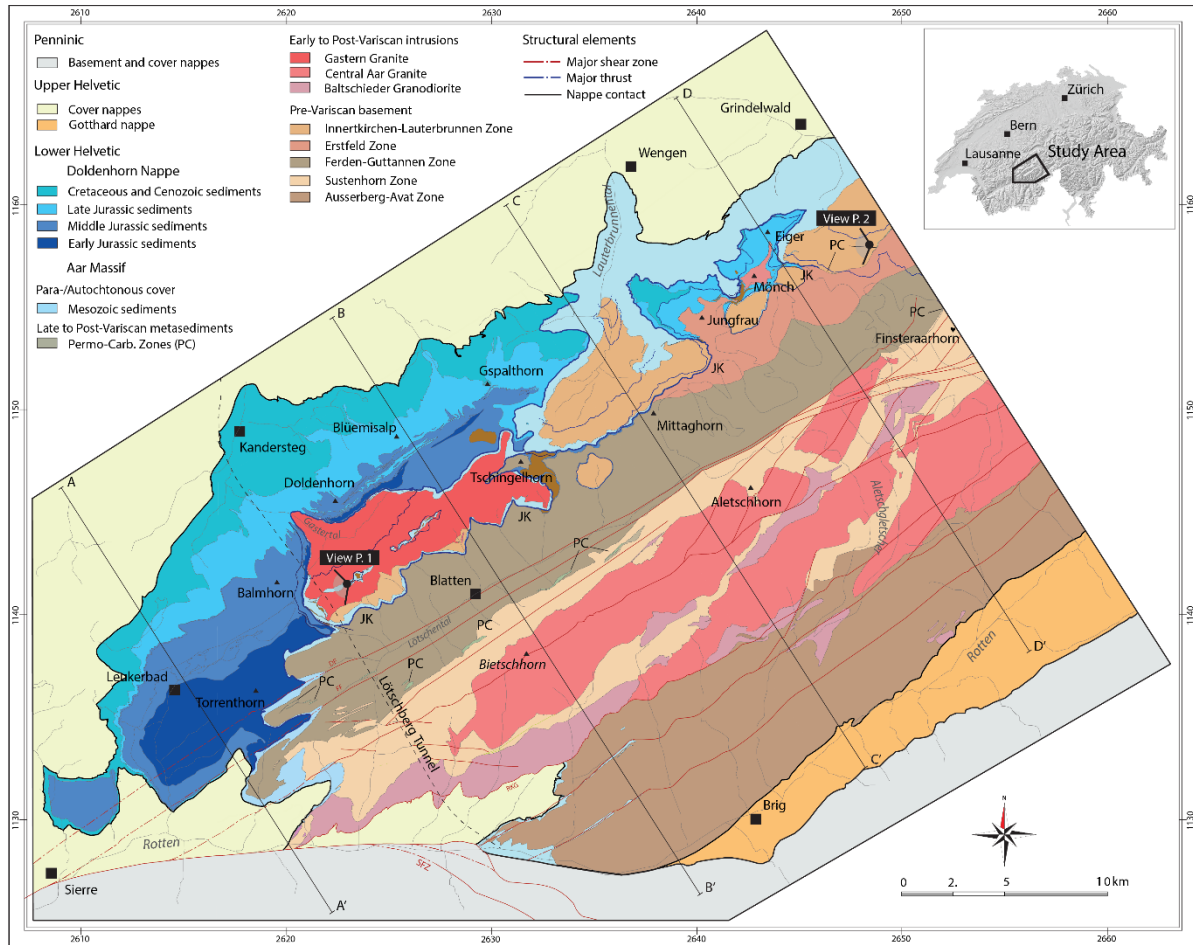
Figure 3.1 - Geological map of the investigated area, (see Appendix B1 for details on data compilation). On the map are indicated: geographic locations, the profile traces of Fig 3.4, the viewpoints (P.1 and 2) of Fig. 3.3, trace of the Lötschberg Railway Tunnel, the locations of the thin sediment wedge called 'Jungfrau Keil', and the location of the Permo-Carboniferous troughs (PC).

In this work, we selected the Doldenhorn Nappe (Central Swiss Alps) to document the 3D complexity of a fold-and-thrust belt. The large amount of structural (Burkhard, 1988; Haenni and Pfiffner, 2001; Herwegh and Pfiffner, 2005; Krayenbuhl and Steck 2009; Pfiffner et al., 2015; Cardello and Mancktelow, 2015; Cardello et al., 2015; Mair et al., 2018), petrologic-geochemical (Frey et al., 1980; Frey, 1987; Arkai et al., 2002; Berger et al.,2020; Girault et al., 2020) and

numerical studies (Bauville and Schmalholz, 2015; von Tscharner et al, 2016; Granado and Ruh, 2019; Spitz et al., 2020) make the Doldenhorn Nappe an excellent example for documenting the impact of inherited structures and along-strike variations on the evolution of a fold-and-thrust belt. Hence, we built a 4D geological reconstruction of the Doldenhorn Nappe during the late-stage Alpine evolution (30 to 0 Ma) to examine how inherited structures

and along-strike variations influenced the structural development of the nappe. In particular, we illustrate how the 3D morphology and variability of former passive continental margin conditions the mechanism and style of basin inversion during the continent-continent collision, and how this is recorded by the along-strike variations in the tectonic architecture. We thus consider the Doldenhorn Nappe as an ideal laboratory that links field-based structural and analogue-numerical modelling studies for an improved understanding of the evolution of a fold-and-thrust belt.

3.2   GEOLOGICAL SETTING

The Helvetic nappe stack in the Central Swiss Alps represents a classical fold-and-thrust belt. It has been intensively studied during the last century and present, because it preserves one of the best-documented ancient rifted passive margin (e.g., Heim, 1922; Ramsay, 1981; Burkhard, 1988; Pfiffner, 1993; Schmid et al., 2004; Cardello and Mancktelow, 2014). This litho-tectonic unit is mainly composed of carbonate-dominated Mesozoic and Palaeogene sediments that are partially or completely detached from their original pre-Triassic crystalline basement.

Throughout the last Alpine cycle, the nappe stack was formed during the compression and related inversion of the basement-cover systems that constituted the proximal part of the European passive continental margin (Burkhard, 1988; Epard, 1990; Steck, 2008; Pfiffner, 2015). The Doldenhorn Nappe, which is the focus of this

1. Niederhorn and Stad Fm.
2. Helvetic Kieselkalk and Betlis Fm.
3. Öhrli and Palfris Fm.
4. Quinten Fm.
5. Schilt Fm.
6. Reischiben Fm.
7. Bommerstein Fm.
8. Torrenthorn Fm.
9. Bachalp and Besoëns Fm.
10. Mels, Röti and Quarten Fm.

11. Permo-Carboniferous trough
12. Aar/Gastern massif basement units
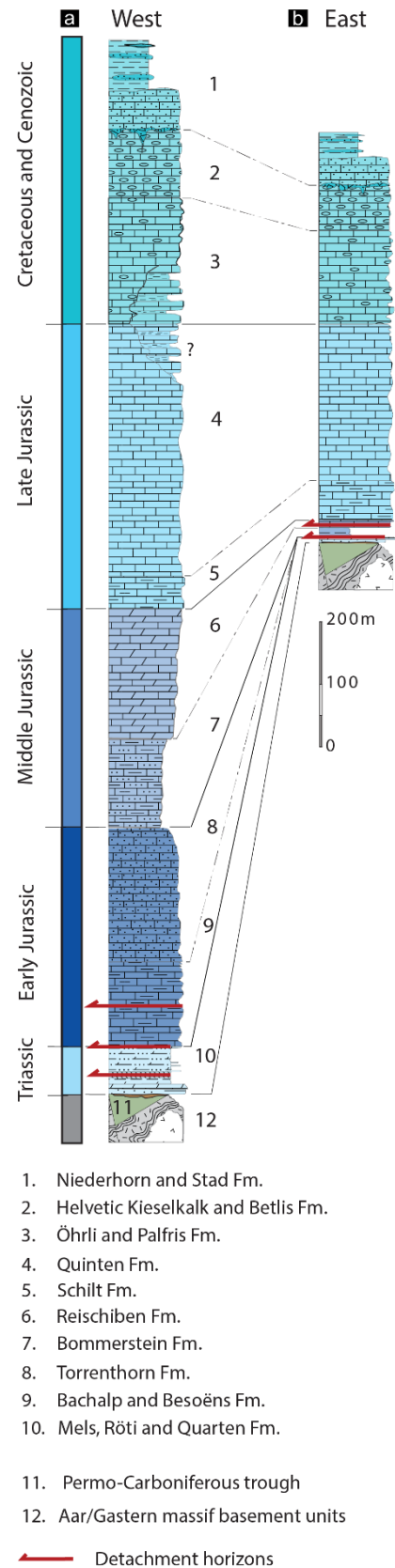
← Detachment horizons

Figure 3.2 – Synthesized stratigraphic columns of the Doldenhorn Nappe in the west (A) and east (B) of the investigated area. The major detachment horizons are indicated with red arrows. Stratigraphic names are from the Lithostratigraphic Lexicon of Switzerland (https://www.strati.ch/en/tectonic/aar-gastern/aar-massiv) and data were compiled from Krebs (1925); Masson et al. (1980); Krayenbuhl and Steck (2009); Ziegler and Isler (2013); Mair et al. (2018) and references therein.

study, is one of the lowermost units of these nappes. It crops out in a 150 km^2 area on the western margin of the Aar/Gastern Massifs, which are one of the External Crystalline Massifs of the Alps (Fig. 3.1). The Doldenhorn Nappe exhibits distinct 3D structural features such as lateral variation of the geometry and deformation style (Epard, 1990).

The crystalline basement of the Aar Massif is mainly composed of pre-Variscan polycyclic metamorphic gneisses and migmatites (Abrecht, 1994; Berger et al., 2017; Herwegh et al., 2020). These gneiss units were intruded by Variscan to post-Variscan plutons. The intrusion of the magma was associated with the formation of

Permo-Carboniferous half-graben structures, which were then filled with volcanoclastic sedimentary sequences. The overlying Doldenhorn Nappe units were deposited during the Mesozoic within a basin situated on the European extended margin. The geometry of this basin and the sedimentation pattern therein were constrained by extensional Mesozoic faults (Burkhard, 1988; Pfiffner, 2015). The sedimentary units that formed in this basin consist of a succession of limestones, marls, shales, and sandstones (Fig. 3.2).

The deformation of the Doldenhorn Nappe started during Oligocene times (~30 Ma; Table 1) and was localized at different levels in the sedimentary units, and in the basement units (Table 1). Between 30 and 20 Ma, the basin from which the Doldenhorn Nappe originated (Doldenhorn Basin) was inverted and incorporated into the Alpine edifice, which resulted in the formation of a large-scale recumbent, isoclinal fold thrusted over the crystalline basement (Fig. 3.3; see also Herwegh and Pfiffner, 2005). This phase, when the sediments were partly detached from the

Age (Ma)	Deformation phase		Deformed units	Deformation style	References
~30 - 20		Ki Kiental	Sedimentary cover *(Doldenhorn Nappe)*	Top- to NW-dominated thrusting and folding	*Burkhard, 1988; Huon et al., 1994; Herwegh and Pfiffner, 2005*
22 - 12		Ha Handegg	Basement *(Aar/Gastern Massifs)*	Steep-reverse S-dipping shearing and faulting	*Wehrens et al., 2016; Berger et al., 2017*
< 12		Pf Pfaffenchopf	Basement *(Aar/Gastern Massifs)*	NW-vergent thrusting along moderately SE dipping shear planes (Northern units)	*Wehrens et al., 2017; Mair et al., 2018; Herwegh et al., 2020*
< 12		Ob Oberaar	Basement *(Aar/Gastern Massifs)*	Dextral Strike-slip shearing and faulting (Southern units) - Negligible-	*Wehrens et al., 2016, 2017; Herwegh et al., 2020*

Table 1 – Literature compilation of deformation phases that characterized the investigated area during the late-stage Alpine orogeny (30 to 0 Ma).
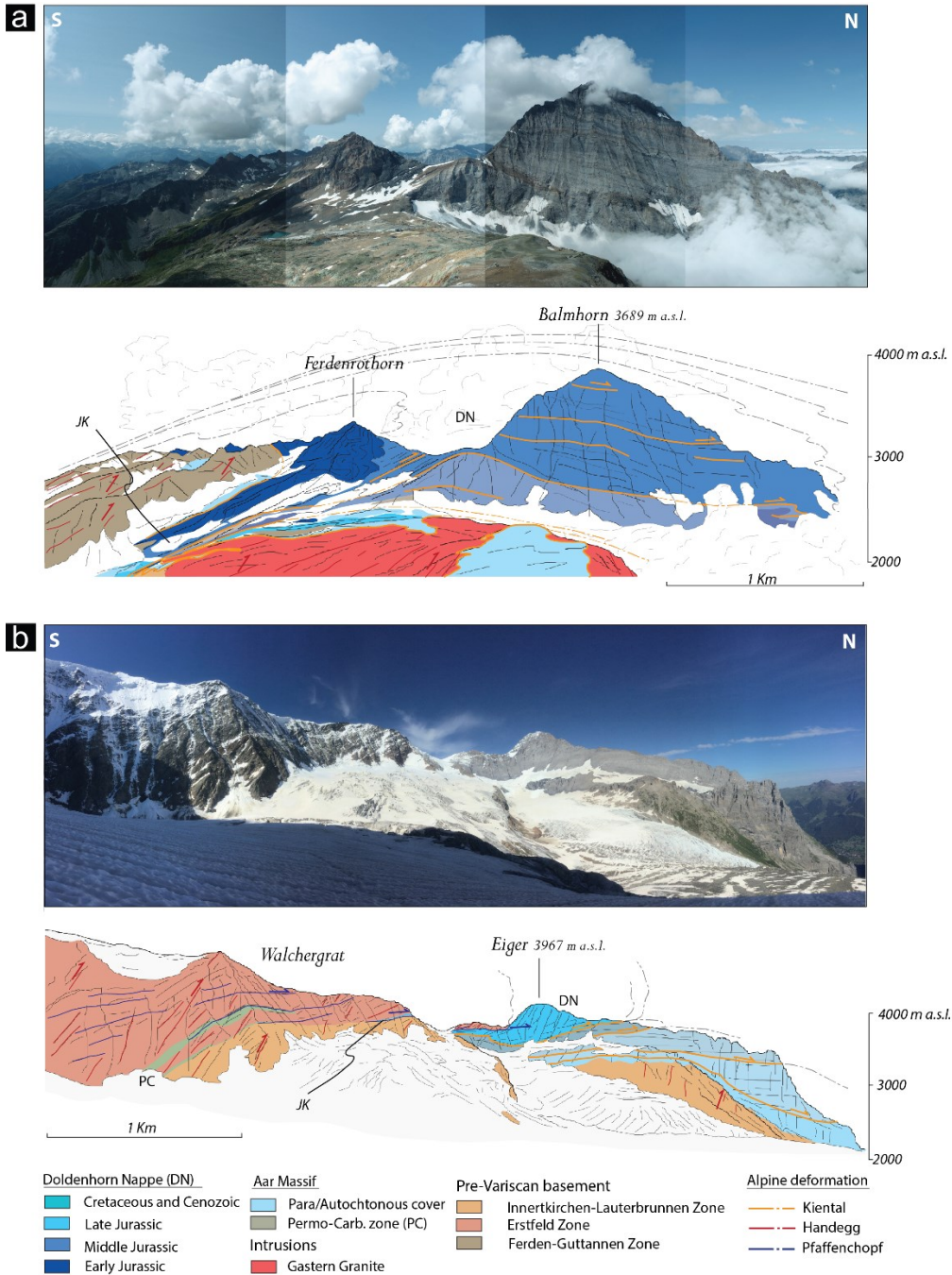
Figure 3.3 - Panoramic view and relative geological interpretation of two key locations of the Doldenhorn Nappe (DN) and basement units. (A) View of the east side of the Balmhorn and Ferdenrothorn (Viewpoint 1, Fig. 3.1). The basement units reach 3000 m a.s.l. and the DN consist of a large-scale recumbent fold that lies over the exhumed basement units. A thick wedge of the DN sediments, named Jungfrau Keil (JK), is present between the basement units. (B) View of the east face of the Eiger and the Walchergrat (Viewpoint 2, Fig. 3.1). The basement units exceed the 4000 m a.s.l and driven by Pfaffenchopf structures are thrusted toward the north. The JK is pinched between the basement units and continues into a thrusted Permo-Carboniferous zone (PC). The DN is a small-scale fold that lies over an imbricate of autochthonous sediments of the Aar Massif.
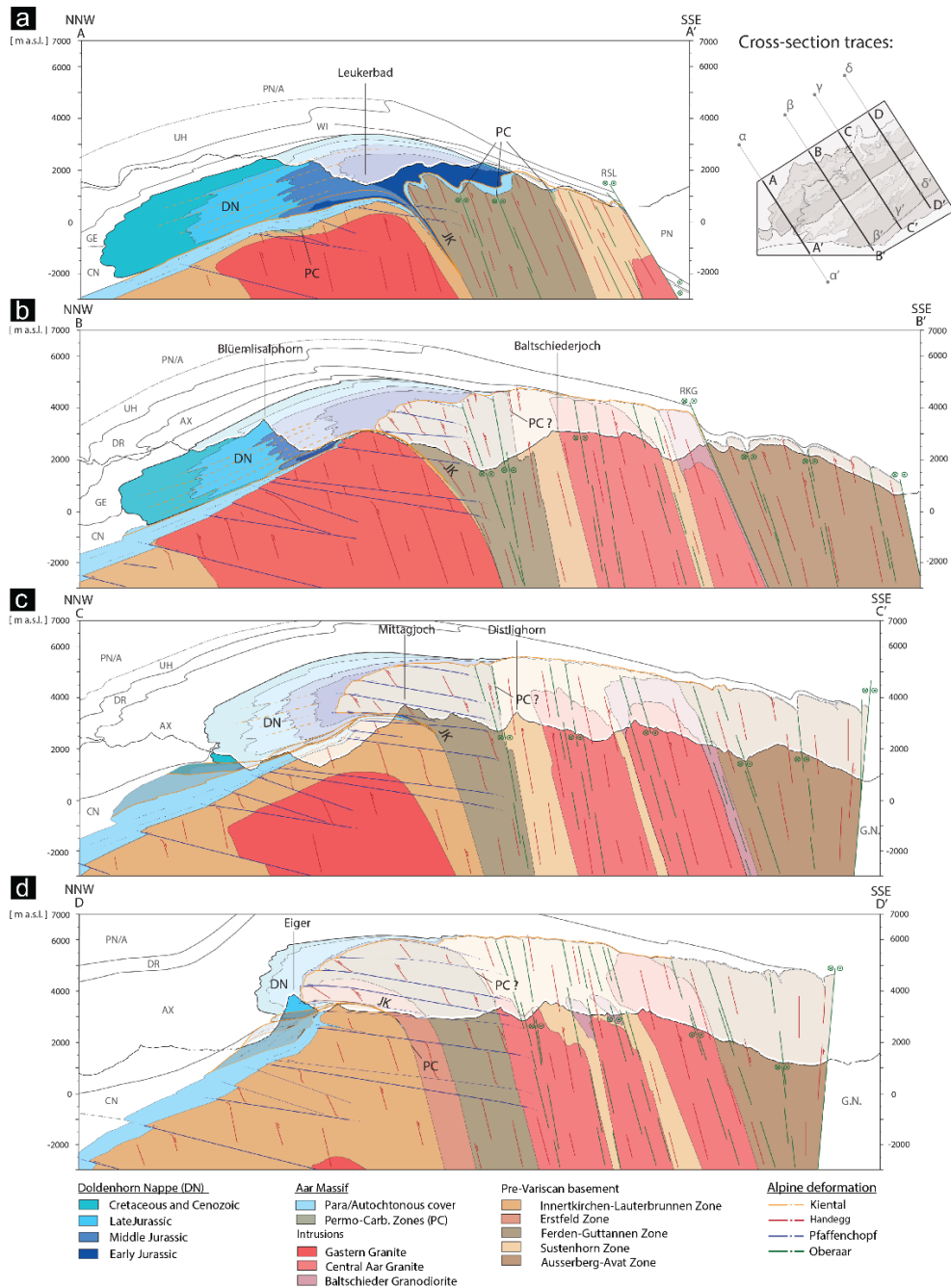
Figure 3.4 – Cross-sections through the investigated area (see Fig. 3.1 for cross-sections traces). In the profiles are indicated: the structural deformation phases, the overlying Helvetic nappes (GE, Gellihorn; WI: Wildhorn; AX: Axen; DR: Drusberg; UH: Ultrahelvetic), including the Cenozoic sediments (CN), and the Penninic and Austroalpine sediments (PN/A). In section A-A' and B-B' the outline of the overlying upper Helvetic nappes were modified after Herwegh and Pfiffner, (2005) and Hänni and Pfiffner, (2001) respectively. (A) Section A-A' where DN is a large-scale recumbent fold with a thick normal limb and a thin and intensively deformed inverted limb. (B) Section B-B', gradual exhumation and thrusting of the basement units, the DN maintains still the shape of a recumbent fold. (C) Section C-C': more pronounced exhumation and thrusting of the basement units. In the North, lies a stack of imbricates of Autochthonous sedimentary cover. (D) Section D-D' the exhumation and thrusting towards the North of the basement units are more prominent compared to what is observable in section AA'. The DN consists of a small-scale fold and the basement units are thrusted in the core of the nappe.

basement, has been referred to as Kiental deformation (Table 1 and references therein). At ~22 Ma further shortening led to the onset of a multistage and pervasive deformation sequence within the crystalline basement units of the future Aar/Gastern Massifs (Table 1). First, between 22 and 12 Ma, during the Handegg phase, the buoyancy-driven sub vertical extrusion of the Aar Massif occurred, which is expressed by steep-reverse shearing and faulting. This led to exhumation of the basement units and passive up doming of the entire nappe stack (Herwegh and Pfiffner, 2005; Cardello et al., 2016; Herwegh et al., 2017; 2020). Secondly, after the Handegg phase, between 12 Ma and today, the northern part of the Aar/Gastern Massifs experienced a period of NW-vergent thrusting along moderately SE dipping shear planes that cut through basement-cover contacts (Pfaffenchopf phase; Table 1, and references therein). This deformation was associated with the generation of steep shear zones and faults with a dextral strike-slip sense of shear in the central and southern part of the Aar Massif (Oberaar phase of Wehrens et al., 2017; Table 1, and references therein).

3.3 METHODS

In order to reconstruct the tectonic evolution of the Doldenhorn Nappe during different stages of continent-continent collision, it was essential to construct a structurally consistent large-scale 3D geological model of the investigated area. To achieve this goal, a 2D dataset was compiled and validated within a geographic information system software (ESRI's ArcGIS, v.10.8). Then, the 3D tectonic architecture was modelled with the software Move^{TM} (Petex, v.2019.1). In a second stage, four geological cross-sections throughout the investigated area were retro-deformed thereby performing area and line balancing in the GIS environment. Finally, the 4D reconstruction of the Doldenhorn Nappe was achieved using the software Move^{TM}, thereby applying interpolation and meshing techniques between the retro-deformed cross-sections for four specific time intervals.

3.3.1 Geological data compilation, establishment of stratigraphic model and fieldwork

A detailed geological bedrock map of the investigated area was constructed by compiling and revising geological, stratigraphic and structural information from previous maps (for a review of the compiled dataset, see Appendix B1). The mapping was conducted at the 1:25 000 scale and considered the major stratigraphic and tectonic boundaries of the cover and basement units, removing the Quaternary cover and interpreting the trend of the underlying contacts. For simplicity, the stratigraphic suite of the Doldenhorn Nappe was synthetized into five larger units (Fig. 3.2): (i) the Triassic units (Mels, Röti and Quarten Formations) composed of dolomites, shales sandstones, and evaporites; (ii) the Late Triassic to Early Jurassic units (Besoëns, Bachalp and Torrenthorn Formations) composed of marly, spary and sandy limestones; (iii) the Middle Jurassic units (Bommerstein and Reischiben Formations or relatedly the Dugny

and Erzegg Formations) made up of calcareous breccia and sandstones; (iv) the Late Jurassic units (Schilt and Quinten Formations) that comprise limestones and thin marly layers; and (v) the Cretaceous and Palaeogene units (Palfris, Öhrli, Betlis and Helvetic Kieselkalk Formations and siderolithic deposits unconformably overlaid by Stad and Niederhorn Formations) that are composed of biogene and spary limestones, and layers of sandstones and shales. The autochthonous sedimentary cover of the Aar/Gastern Massifs was not subdivided (see legend Fig. 3.1 and Fig. 3.2). Here we focus on changes in sediment thickness, for additional information, e.g., on sedimentary facies, we refer to the original studies (Krebs, 1925; Rohr, 1926, Masson et al., 1980 and references therein). These simplifications allow distinguishing the main stratigraphic horizons, which builds the basis to obtain a more comprehensive overview of the lateral structural and sediment thickness variations that occur within the nappe.

The entire dataset was combined and validated in an effort to generate a consistent geological map of the study area (Fig. 3.1). This was accomplished using high-resolution orthophotos (SwissImage with a raster resolution of 0.25 x 0.25 m; provided by swisstopo), a high-resolution digital elevation model (DEM; swiss ALTI3D with a downsampled raster resolution of 2 x 2 m, version 2013 provided by swisstopo), and hillshade maps, which served to verify and update geological boundaries and structures. A lineament map was generated on remotely

sensed images with the aim to expand the structural dataset following the workflow of Baumberger et al. (2022). All data were verified in the field at key locations through mapping and collection of structural field data (see Appendix B1).

3.3.2 3D Geological modelling

Due to the lack of borehole and underground information, 3D geological modelling in mountainous environment is a challenging task. However, high relief, scarce vegetation, and underground data offered by the Lötschberg railway tunnel (see trace in Fig. 3.1, Ziegler and Isler, 2013) and seismic studies (Pfiffner et al. 1997) render the investigated area prone to advanced surface-based 3D modelling. All available 2D data (mapped boundaries and structures, strike and dip data, Lötschberg tunnel and seismic sections) were loaded with the software Move^{TM} and projected on a DEM (raster resolution 35x35 m). Then, throughout the area, a dense regularly spaced (500 m) network of NNW-SSE striking constructional cross-sections was generated, where, with 3D projection techniques and dip information, the tectonic and geological boundaries were digitized with lines (in an along-length sampling interval of 25 m; for more detailed information on the modelling procedure, see Chapter 1). By applying 3D interpolation and meshing techniques (i.e. the spline curve method), lithological and structural boundaries were interpolated between the DEM surface and cross-sections to generate 3D surfaces for each horizon of the model.

Following this approach, the 3D model of the investigated area considers field observations, structural analysis at the outcrop scale, tunnel and literature data, and large-scale seismic profiles.

3.3.3 Cross-section restoration and 4D reconstruction

To reconstruct the tectonic evolution of the Doldenhorn Nappe during the Alpine collision (30 – 0 Ma), four NNW-SSE cross-sections (see traces α, β, γ, δ in Fig. 3.4; ; note that traces are overlying with A-A' to D-D' cross sections, but they are more extended) were retro-deformed by performing line- (i.e. for the basement-cover contact) and area-balancing (i.e. for the Doldenhorn Nappe units) in GIS (see Appendix B2). Additionally, the top basement was restored assuming a precollisional geometry of the Doldenhorn Basin located on an asymmetric half-graben on the proximal part of the European passive continental margin, being bent by ~10° (Nibourel et al., 2018; 2021a) underneath the tectonically active boundary of the overriding plate. The resulting geometry and final depth is constrained by this angle and retrodeformation of the previously mentioned structures. (see Appendix B2 fort detailed information on the restoration). The retro-deformation procedure was performed according to the following four time steps: *Today to 12 Ma:* retro-deformation of the displacement along the youngest northwest vergent thrust deformation of the Aar Massif (Pfaffenchopf structures; Table 1); during this time, a strike-slip movement was also active in the basement units of the Aar Massif (Oberaar phase, Table 1; Wehrens et al. 2016, 2017). In this study however, its contribution to the overall shortening and nappe evolution was considered negligible since the related deformation affected the basement and sedimentary units of the southern most parts of the massif where no Doldenhorn Nappe units accumulated, implying therefore maintenance of the Doldenhorn Nappe volumes throughout the entire Alpine deformation. *12 to 20 Ma:* retro-deformation of the reverse-steep fault related exhumation of the Aar Massif (Handegg phase; Table 1) and of the overlying nappe stack, while using the basement-cover contact as marker horizon. Despite the large degree of exhumation caused by the Handegg phase, the topographic mean elevation along the sections was kept constant, as stated by Campani et al. (2012) and Schlunegger and Kissling (2015). *20 to 30 Ma:* retro-deformation of the Kiental phase (Table 1). Herein, the location of Permo-Carboniferous zones and sediment wedges (Figs. 3.1, 3.3 and 3.4) served as a marker for potential locations of syn-rift faults controlling the opening of the Doldenhorn Basin (more information provided in Appendix B1). Subsequently, the cross-sections representing these stages were digitalized in Move™. A 3D model of each retro-deformation stage was then generated by applying 3D interpolation and meshing techniques (spline curve method) within the digitalized sections.

3.4 RESULTS AND INTERPRETATION

In this section, a structurally consistent characterization of today's architecture of the
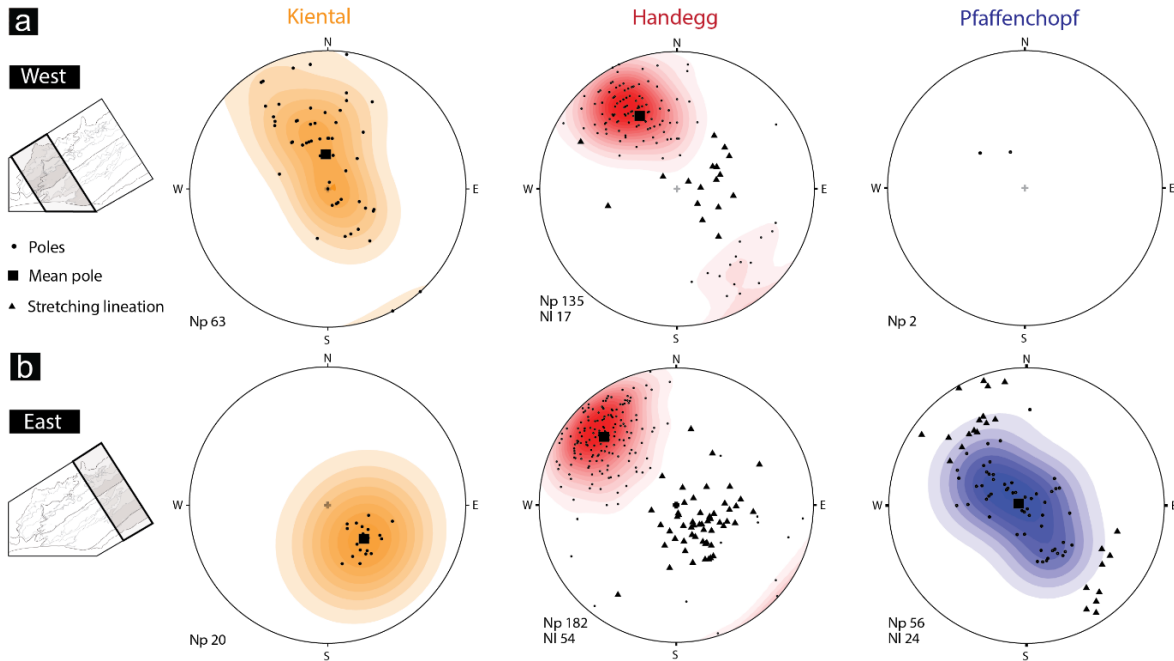
Figure 3.5 - Structural field data (poles and mean poles of the fault and thrusts planes) of the deformation structures in the sediments of the DN (Kiental) and basement units of the Aar Massif (Handegg and Pfaffenchopf). To highlight the differences between the east and west of the investigated area the sets of measurements are subdivided in two-dataset. (A) dataset of the measurements of the western regions of the investigated area, representative for the profile A-A'. (B) Dataset of the measurements in the east of the investigated area, representative for the profile D-D'.

Doldenhorn Nappe and Aar/Gastern Massifs is presented emphasizing the along strike variations in the sedimentary and basement units from west to east of the investigated area. Subsequently, the results of the western- and eastern-most cross-sections restoration (respectively α–α', and δ–δ'; see traces in Fig. 3.4) are discussed in stages punctuated by the major three Alpine deformation phases (Kiental, Handegg, and Pfaffenchopf; Table 1), and highlight the along-strike discrepancies throughout this evolution. Finally, by combining the obtained results, an estimation of the total horizontal shortening and maximum vertical

uplift along the restored cross-sections through the investigated area is derived.

3.4.1 Field data and 3D geological model of Doldenhorn Nappe and Aar/Gastern Massifs

The sedimentary units of the Doldenhorn Nappe show a distinct spatial distribution above the western edge of the Aar Massif basement units. Primarily, the overall thickness of the Doldenhorn Nappe units drastically decreases from the west to the east parallel to the strike of the nappe (see Figs. 3.1 and 3.2). The Early Jurassic units, which are 350 m thick in the west (Fig. 3.2; Masson et al., 1980; Krebs, 1925;
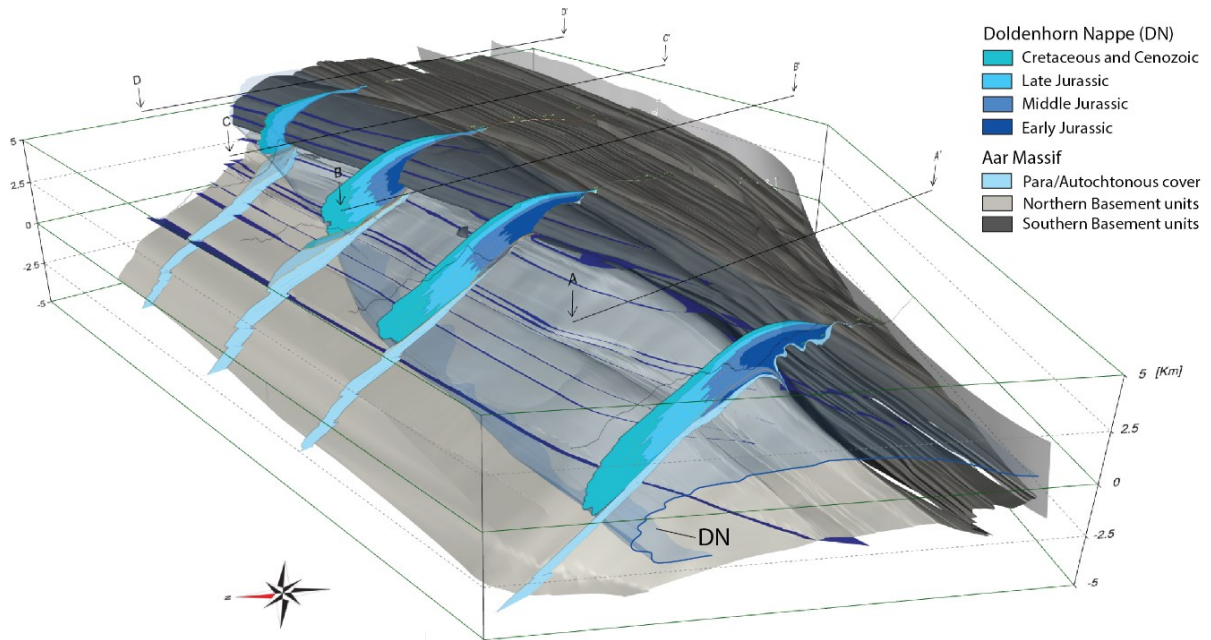
Figure 3.6 - View from the west of the 3D model of the current structural disposition of the DN and basement units. In this image, highlighted by the four cross-sections A, B, C, D (Fig. 3.4), the along-strike changes that occur within DN are illustrated. The basement units are merged into two major groups: the southern basement units (dark gray) and the northern basement units (light gray). The units are gradually exhumed from the west to the east at higher elevations and thrusted toward the north.

Krayenbuhl and Steck, 2009) of the investigated area, progressively thin out and disappear in the east. The thicknesses of the Middle Jurassic units also decrease from 350 m in the west (Masson et al., 1980; Krebs, 1925) to 30 m in the east (Mair et al., 2018). Similarly, the Late Jurassic and Cretaceous/Paleogene units also taper off from 450 m and 460 m to 310 m and 300 m, respectively (Masson et al., 1980; Mair et al., 2018).

From a structural point of view, in the west the Doldenhorn Nappe is a large-scale (distance front to core of 11 km) recumbent isoclinal fold (Fig. 3.3a, see also Herwegh and Pfiffner, 2005) with a 2.0 km-thick normal limb and a 0.7 km-thick inverted limb (Fig. 3.4a). The Kiental thrust

planes, along which the emplacement of the nappe occurred, are bent parallel to the basement-sedimentary cover contact with an average orientation (dip direction/dip angle) of 176/20 (Fig. 3.5a). Below the Doldenhorn Nappe and just above the basement lie the 50 to 500 m-thick autochthonous sediments of the Aar Massif.

In contrast, in the east, the Doldenhorn Nappe displays reduced dimensions with smaller-sized fold structures, much shorter limbs (distance front-core ~2 km) as well as a 1.5 km-thick normal limb and a 0.5 km-thick inverted limb. Here, the Kiental thrust planes gently dip towards the NW with a mean orientation of 314/30 (Fig. 3.5b). Below the Doldenhorn Nappe

lies an imbricate stack mainly consisting of the para-autochthonous sedimentary cover of the Aar Massif (Figs. 3.3b and 3.4d; see also Mair et al., 2018). These imbricates are bound by Kiental thrusts locally incorporating decametre-sized slivers of the Aar Massif basement rocks (see Mair et al., 2018).

The basement units of the western edge of the Aar Massif progressively gain relief moving from the western to the eastern part of the investigated area. In the west, the basement rocks reach an elevation of ~3000 m a.s.l. (Fig. 3.3a). The Handegg structures, along which exhumation of these units was achieved, dissect the basement rocks with SE-dipping semi-brittle to brittle faults that evolved from former ductile shear zones (see Wehrens et al., 2016; Berger et al., 2017; Mair et al., 2018; Herwegh et al., 2020). The average orientation of the fault planes is 153/50. Shear sense indicators on down-dip stretching lineations of these faults indicate preferential upward movements of the southern blocks (Fig. 3.5a). In the eastern part of the investigated area, the basement units exceed an elevation of 4200 m a.s.l. The mean orientation of the Handegg structures is 133/62, with down-dip stretching lineations with kinematic indicators of an up movement of the S-block (Fig. 3.5b).

Furthermore, over the entire northern section of the crystalline units, the Handegg structures are cut and offset by younger Pfaffenchopf thrust planes that have a NW-vergent and moderately SE-dipping orientation (see Wehrens et al., 2017; Mair et al., 2018; Herwegh et al., 2020). Note

that such structures in the NW portion of the investigated area are not well developed at the surface (Fig. 3.5a), but they occur at depth as they were identified in the Lötschberg railway tunnel and on seismic profiles (Ziegler and Isler, 2013; see Pfiffner et al., 1997, NEAT 9001 and Line W1; Figs. 3.4a). However, in the NE part of the investigated area, these structures occur both at the surface (Mair et al., 2018) and at depth (Pfiffner et al., 1997, Line C1; Herwegh et al., 2020; Figs. 3.3b and 3.4d). Along the Pfaffenchopf thrust planes (mean values: 105/05; Fig. 3.5b) the southern basement units (Erstfeld and Ferden-Guttannen Zones; Fig. 3.1) are thrusted over the northern basement units (Gastern Granite and the Innerkirchen-Lauterbrunnen Zone; Figs. 3.1, 3.3b, 3.4c, d, and 3.6). Pinched between the mentioned basement units lies a thin wedge of Doldenhorn Nappe sediments, known in literature as '*Jungfrau Keil*' (e.g., Krayenbuhl and Steck, 2009), which is traceable along the entire strike of the nappe (Fig. 3.1). In the west, the '*Jungfrau Keil*' is associated with Permo-Carboniferous units (Fig. 3.3a) and extends further than 750 m a.s.l. depth, indicating a today's minimum wedge length of 1650 m. In contrast, in the east, the '*Jungfrau Keil*' displays much smaller dimensions with a vertical extent of a few hundreds of meters only. Here the '*Jungfrau Keil*' culminates in a Permo-Carboniferous zone (Fig. 3.3b).

3.4.2 Cross-section restoration and tectonic evolution

To unravel in space and time how the Doldenhorn Nappe reached its current structural

organization during Alpine deformation, four NNW-SSE geological cross-sections (α–α', β-β', γ–γ', δ–δ'; see also traces in Fig. 3.4) were retro-deformed. In the following paragraphs we present the results of the retro-deformation of sections α-α' and δ-δ' as evolutionary steps, starting from the initiation of Alpine deformation to the present-day configuration (Figs. 3.7 and 3.8; the retro-deformed sections β-β' and γ-γ' are available in Appendix B2). Finally, the resulting total horizontal shortening and maximum vertical uplift of each transect (α, β, γ, δ), recorded by the Doldenhorn Nappe and basement-cover interface during the different evolutionary steps is then summarized in the plots of Fig. 3.9.

3.4.2.1 Restoration α–α'

The deformation and emplacement of the Doldenhorn Nappe along the α–α' section was divided into four main stages as follows.

Time step 30 Ma (Fig. 3.7a.). The Doldenhorn Basin sat in a half-graben structure on the former passive continental margin of the European plate and was bent by ~10° (Ebert et al, 2008; and Nibourel et al. 2018; 2021a) underneath the tectonically active boundary of the overriding units (see Appendix B2 for additional information). The basin was 24 km long and dissected by several normal faults often related to smaller-scale Permo-Carboniferous half grabens (see Appendix B1). In the north, the major escarpment displayed a throw of 2 km, and the sedimentary sequence had a maximum thickness of 2.5 km. The Doldenhorn Basin was buried at -15 km depth (see also Berger et al.,

2020) below both the overlying and already emplaced Helvetic nappe stack, and a thick wedge of Penninic and Austroalpine units (Fig. 3.7a). A similar scenario was proposed for the Morcles and Wildhorn nappes at ~27 Ma (e.g., Burkhard, 1988; Cardello et al., 2019). In the mechanically weak Triassic evaporite-rich and Early Jurassic shale layers (Pfiffner, 1993, 2011; Fig. 3.2; see for further details discussion section 3.5.2) deformation begun to be localized, and the Kiental phase detachment horizon was developed (orange line in Fig. 3.7a).

Time interval 30 to 20 Ma (Fig. 3.7b). This interval was primarily affected by thin-skinned deformation and later by the onset of thick-skinned deformation (22 to 20 Ma). Between 30 and 20 Ma, the basin was inverted along the Kiental basal thrust (orange line in Figs. 3.7a, b) and the units were thrusted 18 km to the NNW (Fig. 3.9; Burkhard, 1988; Herwegh and Pfiffner, 2005). The thrusting of the units over the crystalline basement was associated with a large-scale isoclinal fold with a thin inverted limb. With progressive shortening, the overlying nappe stack was passively folded by meso-scale to large-scale folds (Herwegh and Pfiffner, 2005; Girault et al., 2020). In the southern units of the Aar Massif, the exhumation of the basement units started at 22 Ma, triggered by basement internal steep Handegg faults and shear zones (red lines in Fig. 3.7b; Table 3.1). As already observed in the western External Crystalline Massifs (Bellahsen et al. 2014) as well as in the Central to Eastern Aar Massif (Nibourel et al.
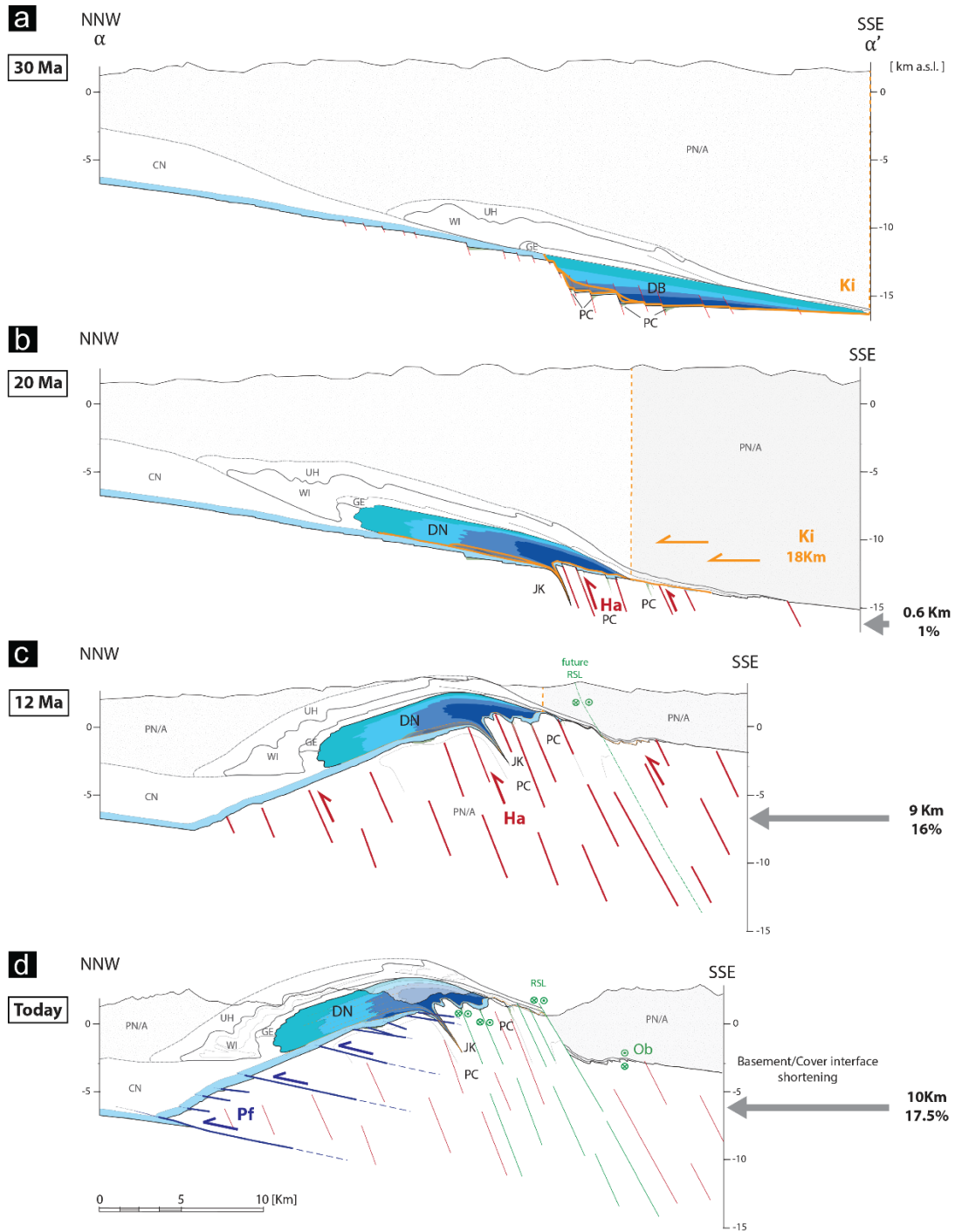
Figure 3.7 – Cross-section restoration of the α–α' transect from 30 Ma to today. At each deformation stage, thicker lines and stronger colors highlight the corresponding deformation phase. (A) The Doldenhorn Basin (DB) at 30 Ma is located in a half-graben of the European passive continental margin. The DB is buried below the already emplaced Helvetic nappe stack (UH: Ultrahelvetic units; WI: Wildhorn nappe; GE: Gellihorn nappe) and Cenozoic sediments (CN) in the north. Above lies a thick wedge of Penninics and Austroalpine units (PN/A). (B) DN at 20 Ma. Handegg deformation (Ha) in the southern basement units is indicated in red colors. (C) Exhumation of the basement units and consequent up-doming of the nappe stack induced by the Handegg deformation at 12 Ma. (D) Current structural disposition of the DN and basement units. Thrusting of the basement units toward the north documented by the Pfaffenchopf structures (Pf).

91

2021a), only a few Jurassic normal faults were directly reactivated. Instead, nearby new reverse faults evolved along which the uplift of the basement in the S-blocks was accomplished. As a consequence of this reverse faulting, thin synformal wedges of Triassic, Early and Middle Jurassic and Permo-Carboniferous sediments formed, the strata of which were steeply dipping and locally even overturned. At the Doldenhorn Basin's border fault, the '*Jungfrau Keil*', one of today's most prominent of such wedges (2.5 km vertical extent, Fig. 3.7b), started to develop.

Time interval 20 to 12 Ma (Fig. 3.7c). Thick-skinned tectonics along steeply south-dipping reverse faults and shear zones (red lines Fig. 3.7c) dominated the Handegg deformation stage (Table 1). Due to sequential deformation, the basement units were gradually exhumed differentially from south to north. This led to an overall 9 km horizontal shortening and an up-to ~17 km vertical uplift of the basement-cover interface (Fig. 3.9). This basement internal differential shearing and reverse faulting therefore caused an overall passive up doming of the entire overlying Helvetic nappe stack including the Doldenhorn Nappe, which resulted in the onset of formation of the dome-shaped geometry of the Aar Massif. This type of deformation were also inferred from paleo-magnetic data in the Helvetic Nappes located further north of the investigated area (Cardello et al., 2016).

Time interval 12 Ma to present-day (Fig. 3.7d). In contrast to the previous time interval, since 12 Ma thick-skinned horizontal tectonics define the deformation style in the region. Flat-to-moderately SE dipping Pfaffenchopf thrust planes (blue lines Fig. 3.7d) dissect the basement units promoting a NW-directed thrusting/shortening. The deformation is mostly localized at depth and leads to an en-bloc exhumation (Herwegh et al., in press; Nibourel et al. 2018, 2021b) of the basement units with a 2.7 km horizontal shortening and a 1 km vertical uplift of the basement-cover interface (Fig. 3.9). This deformation was partially compensated (-1.7 km of shortening) by the strike slip regime with a transtensional component occurring along the Rhone-Simplon Line (RSL in Figs. 3.7d and 3.9; Grosjean et al., 2004; Campani et al., 2014). This completed the deformation sequence and led to an overall horizontal shortening of 10 km and up to ~18 km of vertical uplift of the basement-cover interface (Fig. 3.9).

3.4.2.2 Restoration δ–δ'

The result of the restoration of the δ–δ' section is presented in the identical time intervals of the previous sections, highlighting the differences with what was described above.

Time step 30 Ma (Fig. 3.8a). The Doldenhorn Basin was 16.5 km long and dissected by normal faults often related to Permo-Carboniferous half grabens. In the north, the transition to the Alemannic topographic high (Trümpy, 1952) was gradual and without a major escarpment, while the basin deposits reached a maximum thickness of 0.9 km. The Doldenhorn Basin was buried at -14 km depth below the overlying Helvetic nappe stack, and Penninic and Austrolapine wedge (Fig.
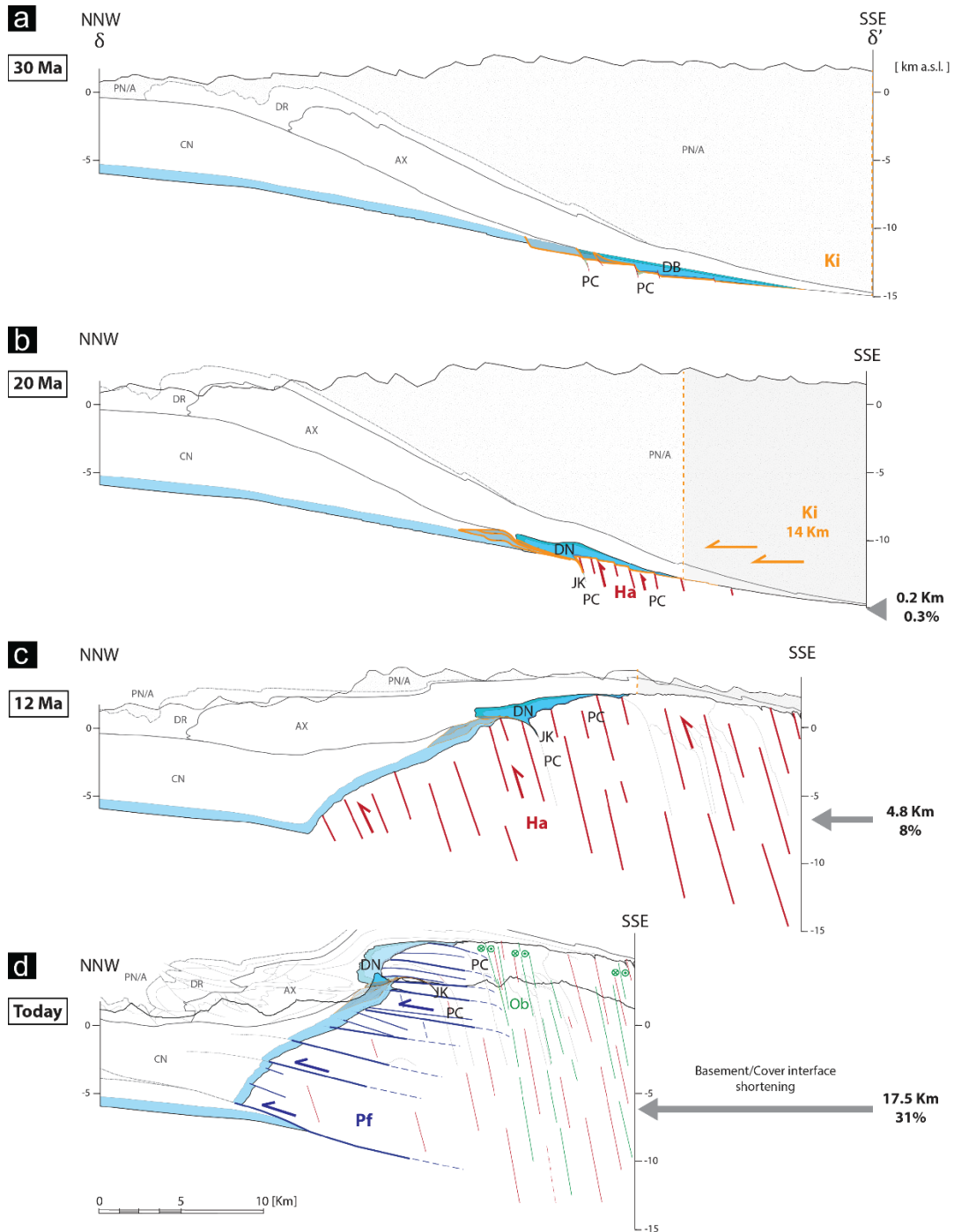
Figure 3.8 – Cross-section restoration of the δ–δ' transect from 30 Ma to today. At each deformation stage, the corresponding active deformation phase is highlighted by larger line weight and color. (A) The Doldenhorn Basin (DB) at 30 Ma is located in a half-graben of the European passive continental margin. The DB is buried below the already emplaced Helvetic nappe stack (AX: Axen nappe; DR: Drusberg nappe) and Cenozoic sediments (CN) in the north. Above lies the wedge of Penninics and Austroalpine units (PN/A). (B) At 20Ma, due to the Kiental deformation the DN is extruded into a small amplitude fold, and in the north lies a stack of three slices of autochthonous sediments. Handegg deformation (Ha) in the southern basement units is indicated in red colors. (C) Exhumation of the basement units and up-doming of the nappe stack induced by the Handegg deformation at 12 Ma. (D) Current structural disposition of the DN and basement units. Significant thrusting of the basement units toward the north driven by the Pfaffenchopf structures (Pf).

93

3.8a). In the south, the Kiental basal thrust was developed in Triassic evaporite-rich and Early Jurassic shale layers. However, toward the northern end of the basin, the thrust splayed into an in-sequence set of thrusts that also extended to the autochthonous sedimentary cover in proximity of the basin (orange lines Fig. 3.8a).

Time interval 30 to 20 Ma (Fig. 3.8b). Between 30 and 20 Ma along the sequence of Kiental thrusts (orange lines in Figs. 3.8a and b) with 14 km of horizontal shortening (Fig. 3.9), the basin was inverted and the sediments were thrusted to the NNW. The resulting Doldenhorn Nappe is a small-amplitude fold with a thin inverted limb. In the north, the in-sequence set of Kienthal thrusts stacked a repetition of slices of autochthonous sedimentary cover of the Aar Massif. At 22 Ma, the Handegg brittle-ductile reverse faults and shear zones were localized in the southern basement units of the basin. Permo-Carboniferous, Triassic, Early and Middle Jurassic sediments were locally pinched between the basement units as synformal sedimentary wedges. As for the previous section, at the northern end of the basin, between the border fault and the basin's basement units, the '*Jungfrau Keil*' sediment wedge was generated (0.9 km vertical extent; Fig. 3.8b).

Time interval 20 to 12 Ma (Fig. 3.8c). The steep reverse faults and shear zones of the Handegg phase induced 4.8 km of horizontal shortening and an up to ~16 km of vertical uplift of the basement-cover interface (Fig. 3.9).

Time interval 12 Ma to present-day (Fig. 3.8d). Thrusting along the Pfaffenchopf thrust planes started both at depth and at higher elevation along the entire northern rim of the basement units. Such deformation led to: (i) considerable steepening of the northern basement-cover interface; (ii) an en-bloc exhumation of the basement units; and to (iii), thrusting of rigid slabs of southern basement units over the northern ones, which were wedged into the core of the Doldenhorn Nappe. The Pfaffenchopf thrusts accommodated 12.7 km of horizontal shortening and an additional up to 3.6 km of vertical exhumation of the basement-cover interface (Fig. 3.9). Thus, the deformation sequence culminated with an overall 17.5 km of horizontal shortening and up to ~20 km of uplift of the basement-cover interface (Fig. 3.9).

3.4.3 Total horizontal shortening and maximum vertical uplift

The plots in Figure 3.9 display the total horizontal shortening and maximum vertical uplift recorded by the Doldenhorn Nappe and basement-cover interface in the α, β, γ, δ transects during the abovementioned restoration time intervals. The horizontal shortening recorded by the Doldenhorn Nappe units (Fig. 3.9a) is induced during the Kiental phase (Fig. 3.9a, orange line 30 to 20 Ma; thin-skinned dominated stage) and followed by shortening localized in the basement units (Fig. 3.9a, gray line 20 Ma to today). Horizontal shortening in the basement units was initiated at 22 Ma. During the Handegg phase (Fig. 3.9, red
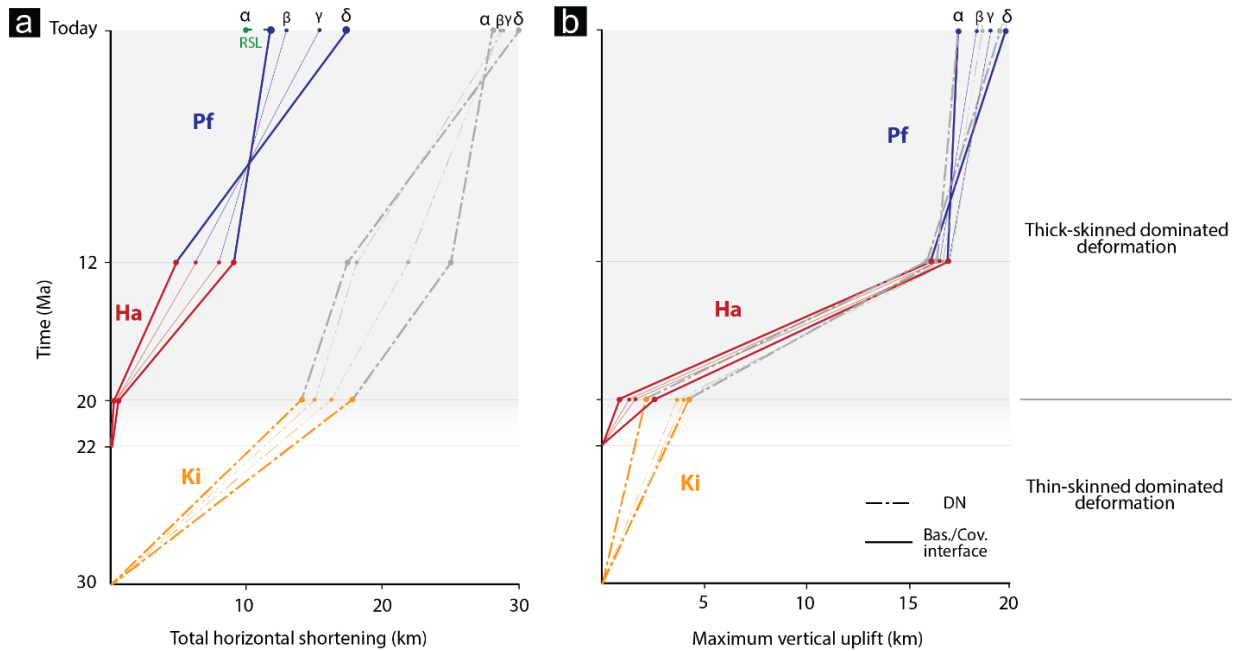
Figure 3.9 - Plots of the total horizontal shortening (A) and maximum vertical uplift (B) recorded by the Doldenhorn Nappe (DN) and basement-cover interface (dashed line and simple line respectively) in the sections α, β, γ, δ during the restoration time intervals. (A) Horizontal shortening recorded by DN sediments induced by the Kiental phase (orange line 30 to 20 Ma) and by the shortening localized in the basement units (gray line 20 Ma to today). Horizontal shortening in the basement units was initiated at 22 Ma. This thick-skinned deformation stage results in a ~12 to 17.5 km horizontal shortening of the basement-cover interface, and 28 to 30 km of the DN. (B) Maximum vertical uplift recorded by the DN and basement-cover interface. The maximum total vertical uplift recorded in each section ranges from 18 to 20 km both for the DN and for the basement-cover interface.

line, 22 to 12 Ma) a differential horizontal shortening (α, large; δ, small) is observed; while during the Pfaffenchopf phase an opposite trend occurs (α, small; δ, large). This thick-skinned deformation stage results in ~12 to 17.5 km horizontal shortening of the basement-cover interface, and 28 to 30 km shortening of the Doldenhorn Nappe.

On the contrary, the maximum vertical uplift recorded by the Doldenhorn Nappe and basement-cover interface (Fig. 3.9b) shows almost an identical trend, recording a strong uplift component during the Handegg phase (Fig.

3.9b, red line, 22 to 12 Ma). This results into a total vertical uplift of 18 to 20 km both for the Doldenhorn Nappe and for the basement-cover interface in each section.

3.5   DISCUSSION

The results obtained through restoring the four cross-sections in the investigated area provide crucial insights into the tectonic evolution of the Doldenhorn Nappe and Aar/Gastern Massifs during the late-stage Alpine evolution, and the broader perspective of a 4D inversion of passive continental margins. By generating a 3D model of each retro-

deformation stage, it was possible to build a 4D reconstruction of the Doldenhorn Nappe. In this section, the 4D reconstruction of the Doldenhorn Nappe is discussed with a particular focus on the deformation processes and structural inheritances (e.g., Butler et al., 2006 and references therein) that controlled the large along-strike variability in the tectonic architecture of the nappe and underlying Aar/Gastern Massifs basement units. Such a reconstruction indeed allows us to establish: (i) an asymmetric Doldenhorn Basin geometry becoming shallower and shorter to the NE, (ii) the rift-related 3D extensional fault architecture whereby the asymmetric basin developed, and (iii) the structural and rheological inheritance, which controls basin inversion as well proximal domain deformation during the late-stage collision between Adria and Europe.

3.5.1 The Doldenhorn Basin

From a geodynamic point of view, proximal domains of rift systems or passive continental margins are characterized by weakly developed rift-related lithospheric and crustal thinning (e.g., Mohn et al., 2011; Peron-Pinvidic et al., 2013). The creation of accommodation space is, therefore, restricted to graben and half-graben basins (e.g., Wilson et al., 2001; Tugend et al., 2015). The Doldenhorn Basin (Fig. 3.10) was located on the proximal part of the European passive continental margin characterized in the NE by the Alemannic topographic high (Trümpy, 1952). The basin itself evolved as an asymmetric half-graben bounded in the north by an east-west striking, south-

dipping rotational normal fault with a larger throw in the West (ca. 2 km) and smaller throw in the east (ca. 0.8 km). This asymmetric tectonic rifting scenario resulted in a differential formation of accommodation space that affected the disposition and stratigraphic thicknesses of the sedimentary units (Figs. 3.2 and 10; e.g., Dolfuss, 1965; Masson et al., 1980; Balázs et al., 2016). Indeed, the Early and Middle Jurassic units are linked to the early stages of the opening of the half-graben and therefore display fluctuations in thicknesses along strike as well as thickening towards footwalls of the normal faults of the basin. The Late Jurassic and Cretaceous/Paleogene units recorded then the late to post-rift evolutional stage of the basin (see also Kempf and Pfiffner, 2004; Cardello and Mancktelow, 2014).

The reconstructed 3-D architecture of the Doldenhorn Basin consists of a series of NE-SW to E-W striking and SE to S dipping rotational high-angle normal faults. (Fig. 3.10; see also Doldenhorn Basin's top-crystalline basement map 30 Ma, in Appendix B2). Furthermore, as also observed in several other locations in the Aar Massif (e.g., Heim, 1922; Rohr, 1926; Krayenbuhl and Steck 2009; Nibourel et al., 2021b), large numbers of normal faults occur in places where Permo-Carboniferous troughs are located (see more information in Appendix B1; Fig. 3.10). The large-scale crustal architecture of the European proximal passive continental margin was dominated by a series of tilted crustal blocks, bound by high-angle Mesozoic normal faults (Masini et al., 2013). The
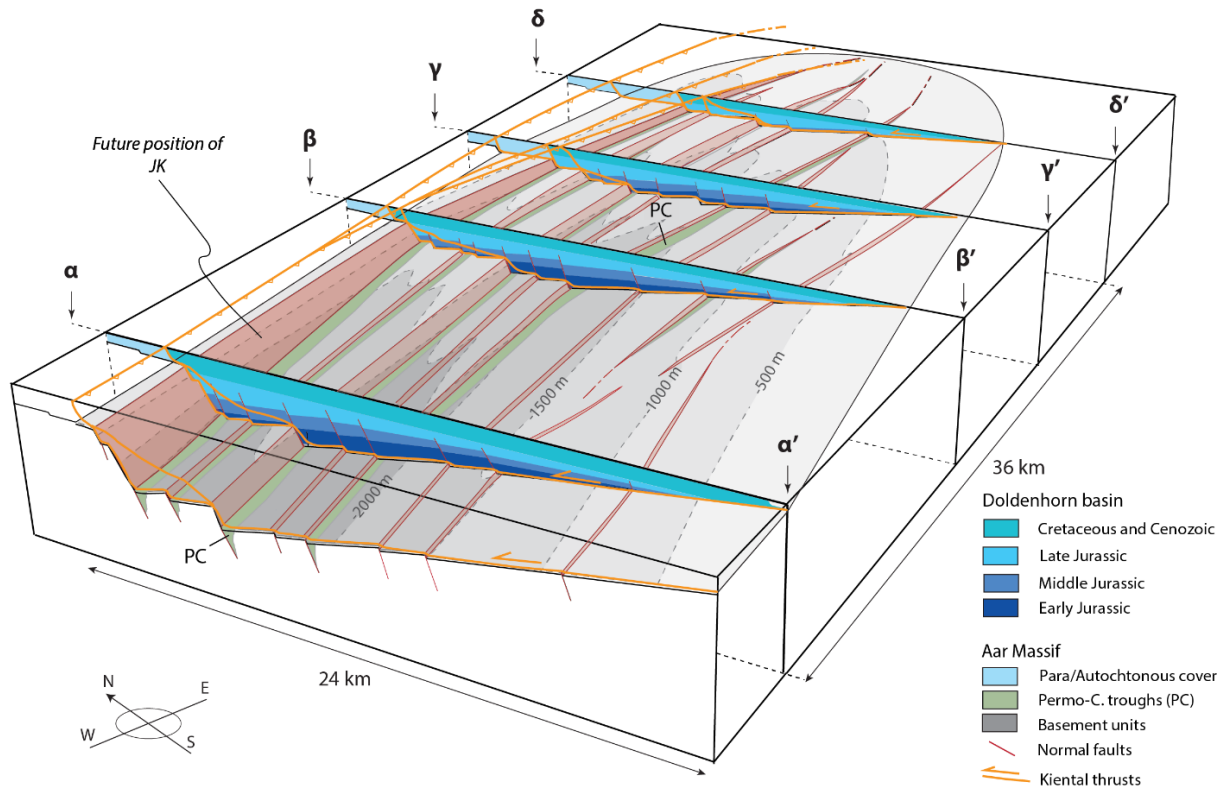
Figure 3.10 - 3D reconstruction of the shape of the Doldenhorn Basin and relative sediment distribution. A series of Jurassic normal faults open an asymmetric half-graben, which is more than 2000 m deep in the west and less than 500 m deep in the east. The major Jurassic normal faults are often localized in Permo-Carboniferous half-graben (PC, green). The distribution of the sedimentary units within the basin reflects the asymmetric shape of the basin: (i) Lower and Middle Jurassic units respectively disappear and taper off in the eastern regions of the basin, whereas (ii) Upper Jurassic and Cretaceous and Cenozoic are reduced in thickness. Furthermore, the distribution of the Kiental basal thrusts (orange lines) evolves from a single basal thrust in the west to an in sequence series of thrusts in the east.

Doldenhorn Basin was sitting in a half-graben on one of these tilted blocks, filled with wedge-shaped syn-rift sedimentary units (e.g., Pfiffner, 2015; Jaquet et al., 2018). Present-day examples of comparable geodynamic settings can be found within the mid-Norwegian, Iberian or Angola-Gabon proximal domains along the Atlantic rift system (e.g., Peron-Pinvidic et al., 2013). Geophysical studies in such proximal domains reveal that the bulk crust is only slightly thinned and the subsidence-related sedimentation is mainly restrained to the stretching basins (e.g., Tugend et al., 2015; Peron-Pinvidic et al., 2017; Lymer et al., 2019). This fact is corroborated, in case of the Doldenhorn Basin, by its long-lasting syn-rift sedimentation ranging from Early Jurassic until Cretaceous/Cenozoic times. Similar styles of sedimentation within asymmetric half-graben basins have been investigated in several recent large-scale examples such as the Jeanne

d'Arc Basin (Welsink and Tankard, 2012; Newfoundland) or the Peniche Basin (Alves et al., 2006; Iberian margin).

Finally, we suggest that the asymmetric geometry of the Doldenhorn Basin relates directly to the reactivation of pre-existing crustal structures within the underlying basement units (e.g., Santantonio and Carminati, 2011; Lafosse et al., 2016; Balàzs et al., 2017). Such reactivations, for example, have been previously inferred for the case of the Bourg d'Oisans (Dumont et al., 2008) or for the Pannonian and Aegean basins (Balázs et al., 2017). In the case of the Doldenhorn Basin, our 3D basin reconstruction indicates that the frequent occurrence of the major Mesozoic normal faults correlates directly with Permo-Carboniferous troughs. Hence, we interpret that the geometry of the Doldenhorn Basin and more generally of the European proximal continental margin was controlled by localization of normal faults within pre-existing Late Carboniferous-Permian crustal structures (e.g., see also Badertscher and Burkhard, 1998; Masini et al., 2013; Ballevre et al., 2018).

3.5.2 Incipient thin-skinned dominated inversion of the Doldenhorn Basin

At 30 Ma, the thick wedge of Penninics, Austroalpine, and detached Helvetic nappes lying on top of the Doldenhorn Basin (Figs. 3.7a and 8a) was moving towards the north and triggered deformation in the Doldenhorn units. The overthrusting of this wedge led to strain localization in the Doldenhorn units and more specifically at the contact between the basement

and the sedimentary units. Indeed, the mechanically weak shale or anhydrite-rich layers of the Early Jurassic and Triassic units at the basement-cover transition provided an abrupt change in mechanical strength (e.g., Suppe 1985; Pfiffner, 1993; Bauville and Schmallholz, 2015). The strain localization, which started at ~30 Ma in the Doldenhorn Basin, was therefore controlled by the initial geometry of the basin in combination with variation in mechanical strength of the involved basement and sedimentary units (Fig. 3.11). Consequently, not only rheological differences but also the variable along-strike top-basement topography and the resulting stratigraphic architecture controlled the deformation style. While a single basal thrust developed in the wider and deeper western region of the basin, the opposite occurred in the eastern regions where the thrust splayed into an in-sequence set of multiple imbricates (Fig. 3.10) consisting both of sediment and basement slices (see Mair et al., 2018). We explain this along-strike change in the development of the basal thrust system by the lateral variation of both the topography of the basement-cover interface as well as the thickness of the sedimentary units. These inferences correlate well with observations from 3D numerical studies (e.g., Pfiffner, 1993; Jammes and Huismans, 2012; Nilfouroushan et al., 2013; Bauville and Schmallholz, 2015). At ~30 Ma, the sedimentary units of Doldenhorn Basin had started to be detached from the basement units, which were then displaced towards the north along the newly developed basal shear zones. Because of

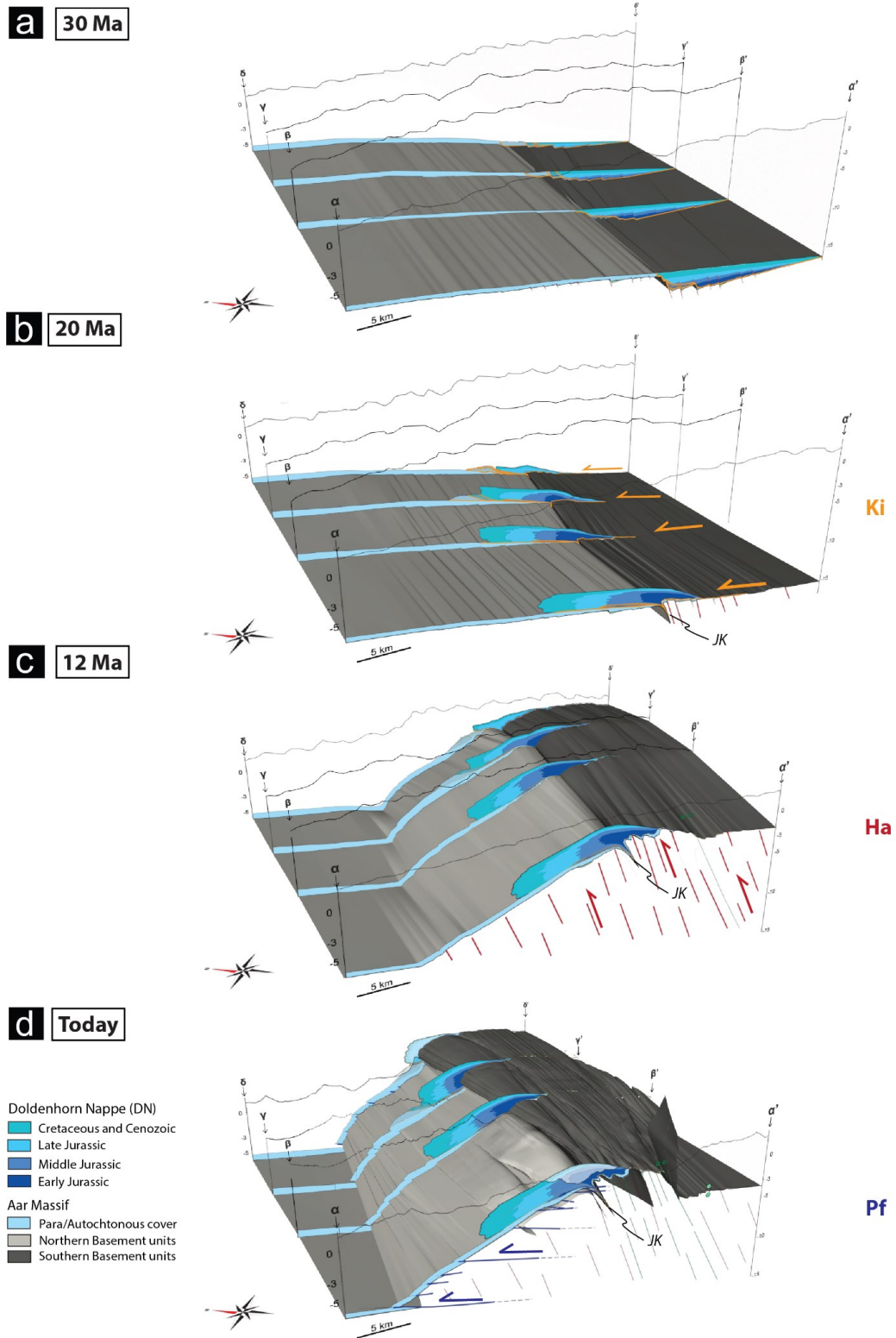**Figure 3.11** - 4D Reconstruction of the evolution of the Doldenhorn Nappe and basement units. (A) Position of the DN basin on the European continental passive margin; (B) Thin-skinned thrusting of the sedimentary units driven by the Kiental thrusts; (C) Exhumation of the basement units induced by the Handegg structures and passive bulging of the overlying DN; (D) Current structural disposition of DN.

the E-W trends in the rheological conditions, thin-skinned inversion tectonics (Kiental phase, Table 1) of the thicker sedimentary portion of the western part of the half-graben, resulted in the large-amplitude recumbent isoclinal fold with an intensively sheared thin overturned limb during progressive shearing and shortening (Figs. 3.7b and 11b). On the contrary, in the east, the Doldenhorn Nappe originated from the thinner portion of the half-graben, displayed only a small-amplitude fold (Figs. 3.8b and 3.11b) and a sequence of autochthonous sediments as well as basement slivers (see Mair et al., 2018). As supported also by 3D numerical simulations (von Tscharner et al., 2016; Spitz et al., 2020), the non-cylindrical shape of the Doldenhorn Nappe (lateral variations in thickness and length of the resulting nappe; compare Figs. 3.6 and 3.10) is therefore a direct consequence of the former basin geometry. Furthermore, structural and 3D analogue studies (e.g., Thomas, 1977; Boyer and Elliott, 1982; Marshak et al., 1992; Macedo and Marshak, 1999; Mouthereau et al., 2002; Lacombe et al., 2003) of several salients of fold-and-thrust belts in the world indicate that the initial large-scale basin architecture and sediment thickness variations strongly affect the development in fold-and thrust-belt salient. In addition, as discussed by Macedo and Marshak (1999) basin-controlled salients result in trend lines that converge at the end of the basin, and this finding is in accordance with the arcuate shape observed for the Doldenhorn thrust front (Fig. 3.11b, see also Doldenhorn Nappe map 20 Ma, in Appendix B2).

3.5.3 Exhumation of the basement units by thick-skinned deformation

At ~22 Ma, the onset of steep basement internal reverse faulting evolved with progressive shortening (onset of Handegg phase, Table 1), leading to a gradual differential uplift from south to north of the basement units. At this stage, strain localization in the basement units led to the generation of several steeply south-dipping brittle-ductile reverse faults and shear zones (see paragraph 3.5.5 and Herwegh et al., 2017). At the footwall of weakly reactivated normal faults, Triassic, Early and Middle Jurassic, and Permo-Carboniferous sediments were locally pinched in synformal sediment wedges, where the strata were steeply dipping and locally overturned (e.g., Bellahsen et al., 2012 and 2014; Nibourel et al. 2021a; see appendix B1 for more information). The large-scale manifestation of such inversion processes occurred at the border normal fault of the basin (Figs. 3.10 and 3.11). At this location, a sediment wedge was pinched between the basement units resulting in the presently exposed 'Jungfrau Keil'. This sediment wedge prominently separates the southern basement units from the northern ones (Fig. 3.11) and is continuous along the strike of the nappe from the west to the east (Fig. 3.1). The border of the basin consisted of a rotational normal fault with a larger throw in the West and a smaller one in the east (Fig. 3.10). Therefore, in the West the 'Jungfrau Keil' forms a > 2 km-deep wedge below the surface, while it only reaches a few hundred meters deep in the east. In terms of temperature-associated ductile deformation,

the trace line of the basement-cover contact (Figs. 3.7c and 3.8c, see basement-cover contact trace), particularly in the case of the aforementioned sediment wedges, motivated a variety of studies to infer 'basement folding' as major deformation process (e.g., Heim, 1922; Ramsay et al., 1983; Ford, 1996; Krayenbuhl and Steck, 2009). However, peak metamorphic temperatures were too low (<400°; Herwegh and Pfiffner, 2005; Berger et al., 2020; Girault et al., 2020) to allow for a pervasive ductile deformation of the granitoid basement units required to induce pervasive basement folds (see also Bellahsen et al., 2012; Lacombe and Bellahsen, 2016; and Appendix B1 for more information). Consequently, a network of steep Handegg shear zones dominated by viscous granular flow of fine-grained quartz-feldspar polymineralic mixtures (Wehrens et al., 2016) accommodated the reverse faulting and a vertical shearing. These movements together with erosion led to differential rock uplift. In contrast, shale rich and calcareous sediment units of the autochthonous and para-autochthonous cover as well as of the overlying sediment nappes were mechanically soft enough to accommodate strain in a fully ductile manner.

3.5.4 A switch back to thick-skinned dominated late-stage horizontal shortening

At 12 Ma, the tectonic style of deformation evolved to a thick-skinned horizontal tectonics stage. Indeed, flat to moderately SE dipping thrust zones with a NW-directed sense of shear initiated at the northern rim of the basement units of the Aar Massif cutting through all the above-mentioned structures and the basement-cover contact. Such discrete lower greenschist facies structures (Pfaffenchopf thrusts; Table 1) led to thrusting of rigid slabs of southern basement over the northern basement units and wedging into the core of the mechanically weaker Doldenhorn Nappe units (Figs. 3.7, 3.8 and 3.11d). With progressive shortening, the thrust-domains progressed into a deeper crustal level, gradually steepening the basement-cover contact (Figs. 3.7, 3.8, and 3.11d) and leading to an en-bloc exhumation of the basement units (Herwegh et al., 2020; Nibourel et al., 2021). It is due to this final thick-skinned horizontal tectonics stage that the impressive steep north walls of the Eiger-Mönch-Jungfrau-Doldenhorn region were emplaced (see also Heim, 1921; Mair et al., 2018).

3.5.5 Implications for the inversion of a passive continental margin

The tectonic evolution of the Doldenhorn Nappe and Aar/Gastern Massifs exemplifies the large impact that basement involvement into the inversion of a proximal passive margin during a late-stage collision can have (see also Lacombe and Mouthereau 2002 and Lacombe and Bellahsen, 2016). Early stages of tectonic inversion of the proximal and distal parts of the former European passive continental margin were dominated by thin-skinned nappe tectonics (Pfiffner et al. 2011; Pfiffner, 2015). However, already at this stage, a major change in deformation occurred. Indeed, the thrusting-associated recumbent folding observed in the

Doldenhorn and Morcles Nappes (lower Helvetics) clearly contrasts with the deformation characteristics of the already emplaced upper Helvetic Nappes (e.g., Pfiffner, 1993; Escher et al. 1993; Escher et al., 1997; Pfiffner et al., 2011; Spitz et al., 2020), where thrusting, imbrication and open to narrow upright folding dominated. The variation in deformation style between upper and lower Helvetic Nappes resulted from the relatively high temperatures during deformation of the latter (275 to 380°C; Herwegh and Pfiffner, 2005; Leloup et al., 2005; Boutoux et al., 2016; Berger et al., 2020; Girault et al., 2020; 2022). This temperature increase allowed shales and calcareous sediments to respond by a pervasive ductile deformation, in contrast with the colder temperatures of deformation during emplacement of the upper Helvetic Nappes. With progressive shortening, subsequent thick-skinned nappe tectonics was initiated. This deformation stage (Handegg phase; Table 1) has been interpreted to be induced by buoyancy forces imposing on mid/upper crustal rocks, which have been decoupled from underlying European lower crust and lithospheric mantle (Herwegh et al., 2017; Kissling and Schlunegger, 2018). Finally, the late-stage horizontal thick-skinned deformation of the Aar Massif basement units (Pfaffenchopf phase; Table 1) is inferred to be kinematically linked to deformation in the Alpine foreland. This deformation phase triggered imbricate thrusting of the Subalpine Molasse (von Hagke et al. 2012, 2014; Mock et al. 2020) as well as thrusting of the Jura along a basal detachment (e.g., Burkhard and Sommaruga,

1998; Sommaruga et al. 2012) or within the basement units (e.g., Becker, 2000; Lacombe and Mouthereau, 2002; Ustaszewski and Schmid, 2006; 2007; Madritsch et al., 2008; Lacombe and Bellahsen, 2016).

From ~22 Ma onwards, the ~12 to 17.5 km horizontal shortening and the 18 to 20 km maximum vertical uplift induced by basement tectonics (Fig. 3.9) had a dramatic impact on the Doldenhorn Nappe, forming the structural configuration presently observable. As discussed by Lacombe and Bellahsen (2016), most of the fold-and-thrust belts in the world, even the 'classic' thin-skinned belts, show evidence of basement-involved shortening (e.g., Taiwan, Zagros). Thus assessing the degree of involvement of basement tectonics is crucial both for understanding the past kinematic evolution of a fold-and-thrust belt, and for predicting their short and long-term potential evolution. For instance, in the Taiwan fold-and-thrust belt the characterization of the degree of crustal coupling within the belt has been essential to identify faulting sources in the process of seismic hazard estimation (Camanni et al., 2014). However, the same concepts are applicable for assessing the potential of natural resources such as geothermal energy (Younas et al 2016) or for selecting potential reservoirs for CO_2 sequestration (e.g., Chevalier et al., 2010).

3.6 CONCLUSION

A 4D reconstruction allowed us to quantitatively describe the structural evolution of the Doldenhorn Nappe and Aar/Gastern

Massifs during the late-stage Alpine collision. The remarkable along-strike variability of the Doldenhorn Nappe and nearby Aar/Gastern Massifs basement units is the result of multiple preconditioning factors and deformation phases that shaped this tectonic complex through space and time. In particular, these are:

i) The Doldenhorn Nappe is the result of the inversion of a basement-cover system originally located along the proximal part of the European continental passive margin. The Doldenhorn Basin was located within an asymmetric half-graben bound by rotational normal faults. The non-cylindrical extension of the Doldenhorn Basin in the N-S and E-W directions resulted from the reactivation of pre-existing crustal fault structures within the basement units. The asymmetric shape of the half-graben affected the nature of the syn-tectonic sedimentary units within the basin, generating fluctuations in thickness along the strike of the basin and thickening towards the footwalls of the extensional faults.

ii) During the incipient thin-skin-dominated inversion of the Doldenhorn Basin, strain localization occurred within the mechanically weak sedimentary units at the basement-cover transition (e.g., within shale-rich and evaporitic layers). Due to the varying topography of the basement-cover interface and thickness of the sedimentary units, the resulting detachment horizon was localized along a single basal thrust in the west, while being split into an in-sequence set of thrusts in the eastern regions of the basin, also incorporating basement slivers. The aforementioned variations in incipient basin sediment thicknesses correlate directly with along-strike amplitude variation of the extruded Doldenhorn Nappe (large amplitude in the west; small amplitude in the east).

iii) The multiphase thick-skinned deformation that overprinted the Doldenhorn Nappe from 22 Ma until present dramatically changed the shape of the investigated area, with a differential vertical exhumation followed by sub-horizontal thrusting of the basement units. The progressive sequence of these deformation phases led (i) to an overall updoming of both the Aar/Gastern Massifs and the entire Helvetic/Penninic/Austroalpine nappe stack on top, as well as (ii) to N-directed thrusting of rigid basement into the core of the Doldenhorn Nappe units.

The 4D reconstruction of the Doldenhorn Nappe and Aar/Gastern Massifs allows visualization of the 3D morphology and variability of a portion of the former proximal passive continental margin, of which current corresponding examples can be found along the Newfoundland or Iberian passive continental margins. The reconstructed subsequent inversion of the Doldenhorn Nappe and Aar/Gastern Massifs, as well as its along-strike variability by inheritance of pre-existing basin geometric and fault patters, correlate well with recent analogue and numerical modelling

studies. Our reconstruction illustrates how thin-skinned nappe formation mechanisms and the nappe geometries are controlled by the initial basement geometry and by the rheological strength contrasts between basement and cover sediments, while basement-involved uplift and shortening controls the late-stage collisional overprint and mechanics of the fold-and-thrust belts.

AUTHOR CONTRIBUTIONS

MH, AB, RB, and AM acquired the foundings for this project. FMP, MH, DM and AB designed the study; whereas FMP, MH and DM carried out the fieldwork. FMP carried out the retrodeformation and modelling with additional scientific input from MH, AB, DM and technical assistance provided from MW and EK. FMP prepared the manuscript and figures with contribution from all co-authors. All authors read and approved the final manuscript. Declaration of Competing Interest The authors declare that they have no known competing financial interests or personal relationships that could have appeared to influence the work reported in this paper.

DATA AVAILABILITY

Data will be made available on request.

REFERENCES

Abrecht, J., 1994. Geologic units of the Aar massif and their pre-Alpine rock associations: a critical review: the pre-Alpine crustal evolution of the Aar-, Gotthard-and Tavetsch massifs. Schweizerische mineralogische und petrographische Mitteilungen, 74(1), 5-27.

Allmendinger, R.W., Jordan, T.E., Kay, S.M., Isacks, B.L., 1997. The evolution of the Altiplano-Puna plateau of the Central Andes. Annual review of earth and planetary sciences 25, 139–174.

Alves, T.M., Moita, C., Sandnes, F., Cunha, T., Monteiro, J.H., Pinheiro, L.M., 2006. MesozoiceCenozoic evolution of North Atlantic continental-slope basins: the Peniche basin, western Iberian margin. AAPG Bulletin 90, 31-60.

Arkai, P., Ferreiro-Ma¨hlmann, R., Suchy, V., Balogh, K., Sykorova, I., Frey, M., 2002. Possible effects of tectonic shear strain on phyllosilicates: a case study from the Kandersteg area, Helvetic domain, Central Alps, Switzerland. Schweiz. Mineral. Petrogr. Mitt. 82, 273– 290.

Badertscher, N., Burkhard, M., 1998. Inversion alpine du graben Permo-Carbonifère de Salvan-Dorénaz et sa relation avec le chevauchement de la nappe de Morcles sus-jacente. Eclogae Geologicae Helvetiae, 91, 359–373.

Balázs, A., Matenco, L., Magyar, I., Horváth, F., Cloetingh, S., 2016. The link between tectonics and sedimentation in back-arc basins: New genetic constraints from the analysis of the Pannonian Basin. Tectonics, 35(6), 1526-1559.

Balázs, A., Burov, E., Matenco, L., Vogt, K., Francois, T., Cloetingh, S., 2017. Symmetry during the syn- and post-rift evolution of extensional back-arc basins: The role of inherited orogenic structures. Earth and Planetary Science Letters, 462, 86-98.

Balestra, M., Corrado, S., Aldega, L., Rudkiewicz, J. L., Morticelli, M. G., Sulli, A., Sassi, W., 2019. 3D structural modeling and restoration of the Apennine-Maghrebian chain in Sicily: Application for non-cylindrical fold-and-thrust belts. Tectonophysics, 761, 86-107.

Ballevre, M., Manzotti, P., Dal Piaz, G. V., 2018. Pre-Alpine (Variscan) inheritance: a key for the location of the future Valaisan Basin (Western Alps). Tectonics, 37(3), 786-817.

Bally, A.W., Gordy, P., Stewart, G.A., 1966. Structure, seismic data, and orogenic evolution of southern Canadian Rocky Mountains. Bulletin of Canadian Petroleum Geology, 14(3), 337–381.

Baumberger, R., Herwegh, M., Kissling, E., 2022. Remote sensing and field data based structural 3D modelling (Haslital, Switzerland) in combination with uncertainty estimation and verification by underground data. 3D Digital Geological Models: From Terrestrial Outcrops to Planetary Surfaces, 159-197.

Bauville, A., Schmalholz, S. M., 2015. Transition from thin-to thick-skinned tectonics and consequences for nappe formation: Numerical simulations and applications to the Helvetic nappe system, Switzerland. Tectonophysics 665, 101–117.

Bauville, A., Schmalholz, S. M., 2017. Tectonic inheritance and kinematic strain localization as trigger for the formation of the Helvetic nappes, Switzerland. Swiss Journal of Geosciences 110 (2), 523–534.

Becker, A., 2000. The Jura Mountains—an active foreland fold-and-thrust belt? Tectonophysics 321, 381-406.

Bellahsen, N., Jolivet, L., Lacombe, O., Bellanger, M., Boutoux, A., Garcia, S., Mouthereau, F., Le Pourhiet, L., Gumiaux, C., 2012. Mechanisms of margin inversion in the external Western Alps: Implications for crustal rheology. Tectonophysics 560, 62–83.

Bellahsen, N., Mouthereau, F., Boutoux, A., Bellanger, M., Lacombe, O., Jolivet, L., Rolland, Y., 2014. Collision kinematics in the western external Alps. Tectonics, 33(6), 1055-1088.

Bellanger, M., Bellahsen, N., Jolivet, L., Baudin, T., Augier, R., Boutoux, A., 2014. Basement shear zones development and shortening kinematics in the Ecrins Massif, Western Alps. Tectonics 33, 84-111.

Berger, A., Wehrens, P., Lanari, P., Zwingmann, H., Herwegh, M., 2017. Microstructures, mineral chemistry and geochronology of white micas along a retrograde evolution: An example from the Aar massif (Central Alps, Switzerland). Tectonophysics, 721, 179-195.

Berger, A., Engi, M., Erne-Schmid, S., Glotzbach, C., Spiegel, C., de Goede, R., Herwegh, M., 2020. The relation between peak metamorphic temperatures and subsequent cooling during continent–continent collision (western Central Alps, Switzerland). Swiss journal of geosciences, 113(1), 1-18.

Bigi, S., Carminati, E., Aldega, L., Trippetta, F., Kavoosi, M. A., 2018. Zagros fold and thrust belt in the Fars province (Iran) I: Control of thickness/rheology of sediments and pre-thrusting tectonics on structural style and shortening. Marine and Petroleum Geology 91, 211-224.

Boutoux, A., Bellahsen, N., Lacombe, O., Verlaguet, A., Mouthereau, F., 2014. Inversion of pre-orogenic extensional basins in the external Western Alps: structure, microstructures and restoration. Journa of Structural Geology 60, 13–29.

Boutoux, A., Bellahsen, N., Nanni, U., Pik, R., Verlaguet, A., Rolland, Y., Lacombe, O., 2016. Thermal and structural evolution of the external Western Alps: Insights from (U–Th–Sm)/He thermochronology and RSCM thermometry in the Aiguilles Rouges/Mont Blanc massifs. Tectonophysics 683, 109-123.

Burkhard, M., 1988. L'Helvétique de la bordure occidentale du massif de l'Aar (évolution tectonique et métamorphique). Eclogae Geologicae Helvetiae, 81(1), 63–114.

Burkhard, M., Sommaruga, A., 1998. Evolution of the western Swiss Molasse basin: structural relations with the Alps and the Jura belt. Geological Society, London, Special Publications 134, 279-298.

Boyer, S. E., Elliott, D., 1982. Thrust systems. Aapg Bulletin 66 (9), 1196–1230.

Brown, D., Alvarez-Marron, J., Schimmel, M., Wu, Y. M., Camanni, G., 2012. The structure and kinematics of the central Taiwan mountain belt derived from geological and seismicity data. Tectonics, 31(5).

Butler, R. W., Tavarnelli, E., Grasso, M., 2006. Structural inheritance in mountain belts: an Alpine–Apennine perspective. Journal of structural geology, 28(11), 1893-1908.

Camanni, G., Chen, C., Brown, D, Alvarez-Marron, J., Wu, Y., Chen, H., Huang, H., Chu, H., Chen, M., Chang, C., 2014. Basin inversion in central Taiwan and its importance for seismic hazard. Geology , 42 (2): 147–150. doi: https://doi.org/10.1130/G35102.1

Campani, M., Mulch, A., Kempf, O., Schlunegger, F., Mancktelow, N., 2012. Miocene paleotopography of the Central Alps. Earth and Planetary Science Letters, 337, 174-185.

Campani, M., Mancktelow, N., Courrioux, G., 2014. The 3D interplay between folding and faulting in a syn-orogenic extensional system: the Simplon Fault Zone in the Central Alps (Switzerland and Italy). Swiss Journal of Geosciences, 107(2), 251-271.

Cardello G. L., Mancktelow N., 2014. Cretaceous syn-sedimentary faulting in the Wildhorn Nappe. Swiss Journal of Geoscience 107(2-3), 223–250. https://doi.org/10.1007/s00015-014-0166-8

Cardello G. L., Mancktelow N., 2015. Veining and post-nappe transtensional faulting in the SW Helvetic Alps (Switzerland). Swiss Journal of Geosciences. 108 (2-3), 1–22. 10.1007/s00015-015-0199-7

Cardello, G. L., Almqvist, B. S., Hirt, A. M., Mancktelow, N. S., 2016. Determining the timing of formation of the Rawil Depression in the Helvetic Alps by palaeomagnetic and structural methods. Geological Society, London, Special Publications, 425(1), 145-168.

Cardello, G. L., Almqvist, B. S., Hirt, A. M., Mancktelow, N. S., 2016. Determining the timing of formation of the Rawil Depression in the Helvetic Alps by palaeomagnetic and structural methods. Geological Society, London, Special Publications, 425(1), 145-168.

Chamberlin, R. T., 1919. The building of the Colorado Rockies. The Journal of Geology, 27(4), 225-251.

Chevalier, G., Diamond, L. W., Leu, W., 2010. Potential for deep geological sequestration of CO_2 in Switzerland: a first appraisal. Swiss Journal of Geosciences, 103(3), 427-455.

Choukroune, P., Gapais, D., 1983. Strain patterin in the Aar granite (Central Alps): orthogneiss developed by bulk inhomogeneous flattening. Journal of Structural Geology 5, 411-418.

Cooper, M., 2007. Structural style and hydrocarbon prospectivity in fold and thrust belts: a global review. Special Publication-Geological Society of London 272, 447.

Curzi, M., Aldega, L., Bernasconi, S. M., Berra, F., Billi, A., Boschi, C., Franchini, S., Van der Lelij, R., Viola, G., Carminati, E., 2020. Architecture and evolution of an extensionally-inverted thrust (Mt. Tancia Thrust, Central Apennines): Geological, structural, geochemical, and K–Ar geochronological constraints. Journal of Structural Geology, 136, 104059.

Doglioni, C., 1992. Relationships between Mesozoic extensional tectonics, stratigraphy and Alpine inversion in the Southern Alps. Eclogae geologicae Helvetiae, 85/1, 105-126.

Dollfuss, S., 1965. Über den helvetischen Dogger ywischen Linth und Rhein. Eclogae geologicae Helvetiae, 58(1), 453-554.

Dumont, T., Champagnac, J. D., Crouzet, C., Rochat, P., 2008. Multistage shortening in the Dauphiné zone (French Alps): the record of Alpine collision and implications for pre-Alpine restoration. Swiss Journal of Geosciences, 101(1), 89-110.

Epard, J.L., 1990. La nappe de Morcles au sud-ouest du Mont-Blanc, PhD thesis, Mém. Géol. Lausanne, 8, 1–158.

Ebert, A., Herwegh, M., Berger, A., Pfiffner, A., 2008. Grain coarsening maps for polymineralic carbonate mylonites: a calibration based on data from different Helvetic nappes (Switzerland). Tectonophysics 457, 128–142.

Escher, A., Masson, H., Steck, A., 1993. Nappe geometry in the western Swiss Alps. Journal of structural Geology 15, 501–509.

Escher, A., Beaumont, C., 1997. Formation, burial and exhumation of basement nappes at crustal scale: a geometric model based on the Western Swiss-Italian Alps. Journal of Structural geology 19, 955-974.

Fagereng, Å., & Toy, V. G., 2011. Geology of the earthquake source: an introduction. Geological Society, London, Special Publications, 359(1), 1-16.

Fitz-Diaz, E., Hudleston, P., Tolson, G., 2011. Comparison of tectonic styles in the Mexican and Canadian Rocky Mountain fold-thrust belt. Geological Society, London, Special Publications, 349(1), 149-167.

Ford, M., 1996. Kinematics and geometry of early Alpine, basement-involved folds, SW Pelvoux Massif, SE France. Eclogae Geologicae Helvetiae 89, 269-295.

Frey, M., Teichmueller, M., Teichmueller, R., Mullis, J., Kuenzi, B., Breitschmid, A., Gruner, U., Schwizer, B., 1980. Very low grade metamorphism in external parts of the Central Alps: illite crystallinity, coal rank and fluid inclusion data. Eclogae Geologicae Helvetiae 73(1), 173–203.

Frey, M., 1987. The reaction-isograd kaolinite+quartz=pyrophyllite+H2O, Helvetic Alps, Switzerland. Schweiz. Mineral. Petrogr. Mitt. 67, 1–11.

Ghani, H., Zeilinger, G., Sobel, E. R., Heidarzadeh, G., 2018. Structural variation within the Himalayan fold and thrust belt: A case study from the Kohat-Potwar Fold Thrust Belt of Pakistan. Journal of Structural Geology 116, 34-46.

Gillcrist, R., Coward, M., Mugnier, J.-L., 1987. Structural inversion and its controls: examples from the Alpine foreland and the French Alps. Geodinamica acta 1 (1), 5–34.

Girault, J.B., Bellahsen, N., Boutoux, A., Rosenberg, C., Nanni, U., Verlaguet, A., Beyssac, O., 2020. 3D thermal structure of the Helvetic nappes of the European Alps: implications for collisional processes. Tectonics. doi: 10.1029/2018TC005334.

Girault, J. B., Bellahsen, N., Bernet, M., Pik, R., Loget, N., Lasseur, E., Rosenberg, C. L.,Balvay, M., Sonnet, M., 2022. Exhumation of the Western Alpine collisional wedge: New thermochronological data. Tectonophysics, 822, 229155.

Granado, P., Ruh, J. B., 2019. Numerical modelling of inversion tectonics in fold-and-thrust belts. Tectonophysics 763, 14–29.

Grosjean, G., Sue, C., Burkhard, M., 2004. Late Neogene extension in the vicinity of the Simplon fault zone (central Alps, Switzerland). Eclogae Geologicae Helvetiae, 97(1), 33-46.

Hamilton, W.B., 1988. Laramide crustal shortening. Interaction of the Rocky Mountain foreland and the Cordilleran thrust belt: Geological Society of America Memoir 171, 27–39.

Hänni, R., Pfiffner, O. A., 2001. Evolution and internal structure of the Helvetic nappes in the Bernese Oberland. Eclogae Geologicae Helvetiae, 94(2), 161-171.

Heim, A., 1922. Geologie der Schweiz. volume 2. CH Tauchnitz.

Herwegh, M., Pfiffner, O.-A., 2005. Tectono-metamorphic evolution of a nappe stack: A case study of the Swiss Alps. Tectonophysics 404 (1-2), 55–76.

Herwegh, M., Berger, A., Baumberger, R., Wehrens, P., Kissling, E., 2017. Large-scale crustal-block-extrusion during late Alpine collision. Scientific reports, 7(1), 1-10.

Herwegh, M., Berger, A., Glotzbach, C., Wangenheim, C., Mock, S., Wehrens, P., Baumberger, R., Egli, D., Kissling, E., 2020. Late stages of continent-continent collision: Timing, kinematic evolution, and exhumation of the Northern rim (Aar Massif) of the Alps. Earth-science reviews, 200, 102959. https://doi.org/10.1016/j.earscirev.2019.102959

Herwegh, M., Berger, A., Bellahsen, N., Rolland, Y., Kissling, E., in press. Evolution of the External Crystalline Massifs of the European Alps. In: Geology of the Alps.

Jammes, S., Huismans, R.S., 2012. Structural styles of mountain building: controls of lithospheric rheologic stratification and extensional inheritance. Journal of Geophysical Research: Solid Earth, 117(B10).

Jaquet, Y., Duretz, T., Grujic, D., Masson, H., Schmalholz, S. M., 2018. Formation of orogenic wedges and crustal shear zones by thermal softening, associated topographic evolution and application to natural orogens. Tectonophysics 746, 512–529

Kempf, O., Pfiffner, O. A., 2004. Early Tertiary evolution of the North Alpine Foreland Basin of the Swiss Alps and adjoining areas. Basin Research, 16(4), 549-567.

Kissling, E., Schlunegger, F., 2018. Rollback orogeny model for the evolution of the Swiss Alps. Tectonics 37, 1097-1115.

Krayenbuhl, T., Steck, A., 2009. Structure and kinematics of the Jungfrau syncline, Faflertal (Valais, Alps), and its regional significance, Swiss Journal of Geosciences, 102, 441–456, https://doi.org/10.1007/s00015-009-1333-1.

Krebs, J., 1925. Geologische Beschreibung der Blümlisalp-Gruppe Beiträge zur Geol. Karte der Schweiz, N.F. 54, Francke, Bern.

Lacombe, O., Mouthereau, F., 2002. Basement-involved shortening and deep detachment tectonics in forelands of orogens: Insights from recent collision belts (Taiwan, Western Alps, Pyrenees). Tectonics 21(4).

Lacombe, O., Mouthereau, F., Angelier, J., Chu, H. T., Lee, J. C., 2003. Frontal belt curvature and oblique ramp development at an obliquely collided irregular margin: Geometry and kinematics of the NW Taiwan fold-thrust belt. Tectonics, 22(3).

Lacombe, O., Bellahsen, N., 2016. Thick-skinned tectonics and basement-involved fold–thrust belts: insights from selected Cenozoic orogens. Geological Magazine 153, 763–810.

Lafosse, M., Boutoux, A., Bellahsen, N., Le Pourhiet, L., 2016. Role of tectonic burial and temperature on the inversion of inherited extensional basins during collision. Geological Magazine 153, 811-826.

Leloup, P.-H., Arnaud, N., Sobel, E.R., Lacassin, R., 2005. Alpine thermal and structural evolution of the highest external crystalline massif: The Mont Blanc. Tectonics 24(4).

Letouzey, J., Werner, P., Marty, A., 1990. Fault reactivation and structural inversion. Backarc and intraplate compressive deformations. Example of the eastern Sunda shelf (Indonesia). Tectonophysics, 183(1-4), 341-362.

Lithostratigraphic Lexicon of Switzerland https://www.strati.ch/en/tectonic/aar-gastern/aar-massiv (accessed 18 May 2022)

Lymer, G., Cresswell, D. J., Reston, T. J., Bull, J. M., Sawyer, D. S., Morgan, J. K., Stevenson, C., Causer, A., Minshull, T. A., Shillington, D. J., 2019. 3D development of detachment faulting during continental breakup. Earth and Planetary Science Letters 515, 90–99.

Macedo, J., Marshak, S., 1999. Controls on the geometry of fold-thrust belt salients. Geological Society of America Bulletin 111 (12), 1808–1822.

Madritsch, H., Schmid, S.M., Fabbri, O., 2008. Interactions between thin-and thick-skinned tectonics at the northwestern front of the Jura fold-and-thrust belt (eastern France). Tectonics 27(5).

Mair, D., Lechmann, A., Herwegh, M., Nibourel, L., Schlunegger, F., 2018. Linking Alpine deformation in the Aar Massif basement and its cover units–the case of the Jungfrau–Eiger mountains (Central Alps, Switzerland). Solid Earth 9, 1099–1122.

Marshak, S., Wilkerson, M., Hsui, A., 1992. Generation of curved fold-thrust belts: Insight from simple physical and analytical models. In: Thrust tectonics. Springer, 83–92.

Masini, E., Manatschal, G., Mohn, G., 2013. The Alpine Tethys rifted margins: Reconciling old and new ideas to understand the stratigraphic architecture of magma-poor rifted margins. Sedimentology, 60(1), 174-196.

Masson, H., Herb, R., and Steck, A., 1980. Helvetic Alps of Western Switzerland, Excusion no. 1, in: Geology of Switzerland – a guide book, Part B, Geological Excursions, edited by: Trümpy, R., 109–153, Wepf & Co, Basel.

McClay, K. R., Whitehouse, P. S., Dooley, T., Richards, M. (2004). 3D evolution of fold and thrust belts formed by oblique convergence. Marine and Petroleum Geology, 21(7), 857-877.

Mock, S., von Hagke, C., Schlunegger, F., Dunkl, I., Herwegh, M., 2020. Long-wavelength late-Miocene thrusting in the north Alpine foreland: implications for late orogenic processes. Solid Earth 11, 1823-1847.

Mohn, G., Manatschal, G., Masini, E., Müntener, O., 2011. Rift-related inheritance in orogens: a case study from the Austroalpine nappes in Central Alps (SE-Switzerland and N-Italy). International Journal of Earth Sciences, 100(5), 937-961.

Mohn, G., Manatschal, G., Beltrando, M., Haupert, I., 2014. The role of rift-inherited hyper-extension in Alpine-type orogens. Terra Nova, 26(5), 347-353.

Mouthereau, F., Deffontaines, B., Lacombe, O., Angelier, J., Byrne, T., Liu, C., 2002. Variations along the strike of the Taiwan thrust belt: Basement control on structural style, wedge

geometry, and kinematics. Special Papers-Geological Society of America 358, 35-58.

Nibourel, L., Berger, A., Egli, D., Luensdorf, N. K., Herwegh, M., 2018. Large vertical displacements of a crystalline massif recorded by Raman thermometry. Geology 46 (10), 879–882.

Nibourel, L., Rahn, M., Dunkl, I., Berger, A., Hermann, F., Diehl, T., Heuberger, S., Herwegh, M., 2021a. Orogen-parallel migration of exhumation in the eastern Aar Massif revealed by low-T thermochronometry. J. Geophys. Res. Solid Earth 126 e2020JB020799.

Nibourel, L., Berger, A., Egli, D., Heuberger, S., Herwegh, M., 2021b. Structural and thermal evolution of the eastern Aar Massif: insights from structural field work and Raman thermometry. Swiss journal of geosciences, 114(1), 1-43.

Nilfouroushan, F., Pysklywec, R., Cruden, A., Koyi, H., 2013. Thermal–mechanicalmodeling of salt-based mountain belts with pre-existing basement faults: application to the Zagros fold and thrust belt, southwest Iran. Tectonics 32 (5), 1212–1226.

Nemcok, M., Mora, A., Cosgrove, J., 2013. Thick-skin-dominated orogens; from initial inversion to full accretion: an introduction. Geological Society, London, Special Publications 377, 1–17.

Peron-Pinvidic, G., Manatschal, G., Osmundsen, P. T., 2013. Structural comparison of archetypal Atlantic rifted margins: A review of observations and concepts. Marine and petroleum geology, 43, 21-47.

Péron-Pinvidic, G., Manatschal, G., Masini, E., Sutra, E., Flament, J. M., Haupert, I., Unternehr, P., 2017. Unravelling the along-strike variability of the Angola–Gabon rifted margin: a mapping approach. Geological Society, London, Special Publications, 438(1), 49-76.

Pfiffner, O.A., 1993. The structure of the Helvetic nappes and its relation to the mechanical stratigraphy. Journal of structural Geology 15, 511–521.

Pfiffner, O.A., Lehner, P., Heitzmann, P., Mueller, S., Steck, A., 1997a. Deep structure of the swiss Alps: results of NRP 20. Birkäuser 1–380.

Pfiffner, O.A., 2006. Thick-skinned and thin-skinned styles of continental contraction. Special Papers-Geological Society of America 414, 153.

Pfiffner, O.A., Burkhard, M., Hänni, R., Kammer, A., Kligfield, R., Mancktelow, N., Menkveld, J.W., Ramsay, J., Schmid, S.M., Zurbriggen, R., 2011. Structural map of the helvetic zone of the swiss alps geological Special map 1:100'000, Bern. Swisstopo 128..

Pfiffner, O.A., 2015. Geologie der Alpen. volume 8416. UTB

Rodgers, J., 1949. Evolution of thought on structure of middle and southern Appalachians. AAPG Bulletin 33(10), 1643–1654.

Ramsay, J., 1981. Tectonics of the Helvetic nappes. Geological Society, London, Special Publications 9, 293–309.

Ramsay, J.G., Casey, M., Kligfield, R., 1983. Role of shear in development of the Helvetic fold-thrust belt of Switzerland. Geology 11, 439–442.

Rohr, K., 1926. Stratigraphische und tektonische Untersuchung der Zwischenbildungen am Nordrand des Aarmassivs (zwischenWendenjoch undWetterhorn), Beiträge zur Geol. Karte der Schweiz, N.F. 57, Francke, Bern.

Sala, P., Pfiffner, O. A., Frehner, M., 2014. The Alpstein in three dimensions: fold-and-thrust belt visualization in the Helvetic zone, eastern Switzerland. Swiss Journal of Geosciences, 107(2), 177-195.

Santantonio, M., Carminati, E., 2011. Jurassic rifting evolution of the Apennines and Southern Alps (Italy): Parallels and differences. GSA Bulletin, 123(3-4), 468-484.

Santolaria, P., Vendeville, B. C., Graveleau, F., Soto, R., Casas-Sainz, A., 2015. Double evaporitic décollements: Influence of pinch-out overlapping in experimental thrust wedges. Journal of Structural Geology, 76, 35-51.

Schlunegger, F., Kissling, E., 2015. Slab rollback orogeny in the Alps and evolution of the Swiss Molasse basin. Nature communications, 6(1), 1-10.

Schmid, S.M., Fügenschuh, B., Kissling, E., Schuster, R., 2004. Tectonic map and overall architecture of the Alpine orogen. Eclogae Geologicae Helvetiae 97, 93–117.

Sommaruga, A., Eichenberger, U., Marillier, F.J.Y., 2012. Seismic Atlas of the Swiss Molasse Basin. Swiss Geophysical Commission, Contribution to the Geology of Switzerland – Geophysics 44, 1-82.

Spitz, R., Bauville, A., Epard, J. L., Kaus, B. J., Popov, A. A., Schmalholz, S. M., 2020. Control of 3-D tectonic inheritance on fold-and-thrust belts: insights from 3-D numerical models and application to the Helvetic nappe system. Solid Earth, 11(3), 999-1026.

Steck, A., 1968. Die alpidischen Strukturen in den zentralen Aaregraniten des westlichen Aarmassivs. Eclogae Geologicae Helvetiae, 61(1), 19-48.

Steck, A., 2008. Tectonics of the Simplon massif and Lepontine gneiss dome: deformation structures due to collision between the underthrusting European plate and the Adriatic indenter. Swiss Journal of Geosciences, 101(2), 515-546.

Tavani, S., Cardello, G. L., Vignaroli, G., Balsamo, F., Parente, M., Sabbatino, M., Raffi, I., Billi, A., Carminati, E., 2021. Segmentation of the Apenninic Margin of the Tyrrhenian Back-Arc Basin Forced by the Subduction of an Inherited Transform System. Tectonics, 40(9), e2021TC006770

Taylor, B., Goodliffe, A., Martinez, F., Hey, R., 1995. Continental rifting and initial sea-floor spreading in the Woodlark Basin. Nature, 374(6522), 534-537.

Thomas, W. A 1977. Evolution of Appalachian-Ouachita salients and recesses from reentrants and promontories in the continental margin. American Journal of Science, 277, 1233-1278.

Trümpy, R., 1952. Der Nordrand der Liasischen Tethys in den Schweizer Alpen. Geologische Rundschau, 40(2), 239-242.Tugend, J., Manatschal, G., Kusznir, N. J., Masini, E., 2015. Characterizing and identifying structural domains at rifted continental margins: application to the Bay of Biscay margins and its Western Pyrenean fossil remnants. Geological Society, London, Special Publications, 413(1), 171-203.

Turrini, C., Lacombe, O., Roure, F., 2014. Present-day 3D structural model of the Po Valley basin, Northern Italy. Marine and Petroleum Geology, 56, 266-289.

Turrini, C., Toscani, G., Lacombe, O., Roure, F., 2016. Influence of structural inheritance on foreland-foredeep system evolution: An example from the Po valley region (northern Italy). Marine and Petroleum Geology, 77, 376-398.

Ustaszewski, K., Schmid, S.M., 2006. Control of preexisting faults on geometry and kinematics in the northernmost part of the Jura fold-and-thrust belt. Tectonics 25, TC5003.

Ustaszewski, K., Schmid, S.M., 2007. Latest Pliocene to recent thick-skinned tectonics at the Upper Rhine Graben–Jura Mountains junction. swiss Journal of Geosciences 100, 293-312.

Vitale, S., Ciarcia, S., 2021. The dismembering of the Adria platforms following the Late Cretaceous-Eocene abortive rift: a review of the tectono-stratigraphic record in the southern Apennines. International Geology Review, DOI: 10.1080/00206814.2021.2004559.

von Hagke, C., Cederbom, C., Oncken, O., Stöckli, D., Rahn, M., Schlunegger, F., 2012. Linking the northern Alps with their foreland: The latest exhumation history resolved by low-temperature thermochronology. Tectonics 31, TC5010.

von Hagke, C., Oncken, O., Evseev, S., 2014. Critical taper analysis reveals lithological control of variations in detachment strength: An analysis of the Alpine basal detachment (Swiss Alps). Geochemistry, Geophysics, Geosystems 15, 176-191.

von Tscharner, M., Schmalholz, S., Epard, J.-L., 2016. 3-D numerical models of viscous flow applied to fold nappes and the Rawil depression in the Helvetic nappe system (western Switzerland). Journal of Structural Geology 86, 32–46.

Watts, A., Lamb, S., Fairhead, J., Dewey, J., 1995. Lithospheric flexure and bending of the Central Andes. Earth and Planetary Science Letters 134, 9–21.

Wehrens, P., Berger, A., Peters, M., Spillmann, T., Herwegh, M., 2016. Deformation at the frictional-viscous transition: Evidence for cycles of fluid-assisted embrittlement and ductile deformation in the granitoid crust. Tectonophysics, 693, 66-84.

Wehrens, P., Baumberger, R., Berger, A., Herwegh, M., 2017. How is strain localized in a meta-granitoid, mid-crustal basement section? Spatial distribution of deformation in the central Aar massif (Switzerland). Journal of structural geology, 94, 47-67.

Welsink, H., Tankard, A., 2012. 14-Extensional Tectonics and Stratigraphy of the Mesozoic Jeanne d'Arc basin, Grand Banks of Newfoundland, Regional Geology and Tectonics:

Phanerozoic Rift Systems and Sedimentary Basins, 1, 337.

Wilson, R.C.L., Manatschal, G., Wise, S., 2001. Rifting along non-volcanic passive margins: stratigraphic and seismic evidence from the Mesozoic successions of the Alps and western Iberia. In: Wilson, R.C.L., Whitmarsh, R.B., Taylor, B., Froitzheim, N. (Eds.), Non-volcanic Rifting of Continental Margins: a Comparison of Evidence from Land and Sea. Geological Society, London, pp. 429-452.
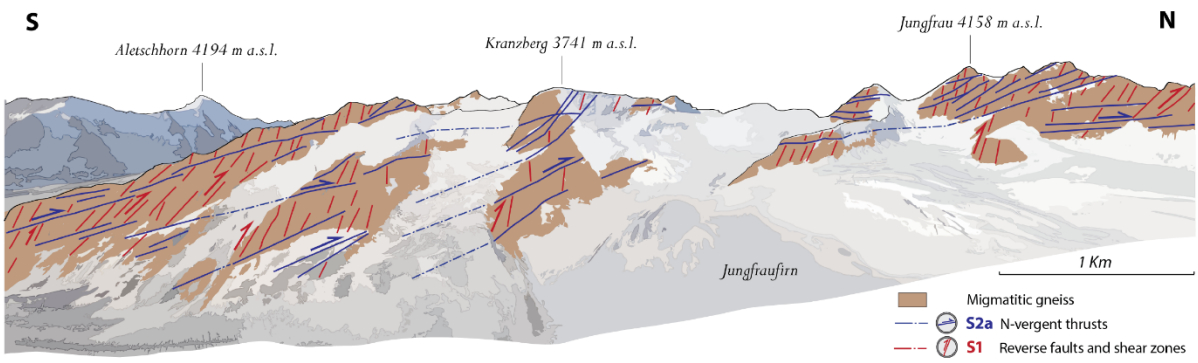
Younas, U., Khan, B., Ali, S. M., Arshad, C. M., Farid, U., Zeb, K., Rehman, F., Mehmood, Y., Vaccaro, A., 2016. Pakistan geothermal renewable energy potential for electric power generation: A survey. Renewable and Sustainable Energy Reviews, 63, 398-413.

Zanchi, A., Berra, F., Mattei, M., Ghassemi, M. R., Sabouri, J., (2006. Inversion tectonics in central Alborz, Iran. Journal of Structural Geology, 28(11), 2023-2037.

Ziegler, H. J., Isler, A., 2013. Zusammenfassender geologischer Schlussbericht Lötschberg-Basistunnel. Landesgeologie (Bundesamt für Landestopografie swisstopo), Wabern, Switzerland

.

Chapter IV

Aletschhorn 4194 m a.s.l.

Kranzberg 3741 m a.s.l.

Jungfrau 4158 m a.s.l.

S

N

Jungfraufirn

1 Km

Migmatitic gneiss
S2a N-vergent thrusts
S1 Reverse faults and shear zones

Panoramic view and geological interpretation of the Jungfraufirn.

Viewpoint: X: 2643825 / Y: 1152462

The control of collisional tectonics over valley morphology: the case of the largest glacier in the European Alps

Ferdinando Musso Piantelli[1&2], Sandro Truttmann[1] and Marco Herwegh[1]

[1] Institute of Geological Sciences University of Bern, Baltzerstrasse 1+3, 3012 Bern, Switzerland
[2] Swiss Geological Survey, Federal Office of Topography swisstopo, Seftigenstrasse 264, 3084 Bern, Switzerland

Keywords

Aletsch Glacier
Fault frequency
Fault orientation
Natural hazards
Valley evolution
Erosional processes

Abstract

Understanding how bedrock properties influence the valley-forming processes of Alpine landscapes is an outstanding challenge. A multi-methodological approach was used to uniformly quantify fault frequency, orientation, and rock hardness of crystalline basement rocks to evaluate their impact on the erosional processes that shaped the valley of the Aletsch Glacier, Switzerland. We show how variations in fault frequency and orientations, imposed by the inherited collisional framework of the area, control the local erodibility of the valley, affecting both hillslopes and channel erosion processes. Our results highlight how tectonic preconditioning exerts a first-order control on the efficiency of erosion in the mountain chain, elucidating an integral link between deep-seated collisional dynamics and surface-based mountain shaping. Moreover, our results express the importance of a uniform, quantitative characterization of bedrock properties to comprehend the interaction and variability of erosional processes and hazards distributed within the valley systems.

4.1   INTRODUCTION

In Alpine landscapes, most valleys form in a complex evolutionary sequence of widening and deepening controlled by channel incision and hillslope erosional processes (MacGregor et al., 2000; Harbor, 1992). Their efficiency is determined by the erosive power of the incising glacio-fluvial system and by the physical parameters of the bedrock. For example, unroofing of basement units in the core of mountain ranges is often associated with their lower erosional susceptibility to fluvial and glacial erosion (e.g., Carroll et al., 2006; Kühni and Pfiffner, 2001). However, such units are commonly affected by a large number of deformation structures (joints, faults, shear zones) induced during orogenesis (e.g., Molnar et al., 2007; Neely et al., 2019). Spatial variations in the occurrence of such deformation structures may lead to significant variability in relief production and erosional susceptibility (Whipple et al., 2000; Steinemann et al., 2021; Patton et al., 2016).

Geomorphological studies demonstrated that, under both glacial and fluvial settings, plucking and abrasion represent the two major channel incision erosional processes. While the first one dominates in densely fractured domains, the second one prevails in unfractured rock masses (Sklar and Dietrich, 2001; Dühnforth et al., 2010). Beside the incision processes, an increased fracture density also affects the stability of slopes resulting in hazardous landslide and rockfall events especially after glacial retreat (Moore et al., 2009; DiBiase et al., 2018).

So far, a direct link between a quantitative survey of fault distribution and valley morphology has received little attention. Yet understanding the spatial distribution and kinematics of fault patterns is a fundamental prerequisite not only for constraining valley-scale relief production and incision, but also for numerical models predicting valley evolution. In this study, a multi-methodological approach was followed to test the role of differential frequency distribution and orientation of faults in the valley morphology evolution of the Aletsch Glacier (Central Switzerland), the largest glacier in the European Alps. This framework was used to evaluate landscape-scale valley morphology as a response to rock strength variation and structural variability to discuss implications for connections between collision geodynamics, landscape evolution, and natural hazards.

4.2 GEOLOGICAL SETTING

The study area is located in the central Aar Massif, one of the External Crystalline Massifs of the European Alps, which recorded a long-lasting exhumation history. Differential uplift occurred along steep massif parallel faults and thrusts, consisting of mylonites, ultramylonites and prograde formation of cataclasites, fault gauges and breccias (see Appendix C1 and references therein). This resulted in both an N-S increasing metamorphic grade (up to the upper greenschist facies ~450°C; Herwegh et al., 2020; Nibourel et al., 2021) as well as a denser fault network. Given the both ductile and brittle nature of the structures, we refer to them in general as faults following the nomenclature of Sibson (1977). The exhumation accelerated in the last 1-2 million years due to the effect of glacial erosion (Fox et al., 2016; Glotzbach et al., 2010; Valla et al., 2011) and is still ongoing, as observed in differential rock uplift and seismic activity (e.g., Schlatter et al., 2005; Fäh et al., 2011).

The valley object of this study is sculpted by the Great Aletsch Glacier and the Massa River (Figs. 4.1A and 1B), with a total length of ~30 km, of which ~22 km is occupied by the Aletsch Glacier. The bedrock units of the valley consist of migmatitic gneisses, granites, and granodiorites (Fig. 4.1A). While the northern and southern part of the valley are underlain by migmatitic gneiss units (Fig. 4.1A; Berger et al., 2017), fluid-altered migmatitic gneisses alternating with granite and granodiorite intrusion bodies occur in the central part (Fig. 4.1A; Berger et. al, 2017). The migmatitic gneiss units display a pre-Alpine foliation along which the faults localized (Wehrens at al., 2016).
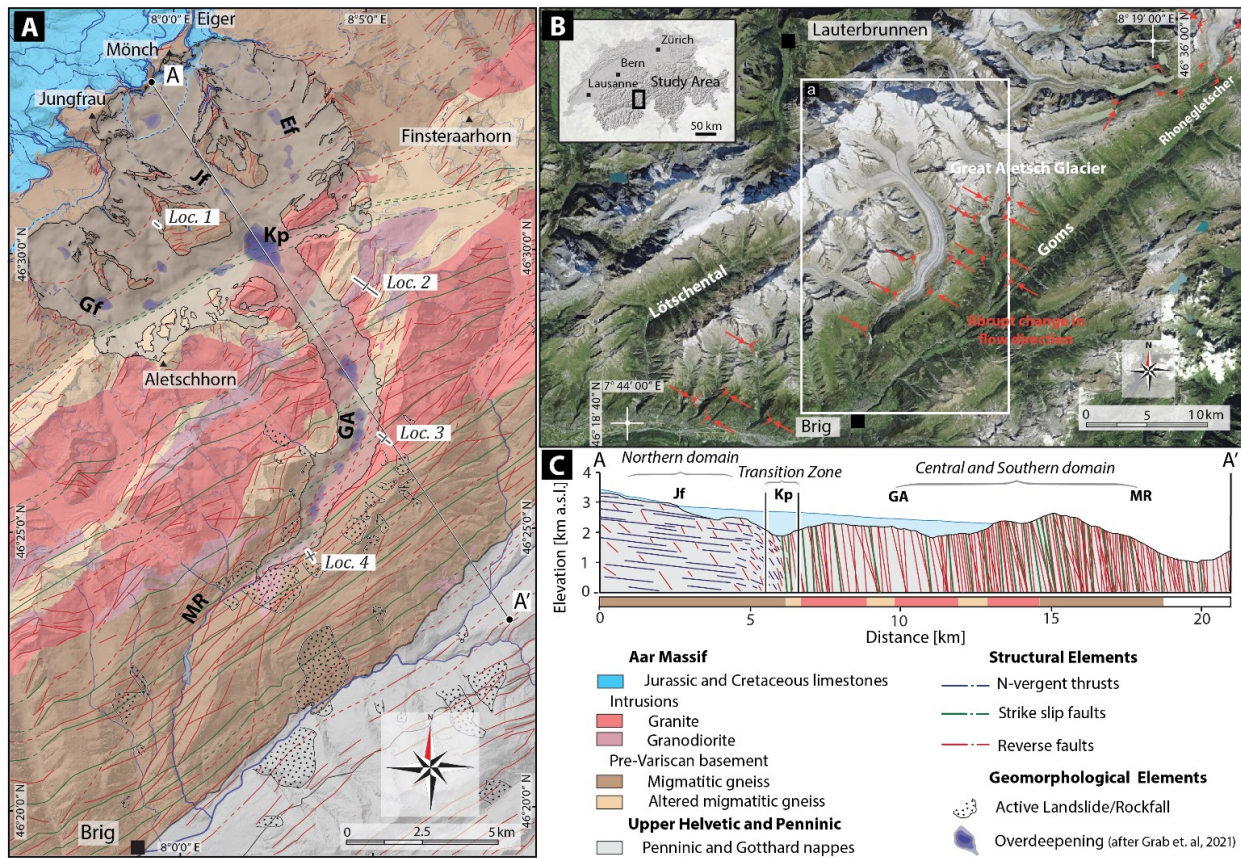
Figure 4.1. (A) Geological map of the investigated area. Purple color-coded overdeepenings and hillshade of the glacier-bed topography after Grab et al, 2021. Active landslide/rockfall distribution from InSAR data (https://sitonline.vs.ch/dangers/dangers_geologiques/de/). Gf – Grosser Aletschfirn; Jf – Jungfraufirn; Ef – Ewigschneefäld; Kp – Konkordiaplatz; GA – Grosser Aletschgletscher; MR – Massa River. WGS84 coordinate system. (B) Large-scale overview (SWISSIMAGE, swisstopo) of the investigated area (white frame). The inset map shows the location within Switzerland. (C) Simplified geological section of the structures in the investigated area. Section trace indicated in panel A.

In the North, three tributary glaciers converge at a triple junction named Konkordiaplatz and feed the main glacier (Fig. 4.1A), coinciding with a large-scale ~350 m overdeepening (after Grab et al., 2021, Fig. 4.1A). Further downstream the Aletsch glacier flows along a relatively straight NW-SW trending section before it abruptly changes its flow into NE-SW direction as induced by a series of ~30-50° turns, punctuated by a sequence of overdeepenings. The southern domains of the area are highly unstable as documented by several large-scale rock slope failures and rockfalls mostly related to recent glacial retreat (Glueer et al., 2019; Truttmann et al., 2021).

4.3 METHODOLOGY

After a detailed field-based structural investigation (see Appendix C1), a multi-methodological approach was employed to

characterize and quantify the bedrock properties and hillslope morphology in a spatially uniform way over the entire study area.

(i) Remote sensing: The frequency distribution of the faults in the area was investigated remotely using a scan-line approach (Brooks and Allmendinger, 1996) continuously applied at the large-scale (1:2500), over the entire area, and at a more detailed scale (1:100) at four field locations (Fig. 4.1A). The large-scale scan-lines consist of a sequence of individual segments oriented perpendicular to the main trend of the faults (Appendix C2). Each linear feature detectable on orthophotos (raster resolution of 0.5 x 0.5 m) and hillshade maps (2 x 2 m raster resolution) being continuous for 100 m across the scan-line was sampled as a fault. The data were then projected onto a unified profile (Fig. 4.1A, trace AA'), and plotted in a frequency histogram. The detailed-scale remote sensing frequency analysis was performed over UAV-based orthophotos and hillshade maps (raster resolution of 2.5 x 2.5 cm) at four different locations (Fig. 4.1A and Tab. C2). At each location, the scan-lines were oriented perpendicular to the main trend of structures, and for locations 2, 3, and 4 also parallel to the main structural trend (Fig. C6). This sampling strategy allowed obtaining the spatial pattern of faults, which in turn provided information about 2D block sizes available for channel and slope erosion processes.

(ii) Relief and slope analysis: To analyze the hillslope morphology of the valley both the hillslope angle and the relief were derived from 120 topographic valley transects perpendicular to the main valley axis with a spacing of 250 m. The average hillslope angle and relief were calculated on the right and left sides of the valley along each valley transect. (See Appendix C2)

(iii) Schmidt hammer profiles: Field-based rock hardness analyses were performed with a Schmidt hammer (Classic 'N' type) along the scan-lines perpendicular to the structures at locations 1-4 (Fig. 4.1A; Appendix C2). The rebound values, together with the type of lithology and the presence of faults, were collected at regular 1 m sampling intervals on exposed rock surfaces parallel to the main foliation or related fault planes. The field locations were chosen in close vicinity to the glacier and within the Little Ice Age limit (Kelly et al., 2004) to ensure minimal weathering of the investigated outcrops.

4.4   RESULTS

Both frequency and typology of faults are not uniform along the valley. According to the orientations and kinematics, three structural domains were characterized in the field (Figs. 4.1C, 4.2; for details Appendix C1): (i) A northern domain that displays gently South-dipping thrusts that cut steep reverse SW-NE striking faults (Figs. 4.1C, 4.2A and B); (ii) a central and southern domain with steep reverse, SW-NE and SSW-NNE striking faults and SW-NE oriented strike-slip to oblique faults (Figs 4.1C, 4.2B and C); and (iii) a transition zone between the two
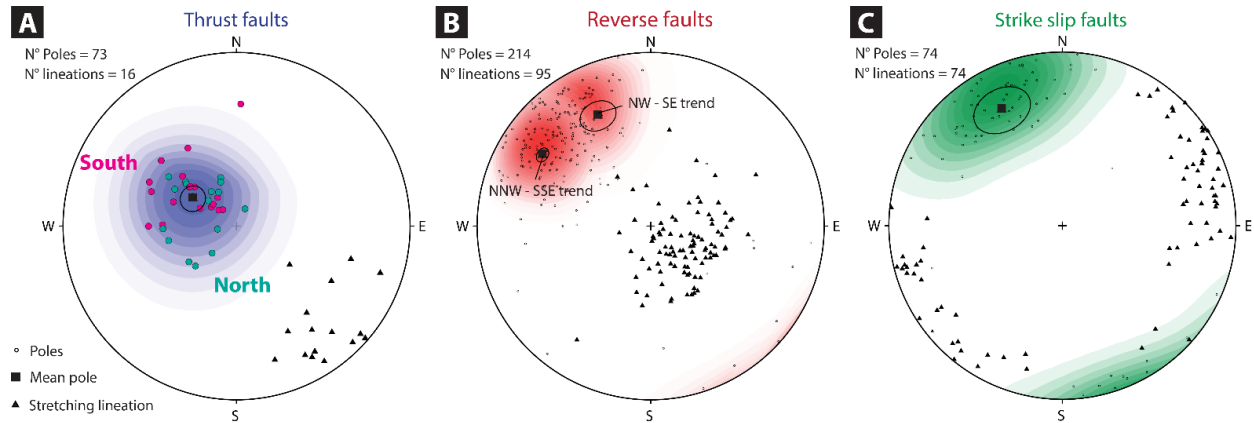
Figure 4.2. Structural field data (poles and mean poles for the fault planes and orientations of associated stretching lineation, lower hemisphere) of the fault structures in the basement units of the investigated area. (A) Stereoplot for the thrusts fault structures. As highlighted by the colour code of the poles, the fault planes increase progressively their dip angle from North to South. (B) Stereoplot for the reverse faults structures. In the plot, the two mean poles highlight the two different trends. (C) Dataset of the measurements of the strike slip faults.
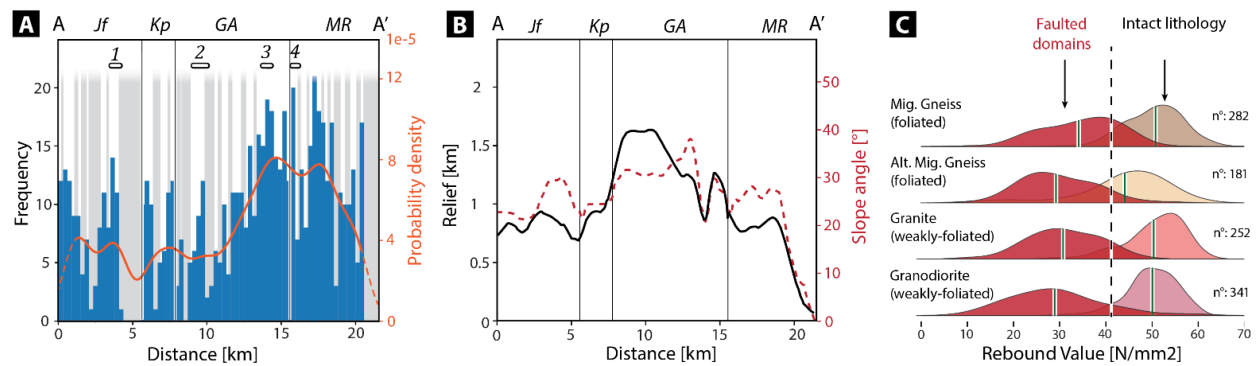

Figure 4.3. (A) Histogram (blue bars) and density curve (orange line) showing the large-scale frequency distribution of structures along the AA' profile (trace and abbreviations indicated in Fig. 1A). Bin size of 300 m; the gray bars indicate no-data areas, i.e. areas covered by Quaternary deposits (see appendix A). (B) Moving averages of the relief (black line) and slope angle analysis (dashed red line) along the AA' profile (see Appendix A). (C) Ridgeline plot of the Schmidt hammer rebound values subdivided into the four lithological groups. The green bars indicate the mean rebound values of the intact and the faulted/sheared domains of each lithology.

aforementioned domains at Konkordiaplatz (TZ, Fig 4.1C, see Appendix C1) where all the thrusts, reverse and strike-slip fault systems coexist. All the described structures are limited in width (dm to few m), but laterally very persistent and frequently traceable over several km.

The large-scale fault frequency analysis reveals variations from North to South (Fig. 4.3A). From km 0 to 12.5 of the AA' transect the faults reach a maximum spacing of 21.5 m. From km 12.5 to 22, the number of faults increases significantly, reaching a spacing of 14 m. These results
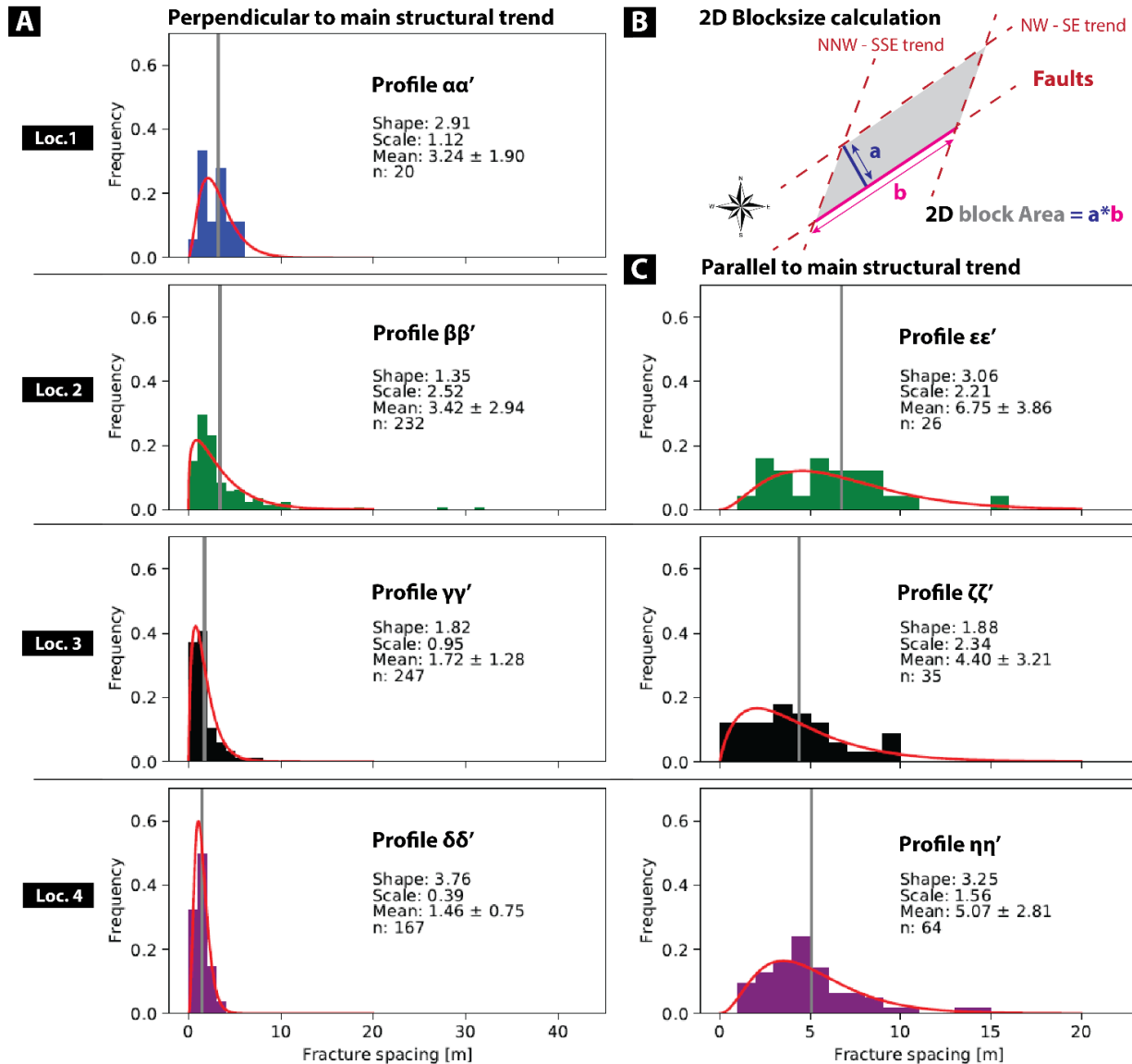
Figure 4.4. Probability density plots, fitted by a gamma distribution, of the fault spacing along each of the detailed scan lines perpendicular (A) and parallel (C) to the main structural trend. (B) Simplified sketch that shows the geometric calculation to derive the 2D block sizes at locations 2, 3, and 4. The block is sketched as a grey rhomboid bounded by the NNW – SSE and NW – SE trends of the fault structures present at the filed locations. (a) and (b) represent the mean fault spacing measured on the detailed scan-lines, respectively, oriented perpendicular and parallel to the main structural trend.

correlate well with the detailed-scale fault frequency analysis (Fig. 4.4). Indeed, transects at locations 1 and 2 reveal an average spacing, of the main structural trend, respectively of 3.24 m ± 1.90, and 3.42 m ± 2.94. This contrasts

significantly with transects at locations 3 and 4 that reveal an average spacing of 1.72 m ± 1.28, and 1.46 m ± 0.75. Also, the calculated 2D block sizes show larger blocks at location 2 (23.1 m^2)

and smaller at locations 3 and 4, 7.5 and 7.4 m^2, respectively.

The relief and slope analyses (Fig. 4.3B) show that the accumulation zone, which lies above 2500 m a.s.l., is weakly incised with gentle slope angles (20 to 30°) and a relief ranging between 700 to 900 m. Strong relief (800 to 1600 m) and steep slopes (20 to 38°) characterize the central sector, whereas the southern sector exhibit gentle hillslopes (>10 to 28°) and a strongly reduced relief (<1000 m).

The field-based Schmidt hammer analysis shows a bimodal distribution of the hardness measurements in all the investigated lithologies (Fig. 4.3C). When not affected by a fault, all the lithologies range within similar hardness values (44 to 51 N/mm^3). However, in presence of a fault, the rocks' hardness drops systematically to significantly lower values of 29 to 34 N/mm^3.

4.5 DISCUSSION AND CONCLUSIONS

The field-based Schmidt hammer investigations demonstrate that while lithological variations and rock foliation do not induce significant changes in rock hardness, the presence of faults considerably reduces the bulk rock hardness. Therefore the variations in orientation and frequency of faults, imposed by the geodynamic collisional framework of the Aar massif, are crucial in controlling: (i) bedrock erosion processes; (ii) valley axes orientation and morphology; and (iii) occurrence of hazardous mass movements in the Aletsch Glacier valley. As a function of those structural parameters, the valley morphology responds with a non-uniform susceptibility to bedrock erosion coupled in both the bedrock channel and hillslopes erosion processes.

4.5.1 Dependency of channel incision processes on fault frequency and orientation

Fault frequency controls the erosional processes incising the valley channel as it defines the sizes of the blocks available for erosion (Whipple et al., 2000; Dühnforth et al., 2010). High-fault frequency bedrock, with mean fault spacing < 2 m, is more prone to entrainment of blocks and therefore affected by high glacial and fluvial quarrying rates (Hallet, 1996; Steinemann et al., 2021; Patton et al., 2016). The enhanced quarrying rates lead to the generation of a large number of overdeepenings and bedrock riegels (Figs. 4.5A, B). In low-fault frequency massive bedrock domains, with a mean fault spacing > 2 m, quarrying becomes ineffective. Hence, the volumetrically less efficient abrasion process dominates generating relatively smooth bedrock sections (Figs. 4.5A, B).

Fault orientation is another important factor since it determines the number of structural sets available for quarrying and the blocks' discharge direction. In the Transition Zone (Fig 4.5A) the three sets of faults render block discharge under quarrying very efficient, creating an ideal convergence point in the Konkordiaplatz overdeepening (> 350 m; Grab et al., 2021). Furthermore, in the southern high-frequency fault domain, the SW-NE and SSW-NNE sets of structures establish the blocks' discharge direction under quarrying; presumably
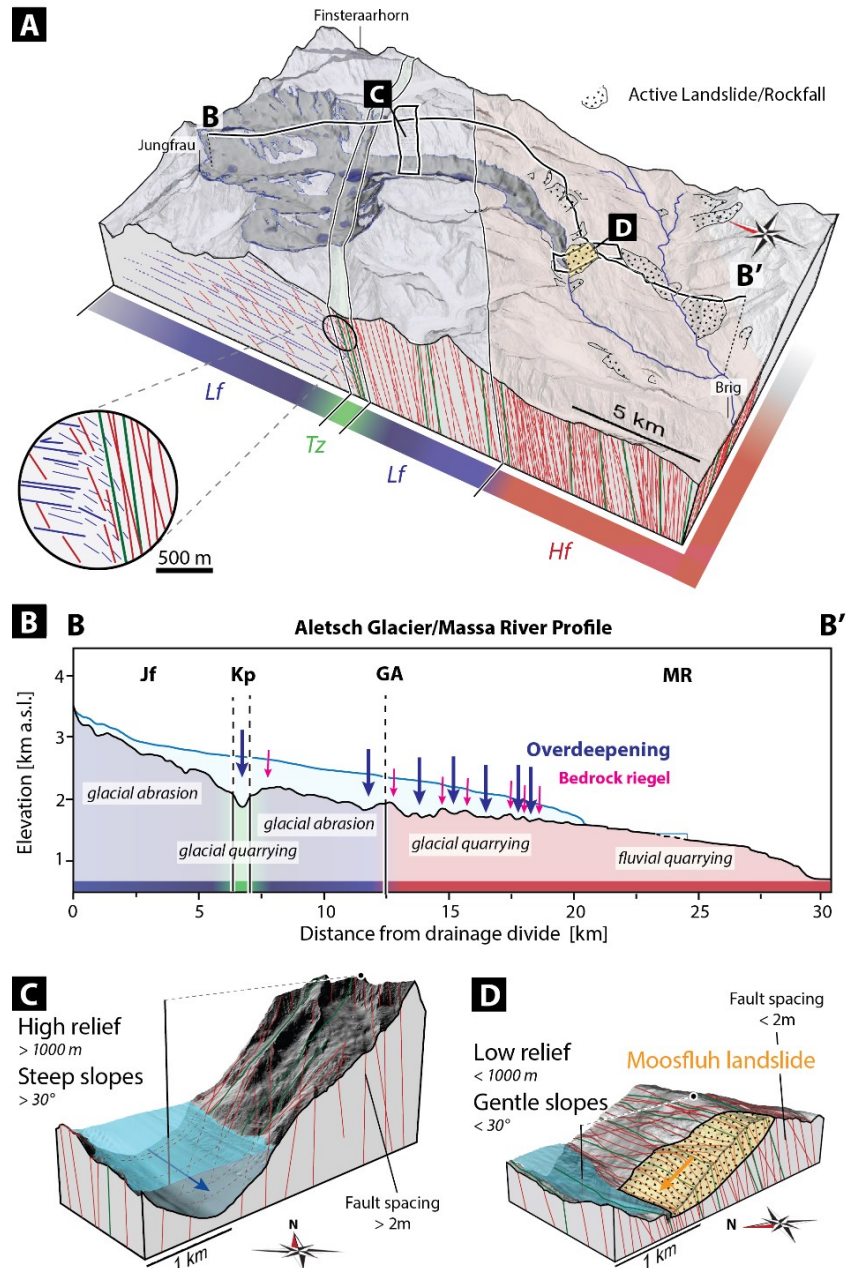
Figure 4.5. (A) 3D block model of the study area with subdivision into three domains based on the faults' frequency and kinematics. Low-frequency (Lf, blue), high-frequency (Hf, red), and transition zone (Tz, green) domains, respectively, with fault spacings of > 2 m, < 2 m and coexistence of reverse and strike-slip faults. (B) Longitudinal valley profile of the Aletsch Glacier and Massa River; profile trace visible in pane A. The Hf and Tz domains coincide with enhanced quarrying activity and the associated presence of overdeepenings and bedrock riegels. Instead, the Lf domains correspond to abrasion-dominated smooth bedrock sections. (C); 3D block model representing the hillslopes in Lf domain, box C in panel A. High slope stability granted by sparse fault spacing allows for the preservation of high relief and steep slope angles. (D) 3D block model representing the hillslopes in Hf domain, box D in pane A. Increased fault density reduces rock mass strength and triggers bedrock mass movements and rockfalls, i.e., as expressed by the Moosfluh bedrock landslide. This results in a lowered relief and gentle slope angles.

further exploiting an already formerly existing torrential system. Consequently, the observed sequences of overdeepenings and bedrock riegels evolved aligned with the two main fault trends inducing the glacier's prominent turns in the flow direction (Figs. 4.1A, 4.2B and 4.5B).

4.5.2 Hillslope morphology dependency on fault frequency

The relief and slope analyses show a strong correlation between increasing fault frequency and decreasing bedrock hillslope-scale strength, expediting the hillslope erosion processes (e.g., Larsen and Montgomery, 2012; DiBiase et al., 2018). Indeed, high relief and steep slope angles characterize slopes in less faulted bedrock domains (Figs. 4.5A and C) indicating high stability thresholds in terms of rockfalls and bedrock landslides. On the contrary, in highly faulted bedrock slopes (Figs. 4.5A and D) low relief and gentle slope angles correspond to unstable slopes. This relation has important societal consequences in mountainous regions since these domains coincide with active hazardous large-scale bedrock landslides and rockfalls in the investigated area; i.e., the currently active Moosfluh deep-seated bedrock landslide, one of the largest mass movements in the Alps (Glueer et al. 2019; Truttmann et al., 2021; Figs. 4.5A and D).

4.5.3 Alpine landscape evolution as a direct result of collisional tectonics?

From a geodynamic point of view, the fault structures evolved as a consequence of vertical tectonics during Alpine collision and exhumation (Herwegh et al., 2020 and references therein). Subsurface faults initiated at the crustal level therefore directly affect the efficiency of erosion in the mountain chain, elucidating an integral link between deep-seated collisional dynamics and surface-based mountain shaping. In other words, the efficiency of erosional processes active in orogenic systems goes hand in hand with the inherited collisional tectonic architecture. Changes in the global climate system enhance then landscape disequilibrium and promote valley incision and relief development through both glacial and fluvial processes (Valla et al., 2011).

The discussed results express the importance of a uniform, quantitative characterization of fault distribution and orientation to comprehend the variability and interaction of erosional processes distributed within valley systems. Such quantification provides fundamental insights into long-term erosional patterns, essential for planning future hazards mitigation at the regional scale. This aspect is of particular societal relevance given the progressively retreating glaciers with consequently exposed oversteepened valley slopes resulting from climate change.

STATEMENT OF SIGNIFICANCE

In this study, we investigate how fault frequency and orientation, imposed by an inherited collisional framework, influence the valley-forming processes in Alpine landscapes. We used a multi-methodological approach to collect a

continuous dataset of fault distribution, orientation, and rock hardness along the valley of the Aletsch Glacier, Switzerland. Our results provide insights into fault-frequency and orientation controlled long-term erosional patterns, fundamental to comprehending the variability and interaction of erosional processes as well as natural hazards distributed within Alpine valley systems. This work represents a novel approach to investigating valley systems combining the structural geology and geomorphology fields. This is of great interest to the scientific community, given the increasing necessity to cope with the Alpine landscape evolution strongly affected by climate change.

ACKNOWLEDGMENTS

AUTHOR CONTRIBUTIONS

MH, acquired the founding for this project. FMP, MH and ST designed the study; FMP and ST carried out the fieldwork. FMP made the 3D modelling and remote sensing detection of the structures. FMP and ST carried out the fault frequency and hillslope analysis with additional scientific input from MH. FMP prepared the manuscript and figures with contribution from all co-authors. All authors read and approved the manuscript.

REFERENCES

Berger, A., Mercolli, I., Herwegh, M., & Gnos E., 2017, Geological Ma of the Aar Massif, Tavetsch and Gotthard Nappes, Federal Office of Topography swisstopo, scale 1 : 100 000.

Brooks, B.A., & Allmendinger, R.W. (1996). Fault spacing in the El Teniente Mine, central Chile: Evidence for nonfractal fault geometry. Journal of Geophysical Research, v. 101, p. 13,633–13,653, doi: 10.1029/96JB00800.

Carroll, A.R., Chetel, L.M., & Smith, M.E. (2006). Feast to famine: Sediment supply control on Laramide basin fi ll. Geology, v. 34, p. 197–201, doi: 10.1130/G22148.1.

DiBiase, R. A., Rossi, M. W., & Neely, A. B. (2018) Fracture density and grain size controls on the relief structure of bedrock landscapes. Geology, 46(5), 399-402.

Dühnforth, M., Anderson, R. S., Ward, D., & Stock, G. M. (2010). Bedrock fracture control of glacial erosion processes and rates. Geology, 38(5), 423-426.

Fäh, D., Giardini, D., Kästli, P., Deichmann, N., Gisler, M., Schwarz-Zanetti, G., Alvarez-Rubio, S., Sellami, S., Edwards, B., Allmann, B., Bethmann, F., Wössner, J., Gassner-Stamm, G., Fritsche, S., & Eberhard, D. (2011). ECOS-09 Earthquake Catalogue of Switzerland Release 2011. Swiss Seismological Service ETH Zürich, Open-File Report 2011., SED/RISK/R/001/20110417.

Fox, M., Herman, F., Willett, S. D., & Schmid, S. M. (2016) .The exhumation history of the European Alps inferred from linear inversion of thermochronometric data. American Journal of Science, 316(6), 505-541.

Glotzbach, C., Reinecker, J., Danišík, M., Rahn, M., Frisch, W., & Spiegel, C. (2010). Thermal history of the central Gotthard and Aar massifs, European Alps: Evidence for steady state, long-term exhumation. Journal of Geophysical Research: Earth Surface, 115(F3), doi:10.1029/2009JF001304.

Glueer, F., Loew, S., Manconi, A., & Aaron, J. (2019). From toppling to sliding: progressive evolution of the Moosfluh Landslide, Switzerland. Journal of

Geophysical Research: Earth Surface, 124(12), 2899-2919.

Grab, M., Mattea, E., Bauder, A., Huss, M., Rabenstein, L., Hodel, E., Linsbauer, A., Langhammer, L., Schmid, L., Church, G., Hellmann, S., Délèze, K., Schaer, P., Lathion, P., Farinotti, D., & Maurer, H. (2021). Ice thickness distribution of all Swiss glaciers based on extended ground-penetrating radar data and glaciological modeling. Journal of Glaciology, 67(266), 1074-1092.

Hallet, B. (1996). Glacial quarrying: A simple theoretical model. Annals of Glaciology, 22, 1-8.

Harbor, J. M. (1992) Numerical modeling of the development of U-shaped valleys by glacial erosion. Geological Society of America Bulletin, 104(10), 1364-1375.

Herwegh, M., Berger, A., Glotzbach, C., Wangenheim, C., Mock, S., Wehrens, P., Baumberger, R., Egli, D., & Kissling, E. (2020). Late stages of continent-continent collision: timing, kinematic evolution, and exhumation of the Northern rim (Aar Massif) of the Alps. Earth-science reviews, 200, 102959 https://doi.org/10.1016/j.earscirev.2019.102959.

Kelly, M. A., Kubik, P. W., Von Blanckenburg, F., & Schlüchter, C. (2004). Surface exposure dating of the Great Aletsch Glacier Egesen moraine system, western Swiss Alps, using the cosmogenic nuclide 10Be. Journal of Quaternary Science: Published for the Quaternary Research Association, 19(5), 431-441.

Kühni, A., & Pfiffner, O. A. (2001). The relief of the Swiss Alps and adjacent areas and its relation to lithology and structure: topographic analysis from a 250-m DEM. Geomorphology, 41(4), 285-307.

Larsen, I. J., & Montgomery, D. R. (2012). Landslide erosion coupled to tectonics and river incision. Nature Geoscience, 5(7), 468-473.

MacGregor, K. R., Anderson, R. S., Anderson, S. P., & Waddington, E. D. (2000). Numerical simulations of glacial-valley longitudinal profile evolution. Geology, 28(11), 1031-1034.

Molnar, P., Anderson, R.S., & Anderson, S.P. (2007). Tectonics, fracturing of rock, and erosion. Journal of Geophysical Research, v. 112, F03014, doi: 10.1029/2005JF000433.

Moore, J. R., Sanders, J. W., Dietrich, W. E., & Glaser, S. D. (2009). Influence of rock mass strength on the erosion rate of alpine cliffs. Earth Surface Processes and Landforms, 34(10), 1339-1352.

Neely, A. B., DiBiase, R. A., Corbett, L. B., Bierman, P. R., & Caffee, M. W. (2019). Bedrock fracture density controls on hillslope erodibility in steep, rocky landscapes with patchy soil cover, southern California, USA. Earth and Planetary Science Letters, 522, 186-197.

Nibourel, L., Berger, A., Egli, D., Heuberger, S., & Herwegh, M. (2021). Structural and thermal evolution of the eastern Aar Massif: insights from structural field work and Raman thermometry. Swiss journal of geosciences, 114(1), 9.

Patton, H., Swift, D. A., Clark, C. D., Livingstone, S. J., & Cook, S. J. (2016). Distribution and characteristics of overdeepenings beneath the Greenland and Antarctic ice sheets: Implications for overdeepening origin and evolution. Quaternary Science Reviews, 148, 128-145.

Schlatter, A., Schneider, D., Geiger, A., & Kahle, H. G. (2005). Recent vertical movements from precise levelling in the vicinity of the city of Basel, Switzerland. International Journal of Earth Sciences, 94(4), 507-514.

Sibson, R. H. (1977). Fault rocks and fault mechanisms. Journal of the Geological Society, 133(3), 191-213.

Sklar, L. S., & Dietrich, W. E. (2001). Sediment and rock strength controls on river incision into bedrock. Geology, 29(12), 1087-1090.

Steinemann, O., Ivy-Ochs, S., Hippe, K., Christl, M., Haghipour, N., & Synal, H. A. (2021). Glacial erosion by the Trift glacier (Switzerland): Deciphering the development of riegels, rock basins and gorges. Geomorphology, 375, 107533.

Truttmann, S., Herwegh, M., Schreurs, G., Ebert, A., & Hardmeier, S. (2021). The effect of pre-existing structures on the Moosfluh landslide and its lateral propagation (Great Aletsch Glacier, Switzerland). Geomorphology, 377, 107530.

Valla, P. G., Shuster, D. L., & Van Der Beek, P. A. (2011). Significant increase in relief of the European Alps during mid-Pleistocene glaciations. Nature geoscience, 4(10), 688-692.

Wehrens, P., Berger, A., Peters, M., Spillmann, T., Herwegh, M. (2016). Deformation at the frictional-viscous transition: evidence for cycles of fluid-assisted embrittlement and ductile deformation in the granitoid crust. Tectonophysics, 693, 66–84.

Whipple, K.X, Hancock, G.S., & Anderson, R.S. (2000). River incision into bedrock: Mechanics and the relative effi cacy of plucking, abrasion, and cavitation. Geological Society of America Bulletin, v. 112, p. 490–503, doi: 10.1130/0016-7606(2000)112<0490:RIIBMA >2.3.CO;2.

CONCLUSION

In this thesis a methodology for the construction of an explicit large-scale 3D geological model of Alpine regions has been developed. In form of a pilot study, this approach allowed us to build a large-scale 3D geological model of the major lithostratigraphic and tectonic boundaries of the Aar Massif, incorporating field observations, outcrop-scale structural analysis, tunnel and literature data, maps and large-scale seismic profiles. In addition, the development of one coherent structural interpretation through the massif, coupled with the knowledge gained from 3D structural modelling, have provided fundamental insights into the 3D shape of today's massif. These efforts have allowed us to study the evolution of the entire massif, ranging from the paleogeographic precursor structures (Permo-Carboniferous and Mesozoic extensions), through the onset of the late Alpine collision (30 Ma), to the recent landscape-forming processes. The three scientific studies designed as part of this thesis have provided constructive answers to the three main questions posed at the beginning of the project:

1. *How do the geometry of the pre-collision passive margin, the rheology and density of the crust, as well as the inhibition/reactivation of inherited crustal structures influence the late-stage thick-skinned evolution of an orogen?*

    Explicit three-dimensional geological modelling, cross-section restoration coupled with metamorphic peak temperature data, allowed us to construct a 4D geodynamic evolution of the crystalline basement units of the Aar massif during the late-stage Alpine orogeny. Our results show that: (i) the Aar massif results from inversion of the proximal passive European margin, consisting of spatially complex asymmetric 3D rifting structures as manifested by laterally variable distribution of local half graben basins and a topographic high (Permian to the Mesozoic). (ii) At the onset of Alpine deformation (22 Ma), peak metamorphism was reached by burial at depths between -8 and -18 km with a horizontal geothermal gradient of 26°C/km. (iii) Exhumation of the basement units occurred in a distinct in-sequence deformation style. Inherited along strike variations in the thickness and density of the basement units induced a non-cylindrical exhumation of the massif by activation of dense networks of revers, thrust and strike-slip faults. Owing to complex interactions of these fault systems, today's shape of the massif evolved. The in-sequence non-cylindrical exhumation of the basement units was controlled by a crucial interplay between deep crustal dynamics and

structural inheritance in the middle to upper crust of the former European passive continental margin.

2. *What is the effect of inherited structures and along strike variations in the thickness of sedimentary units on the evolution of a fold-and-thrust belt?*

The 4D reconstruction of the emplacement of the Doldenhorn Nappe and the Western Aar Massif during the late-stage Alpine collision (30-0 Ma) has allowed a detailed representation of the 3D morphology and variability of a part of the former proximal passive continental margin, with particular emphasis on the sedimentary cover. Indeed, our reconstruction illustrates how variations in the thickness of sedimentary units, defined by the initial basement geometry, control the architecture of the developing fold-and-thrust belt. The non-cylindrical extension of the Doldenhorn Basin resulted from the reactivation of pre-existing crustal structures within the basement units. The asymmetric shape of the half-graben influenced the nature of the syn-tectonic sedimentary units within the basin, and caused fluctuations in thickness along the strike of the basin as well as thickening towards the footwalls of the extensional faults. During the incipient thin-skinned inversion of the Doldenhorn Basin, strain localization occurred within the mechanically weak sedimentary units at the basement-cover transition (e.g., shale-rich and evaporitic layers). Due to the varying topography of the basement-cover interface and the thickness of the sedimentary units, the resulting detachment horizon was localised along a single basal thrust in the west, whereas in the eastern regions of the basin it was split into an in-sequence set of thrusts, including imbricates of basement slices. The aforementioned variations in incipient basin sediment thicknesses correlate directly with today observable along-strike amplitude variation of the extruded Doldenhorn Nappe (large amplitude in the west; small amplitude in the east).

3. *To what extent is the efficiency of the erosive processes active in a mountain chain influenced by tectonic preconditioning due to deep-seated collision dynamics?*

Field-based rock hardness investigations were carried out along the valley of the Aletsch Glacier (Central Switzerland) to assess the susceptibility of landscape-scale valley morphology to variations in crystalline rock hardness and structural variability. The results showed that while lithological variations and rock foliation do not induce significant changes in rock

hardness, the presence of faults considerably reduces the bulk rock hardness. Variations in the orientation and frequency of faults are critical in controlling: (i) bedrock erosion processes; (ii) valley axis orientation and morphology; and (iii) the occurrence of hazardous mass movements. As a function of these structural parameters, the valley morphology responds with a non-uniform susceptibility to bedrock erosion, which is coupled to both bedrock channel and hillslopes erosion processes. In Alpine valleys, changes in the global climate system increase landscape disequilibrium and promote valley incision and relief development through both glacial and fluvial processes. However, the efficiency of erosional processes active in orogenic systems is closely related with the inherited collisional tectonic architecture. Indeed, nowadays exhumed former subsurface faults directly affect the efficiency of erosion in the mountain chain, elucidating an integral link between deep-seated collisional dynamics and surface based mountain shaping. Therefore, it is fundamental to include fault distribution and orientation in the characterising parameters of bedrock units to understand long-term landscape erosion patterns, which are essential for planning future hazard mitigation at a regional scale.

Ton conclude, all the work done and the obtained results in this PhD project highlight the importance of incorporating 3D considerations when investigating complex geological systems, such as a fold-and-thrust belt or even an entire orogen. The case of the Aar Massif and cover nappe has shown that extending single cross-sectional interpretations into the third dimension, allowed incorporating their substantial along-strike 3D variability. This has enabled us to gain a deep understanding of the evolution and dynamics of such systems.

Appendixes

Appendix A

Cross-section retrodeformation and paleogradient reconstruction

4D geodynamic evolution of the Aar Massif: deep dive into the upper crust of the European Alps

Ferdinando Musso Piantelli[1,2*], Lukas Nibourel[3], Alfons Berger[1], and Marco Herwegh[1]

[1] Institute of Geological Sciences University of Bern, Baltzerstrasse 1+3, 3012 Bern, Switzerland

[2] Federal Office of Topography swisstopo, Seftigenstrasse 264, 3084 Bern, Switzerland

[3] ETH Zürich, Dep. of Earth Sciences, Sonneggstrasse 5, 8092 Zürich, Switzerland

[*] Corresponding author: ferdinando.musso@geo.unibe

Geolgical Profile coordinates

Profile		Long.	Lat.
A-A'	A	2604690	1152818
	A'	2627340	1118096
B-B'	B	2626079	1166814
	B'	2647107	1134196
C-C'	C	2644283	1178708
	C'	2662489	1147231
D-D'	D	2666273	1192525
	D'	2682556	1161768
E-E'	E	2690006	1203758
	E'	2704486	1170118
F-F'	F	2709533	1211747
	F'	2723412	1179849
Viepoint 1	VieP.1	2634550	1150655
Viepoint 2	VieP.2	2713679	1185797
Viepoint 3	VieP.3	2676067	1173782

Table A1. Table containing the coordinates of the investigated profiles.

Cross-section restoration

In the following paragraph, we present the results of the retrodeformation of sections A-A', B-B', C-C', E-E', and F-F'(Fig. A1 to A5) as evolutionary steps, starting from the initiation of Alpine deformation (22 Ma) to the present-day configuration. For the description of the deformation and emplacement of the Aar Massif, see the Results and Discussion chapters (4 and 5).
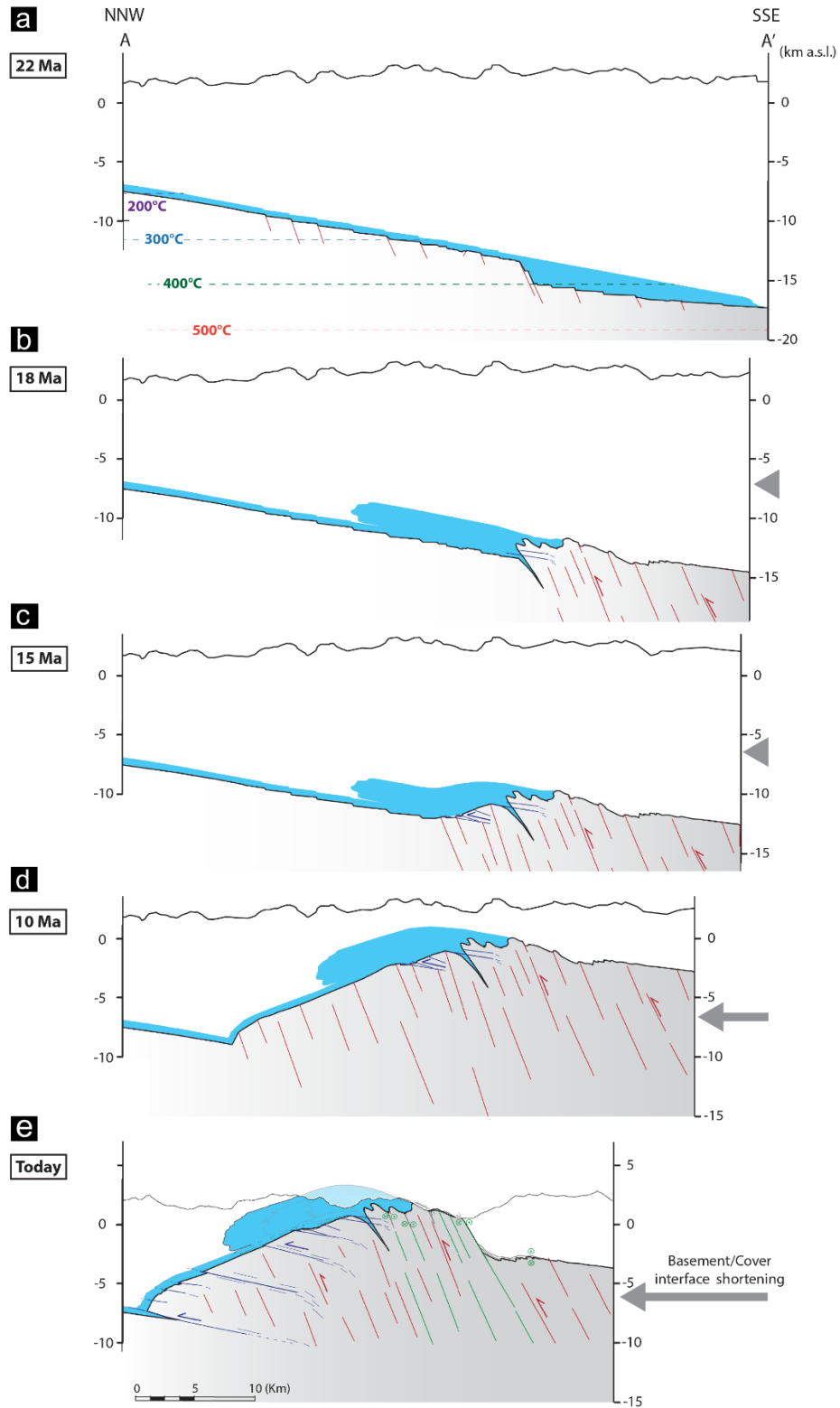
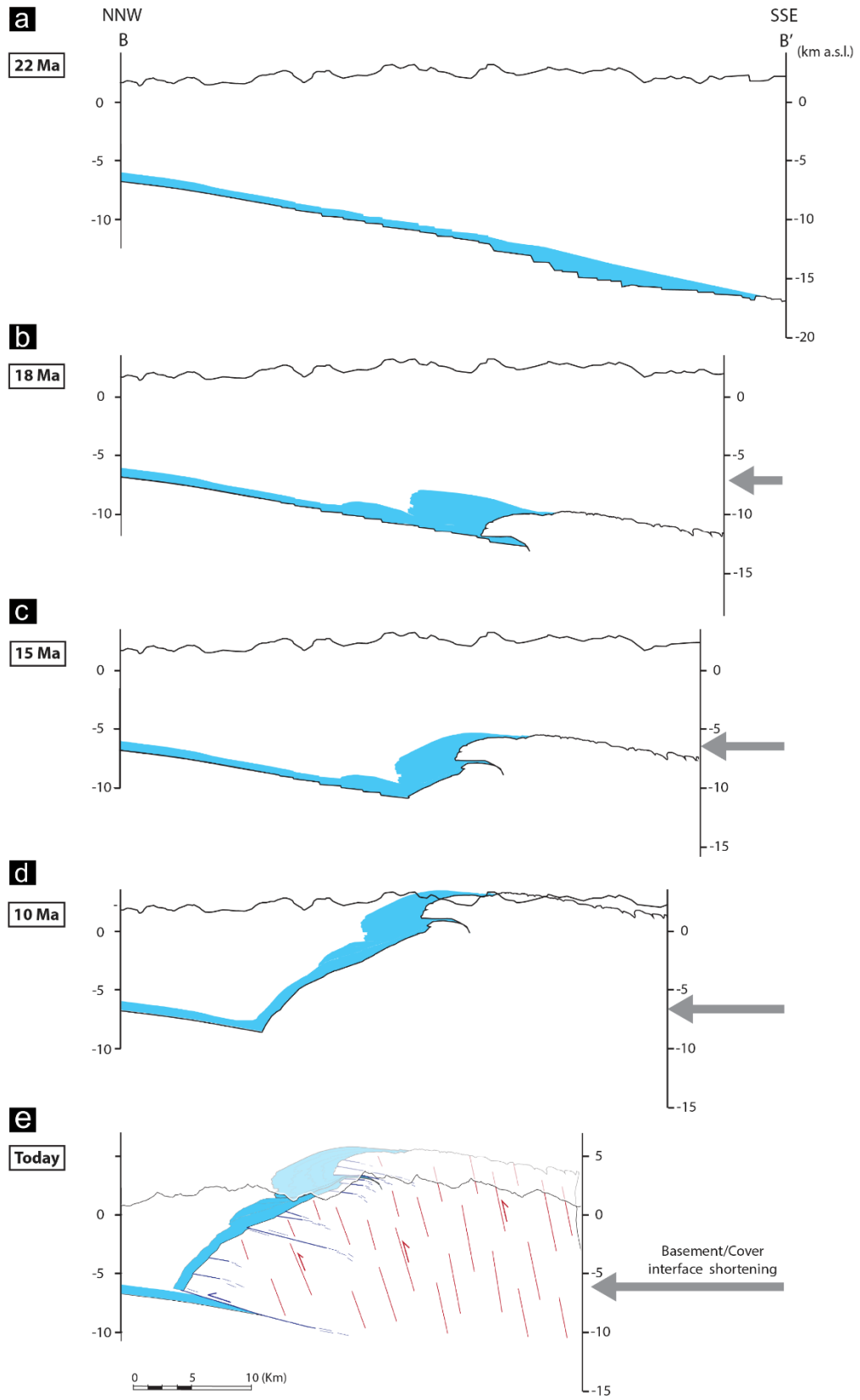**Figure A1** – Cross-section restoration of the AA' section from 22 Ma to today.

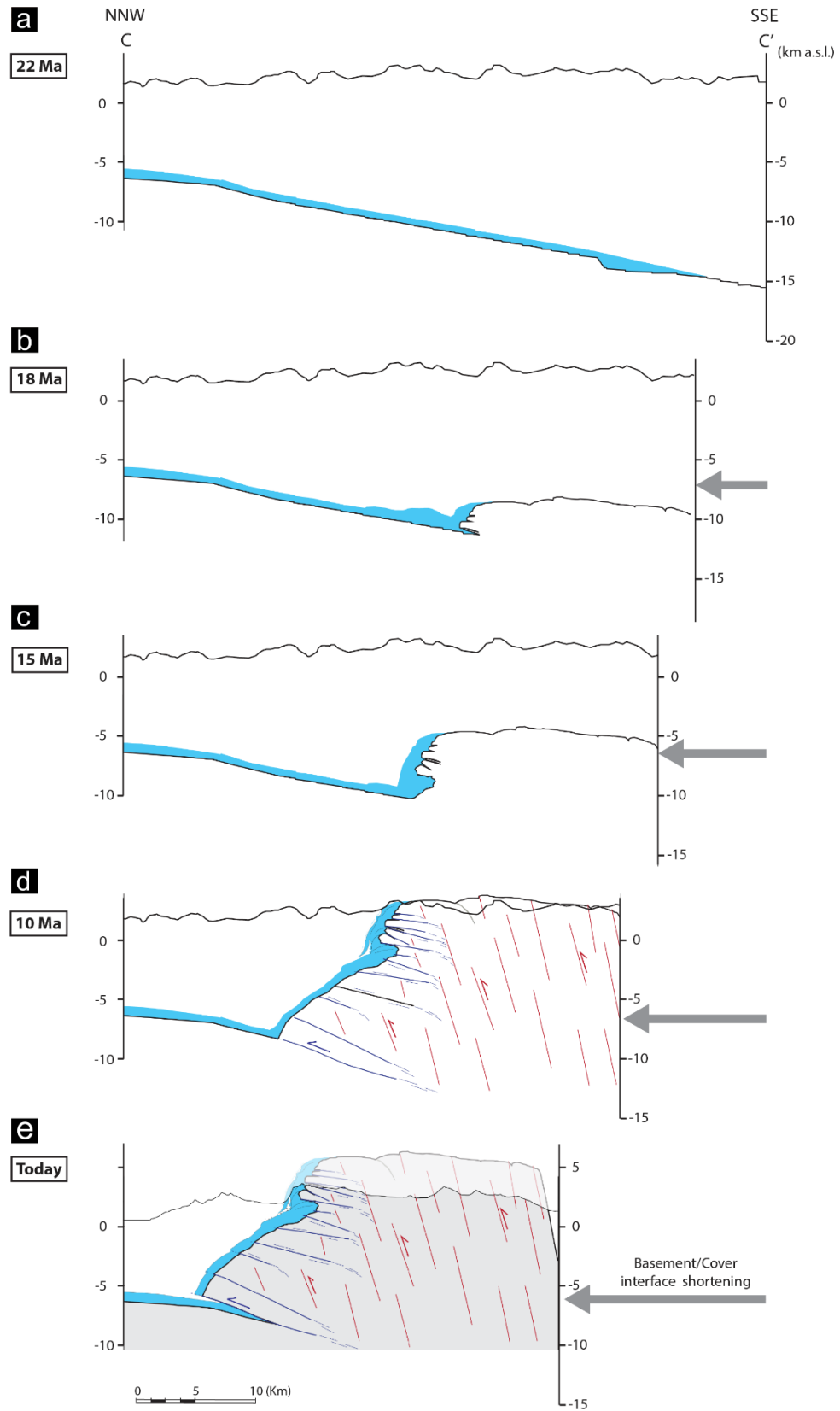**Figure A2** – Cross-section restoration of the BB' section from 22 Ma to today.

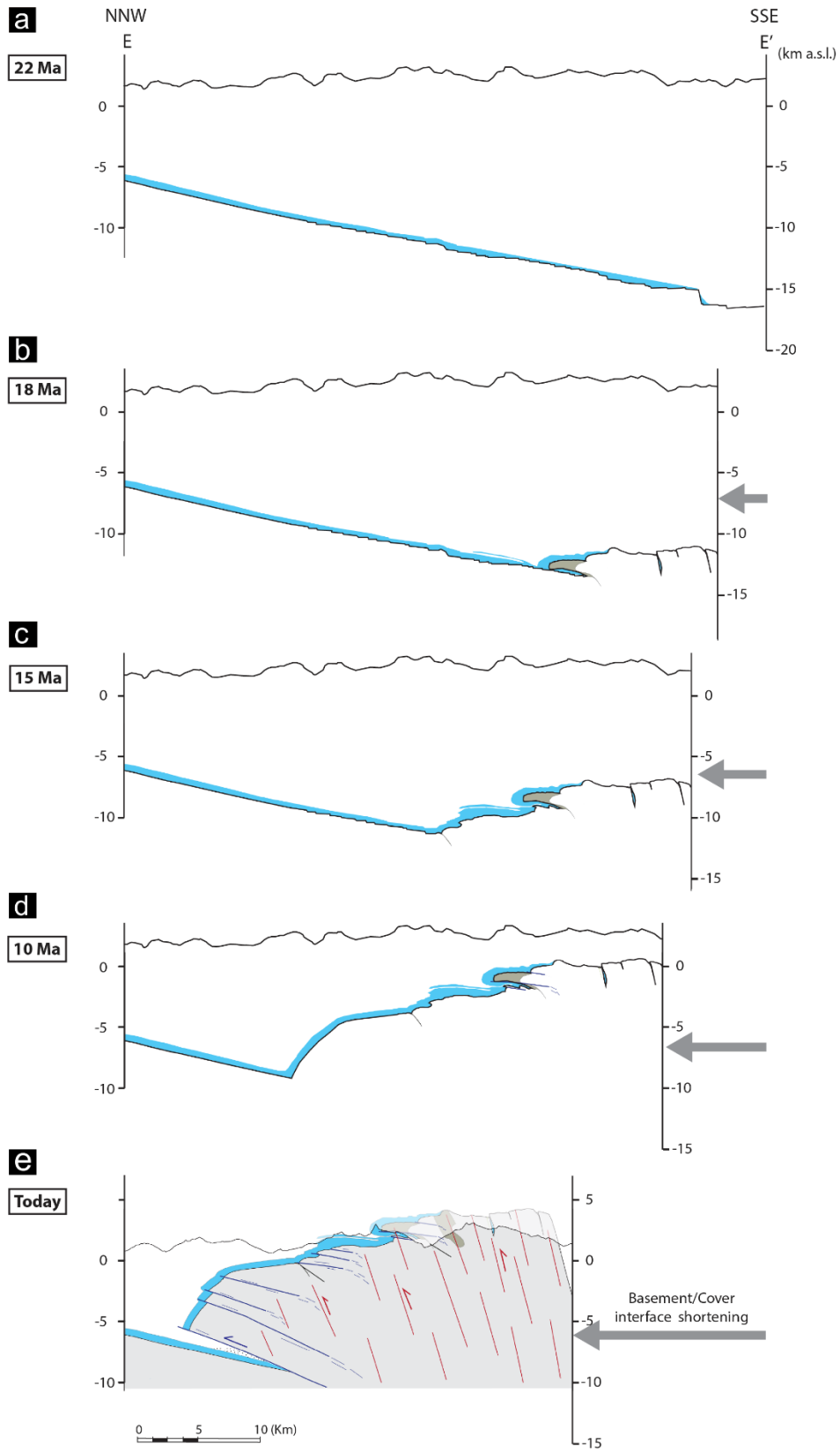**Figure A3** – Cross-section restoration of the CC' section from 22 Ma to today.

Figure A4 – Cross-section restoration of the EE' section from 22 Ma to today.
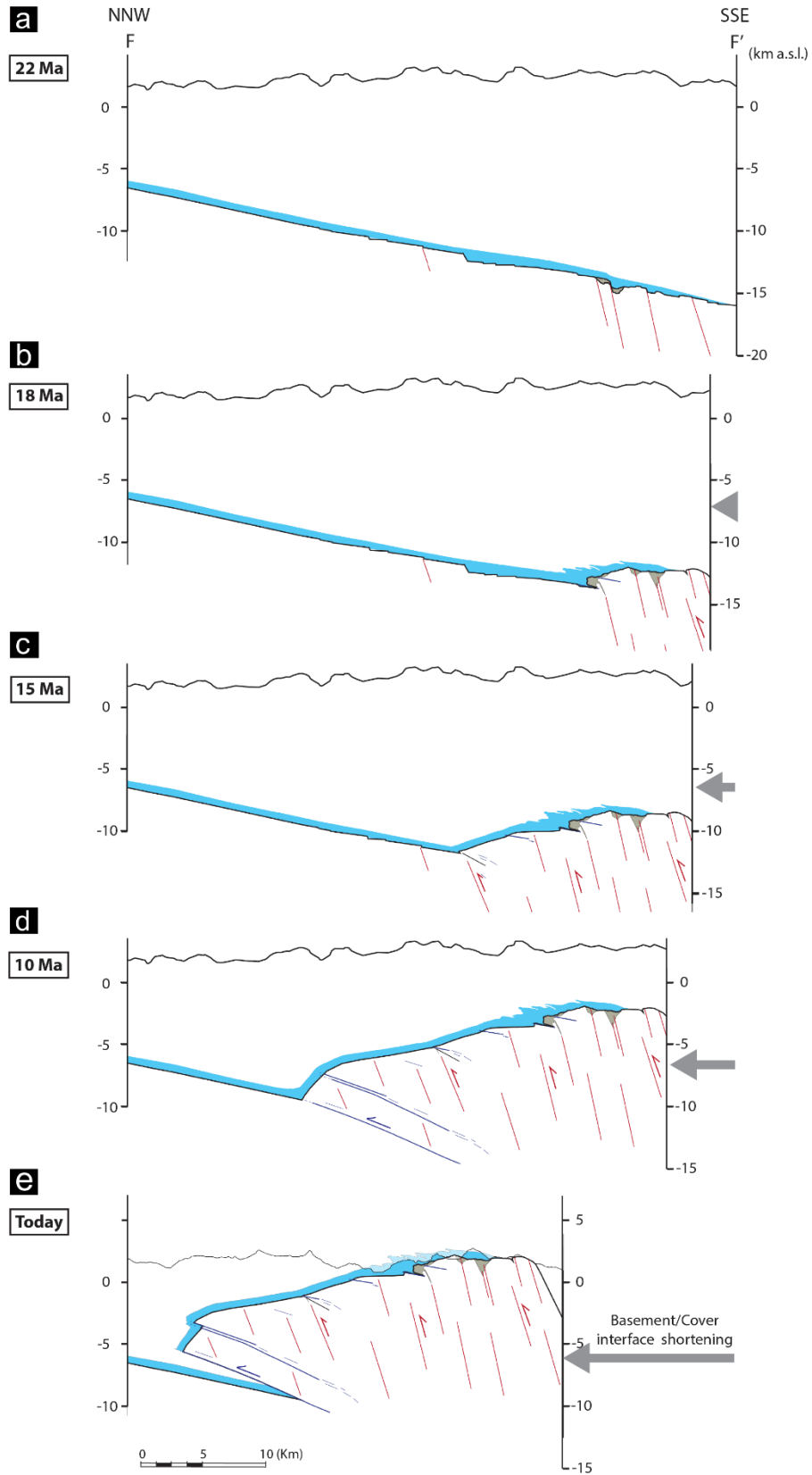
Figure A5 – Cross-section restoration of the FF' section from 22 Ma to today.
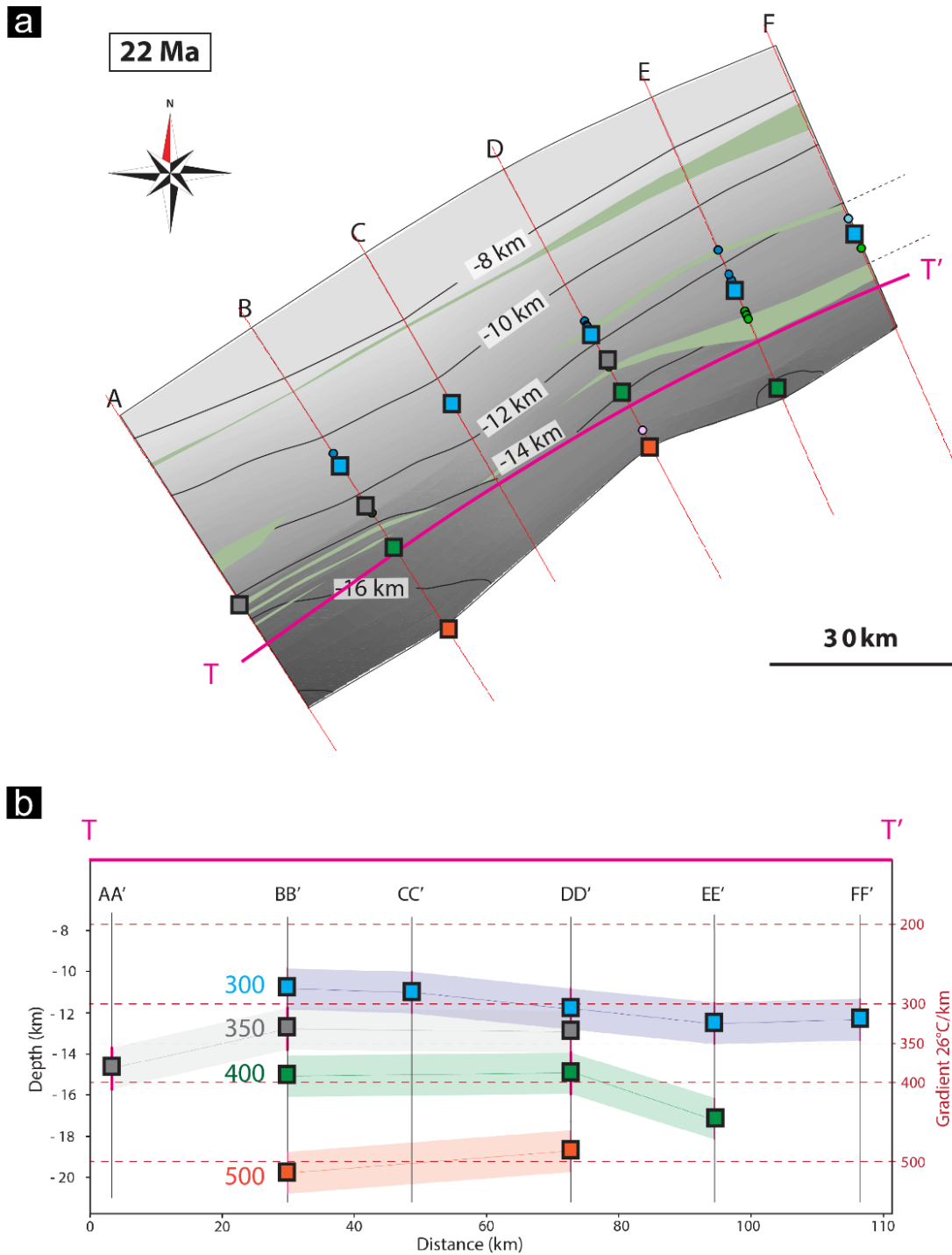
Paleogradient reconstruction

Figure A6 – (a) Map view of the part of the top basement of the passive margin at 22 Ma, from which the Aar Massif developed. The points lying on the cross section traces correspond to the location of the Tmax data retrodeformed with the cross sections. (b) Cross-section TT' where the Tmax data have been normally projected and interpolated with a 26°C/km horizontal geothermal gradient.

The compilation of peak temperature data of Nibourel et al. 2021 (see references therein) was selected for this study to strengthen our cross-section restoration and 4D reconstruction. Each data point located within 4 km on either side of the six cross sections (AA' to FF'; Fig. 2.1) and in close proximity to the sedimentary-basement contact, was selected and incorporated into our reconstruction. This results in a dataset of 50 peak temperature datapoints, which is included in this appendix as Attachment 2 (see additional information and references therein).

These datapoints were normally projected onto the respective profiles. During the subsequent retrodeformation, the datapoints were also retrodeformed up to 22 Ma. We have therefore reconstructed the position of the Tmax datapoint at 22 Ma. The resulting reconstruction is shown in map view in Figure A6a, where the upper basement and Tmax points are located. Consequently, along each profile, where possible, the 300, 350, 400 and 500°C points have been extrapolated or calculated along the shortest connecting lines between the data points. The 300, 350, 400 and 500°C points, with a relative uncertainty of ±50°C, were then normally projected SW-NE along the TT' profile Fig. A6b. Along the resulting profile the gradient of 26°C/km was calculated as the best fitting gradient.

Appendix B1

Geological data compilation and 2D mapping

4D reconstruction of the Doldenhorn nappe-basement system in the Aar massif: iInsights into late-stage continent-continent collision in the Swiss Alps

Ferdinando Musso Piantelli[1*], David Mair[1], Alfons Berger[1], Fritz Schlunegger[1], Michael Wiederkehr[2], Eva Kurmann[2], Roland Baumberger[2], Andreas Möri[2] and Marco Herwegh[1]

[1] Institute of Geological Sciences University of Bern, Baltzerstrasse 1+3, 3012 Bern, Switzerland

[2] Federal Office of Topography swisstopo, Seftigenstrasse 264, 3084 Bern, Switzerland

1   Geological data compilation, mapping, and fieldwork

To build a 3D model of the investigated area, the geological bedrock mapping has been conducted at the scale of 1: 25 000 in ArcGIS (ESRI's ArcGIS, v.10.8) software by compiling and homogenizing a two-dimensional dataset of polylines of the major stratigraphic and tectonic boundaries of the bedrock units (Fig. B1). The initial dataset was compiled from the following pre-existing maps: Krebs (1925), Collet and Paréjas (1928), Mair et al. (2018), and the GeoCover vector dataset (swisstopo) LK: 1228, 1229, 1247, 1248, 1249, 1267, 1268, 1269, 1287, 1288, and 1289. Furthermore, the Geological Special Map 1:100 000 of the Aar Massif, Tavetsch, and Gotthard Nappes of the Swiss Geological Survey (Berger et al., 2017) were used to understand the geological architecture at the regional scale and to define the legend of the map. Due to discrepancies between the individual map sheets, the entire dataset underwent a validation and homogenization procedure to generate a geologically consistent map of the entire area. This was accomplished using high-resolution orthophotos (SwissImage with a raster resolution of 0.25 x 0.25 m; provided by swisstopo), a high-resolution digital elevation model (DEM) (swiss ALTI3D with a downsampled raster resolution of 2 x 2 m, version 2013 provided by swisstopo), and hillshade maps, which served to verify and update geological boundaries and structures. In the case of Quaternary coverage (e.g., moraine deposits, glaciers) the underlying trends of stratigraphic and tectonic boundaries were interpreted providing a uniform bedrock map. Moreover, a lineament map was generated on remotely sensed images to expand the structural dataset following the workflow of Baumberger et al. (2022). A dataset of 442 structural measurements of the Alpine deformation phases (Kiental, Handegg, Pfaffenchopf, and Oberaar; see Table 1 and references therein) (orientation of fault/shear zone planes and stretching lineation) was compiled in the area from the Geocover Vector dataset (measurements N°: 395) and Mair et al. 2018 (measurements N°: 47).
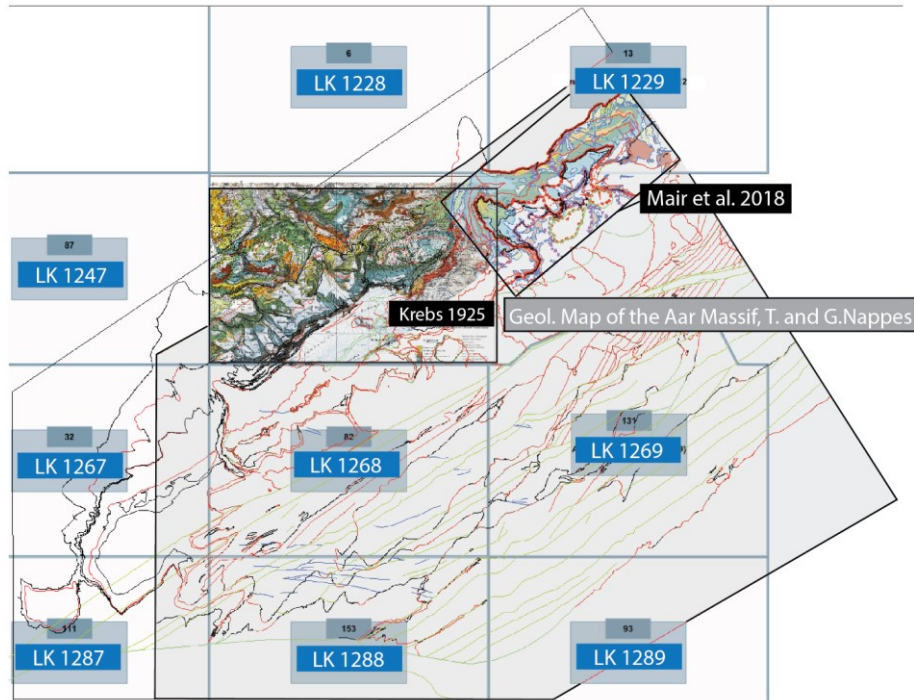
Figure B1 – Map overview of the compiled maps used as starting dataset and resulting polylines dataset of the major stratigraphic and tectonic boundaries.

For this study, during fieldwork at key-locations, additional 684 structural measurements were collected (Fig. B2).

Stratigraphic data are conform to the Lithostratigraphic Lexicon of Switzerland (https://www.strati.ch / en / tectonic/ aar-gastern /aar-massiv) and were compiled from: Krebs, 1925; Masson et al., 1980; Krayenbuhl and Steck, 2009; Ziegler and Isler, 2013; Mair et al., 2018 (see also references therein). Some detailed facies descriptions and discussion of fossils' founding can be found in the original literature (Krebs 1925; Masson et al., 1980 and references therein). However, this information can only be interpreted with caution as their stratigraphic position is contradicting modern stratigraphic interpretations. Unfortunately, there is little modern data on detailed stratigraphy in the Doldenhorn contrary to the studies in the eastern Aar Massif (Gisler et al. 2007).

2   Permo-Carboniferous and sediment wedges as extensional feature markers

The investigated area is located on the western edge of the Aar Massif of which the crystalline basement units outcrop for more than 2000 km^2 of the central Alps of Switzerland. Along the strike of the massif, narrow steep Permo-Carboniferous to Cenozoic sediments are locally preserved in WSW-ENE-trending wedges, synclines, or graben-related structures (e.g., Heim and Heim, 1916; Morgenthaler, 1921; Rohr, 1926; Muller and Arbenz 1938; Burkhard 1988; Kammer 1989; Pfiffner 2015; Berger et al., 2017b; Herwegh et al., 2020; Nibourel et al., 2021). Among such numerous zones stand out: the Tödi zone (Nibourel et al., 2021); the Windgällen-Färnigen zone (Nibourel et al., 2021); the Pfaffenchopf zone (Rohr, 1926) the Dossenkeil (Rohr, 1926); the Wetterhorn zone (Rohr, 1926); the Rote-Kuh-Gampel zone (Berger et al. 2013 and reference therein); and the
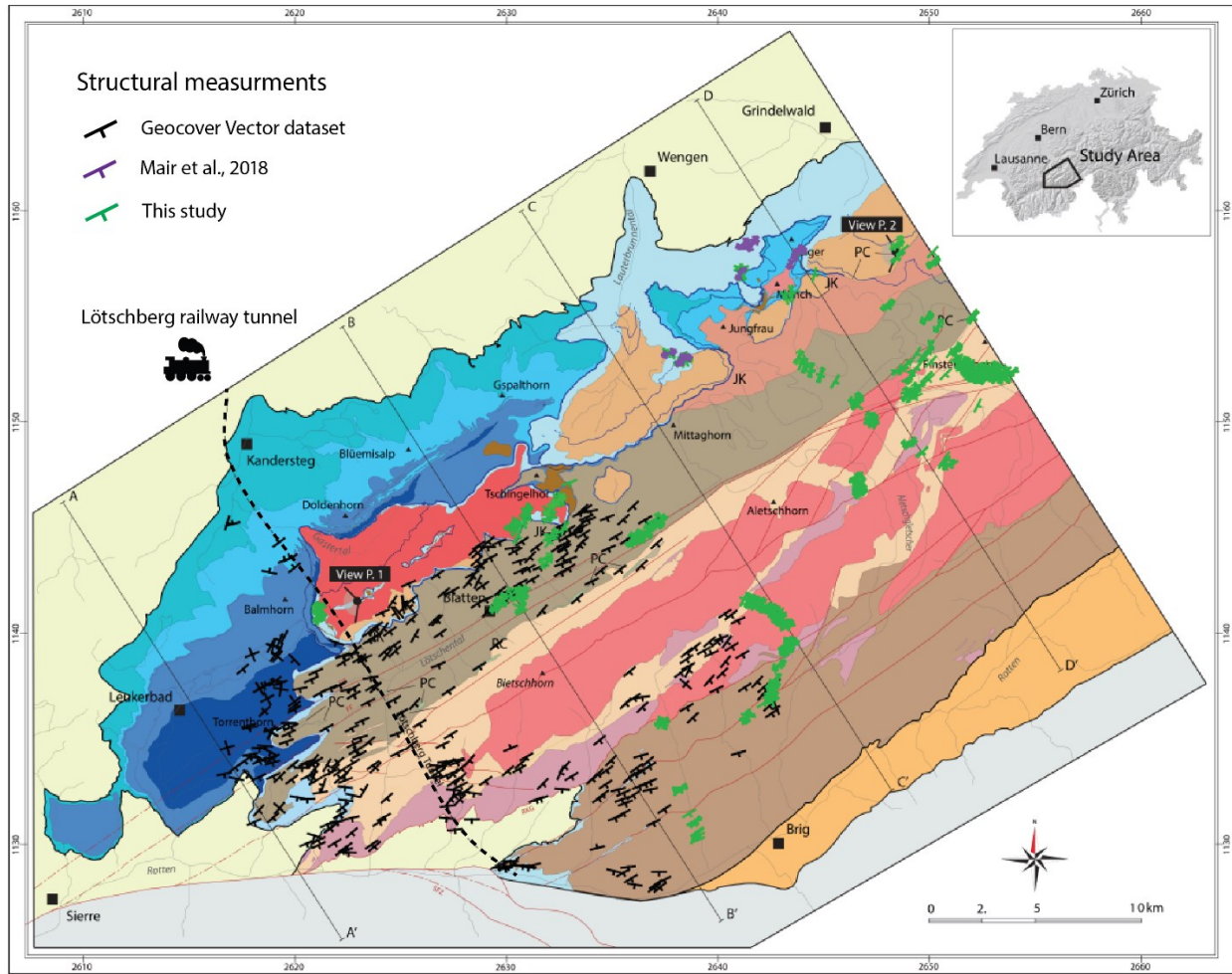
Figure B2 – Map view of the distribution of the compiled and collected geological structural measurements in the area.

Jungfrau Keil (Krayenbuhl and Steck 2009; this study). The occurrence of these wedges is aligned along specific intensively deformed domains of the massif, persistent and traceable over the entire strike of the massif (see Berger et al. 2017a). In addition to these preserved examples, aligned along such domains lay numerous narrow wedges of incomplete sequences of Permo-Carboniferous to Cenozoic sediments pinched between the crystalline basement units (e.g., Agassizjoch; see Fig. B3). The non-cylindrical exhumation and consequent erosion of the basement units coupled with the variation in the lateral extent of such wedges resulted in a different degree of exposure of the latter. As an example, different degrees of erosion of the Färnigen zone have been

simulated in the sketch of Fig. B4. Indeed, different levels of erosion might have left outcropping the lower section of the half graben sequence (Fig. B4b); or only the Permo-Carboniferous sediments (Fig. B4c). Consequently, the narrow stripes of Permo-Carboniferous and sediments currently outcropping in the Aar massif might represent the lower portion of eroded former wider extensional half grabens that during the last Alpine collision have been inverted and wedged into the basement units. Furthermore, observation of early Jurassic half graben extensional structures localized within Permo-Carboniferous sediments (Nibourel et al., 2021) support the hypothesis that such rheological heterogeneities played a first-order
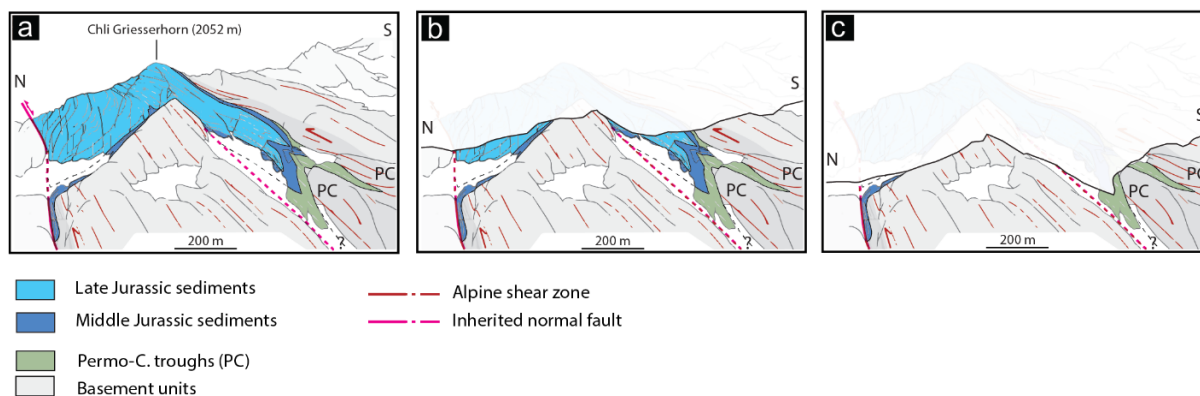
Figure B3 – (A) Map of the investigated area where the numerous Permo-Carboniferous (green) and sediments (blue) wedges have been highlighted. (B) (field location indicated as B in plate A; Coordinates: Long.: 8°03'52"/ Lat.: 46°32'58"). Fine-to coarse-grained clastic metasedimentary rocks with volcanoclastic intercalations observed in this study belonging to the Trift Fm. of the Permo-Carboniferous units (Berger et al., 2017). (C) (field location indicated as C in plate A; Coordinates Long.: 08°07'2"/ Lat.: 46°32'38") Permo-Carboniferous sediments of the Trift Fm. (Berger et al., 2017) observed in this study along the crest of the Finsteraarhorn (4274 m.a.s.l.). The sediments, intensively deformed, are pinched between two gneiss units of the crystalline basement.

146

Figure B4 – Sketch of simulation of different degrees of future erosion of the Färnigen zone (modified after Nibourel et al., 2021). (A) Profile-like view of the current outcropping condition of the Färnigen zone. The zone comprises two synformal sediment wedges, bounded by two early Jurassic normal faults (violet), and associated Permo-Carboniferous sediments. The former half-graben geometry is still recognizable. (B) Progressive erosion might cut out the upper portion of the wedges, leaving two smaller-scale separated sediment and Permo-Carboniferous wedges. (C) Proceeding with erosion the synformal sediment wedges are entirely cut out, leaving three narrow stripes of Permo-Carboniferous and Middle Jurassic sediments. Note the link between stage c and relics of sediments appearing in wedges along faults in Fig. B3a.

control in localizing extensional deformation. Indeed, numerical models (e.g., Lafosse et al., 2016; Balàzs et al., 2017) indicate that in extensional regimes at shallow crustal level (i.e. at low temperatures) pre-existing extensional structures display a high competence contrast and localize deformation. In this study, therefore, the location of Permo-Carboniferous zones and sediment wedges (Fig. B3) served as a marker allowing us to reconstruct the locations of syn-rift faults utilized during the aperture of the Doldenhorn Basin.

During the Alpine inversion (from ~22 Ma onwards; Handegg phase, see Table 1), due to the generation of several steeply south-dipping brittle-ductile reverse faults and shear zones at the footwall of not significantly reactivated normal faults (see Lafosse et al. 2016 and Nibourel et al. 2021), such extensional grabens were locally pinched in synformal sediment wedges. At the scale of the former European passive continental margin, such narrow sediment wedges are prominent features in the eastern External Crystalline Massifs (e.g Mont Blanc/Aiguilles Rouge, and the Aar/Gastern

Massifs; e.g., Bellashen et al., 2014; Nibourel et al., 2021a; Herwegh et al., in press), while they are lacking in the western ones (Argentera, Oisans and Belledonne Massifs; e.g., Bellahsen et al., 2014). The occurrence of such thin sediment wedges is attributed to a combination of the following parameters: (i) aforementioned evolution of subvertical reverse faults during compression of former extensional basins, (ii) ratios >1 of vertical/horizontal displacement components, (iv) the amount of accommodated strain and (iv) the temperature conditions during inversion. Parameters (i-iii), particularly (i), are difficult to explain by horizontal shortening only (see Herwegh et al., 2017). In addition to a pure horizontal shortening, these authors, therefore, suggested the need for an additional buoyancy-induced vertical component (see below). In terms of (iv), 2D thermomechanical modelling conducted by Lafosse et al. (2016) showed how increasing temperature and tectonic burial inhibit inherited normal fault reactivation favouring distributed deformation beneath the basin.

147

3 Basement steep reverse faulting VS 'basement folding'

The trace line of the basement-cover contact (Figs. 3.7c and 3.8c, see basement-cover contact trace), particularly in the case of the aforementioned sediment wedges, observable in the investigated area and in the External Crystalline massifs motivated a variety of studies to infer 'basement folding' as major deformation process (e.g., Heim, 1922; Ramsay et al., 1983; Ford, 1996; Giba, 2016; Krayenbuhl and Steck, 2009). However, peak metamorphic temperatures were too low (<400°; Herwegh and Pfiffner, 2005; Berger et al., 2020; Girault et al., 2020) to allow for a pervasive ductile deformation of the granitoid basement units required to induce pervasive basement folds. Instead, field evidence demonstrates that the steep Handegg shear zones formed a 3D network, which enclosed un- to weakly deformed basement blocks (Steck, 1968; Choukroune and Gapais, 1983; Wehrens et al., 2016, 2017). A variety of recent studies reveals this deformation style to be rather common for basement rocks experiencing greenschist facies metamorphic conditions (e.g., Bellahsen et al., 2012; Bellanger et al., 2014; Boutoux et al., 2016; Lafosse et al., 2016). Such shear zones do not consist anymore of coarse-grained granitic or gneissic rock fabrics but rather of ultrafine-grained polymineralic ultramylonites being mechanically weaker compared to their hosts (Fig. 3.11, see dashed curve). In this sense, this network of steep Handegg-type shear zones, accommodating reverse faulting, allowed for a vertical differential shearing and rock uplift. Consequently, the basement-cover contact acted as a passive marker line, which was bulged upward by this shearing-induced deformation.

4 Tectonic cross-sections

The Construction of geological cross-sections is a crucial step to connect the second and third dimensions. The four NNW – SSE striking geological cross-sections (A – A'; B – B'; C – C'; and D - D' in the area; see fig A2 for traces) constructed over the area have been designed to be perpendicular to the strike of the large-scale structures and boundaries and therefore to be at the most representative of the regional underground geology.

Sections coordinate Points (EPSG: 4326 WGS 84):

A (Long.: 7°33'18"/ Lat.: 46°28'2") A' (Long.: 7°43'42"/ Lat.: 46°16'55")

B (Long.: 7°43'36"/ Lat.: 46°32'26") B' (Long.: 7°57'412"/ Lat.: 46°17'19")

C (Long.: 7°58'1"/ Lat.: 46°35'19") C' (Long.: 8°3'54"/ Lat.: 46°20'36")

D (Long.: 7°56'53.192"/ Lat.: 46°38'11.184") D' (Long.: 8°10'19.36"/ Lat.: 46°23'43.39")

For the construction of the cross-sections, surface and contacts line intersections were collected in the software Move™ (Petex, v.2019.1). Dip-data information, as well as tectonic boundaries in the vicinity (2000 m) of the cross sections, were projected onto the latter to better constrain the geometric and structural relationships of the different units.

A set of profiles produced by Collet and Paréjas (1931), Hänni and Pfiffner (2001), Herwegh and Pfiffner, (2005), Krayenbuhl and Steck (2009), and Mair et al., (2018) as well as the data coming from the construction of the Lötschberg railway tunnel (see the trace in Fig. B2, Ziegler and Isler, 2013) and seismic studies (Pfiffner et al. 1997) were used as a basis or the construction of the profiles. Coordinates of the viewpoints of Fig. 3.3:

1 (Long.: 7°43'20"/ Lat.: 46°25'18"); 2 (Long.: 8°04'06"/ Lat.: 46°34'05. ")

REFERENCES

Balázs, A., Burov, E., Matenco, L., Vogt, K., Francois, T., Cloetingh, S., 2017. Symmetry during the syn- and post-rift evolution of extensional back-arc basins: The role of inherited orogenic structures. Earth and Planetary Science Letters, 462, 86-98.

Baumberger, R., Herwegh, M., Kissling, E., 2022. Remote sensing and field data based structural 3D modelling (Haslital, Switzerland) in combination with uncertainty estimation and verification by underground data. 3D Digital Geological Models: From Terrestrial Outcrops to Planetary Surfaces, 159-197.

Bellahsen, N., Jolivet, L., Lacombe, O., Bellanger, M., Boutoux, A., Garcia, S., Mouthereau, F., Le Pourhiet, L., Gumiaux, C., 2012. Mechanisms of margin inversion in the external Western Alps: Implications for crustal rheology. Tectonophysics 560, 62–83.

Bellahsen, N., Mouthereau, F., Boutoux, A., Bellanger, M., Lacombe, O., Jolivet, L., Rolland, Y., 2014. Collision kinematics in the western external Alps. Tectonics, 33(6), 1055-1088.

Bellanger, M., Bellahsen, N., Jolivet, L., Baudin, T., Augier, R., Boutoux, A., 2014. Basement shear zones development and shortening kinematics in the Ecrins Massif, Western Alps. Tectonics 33, 84-111.

Berger, A., Mercolli, I., Herwegh, M., and Gnos E.: Geological Ma of the Aar Massif, Tavetsch and Gotthard Nappes 1 : 100 000, Federal Office of Topography Swisstopo, Wabern, 2017a

Berger, A., Wehrens, P., Lanari, P., Zwingmann, H., Herwegh, M., 2017b. Microstructures, mineral chemistry and geochronology of white micas along a retrograde evolution: An example from the Aar massif (Central Alps, Switzerland). Tectonophysics, 721, 179-195.

Berger, A., Engi, M., Erne-Schmid, S., Glotzbach, C., Spiegel, C., de Goede, R., Herwegh, M., 2020. The relation between peak metamorphic temperatures and subsequent cooling during continent–continent collision (western Central Alps, Switzerland). Swiss journal of geosciences, 113(1), 1-18.

Boutoux, A., Bellahsen, N., Lacombe, O., Verlaguet, A., Mouthereau, F., 2014. Inversion of pre-orogenic extensional basins in the external Western Alps: structure, microstructures and restoration. Journa of Structural Geology 60, 13–29.

Burkhard, M., 1988. L'Helvétique de la bordure occidentale du massif de l'Aar (évolution tectonique et métamorphique). Eclogae Geologicae Helvetiae 81, 63–114.

Caumon, G., Lepage, F., Sword, C. H., Mallet, J. L., 2004. Building and editing a sealed geological model. Mathematical Geology, 36(4), 405-424.

Choukroune, P., Gapais, D., 1983. Strain patterin in the Aar granite (Central Alps): orthogneiss developed by bulk inhomogeneous flattening. Journal of Structural Geology 5, 411-418.

Collet, L. and Paréjas, E.: Carte géologique de la chaîne de la Jungfrau, 1:25 000, Francke, Bern, 1928.

Collet, L. and Paréjas, E.: Géologie de la chaîne de la Jungfrau, Beiträge zur Geol. Karte der Schweiz, N.F. 63, Francke, Bern, 1931.

Ford, M., 1996. Kinematics and geometry of early Alpine, basement-involved folds, SW Pelvoux Massif, SE France. Eclogae Geologicae Helvetiae 89, 269-295.

Giba, M.O., 2006. Strukturelle Kartierung am Nordrand des Aarmassivs, Berner Oberland. Master thesis Albert-Ludwigs-Universität, Freiburg im Breisgau.

Girault, J.B., Bellahsen, N., Boutoux, A., Rosenberg, C., Nanni, U., Verlaguet, A., Beyssac, O., 2020. 3D thermal structure of the Helvetic nappes of the European Alps: implications for collisional processes. Tectonics. doi: 10.1029/2018TC005334.

Gisler, C., Hochuli, P. A., Ramseyer, K., Bläsi, H., & Schlunegger, F., 2007. Sedimentological and palynological constraints on the basal Triassic sequence in Central Switzerland. Swiss Journal of Geosciences,100 (2), 263–272.

Hänni, R., Pfiffner, O. A., 2001. Evolution and internal structure of the Helvetic nappes in the Bernese Oberland. Eclogae Geologicae Helvetiae, 94(2), 161-171.

Heim, A., 1922. Geologie der Schweiz. volume 2. CH Tauchnitz.

Heim, A., & Heim, A., 1916. Die Juramulde bei Fernigen (Uri). Vjschr. natf. Ges. Zürich,61(3–4), 503–530

Herwegh, M., Pfiffner, O.-A., 2005. Tectono-metamorphic evolution of a nappe stack: A case study of the Swiss Alps. Tectonophysics 404 (1-2), 55–76.

Herwegh, M., Berger, A., Glotzbach, C., Wangenheim, C., Mock, S., Wehrens, P., Baumberger, R., Egli, D., Kissling, E., 2020. Late stages of continent-

continent collision: Timing, kinematic evolution, and exhumation of the Northern rim (Aar Massif) of the Alps. Earth-science reviews, 200, 102959.

Kammer, A., 1989. Alpidische Verformung des aarmassivischen Nordrandes. Schweizerische mineralogische und petrographische Mitteilungen,69(1), 37–53.

Krayenbuhl, T. and Steck, A.: Structure and kinematics of the Jungfrau syncline, Faflertal (Valais, Alps), and its regional significance, Swiss Journal of Geosciences, 102, 441–456, https://doi.org/10.1007/s00015-009-1333-1, 2009.

Krebs, J.: Geologische Beschreibung der Blümlisalp-Gruppe, Beiträge zur Geol. Karte der Schweiz, N.F. 54, Francke, Bern, 1925.

Lafosse, M., Boutoux, A., Bellahsen, N., Le Pourhiet, L., 2016. Role of tectonic burial and temperature on the inversion of inherited extensional basins during collision. Geological Magazine 153, 811-826.

Mair, D., Lechmann, A., Herwegh, M., Nibourel, L., Schlunegger, F., 2018. Linking Alpine deformation in the Aar Massif basement and its cover units–the case of the Jungfrau–Eiger Mountains (Central Alps, Switzerland). Solid Earth 9, 1099–1122.

Masson, H., Herb, R., and Steck, A.: Helvetic Alps of Western Switzerland, Excusion no. 1, in: Geology of Switzerland – a guide book, Part B, Geological Excursions, edited by: Trümpy, R., 109–153, Wepf & Co, Basel, 1980.

Morgenthaler, H., 1921. Petrographisch-tektonische Untersuchungen am Nordrand des Aarmassivs. AAPG Bulletin,16(1), 179–217.

Müller, F., Arbenz, P., 1938. Geologie der Engelhörner, der Aareschlucht und der Kalkkeile bei Inntertkirchen: Berner Oberland: mit 11 Textfiguren und VIII Tafeln. Francke.

Nibourel, L., Berger, A., Egli, D., Heuberger, S., Herwegh, M., 2021. Structural and thermal evolution of the eastern Aar Massif: insights from structural field work and Raman thermometry. Swiss journal of geosciences, 114(1), 1-43.

Pfiffner, O.A., Lehner, P., Heitzmann, P., Mueller, S., Steck, A., 1997a. Deep structure of the swiss Alps: results of NRP 20. Birkauser 1–380.

Pfiffner, O.A., 2015. Geologie der Alpen. volume 8416. UTB

Ramsay, J.G., Casey, M., Kligfield, R., 1983. Role of shear in development of the Helvetic fold-thrust belt of Switzerland. Geology 11, 439–442.

Rohr, K., 1926. Stratigraphische und tektonische Untersuchungen der Zwischenbildungen am Nordrand des Aarmassivs (zwischen Wendenjoch und Wetterhorn). Beiträge zur Geologischen Karte der Schweiz, NF 57.

Steck, A., 1968. Die alpidischen Strukturen in den zentralen Aaregraniten des westlichen Aarmassivs. Eclogae Geologicae Helvetiae 61, 19-48.

Wehrens, P., Berger, A., Peters, M., Spillmann, T., Herwegh, M., 2016. Deformation at the frictional-viscous transition: Evidence for cycles of fluid-assisted embrittlement and ductile deformation in the granitoid crust. Tectonophysics, 693, 66-84.

Wehrens, P., Baumberger, R., Berger, A., Herwegh, M., 2017. How is strain localized in a meta-granitoid, mid-crustal basement section? Spatial distribution of deformation in the central Aar massif (Switzerland). Journal of structural geology, 94, 47-67.

Ziegler, H. J., Isler, A., 2013. Lötschberg-Basistunnel: zusammenfassender geologischer Schlussbericht. Bundesamt für Landestopografie swisstopo.

Appendix B2

Cross-section restoration and Doldenhorn Basin reconstruction

4D reconstruction of a nappe-basement system: insights into late-stage continent-continent collision

Ferdinando Musso Piantelli[1*], David Mair[1], Alfons Berger[1], Fritz Schlunegger[1], Michael Wiederkehr[2], Eva Kurmann[2], Roland Baumberger[2], Andreas Möri[2] and Marco Herwegh[1]

[1] Institute of Geological Sciences University of Bern, Baltzerstrasse 1+3, 3012 Bern, Switzerland

[2] Federal Office of Topography swisstopo, Seftigenstrasse 264, 3084 Bern, Switzerland

1 Introduction

Despite many similarities among fold-and-thrust belts in general, there subsist considerable differences among belts and along strike within individual belts. Note that a single cross-sectional view of a fold-and-thrust belt results to be insufficient to resolve and outline the entire complexity of the belt. The integration of restoration techniques and three-dimensional modelling is thus a crucial and necessary step for characterizing the structural disposition of a fold-and-thrust belt, reconstructing faults network, and detecting inconsistencies in structural interpretations. In this study, we combined these two approaches to unravel how the Doldenhorn Nappe reached its current structural disposition. This appendix presents: (i) the methodology followed for the cross-sections restoration; (ii) the cross-section restoration of the β-β' and γ-γ' transects; and (iii) the map-view of the Doldenhorn Basin at 30 Ma and of the extruded Doldenhorn Nappe at 20 Ma.

2 Cross-section restoration

To reconstruct the 4D evolution of the Doldenhorn Nappe during the Alpine collision

(30 – 0 Ma) four NNW-SSE cross-sections: α–α', β-β', γ-γ', δ-δ' (see traces in Fig. 3.4) have been selected for retro-deformation. Section coordinate Points (EPSG: 4326 WGS 84):

α (Long.: 7°28'17"/ Lat.: 46°33'23") α' (Long.: 7°39'56"/ Lat.: 46°12'38")

β (Long.: 7°38'26.5"/ Lat.: 46°37'54.5") β' (Long.: 7°56'60"/ Lat.: 46°18'4")

γ (Long.: 7°44'59"/ Lat.: 46°40'56.7") γ' (Long.: 8°2'24.7"/ Lat.: 46°22'12.5")

δ (Long.: 7°51'37.7"/ Lat.: 46°43'48.7") δ' (Long.: 8°8'14"/ Lat.: 46°25'59")

The four cross-sections were retro-deformed by performing line- (i.e. for the basement-cover contact) and area-balancing (i.e. for the Doldenhorn Nappe units) in ArcGIS (ESRI's ArcGIS, v.10.8) software (Fig. B5) following an approach based on the recent contributions of Boutoux et al (2014) and Bellashsen et al. (2012). During restoration, we assumed that there was no material displacement outside areas bounded by both stratigraphic interfaces and fold axial surfaces of the Doldenhorn Nappe. Furthermore,
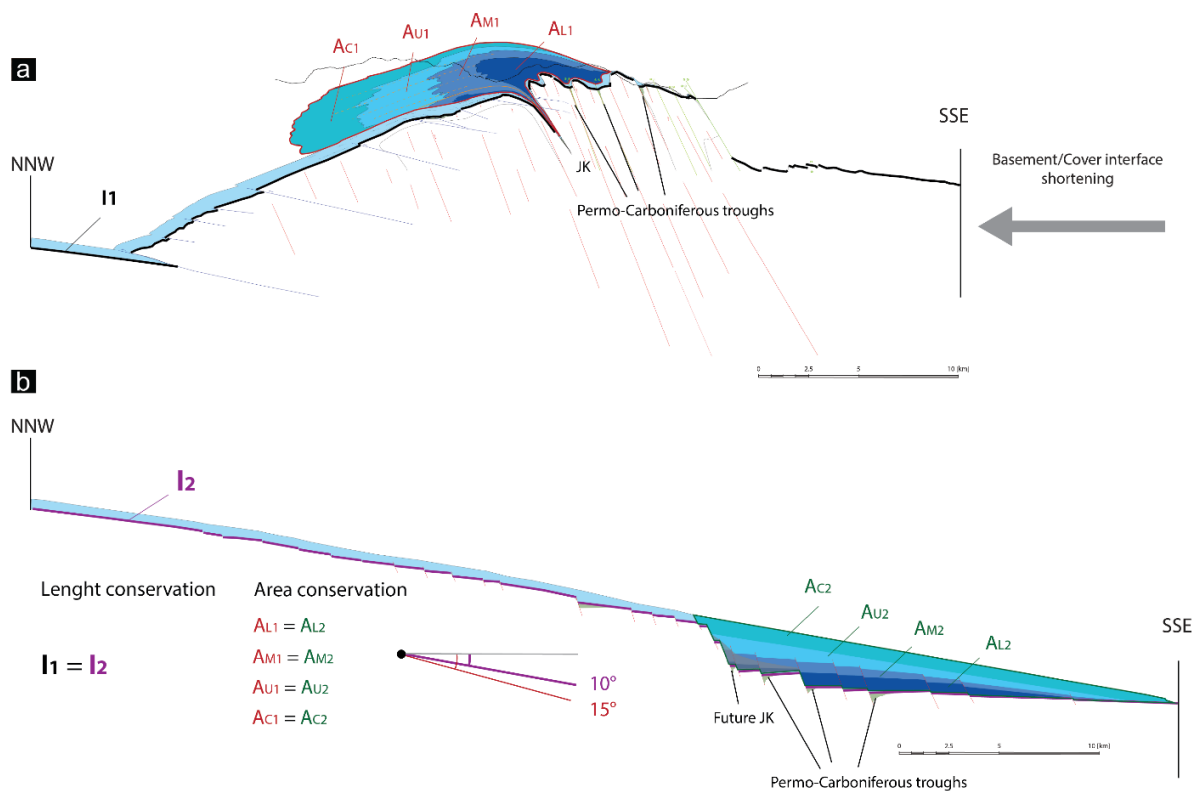
Figure B5 – Cross-section restoration of the Doldenhorn Nappe. The restoration was performed assuming: (1) area conservation of the units of the sedimentary cover (A_C; A_U; A_M; A_L), and (2) conservation of the sedimentary cover/basement interface length (I). (A) Cross-section of the current structural disposition of the Doldenhorn Nappe and basement units. (B) Restored cross-section. The Doldenhorn Basin was restored assuming a bending of ~10° of the European plate. The throw of the northernmost Mesozoic bounding fault was constrained by the length of the 'Jungfrau Keil' (JK, see discussion chapter 5). The presence of additional Mesozoic normal faults was inferred by the occurrence of Permo-Carboniferous troughs. Such pre-existing crustal structures controlled the localization of normal faulting.

as the section strikes parallel to the Alpine stretching lineations, area conservation during Alpine shortening (i.e., Handegg; Pfaffenchopf; NNW-SSE) appears to be a robust assumption. The only exception concerned the Oberaar strike-slip deformation of the basement units (Wehrens et al. 2016, 2017). However, this phase was only active from 12 Ma onwards and restricted to the southern domains of the investigated area, where no Doldenhorn Nappe sediments accumulated (implying therefore maintenance of the Doldenhorn Nappe volumes throughout the entire Alpine deformation). The Triassic layers of the autochthonous sedimentary cover were used as proxies to

characterize the basement top shape and to quantify basement shortening. The top basement was restored assuming a precollisional geometry of the Doldenhorn Basin located on an asymmetric half-graben on the proximal part of the European passive continental margin, being bent by ~10° (Fig. B5b) underneath the tectonically active boundary of the overriding plate (see Nibourel et al. 2018 and 2021). Depth constrains and geometry of the Basin at 30 Ma have been obtained by retrodefroming the Alpine structures to an assumed European passive margin bent 10° towards the SSE. The obtained depth of the Doldenhorn Basins are
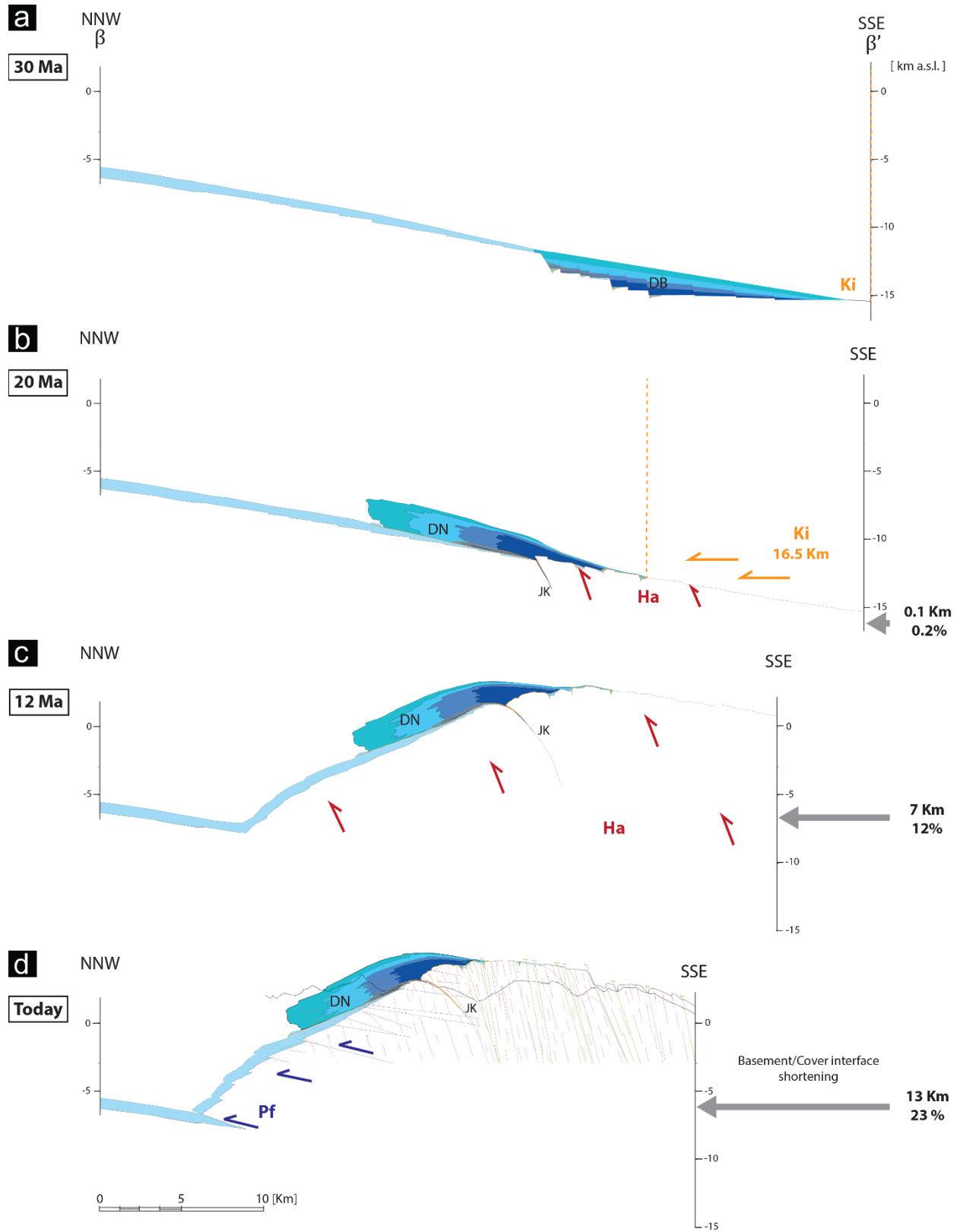
152

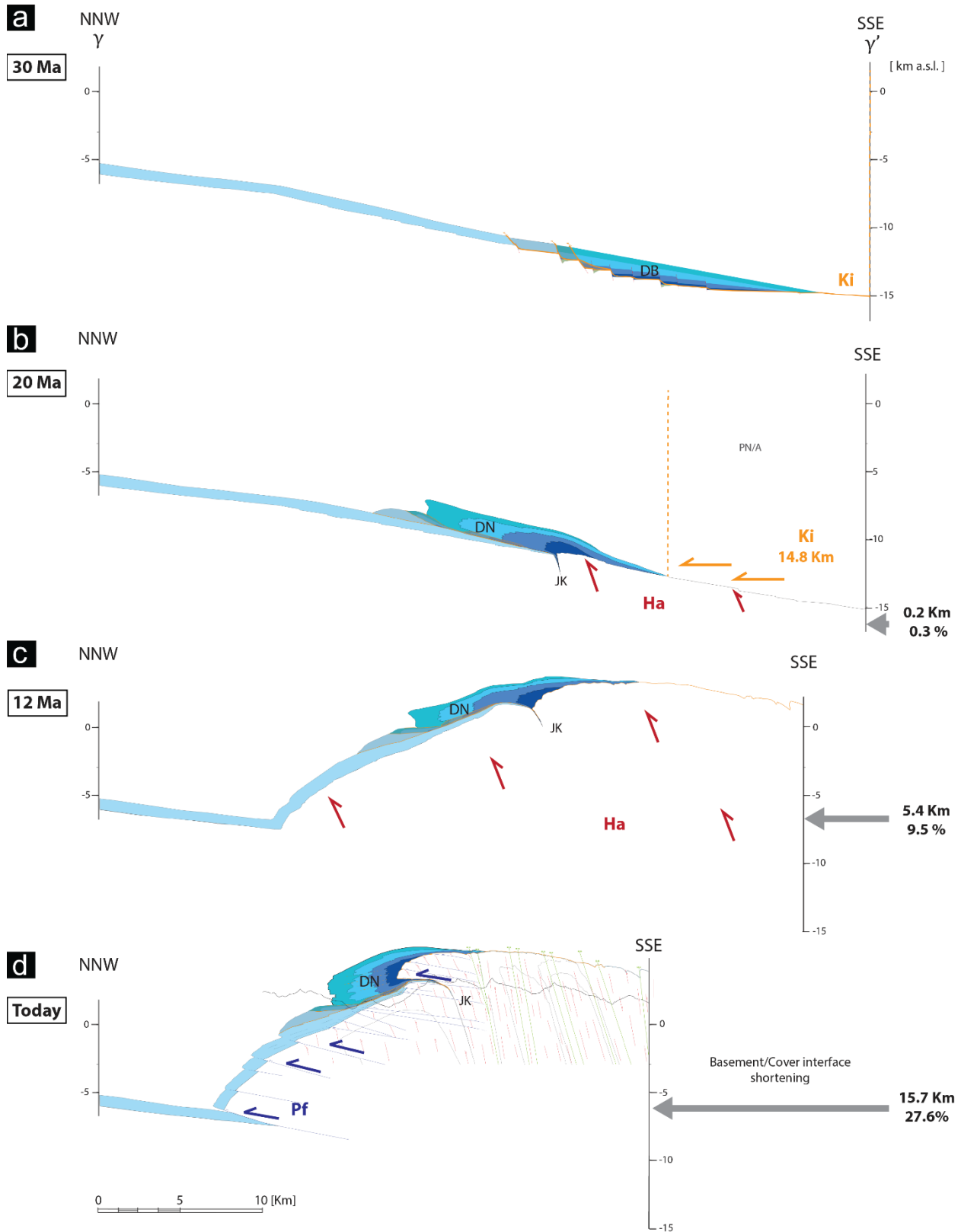**Figure B6** – Cross-section restoration of the β-β' transect from 30 Ma to Today.

Figure B7 – Cross-section restoration of the γ-γ′ transect from 30 Ma to Today.

in agreement with peak temperature studies performed in the area (e.g., Berger et al. 2017). The throw of the northern bounding fault has been constrained by the wedge length of the 'Jungfrau Keil' (e.g., Fig. B5a). Then, the Jurassic Cretaceous and Cenozoic layers were restored considering constant areas (Fig. 3.5).

Practically, the restoration was performed by retrodeforming separately the three Alpine deformation phases which have been widely described in the literature (Pfaffenchopf, Handegg, and Kiental see chapter 2. Geological setting). This resulted in three restoration time steps:

1   *Today to 12 Ma:* retro-deformation of the displacement along the youngest northwest vergent thrust deformation of the Aar Massif (Pfaffenchopf structures) (e.g Fig. B6d to c).

2   *12 to 20 Ma:* retro-deformation of the reverse-steep fault-related exhumation of the Aar Massif (Handegg phase) and the overlying nappe stack, while using the sedimentary-cover contact as marker horizon (e.g., Fig. B6c to b).

3   *20 to 30 Ma:* retro-deformation of the Kiental phase. Herein, the location of Permo-Carboniferous zones and sediment wedges (Figs. 3.1,3.3 and 3.4) served as a marker allowing us to reconstruct the locations of syn-rift faults utilized during the aperture of the Doldenhorn Basin (e.g., Figs. B5b and B6b to a) Furthermore due to stretching parallel to fold axes as well as related to internal ductile deformation of the sedimentary units might have occurred. Therefore, the indication of the sediment thickness within the basin reconstruction is minimum estimate.

2.1 *Cross-section restoration and tectonic evolution of sections ϐ-ϐ' and γ-γ'*

In the following paragraph, we present the results of the retrodeformation of sections β-β'

(Fig. B6) and γ-γ' (Fig. B7) as evolutionary steps, starting from the initiation of Alpine deformation to the present-day configuration. For the description of the deformation and emplacement of the Doldenhorn Nappe along the sections, see the Results and Discussion in Chapter II (3.4 and 3.5).

3 Doldenhorn Basin map-view

The cross-sections representing the abovementioned stages were digitalized in Move^TM. A 3D model of each retrodeformation stage was then generated by applying 3D interpolation and meshing techniques (spline curve method) within the digitalized sections. From the 3D model of the investigated area at 30 and 20 Ma, a Map view was exported and two maps were generated (Figs. B8 and B9):

1   *Map-view of the top-crystalline of the Doldenhorn Basin at 30 Ma: (Fig. B8)* such top crystalline map-view allows improved visualization of the distribution of the Permo-Carboniferous half-grabens in the basin and the reconstructed faults network. The map-view reveals indeed the asymmetric geometry of the Doldenhorn Basin induced by a series of NE-SW to E-W striking and SE to S dipping rotational high-angle normal faults (linked by relay ramps and connecting faults).

2   *Map-view of the extruded Doldenhorn Nappe at 20 Ma (Fig. B9):* this map-view allows visualizing the distribution of horizontal shortening along the strike of the nappe recorded during the Kiental deformation. Furthermore, the non-cylindrical shape of the Doldenhorn Nappe is also expressed by the nappe salients that display a characteristic arcuate shape converging towards the end of the basin.
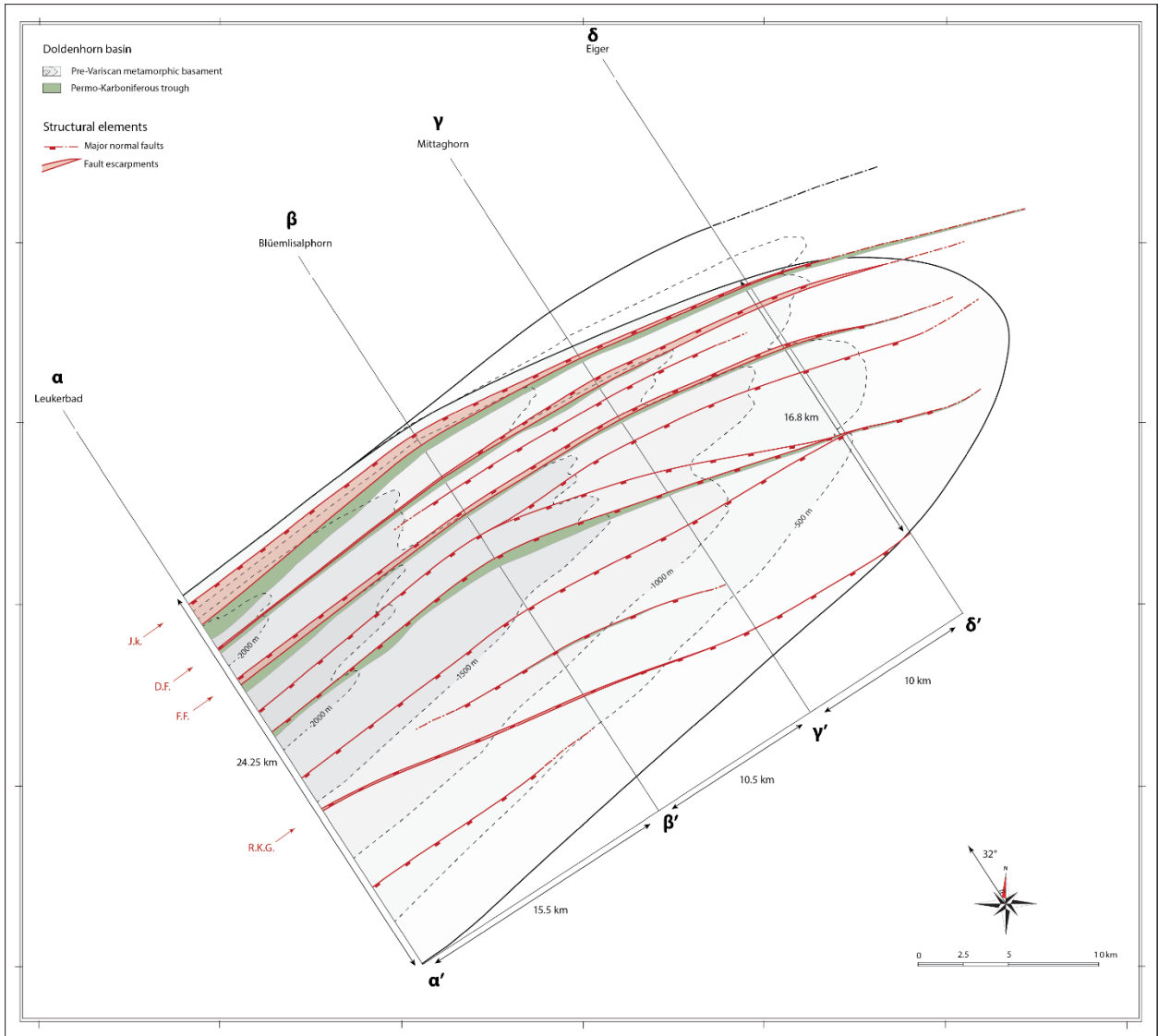
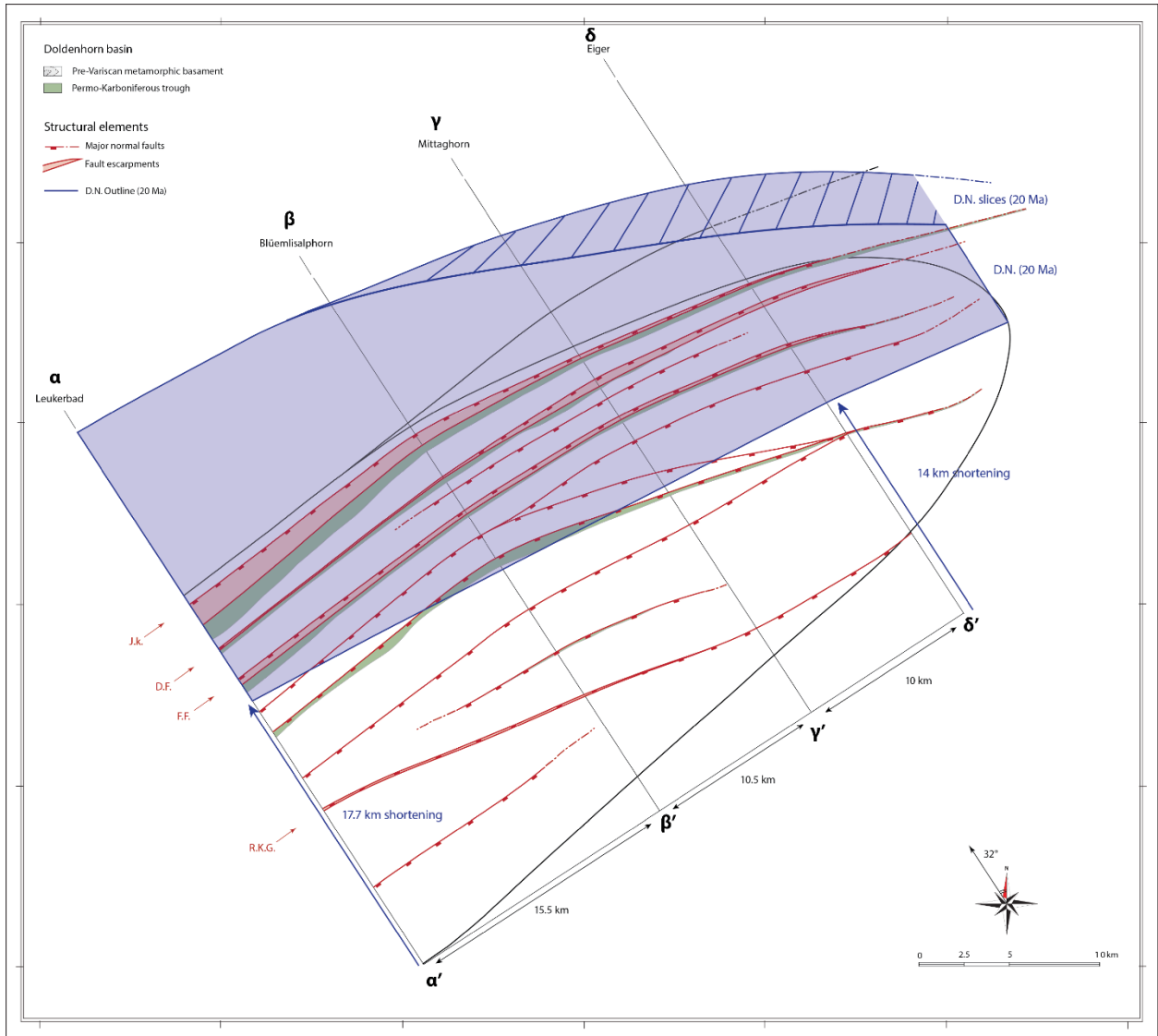**Figure B8** – Map view of the top of the top crystalline units of the reconstructed Doldenhorn Basin at 30Ma.

Figure B9 – Map view of the extruded Doldenhorn Nappe (blue field) at 20Ma.

REFERENCES

Bellahsen, N., Jolivet, L., Lacombe, O., Bellanger, M., Boutoux, A., Garcia, S., Mouthereau, F., Le Pourhiet, L., Gumiaux, C., 2012. Mechanisms of margin inversion in the external Western Alps: Implications for crustal rheology. Tectonophysics 560, 62–83.

Boutoux, A., Bellahsen, N., Lacombe, O., Verlaguet, A., Mouthereau, F., 2014. Inversion of pre-orogenic extensional basins in the external Western Alps: structure, microstructures and restoration. Journa of Structural Geology 60, 13–29.

Ebert, A., Herwegh, M., Berger, A., Pfiffner, A., 2008. Grain coarsening maps for polymineralic carbonate mylonites: a calibration based on data from different Helvetic nappes (Switzerland). Tectonophysics 457, 128–142.

Nibourel, L., Berger, A., Egli, D., Luensdorf, N. K., Herwegh, M., 2018. Large vertical displacements of a crystalline massif recorded by Raman thermometry. Geology 46 (10), 879–882.

Nibourel, L., Rahn, M., Dunkl, I., Berger, A., Hermann, F., Diehl, T., Heuberger, S., Herwegh, M., 2021. Orogen-parallel migration of exhumation in the eastern Aar Massif revealed by low-T thermochronometry. J. Geophys. Res. Solid Earth 126 e2020JB020799.

Wehrens, P., Berger, A., Peters, M., Spillmann, T., Herwegh, M., 2016. Deformation at the frictional-viscous transition: Evidence for cycles of fluid-assisted embrittlement and ductile deformation in the granitoid crust. Tectonophysics, 693, 66-84.

Wehrens, P., Baumberger, R., Berger, A., Herwegh, M., 2017. How is strain localized in a meta-granitoid, mid-crustal basement section? Spatial distribution of deformation in the central Aar massif (Switzerland). Journal of structural geology, 94, 47-67.

Appendix C1

Structural investigation

The control of collisional tectonics over valley morphology: the case of the largest Glacier in the European Alps

Ferdinando Musso Piantelli[1&2*], Sandro Truttmann[1], and Marco Herwegh[1]

[1] Institute of Geological Sciences University of Bern, Baltzerstrasse 1+3, 3012 Bern, Switzerland

[2] Federal Office of Topography swisstopo, Seftigenstrasse 264, 3084 Bern, Switzerland

1. Structural investigation

The analysis of fault structures was conducted at specific field locations within the investigated area as well as several other locations in the vicinity of the area. In addition, we rely on literature data on the Alpine structural evolution of the Aar Massif (see Tab. S1, and references therein) across the entire massif. In light of relative timing, kinematics, and orientations of faults, *three major Alpine deformation phases* have been described in previous studies for the Alpine collision and associated exhumation of the crystalline basement units (Tab. C1):

Reverse faults:

22 to 12 Ma – steep-reverse shearing and faulting of the basement units that led to the buoyancy-driven sub-vertical extrusion and exhumation of the Aar Massif (Handegg phase; Table 1, and references therein). The deformation initiated at peak temperature metamorphic condition that in the southern region of the Aar Massif reached 450°C (Wehrens et al., 2016; Herwegh et al., 2020) and pressure of 6.5 kbar (Goncalves et al., 2012) corresponding to depths of ~18-20 km. At such metamorphic conditions the basement units dominantly deformed by ductile deformation, with occurrence of mylonites and ultramylonites

Age (Ma)	Deformation phase	Deformed units	Deformation style	References
22 - 12	Reverse faults *(Handegg)*	Basement *(Aar/Gastern Massifs)*	Steep-reverse S-dipping shearing and faulting	*Herwegh and Pfiffner, 2005; Herwegh et al. 2017, 2020; Wehrens et al., 2016; Berger et al., 2017*
< 12	Thrust faults *(Pfaffenchopf)*	Basement *(Aar/Gastern Massifs)*	NW-vergent thrusting along moderately SE dipping shear planes (Northern units)	*Wehrens et al., 2017; Mair et al., 2018; Herwegh et al., 2020; Musso Piantelli et al., 2022*
< 12	Strike slip faults *(Oberaar)*	Basement *(Aar/Gastern Massifs)*	Dextral Strike-slip shearing and faulting (Southern units)	*Wehrens et al., 2016, 2017; Herwegh et al., 2020*

Table C1. Compilation of deformation phases that affected the investigated area during late-stage Alpine collision (22 to 0 Ma; modified after Musso Piantelli et al., 2022).
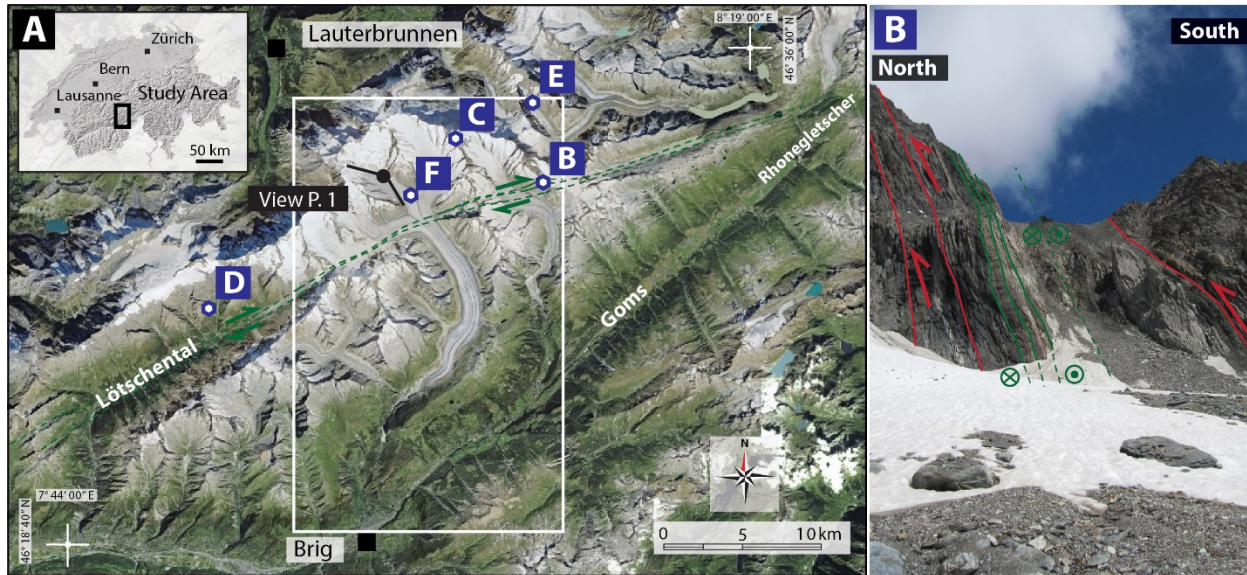
Figure C1. (A) Overview of the study area where locations of the viewpoints and the field image of Figs. 4.3 and 4.4, in the main text, have been collected. (B) (Field location indicated as B in plate A; Coordinates: Long.: 8°8'23"/ Lat.: 46°31'11"). Basement units are dissected by steep reverse faults (Handegg phase) and strike-slip faults (Oberaar deformation). Such a strike-slip system has been interpreted to be present at Konkordiaplatz and was also observed further west in the Lötschental valley (Musso Piantelli et. al, 2022).

(Wehrens et al., 2016; 2017). Subsequently, with ongoing exhumation, the basement units reached shallower crustal level and brittle deformation localized within the ductile precursors forming cataclasites, fault gauges and breccias.

Thrust faults:

Between 12 Ma and today - The northern part of the Aar Massif experienced NW-vergent thrusting along moderately SE dipping shear planes that cut through basement-cover contacts (Pfaffenchopf phase; Table 1, and references therein. The thrusts are characterized by frictional-viscous transition, with formation of low-T mylonites and breccias.

Strike slip faults:

Between 12 Ma and today - In the central and southern part of the Aar Massif Handegg structures were ductilely reactivated by retrograde dextral strike-slip sense of shear

faults and shear zones (Oberaar phase of Wehrens et al., 2017; Table 1, and references therein). Deformation initiated at low greenschist facies conditions.

A dataset of 546 fault measurements (dip direction/dip angle for fault planes; dip direction/plunge for stretching lineations; shear sense indicators, if available in the field) of the Alpine deformation phases was collected for this study (Fig. 4.2). The Handegg deformation phase is present in the entire investigated area (Northern, Central, and Southern domains; Fig. 4.1C) and is subdivided into two major fault plane trends: NNW-SSE trend (mean 123/64); and NW – SE trend (mean 154/64) (Fig. 4.2B). Pfaffenchopf deformation is present in the northern domain (Fig. 4.1C) where NW-vergent thrusts (mean 122/25; Fig. 4.2A) cut through the Handegg structures (Figs. C2 and C3). Oberaar deformation is present in the central and
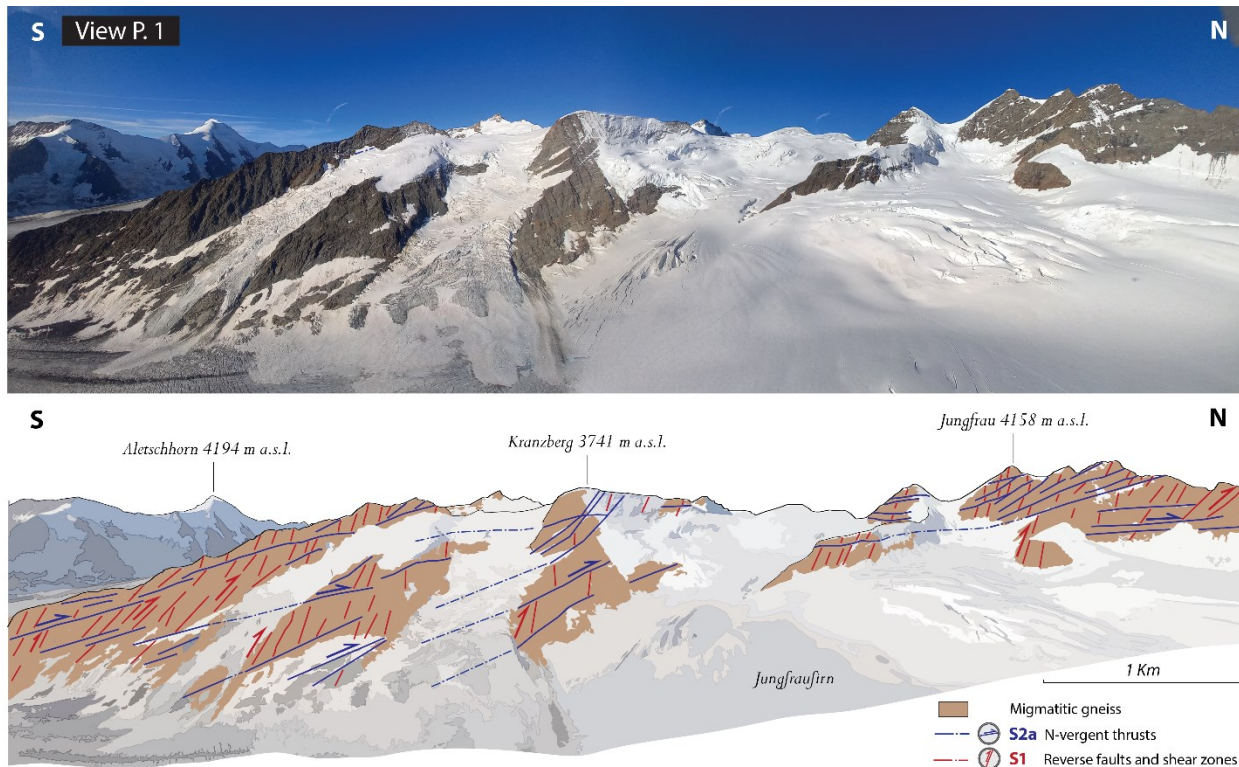
Figure C2. Panoramic view and geological interpretation of the northern domain of the investigated area. The thrust structures cut the reverse fault structures. Note the increase in dip angle of the thrust structures when approaching the transition zone located just south of the image.

southern domain only (Fig. 4.1C), where mainly the NW − SE oriented Handegg faults were reactivated in a dextral strike-slip to oblique-slip sense (average 152/65 dip direction/dip angle) (Figs. 4.2C and C1).

As highlighted by the colour code of the poles in Fig 4.2A, the Pfaffenchopf thrust structures become progressively steeper from North to South cutting gradually with smaller angles than the Handegg structures (Figs. C8). The domain where the thrust structures become almost parallel to the Handegg structures was identified as the transition zone. In such locations, also the appearance of first strike-slip structures was identified. We notify that due to glacial coverage, evidence for occurrence of large-scale strike-slip shearing has to be projected from side-line field locations indicated in Fig. C1 in the case of Konkordiaplatz. Indeed such a strike-slip

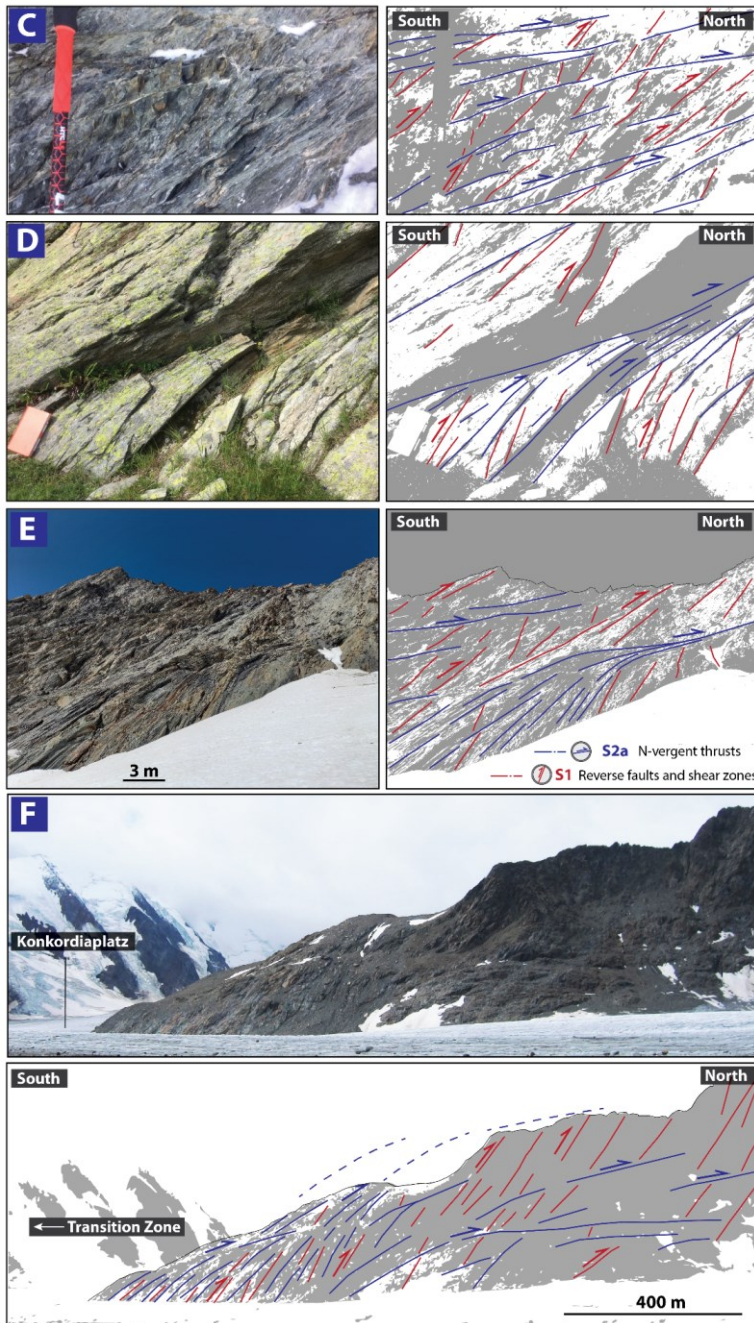system was also observed further West in the Lötschental valley (Musso Piantelli et. al, 2022).

Figure C3. Sequence of field images and corresponding structural interpretations (drawings overlaying grey tone images) from the cm to the km scale showing the thrust structures and their change in orientation approaching the transition zone. (C) (field location indicated as C in Fig. C1 plate A; Coordinates: Long.: 8°03'56"/ Lat.: 46°32'55") Gneiss unit dissected by a pervasive thrust deformation that cuts the Handegg structures. (D) (Field location indicated as D in Fig. C1 plate A; Coordinates: Long.: 7°51'24"/ Lat.: 46°27'07") Gneiss unit dissected by an thrust structure that progressively cuts the Handegg structures to smaller angles. (E) (Field location indicated as E in Fig. C1 plate A; Coordinates: Long.: 8°07'14"/ Lat.: 46°34'37") Same structural scenario of plate D but observed at a larger scale and at a different field location. The gneiss unit is dissected by an thrust structure that progressively cuts the Handegg structures to smaller angles. (F) (Field location indicated as F in Fig. C1 plate A; Coordinates: Long.: 8°01'28"/ Lat.: 46°31'00") The same transition was observed at the D and E plates but observed at the km scale and approaching the transition zone at Konkordiaplatz.

REFERENCES

Berger, A., Wehrens, P., Lanari, P., Zwingmann, H., Herwegh, M., 2017. Microstructures, mineral chemistry and geochronology of white micas along a retrograde evolution: an example from the Aar massif (Central Alps, Switzerland). Tectonophysics 721, 179–195.

Cardello, G.L., Almqvist, B.S., Hirt, A.M., Mancktelow, N.S., 2016. Determining the timing of formation of the Rawil Depression in the Helvetic Alps by palaeomagnetic and structural methods. Geol. Soc. Lond., Spec. Publ. 425 (1), 145–168.

Goncalves, P., Oliot, E., Marquer, D., & Connolly, J. A. D. (2012). Role of chemical processes on shear zone formation: an example from the Grimsel metagranodiorite (Aar massif, Central Alps).Journal of Metamorphic Geology, 30 (7), 703-722.

Herwegh, M., Pfiffner, O.-A., 2005. Tectono-metamorphic evolution of a nappe stack: a case study of the Swiss Alps. Tectonophysics 404 (1–2), 55–76.

Herwegh, M., Berger, A., Baumberger, R., Wehrens, P., Kissling, E., 2017. Large-scale crustal-block-extrusion during late Alpine collision. Sci. Rep. 7 (1), 1–10.

Herwegh, M., Berger, A., Glotzbach, C., Wangenheim, C., Mock, S., Wehrens, P., Baumberger, R., Egli, D., Kissling, E., 2020. Late stages of continent-continent collision: timing, kinematic evolution, and exhumation of the Northern rim (Aar Massif) of the Alps. Earth Sci. Rev. 200, 102959 https://doi.org/10.1016/j.earscirev.2019.102959.

Mair, D., Lechmann, A., Herwegh, M., Nibourel, L., Schlunegger, F., 2018. Linking Alpine deformation in the Aar Massif basement and its cover units–the case of the Jungfrau–Eiger mountains (Central Alps, Switzerland). Solid Earth 9, 1099–1122.

Musso Piantelli, F., Mair, D., Berger, A., Schlunegger, F., Wiederkehr, M., Kurmann, E., Moeri, A., Baumberger, R., and Herwegh, M. (2022). 4D reconstruction of the Doldenhorn nappe-basement system in the Aar massif: Insights into late-stage continent-continent collision in the Swiss Alps. Tectonophysics, 843, 229586.

Nibourel, L., Berger, A., Egli, D., Heuberger, S., & Herwegh, M. (2021). Structural and thermal evolution of the eastern Aar Massif: insights from structural field work and Raman thermometry. Swiss journal of geosciences, 114(1), 9.

Wehrens, P., Berger, A., Peters, M., Spillmann, T., Herwegh, M., 2016. Deformation at the frictional-viscous transition: evidence for cycles of fluid-assisted embrittlement and ductile deformation in the granitoid crust. Tectonophysics 693, 66–84.

Wehrens, P., Baumberger, R., Berger, A., Herwegh, M., 2017. How is strain localized in a meta-granitoid, mid-crustal basement section? Spatial distribution of deformation in the central Aar massif (Switzerland). J. Struct. Geol. 94, 47–67.

Appendix C2

Methods: remote sensing, hillslope morphology analysis, and Schmidt hammer profiles

The control of collisional tectonics over valley morphology: the case of the largest Glacier in the European Alps

Ferdinando Musso Piantelli[1&2*], Sandro Truttmann[1], and Marco Herwegh[1]

[1] Institute of Geological Sciences University of Bern, Baltzerstrasse 1+3, 3012 Bern, Switzerland

[2] Federal Office of Topography swisstopo, Seftigenstrasse 264, 3084 Bern, Switzerland

The methodology employed for this study comprises three major techniques: (i) remote sensing; (ii) hillslope morphology analysis; and (iii) Schmidt hammer field investigations.

1. Remote sensing

To quantify changes in the fault frequencies within the investigated area, remote sensing analysis was applied at two different scales: (1) large-scale; and (2) detailed-scale.

The frequency of the large-scale structures in the area was investigated remotely with a scan line approach (Brooks and Allmendinger, 1996) on digital orthophotos (swiss image with a raster resolution of 0.5 x 0.5 m; provided by swisstopo; Bundesamt für Landestopographie Switzerland, Licence 5708353983), and hillshade maps derived by a 2 x 2 m resolution DEM (swissALTI3D, version 2013 provided by swisstopo; Bundesamt für Landestopographie Switzerland, Licence 5708352793). Such scan lines consisted of a sequence of individual NW-SE trending segments on the valley sides' exposed bedrock, oriented perpendicular to the main trend of the structures (Fig. C4A). Each intersection of the scan line with a linear morphological incision detectable at the fixed scale of 1:2'500 and continuous for 100 m across the scan line was collected (Fig. C4B). Following previous studies in the Aar Massif (e.g., Wehrens et al. 2016, 2017; Herwegh et al. 2020; Baumberger et al. 2022; Nibourel et al., 2021) such continuous incisions were interpreted as faults, an assumption which was verified and testified in the field. For this purpose, detailed logging of the lithologies and fault structures was conducted and compared to what was remotely detected at the large and detailed scale at field locations 1, 2, 3, and 4 (See following Schmidt Hammer paragraph). The collected intersection lines were then vertically projected, i.e. parallel to the main NE-SW trending fault structures, onto the NE-SW AA' profile (Tab. S2) The frequency distribution of the faults along the AA' profile was then analyzed and reproduced in a frequency histogram (Fig. 4.3A). The bin was
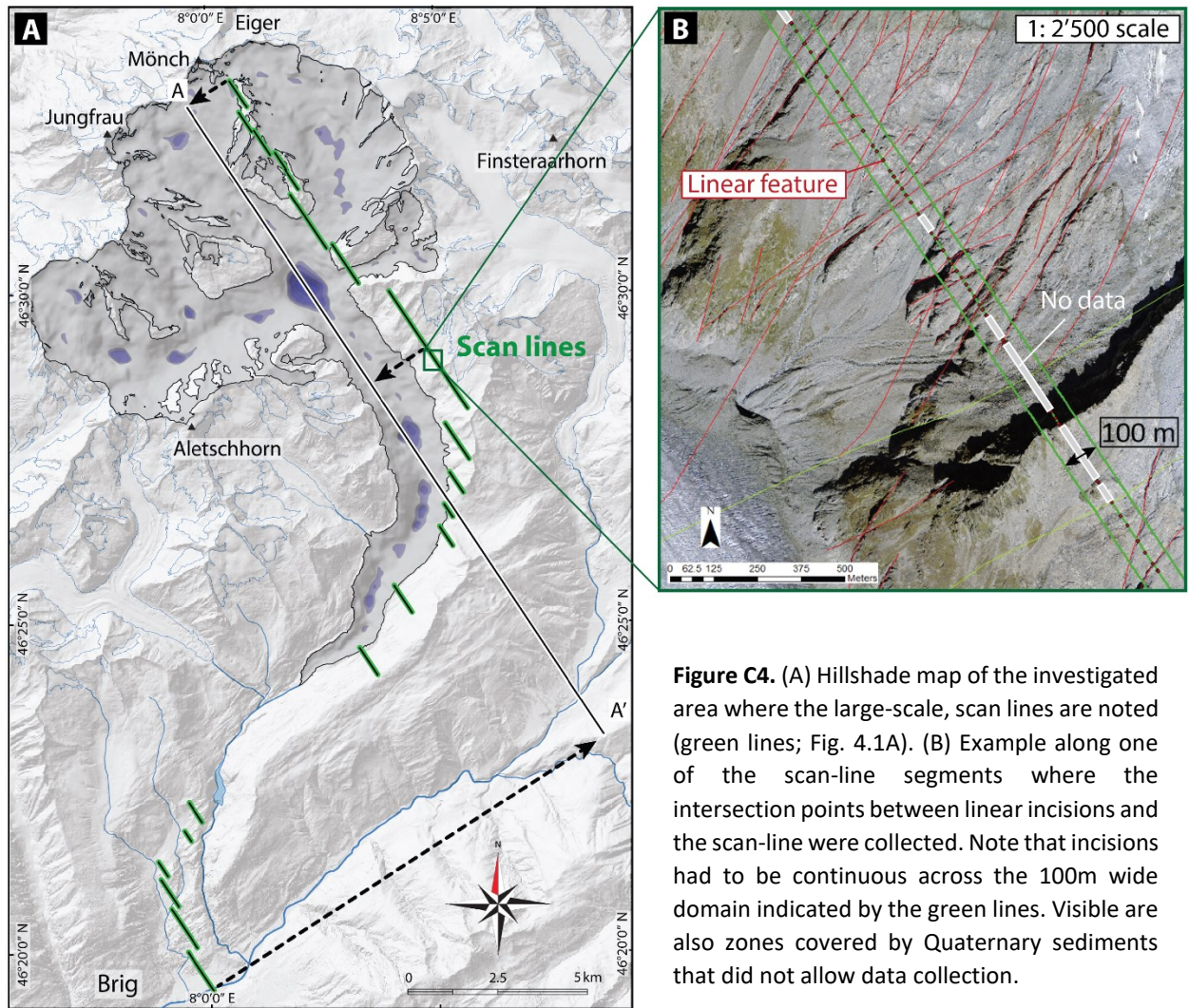
Figure C4. (A) Hillshade map of the investigated area where the large-scale, scan lines are noted (green lines; Fig. 4.1A). (B) Example along one of the scan-line segments where the intersection points between linear incisions and the scan-line were collected. Note that incisions had to be continuous across the 100m wide domain indicated by the green lines. Visible are also zones covered by Quaternary sediments that did not allow data collection.

fixed at the size of 300 m; the gray bars indicate no-data areas, i.e., covered by quaternary deposits. Furthermore, the plot is overlapped by a density curve (Kernel Density Estimation, Fig. 4.3A orange line) to visualize the trend of the distribution. In calculating the density curve, the no-data areas were not included.

The spacing of the structures at the detailed-scale was analyzed over Unmanned Aerial Vehicles -based (DJI Mavic 2 Pro with Hasselblad L1D-20c camera) mosaics at the aforementioned four field locations, 1, 2, 3, and 4 (see Figs. 4.1 and C5). The collected pictures georeferenced with the internal GPS of the drone were processed and analyzed in the software Agisoft Metashape. The derived orthomosaics comprehended orthophotos (raster resolution of 2.5 x 2.5 cm) and hillshades derived from 2.5 x 2.5 cm resolution DEM. Similar to the large-scale approach, also at the detailed-scale scan lines were oriented perpendicular to the main trend of the faults (Fig. C5):

The detailed-scale profiles were oriented perpendicular ($\alpha\alpha'$; $\beta\beta'$; $\gamma\gamma'$; and $\delta\delta'$) and parallel ($\epsilon\epsilon'$; $\zeta\zeta'$; and $\eta\eta'$) to the main structural trend (Fig. C5 and Tab. C2).

166

Profile		Long.	Lat.	Profile length
A-A′	A	7°59'26"	46°32'48"	21.5 km
	A′	8°8'34"	46°23'18"	
B-B′	B	7°58'59"	46°32'41"	30.3 km
	B′	8°0'45"	46°19'46"	
α-α′	α	7°59'30	46°30'27	90 m
	α′	7°59'31	46°30'24	
β-β′	β	8°4'35"	46°29'28"	950 m
	β′	8°5'11"	46°29'10"	
γ-γ′	γ	8°5'12"	46°26'40"	470 m
	γ′	8°5'29"	46°26'31"	
δ-δ′	δ	8°3'19"	46°24'35"	330 m
	δ′	8°3'27"	46°24'26"	
ε-ε′	ε	8°4'47"	46°29'18"	175 m
	ε′	8°4'52"	46°29'22"	
ζ-ζ′	ζ	8°5'15"	46°26'34"	154 m
	ζ′	8°5'19"	46°26'38"	
η-η′	η	8°3'17"	46°24'29"	327 m
	η′	8°3'29"	46°24'36"	

Table C2. Table containing the coordinates information and length of the investigated profiles.

Fig. C5B shows a good overlap between the UAV orthomosaic/DEM and the large large-scale dataset, proving a correct georeferencing of the collected drone images. Based on the sampling strategy at the detailed-scale, spatial 2D fault patterns were obtained, which in turn provided information about the average 2D block sizes available for channel and slope erosion processes (Fig. C5). Along these scan-lines, the spacing of faults was derived and presented as probability density plots, fitted by a gamma distribution (Fig. 4.4). At locations 2, 3, and 4 the mean values of fault spacing perpendicular and parallel to the main structural trends were then used to estimate the 2D block sizes at the specific field locations (see Fig. 4.4 in the main text).

2. Hillslope morphology analysis

To analyze the hillslope morphology of the valley both the hillslope angle and the relief were derived from 120 topographic valley transects sampled over a 2 x 2 m resolution DEM (swissALTI3D, version 2013 provided by swisstopo). The transects were oriented perpendicular to the main valley axis profile (BB′ Figs. 4.3B, C8A, and Tab. C2) with a spacing of 250 m.

The average hillslope angle and relief were derived on the right and left sides of the valley along each valley transect (Figs. C8B and C). The relief has been calculated as the difference between the highest and lowest point within the valley's watershed (Fig. C8B). The hillslope angle was derived by measuring the inclination angle of the line fitting between the highest and lowest point within the valley's watershed (Fig. C8B). In Fig. 4.2B, in the main text, the two resulting moving average lines have been vertically projected onto the AA′ profiles to render comparable the valley morphology to the structural frequency variations in the area.

3. Schmidt hammer profiles

Field-based rock hardness analyses were performed using a Schmidt hammer (Classic 'N' type) along the scan lines, at locations 1, 2, 3, and
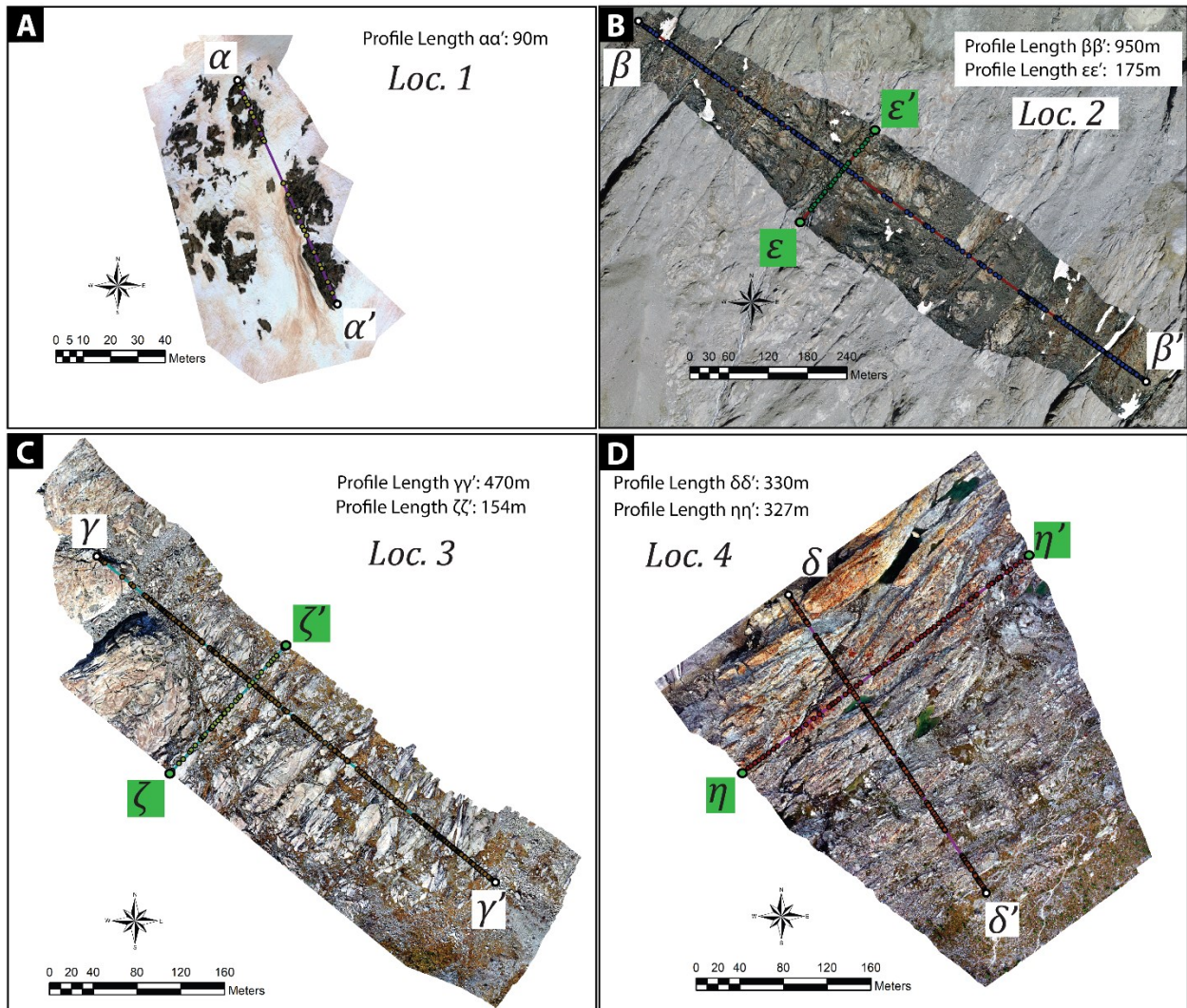
167

Figure C5. Figure collection of the UAV-based orthomosaics collected in the field at the four field locations. (A) Location 1, with profile αα'. (B) Orthomsaic of the field location 2 with the scan lines ββ' (perpendicular to the main structural trend) and εε' (parallel to the main structural trend). The orthomosaic shows no significant offset with the large-scale satellite image in the background. (C) Location 3 with two profiles, γγ' and ζζ', respectively, oriented perpendicular, and parallel to the main structural trend. (D) Location 4, with the δδ' and ηη' scan-lines.

4 (Fig. 4.1A). The rebound values were measured with a regular 1 m sampling equidistance along the αα', ββ', γγ', and δδ' scan lines (Fig. C9), consistently on freshly polished surfaces parallel to the main foliation of the rock or the fault structures. The field locations were chosen in close vicinity to the vertically retreating glacier and within the Little Ice Age limit (Kelly et al., 2004) to ensure minimal weathering of the now non-ice-shielded outcrops. The lithologies along the lines were also logged following the approach of a Porphyry copper mapping method named 'Anaconda' (Einaudi, 1997, Fig. C9). This mapping technique consists in selectively mapping rock information observed along a fixed baseline. For this study, using the chest line as the baseline, we mapped and sampled at regular 1 m intervals: (i) the lithology, (ii) the presence of
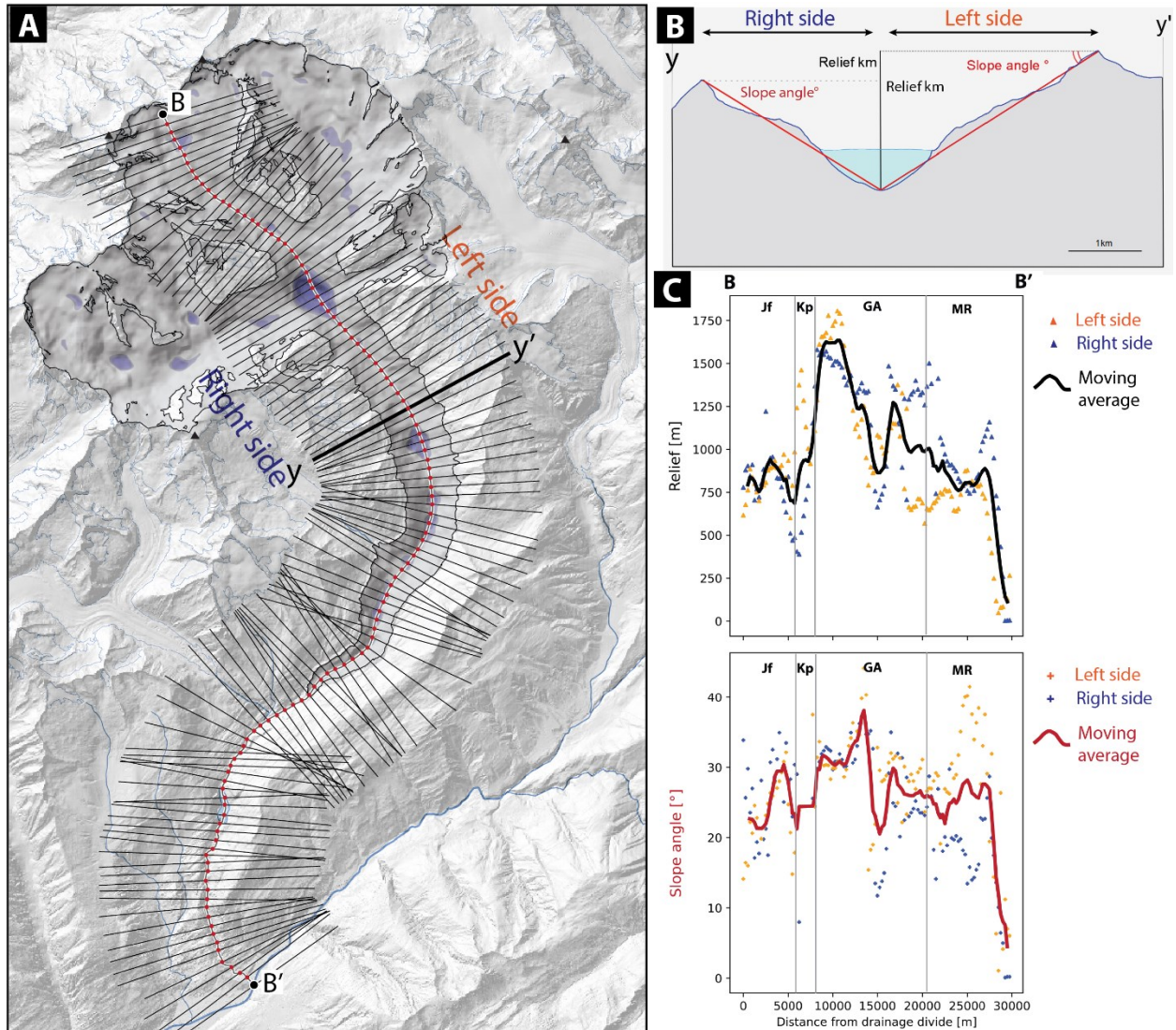
168

Figure C6. (A) Hillshade of the investigated area where the 120 topographic valley transects are noted. Profile BB' follows the valley axes and the transects are oriented perpendicular with a regular spacing of 250 m. (B) Simplified sketch that represents the hillslope angle and valley relief calculations performed along each transect, for the right and left valley sides. (C) Plot of the relief and hillslope angle analysis. From the mean values of the right and left valley sides datasets the moving average was then calculated and displayed.

a fault; and (iii) the Schmidt hammer rebound value. Such mapping and sampling techniques allowed us to test the accuracy of the detailed remote sensing analysis mentioned above. Indeed, in the field, it was possible to confirm the occurrence of remotely detected structures to represent faults, shear zones, or joints. As shown in the example of profile ββ' (Fig. C9B), the detection of fault structures performed with the

remote sensing is largely (green and red triangles Fig. C9B) comparable to what was observed in the field, proofing a good accuracy of the methodology. The presence of structures was detectable with both the rebound values and the direct rock observations in the field. A detailed Schmidt hammer sampling clearly illustrates the difference in rebound values between an intact massive host rock, a
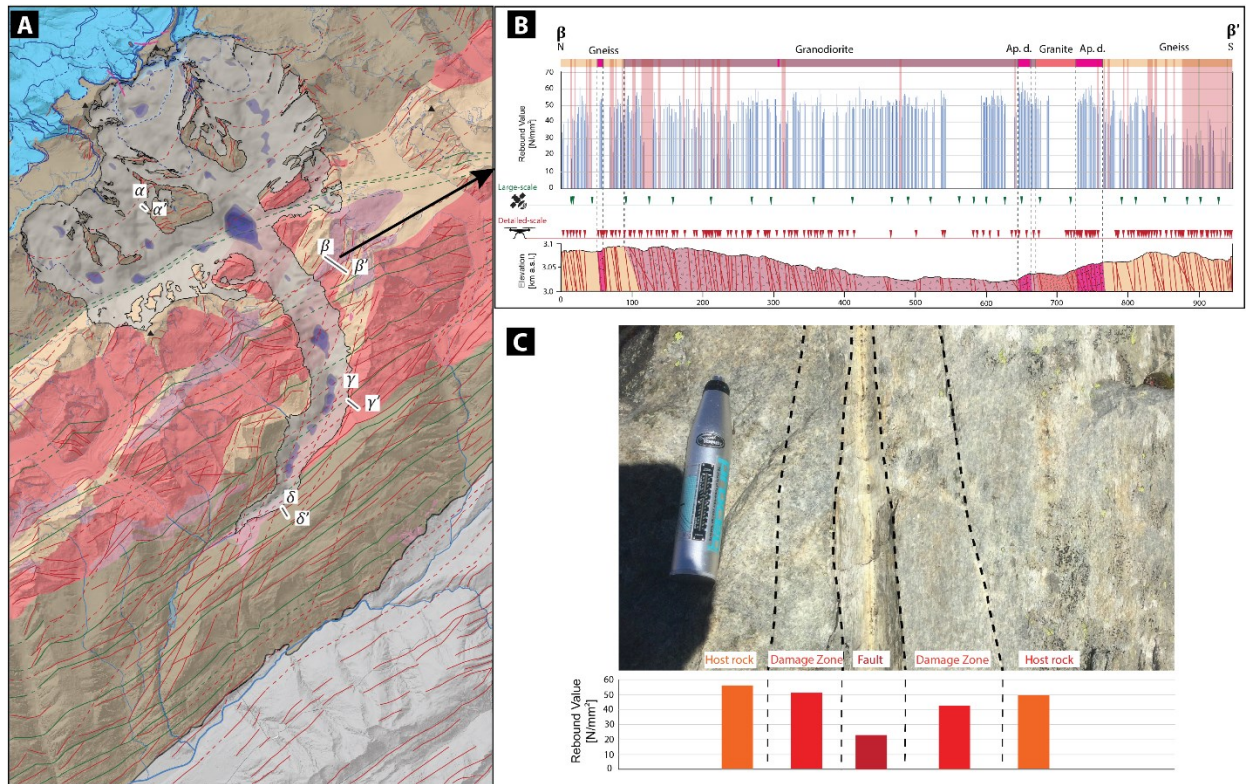
169

Figure C7. (A) Geological map of the study area where the four transects that have been investigated in the field are noted: αα', ββ', γγ', and δδ'. (B) Plate showing one example of datasets collected in the field at each location. The 'Anaconda' mapping technique (Einaudi, 1997) allowed to log the lithologies along the transect noting lithology and presence of fault structures. The profiles also display the remote-sensing collected incisions, which show a good correlation with the faults identified in the field. (C) Exemplary investigation of the transition from an intact massive rock into a faulted domain and associated changes in hardness values. The collected hardness values drop gradually from an average of 55 N/mm^2 (intact rock) to 20 N/mm^2 (faulted domain). In between the damage zones, display an average of 50 N/mm^2.

damage zone, and a faulted domain (Fig. C5C). The rebound values of the hammer display a clear drop in values towards the core of the fault proving a great resolution in detecting the presence of fault structures in the rocks.

REFERENCES

Brooks, B.A., and Allmendinger, R.W., 1996, Fault spacing in the El Teniente Mine, central Chile: Evidence for nonfractal fault geometry: Journal of Geophysical Research, v. 101, p. 13,633–13,653, doi: 10.1029/96JB00800

Einaudi, M. T. (1997). Mapping altered and mineralized rocks: An introduction to the Anaconda method. Unpublished, Stanford University

Declaration of consent

on the basis of Article 18 of the PromR Phil.-nat. 19

Name/First Name: Ferdinando Musso Piantelli

Registration Number: 16-125-437

Study program: PhD in Earth Sciences

Bachelor ☐   Master ☐   Dissertation ☑

Title of the thesis: 4D reconstruction of the Aar Massif: An evolutionary history from a
passive margin to the Central Swiss Alpine valleys

Supervisor: Prof. Marco Herwegh, Prof. Alfons Berger

I declare herewith that this thesis is my own work and that I have not used any sources other than
those stated. I have indicated the adoption of quotations as well as thoughts taken from other authors
as such in the thesis. I am aware that the Senate pursuant to Article 36 paragraph 1 litera r of the
University Act of September 5th, 1996 and Article 69 of the University Statute of June 7th, 2011 is
authorized to revoke the doctoral degree awarded on the basis of this thesis.

For the purposes of evaluation and verification of compliance with the declaration of originality and the
regulations governing plagiarism, I hereby grant the University of Bern the right to process my
personal data and to perform the acts of use this requires, in particular, to reproduce the written thesis
and to store it permanently in a database, and to use said database, or to make said database
available, to enable comparison with theses submitted by others.

Bern, 09.07.2023

Place/Date

Signature

171